Theory of Semiconductor Quantum-Dot Microcavity Lasers

Computational modeling and significance for experimental realization

Dissertation
zur Erlangung des akademischen Grades

doktor rerum naturalium
(Dr.rer.nat.)

genehmigt durch die Fakultät für Naturwissenschaften der
Otto-von-Guericke-Universität Magdeburg

von Dipl.-Phys. Alexander Foerster
geb. am 02.02.1987 in Schönebeck

Gutachter: Prof. Dr. rer. nat. habil. Jan Wiersig
Prof. Dr. rer. nat. Stefan Schumacher

eingereicht am: 15.03.2017
verteidigt am: 19.10.2017

Abstract

This doctoral thesis is concerned with the theoretical description and investigation of semiconductor quantum-dot microcavity lasers with the objective of understanding the results of current experiments and to make predictions for how to further optimize new components.

To accomplish this task, the theory used for description of semiconductor quantum-dot lasers has been thoroughly revised, and a new unified theory is formulated that enables us to see and apply different cluster-expansion approaches in a uniform manner. A known disadvantage of these methods is an increased algebraic effort, which rapidly increases the possibilities of doing the calculations by hand. For this reason, parallel to the newly developed theory, a computer algebra program is developed to carry out these tasks.

In the first half of this thesis, the foundations and the more general theoretical concepts are presented, along with a detailed description of the computer algebra program. To clarify the possibilities and strengths of these new descriptions, two examples of quantum-dot lasers are presented which determine the autocorrelation up to the 5th order. On this basis, it is possible to examine the convergence properties of the theory more precisely. From the physical point of view, however, the concept of the laser threshold can be discussed in detail and, in particular, the properties of lasers without spontaneous losses into the non-lasing modes are investigated, which produce the link to a thresholdless laser.

The second half of the thesis is concerned with the theoretical description of specific experimental situations. Motivated by current results of the group of Prof. Reitzenstein at the TU Berlin, the laser theory is extended to two-mode lasers. We are able to explain superthermal intensity fluctuations by the interaction of the two modes with the common gain material. Thus, the results of the experiments can, not only be reproduced very precisely, but can also be linked with an illustrative explanation. The investigation on the coherence properties of two-mode lasers reveals a formal equivalence to strong coupling and also leads to the introduction of unconventional normal-mode coupling. It allows us to compare not only to previous experiments, but also to make predictions of parameters in which particularly strong changes of linewidth and mode splitting are visible.

The last part is devoted to the question in which way superradiant coupling affects the emission properties of nanolasers. The description of these effects is the most challenging part of this dissertation. A new theory is introduced which makes it possible to switch the superradiant coupling between emitters in the calculations on and off. With this method, we can directly quantify the influence of superradiant coupling. Its importance to current devices is examined in a broad-based parameter study. We found that drastic changes in the optical properties can be found for realistic parameters, e.g. the jump height in the input-output curve, and the photon statistics differ strongly from the case when superradiant coupling is neglected.

Contents

Introduction

Semiconductor quantum devices have enabled remarkable technological progress in the current and last century. The Nobel Committee for Physics underlined this in the year 2000 by awarding Zhores I. Alferov and Herbert Kroemer "for developing semiconductor heterostructures used in high-speed- and opto-electronics". The other half was awarded to Jack S. Kilby "for his part in the invention of the integrated circuit"[Nobelprize.org, 2000]. One of the most important results of their work is the ability to produce lasers that are small, efficient and cheap at the same time - semiconductor lasers. These kinds of miniature lasers are nowadays found in our everyday electronics in various forms like laser printers, laser rangefinders, and CD/DVD/Blu-ray. They also play a key role in communication technology and data transmission for the Internet. To introduce the reader to the "Theory of Semiconductor Quantum-Dot Microcavity Lasers" we like to give a short historical review on the laser itself, that explains the evolution of the quantum-dot lasers.

The history of the laser goes back to 1917 when Albert Einstein published the theoretical foundation for the quantum theory of radiation [Einstein, 1917]. It took roughly 40 years until the first experimental realization came about in the form of the "optical maser" by Charles Hard Townes and Arthur Leonard Schawlow [Schawlow and Townes, 1958]. Later, in 1960, Theodore H. Maiman presented the first functioning ruby laser with an optical wavelength [Maiman, 1960]. Only two years later in 1962 the function principle was transferred to semiconductor material nearly at the same time by Robert N. Hall [Hall et al., 1962] and Marshall Nathan [Nathan et al., 1962] who produced the first gallium arsenide (GaAs) semiconductor diodes. These first diodes were homojunction diodes which had the drawback of a working point at low temperature and a high laser threshold. It took the research of Herbert Kroemer on heterostructures [Kroemer, 1963] to fabricate the first heterojunction diode laser by Zhores I. Alferov in 1970 [Alferov, 1970] which overcame the problems of the first diodes. With the properties of a low threshold and a working point at room temperatures the laser was ready to be commonly used with great success outside the lab.

The development of semiconductor lasers made a leap forward yet again when it was found that the reduction of dimensionality in a semiconductor has tremendous effect on the density of states, and in consequence, on the lasing properties. Reducing the spatial expansion below the size of the de Broglie wavelength in one, two or even three dimensions leads to carrier confinement in structures such as quantum wells, quantum wires, or quantum dots as shown in Fig. 1. We can deduce directly from the changed single-particle density of states that the electronic properties, in terms of carrier interaction and carrier–phonon interaction, are very different for those

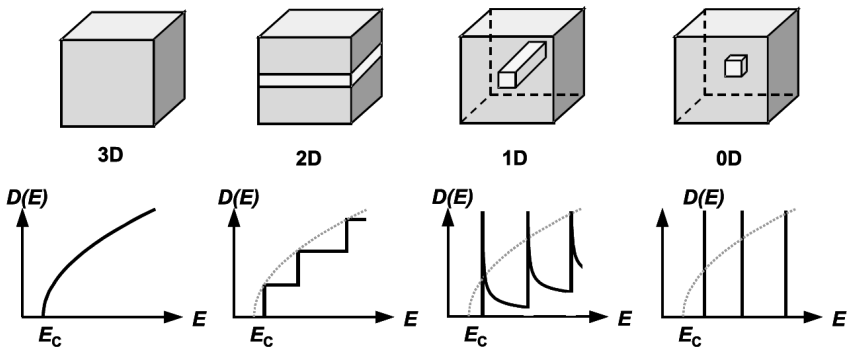

Figure 1: Sketch of the single-particle density of states for varying dimensions [Bimberg et al., 1999]. The density of states changes from a square root behavior in a three dimensional bulk material to a delta peak behavior for zero-dimensional quantum dots.

devices. These properties are responsible for the light-matter interaction and the interesting optical properties of a laser. The density of states for the limiting case of a quantum dot is described by delta-functions. They show no energy dispersion, and in contrast to a bulk semiconductor, have a discrete energy level structure similar to an atom.

After the first experimental proof of two dimensional quantum wells [Dingle et al., 1974], Dingle and Well realized the advantages of quantum wells as active materials for lasers application, and filed a patent application [Dingle and Henry, 1976]. It has been shown that this approach allows for lasers with lower threshold currents. Furthermore, the energy of discrete transition can be influenced by the thickness of the quantum well. Only a few years later Arakawa and Sakaki [Arakawa and Sakaki, 1982] predicted that the beneficial features of a two dimensional quantum well can be surpassed by zero dimensional quantum-dot laser in terms of efficiency and temperature stability. Nowadays there exist dozens of different approaches in nanotechnology to fabricate semiconductor quantum dots out of various materials. These include colloidal synthesis, plasma synthesis, and viral assembly. We like to focus here on techniques that allow for embedding the quantum dots in a bulk semiconductor in order to form an electrical device. One of the most prominent growth methods is the Stranski–Krastanov growth [Bimberg et al., 1999], which is used to produce coherently strained self-assembled quantum dots. It took several years of research to find suitable materials and to produce quantum dots with optical wavelengths of a good quality so that they could be used in a cavity to form a quantum-dot laser [Kirstaedter et al., 1994]. Figure 2 shows a high quality InAs quantum dot on GaAs with a size of under 20 nm.

Since that time, great progress has been made in the quality of tailor-made production of quantum dots. Also, the second crucial part of the laser: the cavity, has been improved a lot. While the first quantum-dot laser was an edge emitter, much more sophisticated approaches for cavities have been found. Among the most used approaches, cavities vary from micro-pillars [Reitzenstein and Forchel, 2010a; Reithmaier et al., 2004] to photonic crystals [Strauf et al., 2006] to microdiscs [Michler

et al., 2000; Vahala, 2003], as shown in Fig. 3. This development has led to the fabrication of "ultralow threshold" lasers or "threshold-less" lasers [Strauf et al., 2006; Noda, 2006].

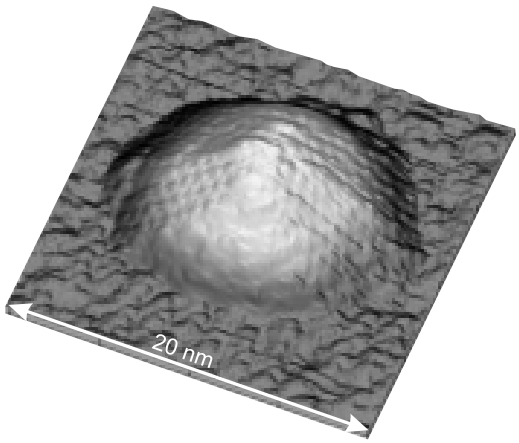

Figure 2: Scanning tunneling microscopy image of an InAs quantum dot [Dähne et al., 2008].

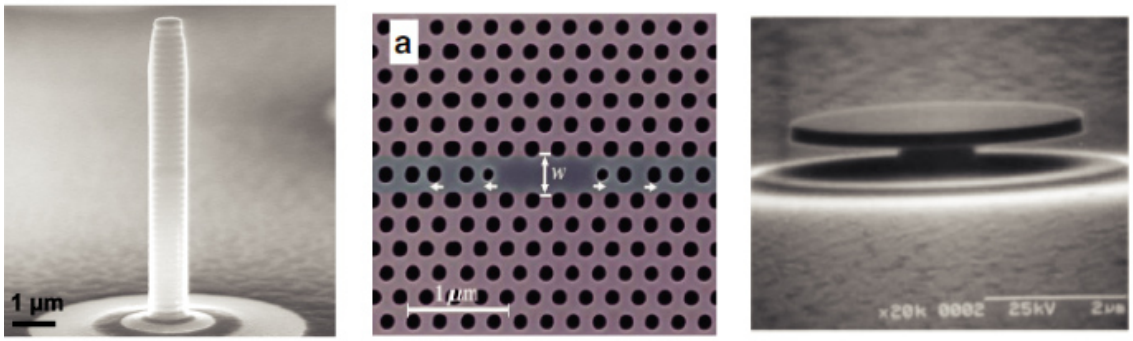

Figure 3: Scanning tunneling microscopy images of different types of microcavities. On the left is a micropillar cavity [Reithmaier et al., 2004], the image in the middle shows a photonic crystal membrane cavity [Strauf et al., 2006], on the right side a microdisc cavity is depicted [Michler et al., 2000].

Quantum-dot microcavities are a very attractive system to study quantum optical effects in the solid state [Reitzenstein, 2012]. Apart from research on fundamental light-matter interaction in the weak and strong coupling regime of cavity quantum electrodynamics [Gérard et al., 1998; Bayer et al., 2001; Vahala, 2003; Reithmaier et al., 2004; Yoshie et al., 2004], they offer the possibility to investigate stimulated emission in a regime that approaches the ultimate limit of a thresholdless laser based on a single zero-dimensional gain center [Noda, 2006]. Studies in this field include, e.g., technological works on optically and electrically pumped microlasers aiming to increase the β-factor, which expresses the fraction of spontaneous emission coupled into the lasing mode [Wang et al., 2005; Strauf et al., 2006; Reitzenstein et al., 2008]. In high β-microlasers it becomes increasingly difficult to identify the transition from

spontaneous emission to stimulated emission at threshold via their input-output characteristics [Björk et al., 1994]. This issue has triggered comprehensive experimental and theoretical research activities on the photon statistics of the emission in terms of an intensity autocorrelation function in order to unambiguously identify the onset of stimulated emission at threshold [Rice and Carmichael, 1994; Ulrich et al., 2007; Wiersig et al., 2009; Chow et al., 2014]. Moreover, the autocorrelation function is very beneficial for identifying single quantum-dot controlled lasing effects [Xie et al., 2007; Reitzenstein et al., 2008; Nomura et al., 2009] and for revealing other effects such as correlations between individual photon emission events [Wiersig et al., 2009] and chaotic behavior of feedback coupled microlasers [Albert et al., 2011].

Semiconductor bulk materials, as well as atomic systems have extensively been investigated in the past. The challenge for this thesis lies in a detailed theoretical description for quantum dots that considers their reduced dimensionality and describes the quantum mechanical effects which distinguish it from a bulk laser. The presented theory includes only the most important quantized states, but has more than two states to keep the difference from an atom. In an atom, two states correctly describe most optical properties since there is a large energy separation between the states. Our description makes sure that not only the discrete structure of the quantum dot is considered, and also its semiconductor nature that makes the difference to an atom laser. This difference manifests in various properties of those lasers. The most obvious one is simply the size, which is macroscopic for an atom laser and microscopic for a quantum-dot laser. Another is its inherent properties differ, e.g. one of the most prominent examples is the saturation of the laser output in quantum-dot lasers which is caused by Pauli-blocking in a quantum-dot device. The basic model that shows these key features and that is used in this thesis is sketched in Fig. 4. The described quantum dots have a cylindrical symmetry, and therefore s and p are good quantum numbers. We use a quantum-dot description that contains two shells: an s- and a p-shell. In our model, the pump process is described as the symmetrical creation of electrons and holes in the p-shell. The pump process in experiments can either be initiated through optical pumping or through electrical pumping in the wetting layer. As it would be a research project on its own to describe the electron and hole creation in the quasicontinuum states of the wetting layer, we assume that the pump process in the p-shell is a good approximation for the kind of devices that are studied here. The starting point of this thesis is a model that is a slight variation of the semiconductor model for quantum-dot-based microcavity lasers introduced in [Gies et al., 2007]. In the following theory, the model is developed further to allow for the study of current experimental situations with extended questions like bimodal lasers or superradiant lasers.

To fulfill the requirements the modelling on the theoretical side we introduce a new generalized formalism of the cluster expansion approach [Fricke, 1996a; Gies et al., 2007; Kira and Koch, 2008]. This is to study many body quantum mechanical systems that are too big to be solved with exact numerical methods or are too small to be studied with well known statistical methods. Simultaneously with the development of the theoretical background we develop a computer algebra program that is capable of deriving more complex equations of motion than it would be possible by hand. This computer aided approach also has the advantage of having

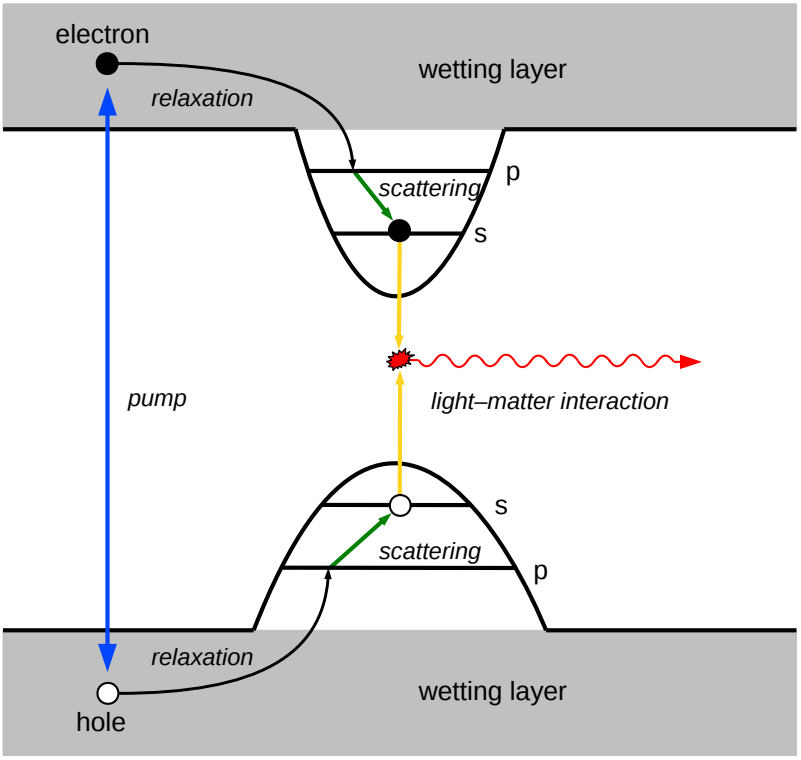

Figure 4: Sketch of the quantum-dot model in the electron-hole picture. Electrons and holes are created in the quasicontinuum states of the wetting layer by a pump process, which is typically realized electrically in experiments. The created excitation relaxes into the energetically highest states of the quantum dot. To further simplify the model, we assume that these relaxation processes are very fast and therefore we can assume that the pump process takes place directly in the energetically highest states of the quantum dot. The quantum dot in our model contains two shells, a s- and a p-shell. The electrons and holes can scatter further into the s-shell, where the light-matter interaction takes place. Due to the light-matter interaction an electron hole pair can recombine to a photon and vice versa.

various models and variations that could be tested to understand the underlying physics. As this subject is certainly the most versatile aspect of our research, we put a special emphasis on it.

Finally, the physical results that have been obtained with the newly developed theory and the computer algebra program provide progress for novel light sources that are important for application in future technology. Although our research must be regarded as fundamental research, the reader will find some ideas for new laser devices and multi-photon spectroscopy as promising candidates that can benefit from our investigation on quantum-dot microcavity lasers.

As mentioned before, this thesis addresses two main parts. The dirst part is the new formulation of a general description of open quantum many-particle systems that is suitable to be applied by a computer. The second part is the investigation of state-of-the-art semiconductor quantum-dot lasers with focus on current experimental data and results of micropillar-lasers.

This thesis is organized as follows: We start with the general theoretical concepts and innovations of this work in the first chapters and continue with the application of the theory to two types of semiconductor quantum-dot lasers: bimodal and superradiant lasers. The structure here does not follow the historical development of the different parts. For this reason, we will give the relevant description to the used model in each particular chapter.

In Chapter 1 we give a short overview of the general description of open quantum many-particle systems and describe the derivation of the Hamiltonian. We introduce the Lindblad formalism that we use to describe the openness of our systems and explain the Lindblad terms that are relevant for our devices. The focus lies on the theoretical description of light-matter interaction in semiconductor quantum-dot lasers.

In Chapter 2 we develop our approach and formulation of the cluster expansion: the expectation value based cluster expansion. It is developed to be well structured and universal enough to contain the key ideas of various cluster expansion methods, so that it is suitable to be the basis for a computer program. We show how one can define operators that can symbolize the necessary steps to derive a closed set of equation of motions with various approximation schemes. This chapter is completed with a revision of current literature that uses the cluster expansion from the viewpoint of the expectation value based cluster expansion. An investigation on higher-order photon-autocorrelation functions in quantum-dot lasers demonstrates the central ideas of our theory.

In Chapter 3 we translate the ideas of Chapter 2 into a computer program that is further referred as the computer-aided cluster expansion. We explain the operators of the expectation value based cluster expansion that are necessary to implement the computer-aided cluster expansion. Step by step we show how the mathematical ideas are transformed into computer code in the programming language `FORM`. The program implementation is illustrated on basis of a quantum-dot laser model. As a working example, we study a laser with a β-factor close to one and demonstrated the efficiency of our program.

Chapter 4 is concerned with the analysis of bimodal microcavity lasers. This chapter is highly motivated by current experimental results of quantum-dot microlasers that show surprisingly strong photon bunching. We develop a theoretical model that is able to reflect the underlying physics and provide understanding of the experimental results. The theory is further complemented with the description of multi-time correlation functions that also allows for the comparison of spectral and temporal coherence properties. As the main result, we are able to track this features back to a formulation that is strongly related to normal-mode coupling.

Chapter 5 provides new theoretical insight into sub- and superradiance in quantum-dot nanolasers. A completely new theory is developed to fulfill the requirements of the description of sub- and superradiance in this context: the configuration based cluster expansion. This theory allows for a quantitative comparison between lasers that couple quantum dots superradiantly. It is shown that the results can have pounced influence on the properties of state-of-the-art nanolasers. A short outlook on inhomogeneously broadened quantum dots and a more intuitively approach to understand the observed features concludes this chapter.

Chapter 6 gives a summary of the achievements and an outlook of the impact of the presented results as well as an overview on possible future studies.

Chapter 1

Theoretical description of light-matter interaction in semiconductors

This chapter provides an overview about the theoretical framework that is needed to describe semiconductor quantum dots (QDs). This concerns two major parts: First the general description of open quantum-mechanical many-body systems with the density operator and the von Neumann-Lindblad equation. Second the concrete formulation of a Hamiltonian and Lindblad terms that can be inserted into the general formalism.

In the first part, we show how to derive equation of motion (EoM) for the time evolution of time t as well as the multi-time expectation values that introduce a second time τ that is relative to t. These multi-time expectation values are of particular interest for open quantum-mechanical systems since they give new insight into their properties, e.g. they are needed to calculate the power spectrum[Mandel and Wolf, 1995]. We focus on the treatment of the openness of our system via Lindblad terms that allows for more consistent results than a simpler heuristic scattering-process description [Florian et al., 2013b].

The second part is concerned with the derivation of a Hamiltonian for semiconductor QD lasers. To formulate a microscopic QD theory we have to find a Hamiltonian that suites the intended situation. To this end, we make special assumptions that fit to the experimental material (III−V compound semiconductors), the low-temperature regime of the experiment $\approx 4K$, the wavelength of the light in comparison to the size of the QDs and the situation of a high-Q cavity. We use a Hamiltonian that consists of four parts

$$\hat{H} = \hat{H}_{\mathrm{Ph}} + \hat{H}^{0}_{\mathrm{Carr}} + \hat{H}_{\mathrm{Coul}} + \hat{H}_{\mathrm{D}}, \tag{1.1}$$

the first part describes the electromagnetic field in the cavity, the second the carriers that are confined in the QDs, the third the Coulomb interaction of the carriers and the fourth the light-matter interaction. The origin and the concrete form of these four parts is explained in the following sections. The commonly used Lindblad terms for this kind of systems are motivated and introduced in a separate section 1.6.

The hat $\hat{}$ indicating an operator is only used in this chapter to distinguish quantum-mechanical operators from classical quantities.

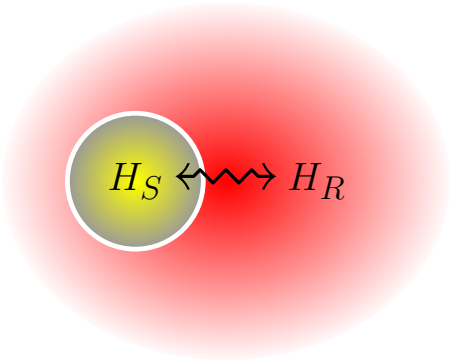

Figure 1.1: Illustration of an open quantum-mechanical system, that can be described in an interacting system-reservoir picture. The back-reaction on the reservoir is neglected in the Markov approximation.

1.1 General approach to open quantum-mechanical many-body systems

In this section, we introduce the quantum-mechanical Markovian master equation in Lindblad form to determine the time evolution of the density operator. The derivation that is presented here follows [Carmichael, 1999; Breuer and Petruccione, 2002] where more details can be found. With the term open quantum-mechanical many-body system we assume that the whole system can be divided into a subsystem S and a reservoir R. Therefore we can split the Hamiltonian in a part that describes the subsystem $\hat{H}_S$, that we are interested in, and a part that describes the reservoir $\hat{H}_R$ as illustrated in Fig. 1.1. A third term $\hat{H}_{SR}$ than describes the interaction of those two subsystems

$$\hat{H}_{SR} = \hbar \sum_i \hat{L}_i \hat{\Gamma}_i, \tag{1.2}$$

with the Lindblad operators $\hat{L}_i$ that act in the Hilbert space of the system S and the operators $\hat{\Gamma}_i$ that act in the Hilbert space of the reservoir R. The complete Hamiltonian can be written as

$$\hat{H} = \hat{H}_S + \hat{H}_R + \hat{H}_{SR}. \tag{1.3}$$

Since we are not interested in the dynamics of the reservoir, it enters the calculation only with its general properties like temperature and the density of states. Starting from this idea we apply the Liouville von Neumann equation for the density operator $\hat{\rho}$

$$\frac{d}{dt}\hat{\rho} = \frac{i}{\hbar}\left[\hat{\rho}, \hat{H}\right], \tag{1.4}$$

to obtain a master equation for density operator of the system $\hat{\rho}_S$ by taking the partial trace over the reservoir

$$\hat{\rho}_S = \mathrm{tr}_\mathrm{R}\left\{\hat{\rho}(t)\right\} = \mathrm{tr}_\mathrm{R}\left\{\hat{U}(t)\hat{\rho}(0)\hat{U}^\dagger(t)\right\}. \tag{1.5}$$

$\hat{U}(t)$ denotes the unitary time evolution operator. At this point we apply the Markov approximation, which relies on the fact that the relaxation time of the reservoir R is much smaller than the relaxation time of subsystem S, which is usually valid for wetting layer compared to the QDs. In consequence, the reservoir correlations vanish immediately

$$\langle \hat{\Gamma}_i(t)\hat{\Gamma}_j(t')\rangle_R \propto \delta(t-t'). \tag{1.6}$$

Additionally, we apply the Born approximation, which means that the subsystem S does not affect the reservoir R and the reservoir affect the system only with its general parameters that are time-independent. Exemplary we use the temperature T here as the bath parameter so that the whole density operator writes as

$$\hat{\rho}(t) \approx \hat{\rho}_S(t)\hat{\rho}_R(T). \tag{1.7}$$

With these approximations, the most general form of a trace-preserving Markovian master equation [Breuer and Petruccione, 2002] can be derived

$$\frac{d}{dt}\hat{\rho}_S = \frac{i}{\hbar}\left[\hat{\rho}_S, \hat{H}_S\right] + \sum_{\nu,\nu'} \lambda_{\nu\nu'}\left(2\hat{L}_\nu\hat{\rho}_S\hat{L}^\dagger_{\nu'} - \hat{L}^\dagger_\nu\hat{L}_{\nu'}\hat{\rho}_S - \hat{\rho}_S\hat{L}^\dagger_\nu\hat{L}_{\nu'}\right), \tag{1.8}$$

which is called von Neumann-Lindblad equation. The first part is equal to equation (1.4) and describes the unitary dynamics of S. The second part is the Lindblad part and describes the influence of the reservoir, where $\lambda_{\nu\nu'}$ are the rates that depend on the bath parameters. This part describes irreversible dynamics [Breuer and Petruccione, 2002], e.g. the entropy production per time unit $\sigma(\rho_S(t)) \geq 0$.

As we are interested in certain expectation values it is useful to apply the von Neumann-Lindblad equation also for a specific system operator $\langle\hat{A}\rangle = \mathrm{tr_S}(\hat{A}\hat{\rho}_S)$

$$\begin{aligned}\frac{d}{dt}\left\langle\hat{A}\right\rangle &= \frac{i}{\hbar}\left\langle\left[\hat{H}_S, \hat{A}\right]\right\rangle + \sum_{\nu,\nu'}\lambda_{\nu\nu'}\langle 2\hat{L}^\dagger_\nu\hat{A}\hat{L}_{\nu'} - \hat{L}^\dagger_\nu L_{\nu'}\hat{A} - \hat{A}\hat{L}^\dagger_\nu\hat{L}_{\nu'}\rangle \\ &= \frac{i}{\hbar}\left\langle\left[\hat{H}_S, \hat{A}\right]\right\rangle + \sum_i \langle C_i(\hat{A})\rangle \\ &= \left\langle\mathcal{L}(\hat{A})\right\rangle,\end{aligned} \tag{1.9}$$

which is called the generalized Ehrenfest EoM[1]. The operator functions $C_i(\hat{A})$ are called the Lindblad processes and can be found in the section 1.6. $\mathcal{L}$ is called superoperator and is used as short form for symbolic calculation in later chapters.

1.2 Multi-time expectation values

In the last section, we have shown how the time dynamics of the (reduced) density operator (1.8) and the observables (1.9) can be calculated. The fact that we are

[1]This is not a generalized Heisenberg EoM. A Heisenberg equation is an EoM for an operator in the Heisenberg picture. Equation (1.9) is an EoM for an EV and can only be derived from the vNL Eq. (1.8) in the Schrödinger picture and not from the Heisenberg equation.

describing open quantum-mechanical many-body systems has the consequence that more information about the system can be obtained with the help of multi-time expectation values [Gies et al., 2012]. A typical example is the first-order photon correlation function $\langle \hat{b}^\dagger(t+\tau)\hat{b}(t)\rangle$ that can be measured with an interferometer. Also the power spectrum can be calculated with the help of the Wiener-Chintschin-theorem [Mandel and Wolf, 1995] by applying the Fourier transform on $\langle \hat{b}^\dagger(t+\tau)\hat{b}(t)\rangle$. The central idea to calculate these two-time expectation values is that the time evolution of times t and τ are well separated and the quantum regression theorem [Lax, 1967; Meystre and Murray, 1999; Breuer and Petruccione, 2002] can be applied. The clearest prove is to assume that the system is described by a closed set of differential equations for the operators $\{\hat{A}_i\}$ that can be derived with (1.9)

$$\frac{d}{dt}\left\langle \hat{A}_i(t)\right\rangle = \sum_j G_{ij}\left\langle \hat{A}_j\right\rangle, \tag{1.10}$$

with a corresponding coefficient matrix G_{ij}. The quantum regression theorem now states that the two-time expectation values are described by the same differential equations

$$\frac{d}{d\tau}\left\langle \hat{A}_i(t+\tau)\hat{A}_k(t)\right\rangle = \sum_j G_{ij}\left\langle \hat{A}_j(t+\tau)\hat{A}_k(t)\right\rangle. \tag{1.11}$$

In chapter 2.3.4 we show that this concept can also be applied on the truncated EoM, that are derived with the cluster expansion.

1.3 Quantization of the electromagnetic field

The Hamiltonian $\hat{H}_{\mathrm{Ph}}$ describes the quantized electromagnetic field and is the quantized version of the electromagnetic field energy. Starting from the Maxwell equations we have to apply the formalism of the second quantization [Haug and Koch, 2004]. To this end, we use the Coulomb gauge

$$\nabla \cdot \mathbf{A}(\mathbf{r},t) = 0, \tag{1.12}$$

to make the vector potential $\mathbf{A}(\mathbf{r},t)$ transversal. The wave equation for the vector potential in a cavity can be written as

$$\nabla^2\mathbf{A}(\mathbf{r},t) = \frac{n^2(\mathbf{r})}{c^2}\partial_{tt}\mathbf{A}(\mathbf{r},t), \tag{1.13}$$

with the refractive index $n(\mathbf{r})$, that describes the material of the resonator. We expand the vector potential $\mathbf{A}(\mathbf{r},t)$ into modes $\mathbf{u}_\xi(\mathbf{r})$

$$\mathbf{A}(\mathbf{r},t) = \sum_\xi c_\xi(t)\mathbf{u}_\xi(\mathbf{r}) + c_\xi^*(t)\mathbf{u}_\xi{}^*(\mathbf{r}), \tag{1.14}$$

with the time dependence $c_\xi(t) = c_\xi(0)e^{-i\omega_\xi t}$. The notation of the mode index ξ here also includes the polarization vector of the light. The explicit form of $\mathbf{u}_\xi(\mathbf{r})$ and the

frequencies ω_ξ depend on the shape of the cavity and the refractive index $n(\mathbf{r})$ and must be determined by solving the Maxwell equations. For the general consideration we do not have to know the modes of the specific resonator. However, for more detailed information about dielectric microcavities we refer to [Vahala, 2003; Cao and Wiersig, 2015]. In the next step, we apply the canonical quantization $c_\xi(t) = A_\xi \hat{b}_\xi$ with the factor $A_\xi = \sqrt{\frac{\hbar}{2\epsilon_0 w_\xi vol_\xi}}$, the mode-volume vol_ξ and the permittivity ϵ_0. The operators $\hat{b}_\xi, \hat{b}_\xi^\dagger$ fulfill the standard bosonic commutation relations

$$\left[\hat{b}_\xi, \hat{b}_{\xi'}^\dagger\right] = \delta_{\xi,\xi'} \tag{1.15}$$

$$\left[\hat{b}_\xi, \hat{b}_{\xi'}\right] = 0 = \left[\hat{b}_\xi^\dagger, \hat{b}_{\xi'}^\dagger\right]. \tag{1.16}$$

The quantized vector potential can now be written as

$$\mathbf{A}(\mathbf{r}, t) = \sum_\xi \hat{b}_\xi \mathbf{u}_\xi(\mathbf{r}) + \hat{b}_\xi^\dagger \mathbf{u}_\xi{}^*(\mathbf{r}), \tag{1.17}$$

and we find an expression for quantized field energy

$$\hat{H}_{\mathrm{Ph}} = \sum_\xi \hbar\omega_\xi \left(\hat{b}_\xi^\dagger \hat{b}_\xi + \frac{1}{2}\right). \tag{1.18}$$

Later in this thesis we shift the zero energy so that the $+\frac{1}{2}$ does not appear.

1.4 Single-particle states

The single-particle (carrier) states are needed for the evaluation of the parts of the Hamiltonian that describes the semiconductor material. The calculation of single-particle states is a research topic on its own, that strongly depends on the type of material, the experimental situation, e.g. temperature, size of the semiconductor and the calculation power that one can invest. We focus on III−V compound semiconductors like InGaAS QDs on a GaAs substrate. High accuracy calculation for this kind of materials are possible with microscopic theories like the tight-binding method [Singleton, 2001; Sheng et al., 2005; Schulz et al., 2006], the empirical tight-binding method [Santoprete et al., 2003; Lee et al., 2004] or the empirical pseudopotential method [Kim et al., 1998] that are able to take into account the symmetry of the underlying lattice. The optical properties of self-organized wurtzite InN/GaN QDs have been studied with tight-binding method and full configuration interaction calculation [Baer et al., 2005]. It has been shown that also phenomenological theories like the the 8-band k·p wave functions are in good agreement for InGaAs/GaAs QDs [Schliwa and Winkelnkemper, 2008]. A study of the electronic and optical properties of strained QDs modeled by 8-band k·p theory can be found [Stier et al., 1999].

As this thesis focuses more on the interaction of QDs and photons than on a realistic component simulation we present here a much simpler approach - the envelope function ansatz [Haug and Koch, 2004; Yu and Cardona, 2010], which provides still a sufficient accuracy for our purpose [Bimberg et al., 1999]. In the envelope function

ansatz the wave function $\psi_\nu^\lambda(\mathbf{r})$ of the band λ and the single-particle state $|\nu\rangle$ of our semiconductor is assumed to be the product of the periodic Bloch function at the band edge $u_{k\approx 0}(\mathbf{r})$, describing the volume material, times the envelope function that describes the additional confinement of the QD $\phi_\nu^\lambda(\mathbf{r})$

$$\psi_\nu^\lambda(\mathbf{r}) = u_{k\approx 0}^\lambda(\mathbf{r})\phi_\nu^\lambda(\mathbf{r}). \tag{1.19}$$

The stationary Schrödinger equation for the QD can now be written

$$\left(-\frac{\hbar^2}{2m^\lambda}\Delta + V(\mathbf{r})\right)\phi_\nu^\lambda(\mathbf{r}) = \epsilon_\nu^\lambda\phi_\nu^\lambda(\mathbf{r}), \tag{1.20}$$

where m^λ denotes the effective mass and $V(\mathbf{r})$ an approximate confinement potential. The concrete confinement potential depends on the shape of the QDs, e.g. for typical lense shaped QDs the harmonic disc model [Bimberg et al., 1999] yields to convincing solutions

$$V(\mathbf{r}) = \frac{m^\lambda\omega^2}{2}(x^2+y^2) + V_0\left(\theta(z-\frac{L}{2}) + \theta(-z-\frac{L}{2})\right). \tag{1.21}$$

This is a composition of a potential well that describes the strong confinement in growth direction (z), with the confinement energy V_0 and its extension L and a harmonic oscillator potential in the x-y-plane. The field operator can now be constructed with the single-particle wave functions [Schwabl, 2008]

$$\hat{\Psi}(\mathbf{r},t) = \sum_{\lambda,\nu}\hat{a}_{\lambda,\nu}(t)\psi_\nu^\lambda(\mathbf{r}), \tag{1.22}$$

where the operators $\hat{a}_k, \hat{a}_k^\dagger$ fulfill the standard fermionic anticommutation relations

$$\begin{aligned}\left[\hat{a}_k, \hat{a}_{k'}^\dagger\right]_+ &= \delta_{k,k'}\\ \left[\hat{a}_k, \hat{a}_{k'}\right]_+ &= 0 = \left[\hat{a}_k^\dagger, \hat{a}_{k'}^\dagger\right]_+,\end{aligned} \tag{1.23}$$

for any indices k.

The number of states $|\nu\rangle$ and levels is determined by the depth of the confinement potential. The simplest and still widely used approach is a two-level description [del Valle et al., 2009; Mu and Savage, 1992; Lodahl et al., 2004; Richter et al., 2009]. As one step further to more realistic model we take 4 levels and two electrons into account [Gies et al., 2011, 2007]. Due to the cylindrical symmetry of the potential the angular momentum is a good quantum number and from here on s and p will label the names of the shells (similar to an atom). For the calculation in this thesis we restrict our model on one spin subsystem. Taking all configurations and both spin-direction for a 4-level-system into account would lead to $2^{2*4} = 256$ possible configurations, while one spin subsystem reduces the number of configuration to $2^4 = 16$. Taking only symmetrical pumping of electrons and holes into account further reduces the number of configurations to 6, which is used in this thesis. However, the restriction to one spin-subsystem is usually an approximation which validity depends

on the specific experimental situation. For optical pumping with circularly polarized light only one spin subsystem is excited [Gies et al., 2012]. In comparison to the spin-flip dynamics the relaxation and recombination dynamics are fast and therefore the restriction is valid. In systems with other excitation processes, the quality of the approximation mainly depends on the magnitude of the Coulomb coupling strength of the two spin-sub-systems in comparison to the Coulomb coupling strength of the carriers in one spin-subsystem. In [Gies et al., 2012] the authors showed that for typical parameters used in InGaAS QD experiment, the calculation of only one spin subsystem leads to satisfying results.

1.5 The many-body Hamiltonian

The many-body Hamiltonian $\hat{H}^0_{\mathrm{Carr}}, \hat{H}_{\mathrm{Coul}}, \hat{H}_{\mathrm{D}}$ is obtained as a result of single-particle field operator inserted in the specific Hamiltonian parts. The Hamiltonian of the free particles reads as

$$\hat{H}^0_{\mathrm{Carr}} = \int d^3\mathbf{r}\ \hat{\Psi}^\dagger(\mathbf{r},t)\left(-\frac{\hbar^2}{2m}\Delta + V(\mathbf{r})\right)\hat{\Psi}(\mathbf{r},\mathbf{t}), \tag{1.24}$$

which is a diagonal sum

$$\hat{H}^0_{\mathrm{Carr}} = \sum_{\lambda,\nu} \epsilon^\lambda_\nu \hat{a}^\dagger_{\lambda,\nu}\hat{a}_{\lambda,\nu}, \tag{1.25}$$

over the particle number operator $\hat{n} = \hat{a}^\dagger_{\lambda,\nu}\hat{a}_{\lambda,\nu}$ with the single-particle energy ϵ^λ_ν. The Coulomb Hamiltonian is constructed in a similar way with the Coulomb matrix element

$$V^{\lambda\lambda'}_{\alpha'\nu,\nu'\alpha} = \int d^3\mathbf{r} \int d^3\mathbf{r}'\ \hat{\Psi}^{\lambda\dagger}_{\alpha'}(\mathbf{r},t)\hat{\Psi}^{\lambda'\dagger}_{\nu}(\mathbf{r}',t)V_C(\mathbf{r}-\mathbf{r}')\hat{\Psi}^{\lambda'}_{\nu'}(\mathbf{r}',t)\hat{\Psi}^{\lambda}_{\alpha}(\mathbf{r},t), \tag{1.26}$$

that contains the Coulomb potential $V_C(\mathbf{r}) = \frac{e^2}{4\pi\epsilon_0\epsilon|\mathbf{r}|}$ with the elementary charge e, the relative permittivity ϵ, and the vacuum permittivity ϵ_0. The complete Coulomb Hamiltonian in second quantization reads

$$\hat{H}_{\mathrm{Coul}} = \sum_{\alpha',\nu,\nu',\alpha,\lambda,\lambda'} V^{\lambda\lambda'}_{\alpha'\nu,\nu'\alpha}\hat{a}^\dagger_{\lambda,\alpha'}\hat{a}^\dagger_{\lambda',\nu}\hat{a}_{\lambda,\nu'}\hat{a}_{\lambda',\alpha}, \tag{1.27}$$

where the Coulomb matrix element mediates an electrostatic repulsion of carriers in the same band as well as the attraction of carriers in valence and conduction band.

The light-matter interaction is described in dipole approximation, that is valid whenever the wavelength of the mode is much bigger than the size of the QD. The mode function in conclusion is nearly constant in the vicinity $\mathbf{r_0}$ of the QD $\mathbf{u}_\xi(\mathbf{r}) \approx \mathbf{u}_\xi(\mathbf{r_0})$. The dipole Hamiltonian can be written as

$$\hat{H}_{\mathrm{D}} = \int d^3\mathbf{r}\ \hat{\Psi}^\dagger(\mathbf{r})\left(-e\mathbf{E}_T(\mathbf{r_0})\right)\hat{\Psi}(\mathbf{r},\mathbf{t}), \tag{1.28}$$

where we can use the mode expansion (1.17) to determine the electrical field $\mathbf{E}_T = -\frac{\partial}{\partial t}\mathbf{A}$. The strength of the light-matter coupling is determined by the dipole matrix elements

$$g_{\xi\alpha\nu}^{\lambda\lambda'} = \sqrt{\frac{\hbar w_\xi}{2\epsilon\epsilon_0 vol_\xi}} \int d^3r\, \psi_\alpha^{\lambda *}(\mathbf{r}) e\mathbf{r}\mathbf{u}_\xi(\mathbf{r_0})\psi_\nu^{\lambda'}(\mathbf{r}), \tag{1.29}$$

where the prefactor is called the vacuum amplitude which contains the normalizing mode-volume vol_ξ of mode ξ. With this definition we can write the complete dipole Hamiltonian

$$\hat{H}_{\mathrm{D}} = -i \sum_{\xi,\alpha',\nu,\nu',\alpha,\lambda,\lambda'} g_{\xi\alpha\nu}^{\lambda\lambda'} \hat{a}_{\lambda,\alpha}^\dagger \hat{a}_{\lambda',\nu} \left(\hat{b}_\xi^\dagger + \hat{b}_\xi\right) + H.c., \tag{1.30}$$

that describes the emission and the absorption of a photon in mode ξ triggered by a transition of a carrier from band λ' in state ν to band λ in state α as well as the conjugate process. To simplify calculations further we use the equal envelope approximation for valence- and conduction-bands $g_{\xi\alpha\nu}^{\lambda\lambda'} = \mathbf{u}_\xi(\mathbf{r_0}) d_{\lambda\lambda'}\delta_{\alpha\nu}$ [Baer et al., 2006] with the inter-band matrix elements $d_{\lambda\lambda'}$. Furthermore we use the Rotating Wave Approximation where we neglect the fast oscillating terms in the dipole Hamiltonian. This approximation is valid for situations of weak coupling near the resonance [Wu and Yang, 2007].

Applying these approximations to the many-body Hamiltonian for the case of two shells (s- and p-shell) as sketched in Fig. 4 the Hamiltonian can be written more intuitively by using the fermionic operators $\hat{c}_j$ ($\hat{c}_j^\dagger$) and $\hat{v}_j$ ($\hat{v}_j^\dagger$) that annihilate (create) a conduction-band carrier in the state $|j_c\rangle$ and a valence-band carrier in the state $|j_v\rangle$, respectively. In the following all indices describe either the s- or the p-shell $j, k, k' \in \{s, p\}$. Using this notation the single-particle Hamiltonian can be written as

$$\hat{H}_{\mathrm{Carr}}^0 = \sum_j \varepsilon_j^c \hat{c}_j^\dagger \hat{c}_j + \sum_j \varepsilon_j^v \hat{v}_j^\dagger \hat{v}_j, \tag{1.31}$$

with the energies for conduction and valence band carriers $\varepsilon_j^{c,v}$. The two-particle Coulomb Hamiltonian is given by

$$\hat{H}_{\mathrm{Coul}} = \frac{1}{2} \sum_{k'jj'k} (V_{k'jj'k}^{cc} \hat{c}_{k'}^\dagger \hat{c}_j^\dagger \hat{c}_{j'} \hat{c}_k + V_{k'jj'k}^{vv} \hat{v}_{k'}^\dagger \hat{v}_j^\dagger \hat{v}_{j'} \hat{v}_k) + \sum_{k'jj'k} V_{k'jj'k}^{cv} \hat{c}_{k'}^\dagger \hat{v}_j^\dagger \hat{v}_{j'} \hat{c}_k, \tag{1.32}$$

and the dipole Hamiltonian by

$$\hat{H}_{\mathrm{D}} = -i \sum_{\xi,j} (g_{\xi j} \hat{c}_j^\dagger \hat{v}_j \hat{b}_\xi - g_{\xi j}^* \hat{v}_j^\dagger \hat{c}_j \hat{b}_\xi^\dagger). \tag{1.33}$$

1.6 Lindblad processes

In this section, we give the specific Lindblad terms $C_i(\hat{A})$ (1.9), that are used for QD model in this thesis. This terms are very intuitive since we can recognize the intended

process directly [Gies et al., 2012]. The inter-band carrier scattering between the two different levels of the QD is in general described with

$$C_{\text{scatt}}(\hat{A}) = \sum_{i,j} \gamma_{ij} \left(2\hat{a}_i^\dagger \hat{a}_j \hat{A} \hat{a}_j^\dagger \hat{a}_i - \hat{a}_j^\dagger \hat{a}_i \hat{a}_i^\dagger \hat{a}_j \hat{A} - \hat{A} \hat{a}_j^\dagger \hat{a}_i \hat{a}_i^\dagger \hat{a}_j \right), \tag{1.34}$$

where the rates γ_{ij} denote the scattering from level j to level i. The specific rates can either be measured experimentally or be calculated e.g. by Fermi's golden rule. As we are describing experiments in the low temperature regime, it appears obvious that the scattering rates into energetic favorable states will be the dominating process [Gies et al., 2012].

The pump process in the model is described as a transfer from a carrier in the valence band ($\hat{v}$) to the conduction band ($\hat{c}^\dagger$) and has the same shape as the scattering term

$$C_{\text{P}}(\hat{A}) = \sum_{i,j} \text{P}_{ij} \left(2\hat{c}_i^\dagger \hat{v}_j \hat{A} \hat{v}_j^\dagger \hat{c}_i - \hat{v}_j^\dagger \hat{c}_i \hat{c}_i^\dagger \hat{v}_j \hat{A} - \hat{A} \hat{v}_j^\dagger \hat{c}_i \hat{c}_i^\dagger \hat{v}_j \right), \tag{1.35}$$

where P_{ij} denotes the pump rate. This kind of pump process is guaranteed if we excite the carriers optically e.g. via a laser that is tuned in resonance to the level transition. For the electrical pumping via the wetting layer this kind of pumping is only an approximation. In a more complex model one would have to take non-symmetric capturing of carriers into account. Again, this would lead to more possible configurations in the QD-model since it leads to the lifting of carrier conservation in the QD.

The reservoir coupling also influences the optical processes in the QD-laser system. First, we have to take spontaneous losses of carrier excitation into non-lasing modes into account

$$C_{\text{nl}}(\hat{A}) = + \sum_{i,j} \gamma_{ij}^{\text{nl}} \left(2\hat{v}_i^\dagger \hat{c}_j \hat{A} \hat{c}_j^\dagger \hat{v}_i - \hat{c}_j^\dagger \hat{v}_i \hat{v}_i^\dagger \hat{c}_j \hat{A} - \hat{A} \hat{c}_j^\dagger \hat{v}_i \hat{v}_i^\dagger \hat{c}_j \right), \tag{1.36}$$

where the non-lasing rate γ_{ij}^{nl} determines the $\beta-$ factor. For example $\gamma_{ij}^{\text{nl}} = 0$ describes a laser with $\beta = 1$ where all of the spontaneous emission goes directly into the lasing mode. The second process originates from the leakiness of the resonator

$$C_{\text{C}}(\hat{A}) = \sum_{i} \kappa_\xi \left(2\hat{b}_\xi \hat{A} \hat{b}_\xi^\dagger - \hat{b}_\xi^\dagger \hat{b}_\xi \hat{A} - \hat{A} \hat{b}_\xi^\dagger \hat{b}_\xi \right), \tag{1.37}$$

where κ_ξ describes the cavity losses for each mode. The magnitude is determined by the shape and the quality of the mode and is usually determined experimentally via the line-widths in the light-spectrum. Also, there are processes that are related to phonon-mediated off-resonant coupling [Florian et al., 2013a]

$$\begin{aligned} C_{\text{Ph}}(\hat{A}) = & \sum_{i,j,\xi} \gamma_{ij\xi}^{\text{in}} \left(2\hat{b}_\xi^\dagger \hat{a}_i^\dagger \hat{a}_j \hat{A} \hat{b}_\xi \hat{a}_j^\dagger \hat{a}_i - \hat{b}_\xi \hat{b}_\xi^\dagger \hat{a}_j^\dagger \hat{a}_i \hat{a}_i^\dagger \hat{a}_j \hat{A} - \hat{A} \hat{b}_\xi \hat{b}_\xi^\dagger \hat{a}_j^\dagger \hat{a}_i \hat{a}_i^\dagger \hat{a}_j \right) \\ & + \gamma_{ij\xi}^{\text{out}} \left(2\hat{b}_\xi \hat{a}_i^\dagger \hat{a}_j \hat{A} \hat{b}_\xi^\dagger \hat{a}_j^\dagger \hat{a}_i - \hat{b}_\xi^\dagger \hat{b}_\xi \hat{a}_j^\dagger \hat{a}_i \hat{a}_i^\dagger \hat{a}_j \hat{A} - \hat{A} \hat{b}_\xi^\dagger \hat{b}_\xi \hat{a}_j^\dagger \hat{a}_i \hat{a}_i^\dagger \hat{a}_j \right), \end{aligned} \tag{1.38}$$

where the absorption $\gamma^{\text{in}}_{ij\xi}$ of a photon in mode ξ and the loss of a photon $\gamma^{\text{out}}_{ij\xi}$ is described. This process becomes important if we assume the QDs to be homogeneous broadened. With this process it becomes more likely that QDs that are detuned to the lasing-mode couples mediated by a phonon. In some cases, it is necessary to introduce a pure dephasing rate that broadens the homogeneous linewidth of the QDs[Auffèves et al., 2009]

$$C_{\text{D}}(\hat{A}) = \sum_i \gamma^{\text{D}}_{ii} \left(2\hat{a}_i^\dagger \hat{a}_i \hat{A} \hat{a}_i^\dagger \hat{a}_i - \hat{a}_i^\dagger \hat{a}_i \hat{a}_i^\dagger \hat{a}_i \hat{A} - \hat{A} \hat{a}_i^\dagger \hat{a}_i \hat{a}_i^\dagger \hat{a}_i \right), \tag{1.39}$$

similar to its name this process only introduces some dephasing γ^d_{ii}, that is proportional to the occupation of the state i. This effect can experimentally be observed by a broadening of the homogeneous line-width [Auffèves et al., 2009].

1.7 Statistical properties of light

An essential tool to analyze the properties of a light source is the investigation of the statistical properties of light. In most cases the full photon statistics are neither experimentally nor theoretically accessible and instead we study the photon-autocorrelation functions. This functions allow us to distinguish between different light sources and their coherence properties.

First-order photon-autocorrelation function The first-order photon-autocorrelation function $g^{(1)}(t,\tau)$ is the normalized amplitude-amplitude correlation. It is typically used to study the coherence properties of light. In experiments it is commonly measured with a linear optical interferometer such as the Michelson interferometer, the Mach-Zehnder interferometer or the Sagnac interferometer [Mandel and Wolf, 1995]. We can write it as

$$g^{(1)}(t,\tau) = \frac{G^{(1)}(t,\tau)}{\langle \hat{b}^\dagger(t)\hat{b}(t)\rangle} = \frac{\langle \hat{b}^\dagger(t+\tau)\hat{b}(t)\rangle}{\langle \hat{b}^\dagger(t)\hat{b}(t)\rangle}, \tag{1.40}$$

with the time t and the delay time τ. The function it normalized to one for $\tau = 0$ and the time span that it takes for the function to relax to zero is referred as the coherence time.

Second-order photon-autocorrelation functions The second-order photon-autocorrelation function $g^{(2)}(t,\tau)$ is the normalized intensity-intensity correlation. In experiments it can be measured with the Hanbury Brown–Twiss setup [Mandel and Wolf, 1995]. In the same way as $g^{(1)}(t,\tau)$ we can write it as

$$g^{(2)}(t,\tau) = \frac{G^{(2)}(t,\tau)}{\left\langle \hat{b}^\dagger(t)\hat{b}(t)\right\rangle \left\langle \hat{b}^\dagger(t+\tau)\hat{b}(t+\tau)\right\rangle} = \frac{\left\langle \hat{b}^\dagger(t)\hat{b}^\dagger(t+\tau)\hat{b}(t+\tau)\hat{b}(t)\right\rangle}{\left\langle \hat{b}^\dagger(t)\hat{b}(t)\right\rangle \left\langle \hat{b}^\dagger(t+\tau)\hat{b}(t+\tau)\right\rangle}, \tag{1.41}$$

with the time t and the delay time τ. In most cases in this thesis we are interested in the second-order photon-autocorrelation function with zero delay time $\tau = 0$ that we write from now on:

$$g^{(2)}(0) = \frac{\langle \hat{b}^{\dagger 2} \hat{b}^2 \rangle}{\langle \hat{b}^\dagger \hat{b} \rangle^2}. \tag{1.42}$$

With the help of $g^{(2)}(0)$ we can determine whether the emitted photons are uncorrelated as in laser light $g^{(2)}(0) = 1$, or if the photons are correlated and emitted in bunches $g^{(2)}(0) > 1$ or if the photons are anticorrelated and display an antibunching behavior $g^{(2)}(0) < 1$ (see Fig 1.2)

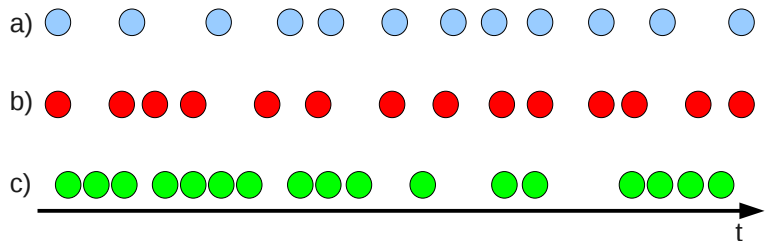

Figure 1.2: Illustration of the characterization of light via the photon statistics. a) displays the antibunching of photons that is typical for single photon sources $g^{(2)}(0) < 1$. b) displays a photon statistic of uncorrelated photons that is typical for a coherent light source like a laser. The intensity correlation function has a value of $g^{(2)}(0) = 1$. c) displays the bunching of photons. This is behavior is characteristic for thermal light sources or other highly fluctuating emitters. The intensity correlation functions has a value of $g^{(2)}(0) > 1$.

As a natural generalization of the second-order coherence we also define the photon-autocorrelation function of order n

$$g^{(n)}(0) = \frac{\langle \hat{b}^{\dagger n} \hat{b}^n \rangle}{\langle \hat{b}^\dagger \hat{b} \rangle^n}, \tag{1.43}$$

which will be part of our research in the next chapters. Similar as for $g^{(2)}(0)$ we can calculate analytically the values for the special cases of thermal light $g^{(n)}(0) = n!$ and coherent light $g^{(n)}(0) = 1$.

Chapter 2

Expectation value based cluster expansion

In this chapter, we proceed from the general approach to open quantum-mechanical many-body systems Sec. 1.1 to a new and more specific method to formulate equations of motion(EoM) - the expectation value based cluster expansion (EVCE). Our approach allows for a numerically exact treatment as well as for approximations necessary in large systems and can be applied to systems involving both bosonic and fermionic particles. The method generalizes the cluster expansion (CE) technique by using expectation values (EVs) instead of correlation functions (CFs). At the same time, we develop a scheme to derive the EoM that paves the way for the computer-aided cluster expansion in chapter 3. The use of expectation values not only makes the equations more transparent, but also considerably reduces the algebraic effort to derive the equations. Since we focus on the description of open systems, the deviation of multi-time EVs (see also Sec. 1.2) in terms of the EVCE is discussed explicitly. We demonstrate the application and the convergence of the EVCE on the Jaynes-Cummings model [Jaynes and Cummings, 1963; Shore and Knight, 1993] and the QD-based microcavity lasers model [Gies et al., 2007]. Finally the proposed formulation offers a unified view on various approximation techniques presented in the literature.

Parts of this chapter are published in [Leymann et al., 2014, 2013b]. The basic theoretical concept of the EVCE is developed by A. Foerster in collaboration with H.A.M. Leymann, the analytical EoM where mainly derived by H.A.M. Leymann, computational derivation of EoM and the numerical integration of the EoM was mainly done by A. Foerster, all authors of [Leymann et al., 2014, 2013b] discussed the results and physical implications of the results.

2.1 Motivation of the expectation value based cluster expansion

Interacting many-particle systems can drive strong correlations between the interacting particles. A straight forward way to describe the dynamics of many-particle systems is to derive the EoM for the quantities of interest. The ideas of the EVCE

were developed parallel with the task to write a computer program that is capable to derive EoM like the ones presented in [Gies et al., 2007]. Our new formulated EoM technique is a general procedure that allows for all freedoms of modelling and is still clear enough to be executed by a computer.

Equation of motion techniques have been used successfully to realize microscopic descriptions of quantum systems, and are a way to systematically incorporate many-particle correlations into the description of exciton dynamics in quantum wells [Hoyer et al., 2003], ultracold Bose gases [Köhler and Burnett, 2002], spin dynamics [Kapetanakis and Perakis, 2008], photoluminescence [Kira et al., 1998], resonance fluorescence [Kira et al., 1999], cavity phonons [Kabuss et al., 2012], cavity-quantum-electrodynamics [Carmele et al., 2010], and microcavity quantum dot (QD) lasers [Gies et al., 2007]. The basic idea of EoM approaches is to truncate the hierarchy of differential equations at a certain level, to allow for a numerical integration. The details of the truncation depend strongly on the used technique and the investigated system and are the subject of this chapter. Many different formulations and approximation techniques are known in the field of EoM approaches. However, we will distinguish between two basic types of formulation using CFs [Wiersig et al., 2009; Kapetanakis and Perakis, 2008; Kira et al., 1998, 1999; Hoyer et al., 2003; Hohenester and Pötz, 1997] as in the cluster expansion [Fricke, 1996a; Hoyer et al., 2004] on the one hand and EVs on the other hand [Gartner, 2011; Richter et al., 2009; Witthaut et al., 2011; Kabuss et al., 2012; Carmele et al., 2010]. The formulation in CFs is algebraically demanding but has proven to be very effective in approximately describing large systems. Expectation value based formulations are algebraically less demanding and produce a linear and very clear system of EoM, but are usually limited to small systems. The proposed approach combines the two formulations with their respective advantages and adds a new perspective on former techniques.

The outline of this chapter is as follows. In Sec. 2.2, we revisit the general concept of CFs and the factorization of EVs. The approximation techniques presented in Sec. 2.2 are the basis for the truncation variants presented in Sec. 2.3. Section 2.3 is devoted to the derivation of EoM and we show how the introduced formulation can be used to truncate the unfolding hierarchy of EoM. We focus on the truncation of EoM for systems involving bosons and fermions and provide details on various truncation possibilities. The deviation of multi-time EoM is discussed in detail for the first and second order coherence functions 2.3.4. In Sec. 2.4, we give an example for the EoM of a coupled quantum system and show how different truncation schemes result in known models. We also present an extension of the semiconductor QD laser model introduced by Gies et al. [2007]. This extension is used to monitor the lasing transition in higher-order photon-autocorrelation functions. Numerical results of the applications in Sec. 2.4 are used to study the convergence properties of the EVCE. Finally, in Sec. 2.5, various methods found in the literature are compared and interpreted according to the formulation introduced.

2.2 The concept of correlation functions

In the following, we recapitulate and work out the details of the CF concept. The fundamental definitions of CFs and a formal introduction to CFs can be found in Fricke [1996a]. We introduce a new formulation that will facilitate switching between a formulation in EVs or CFs. With this flexibility in the formulation we give detail to the various approximations that are related to the neglection of EVs and CFs.

2.2.1 Definition of correlation functions

A key point of this section is the fact that one can represent every EV $\langle b_1 b_2 \cdots b_k \rangle$ of operators b_i as a sum of products of CFs in a unique way. In this part, we stick to bosonic operators to keep the general ideas clear.

For the mathematical framework, we define a set of indices $I = \{1, 2, \cdots, k\}$ and a product of operators $b^I = b_1 b_2 \cdots b_k$. P is a partition of the set I meaning a set family of disjoint nonempty subsets J of I with $\cup_{J \in P} J = I$, and finally P_I is defined as the set of all partitions of I. We introduce the factorization operator $\mathbf{F}$. This operator does not change the value of the complex number $\langle b^I \rangle$, instead $\mathbf{F}$ changes the representation of the EV similar to a passive transformation of a vector. With these preliminaries we can now give a general definition of the CFs $\delta(b^J)$:

$$\mathbf{F} \langle b^I \rangle = \delta(b^I) + \delta(b^I)_F = \sum_{P \in P_I} \prod_{J \in P} \delta(b^J). \tag{2.1}$$

where $\delta(b^I)_F$ is a short notation for the sum of products of all possible factorizations of the operator EV $\langle b^I \rangle$ into CFs containing a smaller number of operators than the cardinality of I, $\#(I)$. We show as an example the factorizations of the first EVs containing products of up to three operators according to Eq. (2.1):

$$\begin{aligned} \mathbf{F} \langle b_1 \rangle &= \delta(b_1), \\ \mathbf{F} \langle b_1 b_2 \rangle &= \delta(b_1 b_2) + \delta(b_1)\delta(b_2), \\ \mathbf{F} \langle b_1 b_2 b_3 \rangle &= \delta(b_1 b_2 b_3) + \delta(b_1 b_2)\delta(b_3) + \delta(b_1 b_3)\delta(b_2) \\ &\quad + \delta(b_2 b_3)\delta(b_1) + \delta(b_1)\delta(b_2)\delta(b_3). \end{aligned} \tag{2.2}$$

One can define the inverse operation $\mathbf{F}^{-1}\mathbf{F} = \mathbf{1}$ as well. Applying $\mathbf{F}^{-1}$ to Eq. (2.1),

$$\mathbf{F}^{-1}\delta(b^I) = \langle b^I \rangle - \mathbf{F}^{-1}\delta(b^I)_F, \tag{2.3}$$

gives an implicit definition of $\mathbf{F}^{-1}$. As well as $\mathbf{F}$, the operator $\mathbf{F}^{-1}$ does not change the value of the complex number $\delta(b^I)$, but rather its representation. By successively applying Eq. (2.3) to itself one arrives at the form

$$\mathbf{F}^{-1}\delta(b^I) = \sum_{P \in P_I} c_P \prod_{J \in P} \langle b^J \rangle \tag{2.4}$$

with $c_P = (-1)^{\#(P)-1}(\#(P) - 1)!$, where the CF is represented entirely by EV. Due to the implicit definition of $\mathbf{F}^{-1}$ the coefficients c_P are not equal to $+1$ as in Eq. (2.2). The first three 'refactorized' CFs according to Eq. (2.4) are:

$$\begin{aligned}
\mathbf{F}^{-1}\delta(b_1) &= \langle b_1\rangle\,, \\
\mathbf{F}^{-1}\delta(b_1b_2) &= \langle b_1b_2\rangle - \langle b_1\rangle\langle b_2\rangle\,, \\
\mathbf{F}^{-1}\delta(b_1b_2b_3) &= \langle b_1b_2b_3\rangle - \langle b_1b_2\rangle\langle b_3\rangle - \langle b_1b_3\rangle\langle b_2\rangle \\
&\quad - \langle b_2b_3\rangle\langle b_1\rangle + 2\langle b_1\rangle\langle b_2\rangle\langle b_3\rangle\,.
\end{aligned} \tag{2.5}$$

With the recursive definition one can easily prove by induction that every EV can be represented in an unambiguous way by CFs and every CF can be represented by EVs as well. The definition of the lowest-order CF is linear and therefore obviously unambiguous. By using this first definition one can solve the second-order equation unambiguously and with these two solutions one can solve the third-order equation unambiguously and so on, therefore $\mathbf{F}^{-1}\mathbf{F} = \mathbf{F}\mathbf{F}^{-1} = 1$ holds for every order. Note that a similar definition of CFs can be introduced for fermionic operators f_i, if the sign of $\delta(f^J)$ is changed for every commutation of operators corresponding to identical fermionic particles that is performed in the factorization of $\delta(f^I)$.

2.2.2 Approximations by lower-order quantities

In this section, we show how the concept of representing a quantity by a sum of products of another quantity can be exploited for approximation schemes. To this end we introduce the abbreviated notation $\delta(N)$, representing any function of CFs $\delta(b^I)$ of order N or smaller ($O[\delta(b^I)] = \#(I) \leq N$). As an example, we display the third line of Eqs. (2.2) in this fashion:

$$\mathbf{F}\langle b_1b_2b_3\rangle \equiv \delta(3) + 3\delta(2)\delta(1) + \delta(1)^3 \equiv \delta(3).$$

To symbolize neglections we define the truncation operator $\Delta_{\delta(N)}$. Applied to any function of CFs, all CFs of order larger than N are neglected

$$\Delta_{\delta(N)}\delta(N+1) = \delta(N). \tag{2.6}$$

To further illustrate this notation we apply $\Delta_{\delta(2)}$ on the third line in Eqs. (2.2)

$$\Delta_{\delta(2)}\left(\delta(3) + 3\delta(2)\delta(1) + \delta(1)^3\right) = 3\delta(2)\delta(1) + \delta(1)^3 \equiv \delta(2),$$

leaving an expression that contains only CFs up to order two. Whether this neglection is justified depends on the physical system under investigation. An analogous definition can be made for the neglection of EVs, here $\langle N\rangle$ is a short notation for any function of EVs addressing N or less operators. The application of the truncation operator $\Delta_{\langle N\rangle}$,

$$\Delta_{\langle N\rangle}\langle N+1\rangle = \langle N\rangle\,, \tag{2.7}$$

reduces any function of EV $\langle N+1\rangle$ of order $(N+1)$ to a function of EVs containing only EVs of order N or smaller by setting $\langle N+1\rangle$ to zero.

The application of the truncation operator is simple when $\Delta_{\delta(N)}$ is applied to CFs, and $\Delta_{\langle N\rangle}$ is applied to EVs. However, the representation of the quantities in

EV or CF is independent from the approximation one applies. One can formulate all quantities in CFs and make an approximation by neglecting higher-order CFs. Alternatively, one can formulate all quantities in EV and still apply the very same approximation. Using the factorization operators $\mathbf{F}^{(-1)}$ we can apply $\Delta_{\delta(N)}$ to EVs as well. The EV must be rewritten into CFs (by application of $\mathbf{F}$), then the highest order CF is set to zero (by application of $\Delta_{\delta(\#I-1)}$) and finally the remaining CFs are rewritten as EVs (by application of $\mathbf{F}^{-1}$). The EV $\left\langle b^I \right\rangle$ is approximated by

$$\mathbf{F}^{-1}\Delta_{\delta(\#I-1)}\mathbf{F}\left\langle b^I \right\rangle = -\sum_{P\in P_I\setminus I} c_P \prod_{J\in P}\left\langle b^J \right\rangle, \tag{2.8}$$

a sum of products of lower-order EVs. We show in Sec. 2.3.2 that this approximation scheme is very useful when it is necessary to describe systems with a large number of particles and many degrees of freedom. To illustrate the approach, we apply $\Delta_{\delta(1)}$ to $\langle b_1 b_2\rangle$ and $\langle b_1 b_2 b_3\rangle$ and$\Delta_{\delta(2)}$ to $\langle b_1 b_2 b_3\rangle$:

$$\begin{aligned}
\mathbf{F}^{-1}\Delta_{\delta(1)}\mathbf{F}\langle b_1 b_2\rangle &= \langle b_1\rangle\langle b_2\rangle, && (2.9)\\
\mathbf{F}^{-1}\Delta_{\delta(1)}\mathbf{F}\langle b_1 b_2 b_3\rangle &= \langle b_1\rangle\langle b_2\rangle\langle b_3\rangle, && (2.10)\\
\mathbf{F}^{-1}\Delta_{\delta(2)}\mathbf{F}\langle b_1 b_2 b_3\rangle &= \langle b_1 b_2\rangle\langle b_3\rangle + \langle b_1 b_3\rangle\langle b_2\rangle && (2.11)\\
&\quad + \langle b_2 b_3\rangle\langle b_1\rangle - 2\langle b_1\rangle\langle b_2\rangle\langle b_3\rangle.
\end{aligned}$$

The reader will recognize Eq. (2.9) as the mean-field approximation and Eq. (2.10) as related to the second Born approximation [Hoyer et al., 2003]. Equation (2.11) reproduces the so-called Bogoliubov back-reaction method recently used by Witthaut et al. [2011]; Trimborn et al. [2011].

Since we have defined unambiguous transformations between CFs and EVs, it is also possible to formulate analogous approximations for CF $\delta(b^I)$. In this case, the truncation operator $\Delta_{\langle N\rangle}$ is applied to a CF:

$$\mathbf{F}\Delta_{\langle N-1\rangle}\mathbf{F}^{-1}\delta(b^I) = -\sum_{P\in P_I\setminus I}\prod_{J\in P}\delta(b^J). \tag{2.12}$$

A CF is approximated by a sum of products of lower-order CFs, since the corresponding EV vanishes. One can find this way of approximation in Florian et al. [2013b], were the finite number of carriers confined in a single QD is considered by replacing higher CFs with their factorizations.

We have formulated the two different approximations in a very symmetric fashion. Nevertheless, the two approximations are quite the opposite of each other: when a system has many degrees of freedom and a CF of certain order is negligible, the corresponding EV is not,

$$\delta(b^I) = 0 \qquad \Rightarrow \qquad \left\langle b^I \right\rangle = \mathbf{F}^{-1}\delta(b^I)_F,$$

but has to be replaced by products of non-zero EVs of lower order. If a system has only a limited number of particles and certain normal ordered EVs vanish

$$\left\langle b^I \right\rangle = 0 \qquad \Rightarrow \qquad \delta(b^I) = -\delta(b^I)_F,$$

the corresponding CF cannot be neglected but must be replaced by its factorization. In Sec. 2.4.1 we will give a specific example on the difference of the two approaches and see how badly a system with vanishing EV can be described by EoM in which CFs are neglected.

We emphasize that up to this point our considerations are of entirely formal nature. We worked out the case of a vanishing CF and the effect this has on the corresponding EV and vice versa. It depends on the investigated physical system whether one of these approximations is adequate.

2.3 Equations of motion

In this section, we show how EVs and CFs are used to derive EoM for a given physical system. We work out how the suggested approximation schemes can be applied to different systems of EVs or CFs. We also discuss the situation of a mixed Hilbert space describing different types of particles.

2.3.1 Infinite hierarchy

The dynamics of an open quantum mechanical system with the Hamiltonian H is described by the von Neumann-Lindblad equation (vNL) (1.8) for the density operator ρ. For many systems, an exact solution of $\rho(t)$ is not feasible due to the size of the system and the interaction part of H. Moreover, a solution of $\rho(t)$ is not necessary for many applications and it is enough to know the dynamics of some EVs $\langle A\rangle = \mathrm{Tr}(A\rho)$. Equation (1.8) can be used to derive generalized Ehrenfest EoM Eq. (1.9) for the desired operator EVs $\langle A\rangle$. In Eq. (1.9), $\mathcal{L}$ is a superoperator that stands for the application of the Lindblad form and the commutator with H to the operator A. When deriving Ehrenfest EoM, the interaction part of the Hamiltonian and the scattering terms in the Lindblad form lead to a hierarchy of EoM. These terms couple a first-order quantity to a second-order quantity and a second order to a third-order quantity and so on. Symbolically this reads:

$$\begin{aligned} \frac{d}{dt}\langle 1\rangle &= \langle \mathcal{L}(1)\rangle = \langle 2\rangle \\ \frac{d}{dt}\langle 2\rangle &= \langle \mathcal{L}(2)\rangle = \langle 3\rangle \\ &\vdots \quad \vdots \quad \vdots \end{aligned} \tag{2.13}$$

and without any truncation the hierarchy would go up to infinite order. In many cases, it is possible to calculate the effect of $\mathcal{L}$ for a whole family of operators A_a and to formulate an inductive scheme for arbitrary high orders [Gartner, 2011; Kabuss et al., 2011]. When the system contains only n particles, then normal ordered EVs addressing $n+1$ particles vanish,

$$\langle b^\dagger \cdots b^\dagger \underbrace{b \cdots b}_{n+1}\rangle = 0$$

which has the same effect as the application of the truncation operator $\Delta_{\langle N\rangle}$ with $N = 2n$:

$$\langle 2n+1\rangle \approx \Delta_{\langle 2n\rangle} \langle 2n+1\rangle = \langle 2n\rangle \,. \tag{2.14}$$

Note that in the case of finite particle numbers the total number of normal ordered operators is not important, but the number of annihilation (creation) operators is. However, we do not focus on this point because in every practical case one can unambiguously identify the vanishing EV. The truncation operator $\Delta_{\langle N\rangle}$ applied on the Nth line of the hierarchy in Eqs. (2.13) leads to a finite system of linear differential equations:

$$\begin{aligned} \frac{d}{dt}\langle 1\rangle &= \langle \mathcal{L}(1)\rangle = \langle 2\rangle \\ &\vdots \quad \vdots \quad \vdots \\ \frac{d}{dt}\langle N\rangle &= \langle \mathcal{L}(N)\rangle \approx \Delta_{\langle N\rangle}\langle N+1\rangle = \langle N\rangle \,. \end{aligned} \tag{2.15}$$

Figure 2.1 gives a visualization of the coupled linear EoM in system (2.15). This truncation scheme is useful when the system contains a small number of particles occupying a limited number of states, i.e. ,the Hilbert space is finite and manageable with numerical methods. If a system can be described by this method it is, in principle, also possible to solve the vNL Eq. (1.8) directly, since the corresponding matrix equation can be solved in the basis of configurations the finite number of particles occupy. These approaches are often called numerically exact methods.

Figure 2.1: Illustration of an EV hierarchy. The black lines indicate the linear coupling between the EV of increasing order. One can imagine the hierarchy as a line of EVs coupled by linear differential equations to the next order. The hierarchy is truncated by setting the $(N+1)$ EV to zero, i.e. applying the truncation operator $\Delta_{\langle N\rangle}$.

When the physical system under consideration is too large to be described by a finite Hilbert space, the cluster expansion method has proven beneficial. In this method: the EoM are derived for the CFs and the CFs of certain order are neglected. To derive the EoM for the CF $\delta(b^I)$, the Ehrenfest EoM (1.9) has to be applied to the corresponding EV and the resulting EVs have to factorized into CFs again and finally the previously calculated derivatives of the lower-order factorizations have to be subtracted:

$$\frac{d}{dt}\delta(b^I) = \mathbf{F}\left\langle \mathcal{L}(b^I)\right\rangle - \frac{d}{dt}\delta(b^I)_F. \tag{2.16}$$

As well as for the EV hierarchy, the interaction and scattering terms in $\mathcal{L}$ give rise to an infinite hierarchy of CFs:

$$\begin{aligned} \frac{d}{dt}\delta(1) &= \mathbf{F}\langle\mathcal{L}(1)\rangle - \frac{d}{dt}\delta(1)_F = \delta(2), \\ \frac{d}{dt}\delta(2) &= \mathbf{F}\langle\mathcal{L}(2)\rangle - \frac{d}{dt}\delta(2)_F = \delta(3), \\ &\vdots \quad \vdots \quad \vdots \end{aligned} \tag{2.17}$$

The infinite hierarchy displayed in the set of Eqs. (2.17) is equivalent to the infinite hierarchy in Eqs. (2.13) and the two systems of EoM produce exactly the same results if they were formulated up to infinite order and solved exactly.

For a large system with sufficiently weak interaction, CFs $\delta(b^I)$ of order $\#(I) > N$ can be neglected and the hierarchy of CFs can be truncated. This is equivalent to the application of the truncation operator $\Delta_{\delta(N)}$ (from Eq. (2.6)) to the Nth line of the hierarchy in Eqs. (2.17)

$$\begin{aligned} \frac{d}{dt}\delta(1) &= \mathbf{F}\langle\mathcal{L}(1)\rangle - \frac{d}{dt}\delta(1)_F = \delta(2), \\ &\vdots \quad \vdots \quad \vdots \\ \frac{d}{dt}\delta(N) &= \mathbf{F}\langle\mathcal{L}(N)\rangle - \frac{d}{dt}\delta(N)_F \\ &\approx \Delta_{\delta(N)}\mathbf{F}\langle\mathcal{L}(N)\rangle - \frac{d}{dt}\delta(N)_F = \delta(N). \end{aligned} \tag{2.18}$$

This system of Eqs. (2.18) visualized in Fig. 2.2 is no longer equivalent to the truncated hierarchy of EVs in Eqs. (2.15) due to the application of different truncation operators. In fact, Eqs. (2.15) and Eqs. (2.18) describe opposite situations in the same sense as pointed out at the end of Sec. 2.2.2.

Figure 2.2: Illustration of a CF hierarchy. The CF of a certain order couple linearly to the CF of the next order indicated by the black line, but also to products of lower-order CF indicated by the blue merging lines on top. To truncate the hierarchy at order N the $(N+1)$th CF is set to zero i.e. the truncation operator $\Delta_{\delta(N)}$ is applied. In contrast to the EV hierarchy depicted in Fig. 2.1 the CF hierarchy cannot be imagined as a straight line, due to the nonlinear coupling of the CF. The structure of this hierarchy is nonlinear and can be imagined as an intertwined chain.

Let us compare the hierarchies (2.13,2.15) of EVs to the hierarchies (2.17,2.18) of CFs. On the one hand Eqs. (2.13,2.15) are entirely linear since they originate from the linear Ehrenfest EoM (1.9). The only necessary algebraic operation to derive these equations is the normal ordering of $\mathcal{L}(b^I)$. The truncated version in

Eqs. (2.15) can be used to describe the dynamics of a finite quantum system. On the other hand Eqs. (2.17,2.18) are nonlinear for all orders larger than one. To derive these equations, $\mathcal{L}(b^I)$ has to be normal ordered, the resulting EV has to be factorized and time derivative of the lower-order factorizations has to be subtracted. Without advanced methods the algebraic effort is very high since the factorization ($\mathbf{F}\left\langle\mathcal{L}(b^I)\right\rangle$) and the time derivative of the products of the lower-order CFs ($\frac{d}{dt}\delta(b^I)_F$) are demanding and error intensive operations and have to be performed for every single order in the hierarchy. The benefits of this effort are that Eqs. (2.18) can be used to describe the dynamics of a large system with small correlations that would in fact be too large to be described by the set of Eqs. (2.15).

2.3.2 Expectation value based cluster expansion

We will now give detail to the main concept of the EVCE, the independence of the formulation of the EoM in EVs or CFs from the principle of approximation that is used to truncate the infinite hierarchy of EoM. We have shown in Sec.2.2.2 that one can apply $\Delta_{\delta(N)}$ to EVs and $\Delta_{\langle N\rangle}$ to CFs as well. The consequence is that we can apply the truncation operator $\Delta_{\delta(N)}$ also on the Nth line of Eqs.(2.13) and obtain a system of EoM formulated in EVs that is equivalent to the CF system Eqs.(2.18):

$$\begin{aligned}
\frac{d}{dt}\langle 1\rangle &= \langle\mathcal{L}(1)\rangle = \langle 2\rangle \\
&\vdots \quad \vdots \quad \vdots \\
\frac{d}{dt}\langle N\rangle &= \langle\mathcal{L}(N)\rangle \approx \mathbf{F}^{-1}\Delta_{\delta(N)}\mathbf{F}\langle N+1\rangle = \langle N\rangle\,.
\end{aligned} \tag{2.19}$$

Equations (2.19) are equivalent to Eqs. (2.18), and produce the same results, since the same truncation scheme ($\Delta_{\delta(N)}$) is used. Note that equations (2.19) are almost linear, only the EoM where actual approximations are made are nonlinear. An infinite system of linear equations is approximated by a finite set of nonlinear equations in which the non-linearity arises from the approximation. A visualization of Eqs. (2.19) can be found in Fig. 2.3. We emphasize that it is much less demanding to

Figure 2.3: Illustration of an EV hierarchy truncated by neglecting CFs. This hierarchy is equivalent to the hierarchy illustrated in Fig. 2.2 though in its structure it is very similar to the EV hierarchy illustrated in Fig. 2.1. The EVs of a certain order couple linearly to the next order. The truncation here is not achieved by setting the $(N+1)$th EV to zero but by substituting it by products of lower-order EVs indicated by the merging blue line entering the Nth EV from the side mediated by the truncation operator. In consequence, this hierarchy can be imagined as an "almost" straight line where only the last order couples nonlinearly to products of lower-order quantities.

derive Eqs. (2.19) than Eqs. (2.18) since an inductive scheme can be used to derive Eqs.(2.19) up to line N. The factorizations that are required in $\mathbf{F}^{-1}\Delta_{\delta(N)}\mathbf{F}\langle N+1\rangle$ can be listed as indicated in Eqs. (2.9-2.11) and all emerging EVs of order larger than N can be substituted according to such a list. Though this formulation is very different from the "traditional" cluster expansion it can still be called so, since its approximations and results are exactly the same.

For the sake of completeness, we will also show a system of equations equivalent to Eqs. (2.15) but entirely formulated in terms of CFs:

$$\begin{aligned}
\frac{d}{dt}\delta(1) &= \mathbf{F}\langle\mathcal{L}(1)\rangle - \frac{d}{dt}\delta(1)_F = \delta(2), \\
&\vdots \quad \vdots \quad \vdots \\
\frac{d}{dt}\delta(N) &= \mathbf{F}\langle\mathcal{L}(N)\rangle - \frac{d}{dt}\delta(N)_F \\
&\approx \mathbf{F}\Delta_{\langle N\rangle}\langle\mathcal{L}(N)\rangle - \frac{d}{dt}\delta(N)_F = \delta(N).
\end{aligned} \tag{2.20}$$

The visualization of this system of equations is displayed in Fig. 2.4. It is obvious

Figure 2.4: Illustration of a CF hierarchy truncated by neglecting EVs. This hierarchy is equivalent to the hierarchy illustrated in Fig. 2.1 though in its structure it is very similar to the CF hierarchy illustrated in Fig. 2.2. The CF of a certain order couple linear to the CF of the next order indicated by the black line, but also to products of lower-order CF indicated by the blue merging lines on top. The truncation here is not achieved by setting the $(N+1)$th CF to zero but by substituting it by products of lower-order CF indicated by the merging blue line entering the Nth CF from the right side.

that it is clearer and easier to derive Eqs. (2.15) than it is to derive Eqs. (2.20), but we see that it is possible to describe a finite system exactly by EoM formulated in CFs.

We conclude this subsection with the suggestion to formulate all EoM in terms of EVs. If the neglection of CFs is required the truncation operator in combination with the factorization operators $\mathbf{F}^{-1}\Delta_{\delta(N)}\mathbf{F}$ can be used. By this approach, one can use simple inductive algebra to derive Ehrenfest EoM for the EVs and then make the factorizations only in the highest order EVs. The resulting EoM are much simpler in structure than the equivalent ones formulated in CFs and are much easier to obtain. Another advantage of the formulation in terms of EVs is that the effect of the neglection of CFs is directly marked in the equations by the nonlinearities in the otherwise linear equations.

2.3.3 Equation of motion for mixed Hilbert spaces

The advantage of the formulation of the EoM via EV becomes even more evident when one investigates the dynamics of a coupled system, in which the various types of particles have different constraints and correlation strength. For example, let us consider a system coupling fermionic carriers described by creation/annihilation operators from the set $\mathcal{F} = \{f_1^\dagger, \ldots, f_n^\dagger, f_1, \ldots, f_n\}$ to a quantized light field described by bosonic creation/annihilation operators $\mathcal{B} = \{b_1^\dagger, \ldots, b_m^\dagger, b_1, \ldots, b_m\}$. A general normal ordered EV in this system would be $\left\langle b^I f^K \right\rangle = \langle b_i^\dagger \ldots b_l f_o^\dagger \ldots f_r \rangle$, where I and K are index sets addressing elements in $\mathcal{B}$ and $\mathcal{F}$ respectively. In analogy, to the abbreviated notation introduced at the beginning of Sec. 2.2.2 we will write $\langle N, M \rangle$ for any function of EVs $\left\langle b^I f^K \right\rangle$ with a maximum order N, M given by the cardinality of the index sets ($\#I \leq N, \#K \leq M$). And we will write $\delta(N, M)$ for an arbitrary function of CFs $\delta(b^I f^K)$ with a maximum order N, M. In Sec. 2.2.2 we have introduced the truncation operators $\Delta_{\langle N \rangle / \delta(N)}$ acting either on EVs or CFs. For mixed Hilbert spaces the truncation operator must be specified further to indicate on which part of the EV/CF Δ it is acting on. The upper index $\mathcal{B}, \mathcal{F}$ specifies whether Δ is applied on the bosonic or on the fermionic part of the quantity. We give examples for $\Delta_{\delta(N/M)}$ acting on CFs

$$\Delta^{\mathcal{B}}_{\delta(N-1)} \delta(N, M) = \delta(N-1, M), \tag{2.21}$$

$$\Delta^{\mathcal{F}}_{\delta(M-1)} \delta(N, M) = \delta(N, M-1), \tag{2.22}$$

$$\Delta^{\mathcal{B}+\mathcal{F}}_{\delta(N+M-1)} \delta(N+M) = \delta(N+M-1). \tag{2.23}$$

In our example $\Delta^{\mathcal{B}}_{\delta(N)}$ neglects bosonic correlations in Eq. (2.21), $\Delta^{\mathcal{F}}_{\delta(M)}$ neglects fermionic correlations in Eq. (2.22) and $\Delta^{\mathcal{B}+\mathcal{F}}_{\delta(N+M)}$ neglects $(N+M)$-particle correlations in Eq. (2.23), which can be reasonable in large systems with a direct coupling between the different particles. There are many cases were the weighting of the operators is not symmetrical $(\mathcal{B} + \mathcal{F})$ but weighted $(\mathcal{B} + w\mathcal{F})$ with w being the weighting factor[Kira et al., 1999]. This is for instance the case when a large system is dominated by the dipole Hamiltonian $b^\dagger f_g^\dagger f_e + b f_e^\dagger f_g$. In this case one boson operator is coupled to two fermi operators and the weighting factor is 1/2.

2.3.4 Multi-time equation of motion

In this section, we show how the EVCE can be applied to calculate multi-time EoM. This topic is especially relevant for the description of open quantum systems since some properties can be obtained with the help of multi-time expectation values [Meystre and Murray, 1999; Ates et al., 2008; Gies et al., 2012]. Typical quantities that can for example be measured in optical experiments are the autocorrelation functions of first and second order for which the EVs $\langle b^\dagger(t+\tau) b(t) \rangle$ and $\langle b^\dagger(t) b^\dagger(t+\tau) b(t+\tau) b(t) \rangle$ have to be calculated.

For the von Neumann-Lindblad equation we have discussed this subject already in chapter 1.2. If the system can be described with a finite density matrix(closed set of linear differential equation) the multi-time EoM are described by the same EoM Eq. (1.11) due to the quantum regression theorem [Meystre and Murray, 1999;

Breuer and Petruccione, 2002]. In the formalism of the EVCE we have the choice of the two fundamentally different approximation schemes. The first possibility is to use $\Delta_{\langle N\rangle}$. Since in this case we end up with a linear set of differential equations, there is no principal difference to Eq. (1.11). The second possibility is to use $\Delta_{\delta(N)}$. In this case the time dynamics are described by a closed set of nonlinear differential equations and it is not possible to use the single-time EoM for the description of the multi-time EoM.

In particular we are going to derive EoM of the type $\frac{d}{d\tau}\left\langle b^I(t+\tau)b(t)\right\rangle$ for the first and $\frac{d}{d\tau}\left\langle b^\dagger(t)b^I(t+\tau)b(t)\right\rangle$ for the second order coherence functions that arise in the hierarchy of the EoM. Without loss of generality we restrict ourselves again to bosonic operators where b^I that stands for a combination of creation and annihilation operators. The calculation of a two-time EV can be understood in the following way: first we calculate the t dynamics until a certain time t_C is reached and afterwards we are going to calculate the τ dynamics from this point on. For a convenient presentation, we discuss here only the case of the stationary regime $t\to\infty$ that is already enough for many applications. We can concentrate on the τ dynamics and write the differential equations $\frac{d}{d\tau}\left\langle b^I(\tau)b_\infty\right\rangle$ or respectively $\frac{d}{d\tau}\left\langle b_\infty^\dagger b^I(\tau)b_\infty\right\rangle$ where $b_\infty = b(t=\infty)$.

First-order coherence

For the calculation of the first-order coherence function we have to derive EoM for EV of the type $\left\langle b^I(\tau)b_\infty\right\rangle$, where $b^I(\tau)$ stands for a combination of creation and annihilation operators. Applying the quantum regression theorem [Lax, 1967; Meystre and Murray, 1999; Breuer and Petruccione, 2002] to the density operator we can write down an equation similar to the generalized Ehrenfest EoM (1.9) for the τ dynamics at time τ

$$\begin{aligned}\frac{d}{d\tau}\left\langle b^I(\tau)b_\infty\right\rangle &= \frac{i}{\hbar}\left\langle\left[H,b^I(\tau)\right]b_\infty\right\rangle \\ &+\sum_{\nu,\nu'}\lambda_{\nu,\nu'}\left\{2\left\langle L_\nu^\dagger b^I(\tau)L_{\nu'}^\dagger b_\infty\right\rangle-\left\langle L_\nu^\dagger L_{\nu'}b(\tau)^I b_\infty\right\rangle-\left\langle b(\tau)^I L_\nu^\dagger L_{\nu'}b_\infty\right\rangle\right\},\end{aligned} \tag{2.24}$$

where we obtain an infinite hierarchy of EoM. Following the concept of the EVCE the new EVs can be factorized in the same manner as the EV that depend solely from time t using Eq. (2.8)

$$\mathbf{F}^{-1}\Delta_{\delta(\#I'-1)}\mathbf{F}\langle b^{I'}(\tau)\rangle = -\sum_{P\in P_{I'}\setminus I'} c_P\left(\left\langle b^K(\tau)b_\infty\right\rangle\prod\left\langle b^J(\tau)\right\rangle\right), \tag{2.25}$$

with $b^{I'}(\tau)=b^I(\tau)b_\infty$ and $J,K\subset I'$. The truncated EoM now consists of a sum of products of two types of lower-order EVs. Since there is only one operator b_∞ in the EV every summand of the factorization contains only one EV of the type $\left\langle b^K(\tau)b_\infty\right\rangle$ and potentially a product of $\left\langle b^J(\tau)\right\rangle$. The EoM are vastly simplified in the case of the stationary regime using the fact that $\langle b^J(t+\tau)\rangle = \langle b^J(\infty+\tau)\rangle = \langle b^J(\infty)\rangle = \langle b_\infty^J\rangle$ we find that the closed set of EoM is a linear set of ODEs with the initial condition from the nonlinear t system $\langle b^{I'}(\tau=0)\rangle = \langle b_\infty^I b_\infty\rangle$. The general form of the EoM

for the first order coherence function, can be written as

$$\frac{d}{d\tau}\left\langle b_i(\tau)b_k\right\rangle = \sum_j G_{ij}\left\langle b_j(\tau)b_k\right\rangle . \tag{2.26}$$

with a corresponding coefficient matrix G_{ij} that consists of coefficients from the Hamiltonian and the Lindblad processes as well as the stationary values with respect to τ.

Second-order coherence

For the calculation of the second-order coherence function we have to derive EoM for EV of the type $\left\langle b_\infty^\dagger b^I(\tau)b_\infty\right\rangle$, where $b(\tau)^I$ stands for a combination of creation and annihilation operators. Just in the same way we derived the EoM for the first-order coherence function we can derive an Ehrenfest alike EoM for the second-order coherence function

$$\begin{aligned}\frac{d}{d\tau}\left\langle b_\infty^\dagger b^I(\tau)b_\infty\right\rangle = &\frac{i}{\hbar}\left\langle b_\infty^\dagger\left[H, b^I(\tau)\right]b_\infty\right\rangle \\ &+\sum_{\nu,\nu'}\lambda_{\nu,\nu'}\left\{2\left\langle b_\infty^\dagger L_\nu^\dagger b^I(\tau)L_{\nu'}b_\infty\right\rangle - \left\langle b_\infty^\dagger L_\nu^\dagger L_{\nu'}b^I(\tau)b_\infty\right\rangle\right. \\ &\left.-\left\langle b_\infty^\dagger b^I(\tau)L_\nu^\dagger L_{\nu'}b_\infty\right\rangle\right\}\end{aligned} \tag{2.27}$$

and obtain an infinite hierarchy for this new type of EVs. Using Eq. (2.8) to factorize EVs of the type $\left\langle b_\infty^\dagger b^I(\tau)b_\infty\right\rangle$ we have

$$\mathbf{F}^{-1}\Delta_{\delta(\#I'-1)}\mathbf{F}\langle b^{I''}\rangle = -\sum_{P\in P_{I'}\setminus I'} c_P\prod\left\langle b^J(\tau)\right\rangle \tag{2.28}$$

$$\left(\left\langle b_\infty^\dagger b^K(\tau)\right\rangle\left\langle b^L(\tau)b_\infty\right\rangle + \left\langle b_\infty^\dagger b^M(\tau)b_\infty\right\rangle\right), \tag{2.29}$$

with $\langle b^{I''}\rangle = \left\langle b_\infty^\dagger b^I(\tau)b_\infty\right\rangle$ and $J, K, L, M \subset I'$. This factorization consists a sum of products of three types of lower-order EVs. Since there is only one operator b_∞ and one operator $b_\infty^\dagger$ in the initial EV there are two possibilities how these two operators can be distributed. Either in one EV $\left\langle b_\infty^\dagger b^M(\tau)b_\infty\right\rangle$ or in a product of two EVs $\left\langle b_\infty^\dagger b^K(\tau)\right\rangle\left\langle b^L(\tau)b_\infty\right\rangle$. In the same way we could simplify the first-order coherence function, we can again evaluate the EoM for $t\to\infty$ with $\langle b^J(\tau)\rangle = \langle b_\infty^J\rangle$. Now the EoM form a nonhomogeneous linear set of ODEs

$$\frac{d}{d\tau}\left\langle b_\infty^\dagger b^I(\tau)b_\infty\right\rangle = \sum_J \tilde{G}_{IJ}\left\langle b_\infty^\dagger b^J(\tau)b_\infty\right\rangle + f(\tau). \tag{2.30}$$

with a corresponding coefficient matrix $\tilde{G}_{ij}$ that consists of coefficients from the Hamiltonian and the Lindblad processes as well as the stationary values wit respect to τ and a homogeneity $f(\tau)$ that consists of products of first-order coherence EVs $\left\langle b_\infty^\dagger b^K(\tau)\right\rangle\left\langle b^L(\tau)b_\infty\right\rangle$. The homogeneous solution of Eq. (2.30) can be found in the same way as for Eq. (2.26) while the particular solution can be found using $\frac{d}{d\tau}\langle b_i(\tau)b_k\rangle = 0$ for $\tau\to\infty$, where the value of $f(\tau=\infty)$ can be determined with Eq. (2.26).

2.4 Applications

To illustrate our approach, we give a specific example for a hierarchy of EoM describing a coupled electron-photon system. We give details on how the derived EoM can be used to describe very different physical systems depending on the approximations that are made to truncate the hierarchy. We show how our approach can be used to exploit the cluster expansion further for one specific example. The transition from thermal to laser light is monitored in higher-order photon-autocorrelation functions for a microscopic semiconductor QD laser model. And we show for this system the validity of the cluster expansion. To conclude this section we interpret former EoM techniques according to our approach.

2.4.1 Hierarchy induced by the dipole Hamiltonian

For systems with coupling in-between the different kinds of particles, the hierarchy unfolds into various directions. In this example, the dipole Hamiltonian

$$H_D = \sum g_m b^\dagger f_{g_m}^\dagger f_{e_m} + h.c., \tag{2.31}$$

for a single optical mode in rotating wave approximation (see, for example, [Meystre and Murray, 1999]) couples the operators $b^{(\dagger)} \in \mathcal{B}$ annihilating (creating) a photon in the cavity mode, $b|n\rangle^{\mathcal{B}} = \sqrt{n}|n-1\rangle^{\mathcal{B}}$, to the operators $f_{e/g_m}^{(\dagger)} \in \mathcal{F}$ annihilating (creating) a carrier in the state $|e/g;m\rangle^{\mathcal{F}}$. In this context e/g specifies the energetic state of the electron in the exited or ground level (conduction and valance band in a semiconductor context) and m is a place holder for all remaining quantum numbers specifying the carriers state. The EoM for the generalized electron density

$$\begin{aligned}\left.\frac{d}{dt}\right|_{H_D} \left\langle b^{\dagger a} b^a f_{e_i}^\dagger f_{e_i}\right\rangle &= -2g_i \mathrm{Re}\left\langle b^{\dagger a+1} b^a f_{g_i}^\dagger f_{e_i}\right\rangle \\ &\quad - 2a\sum g_m \mathrm{Re}\left\langle b^{\dagger a} b^{a-1} f_{e_i}^\dagger f_{g_m}^\dagger f_{e_i} f_{e_m}\right\rangle,\end{aligned} \tag{2.32}$$

or more schematically

$$\begin{aligned}\left.\frac{d}{dt}\right|_{H_D} \langle 2a,2\rangle &= -2g_i \mathrm{Re}\langle 2a+1,2\rangle \\ &\quad - 2a\sum g_m \mathrm{Re}\langle 2a-1,4\rangle,\end{aligned} \tag{2.33}$$

is a quantity of order $(2a,2)$. It couples to the photon-assisted polarization of order $(2a+1,2)$ and to EVs correlating polarizations in other shells m with the presence of a second carrier in state $|e;i\rangle$, this term has the order $(2a-1,4)$ (compare to Eq. (2.33)). The EoM for the photon-assisted polarization

$$\left.\frac{d}{dt}\right|_{H_D} \left\langle b^{\dagger a+1} b^a f_{g_i}^\dagger f_{e_i} \right\rangle = (a+1) g_i \left\langle b^{\dagger a} b^a f_{e_i}^\dagger f_{e_i} \right\rangle \tag{2.34}$$
$$+ g_i \left\langle b^{\dagger a+1} b^{a+1} (f_{e_i}^\dagger f_{e_i} - f_{g_i}^\dagger f_{g_i}) \right\rangle$$
$$+ (a+1) \sum g_m \left\langle b^{\dagger a} b^a f_{e_m}^\dagger f_{g_i}^\dagger f_{e_i} f_{g_m} \right\rangle$$
$$- a \sum g_m \left\langle b^{\dagger a+1} b^{a-1} f_{g_i}^\dagger f_{g_m}^\dagger f_{e_i} f_{e_m} \right\rangle,$$

$$\left.\frac{d}{dt}\right|_{H_D} \langle 2a+1, 2 \rangle = (a+1) g_i \langle 2a, 2 \rangle \tag{2.35}$$
$$+ g_i \langle 2a+2, 2 \rangle$$
$$+ (a+1) \sum g_m \langle 2a, 4 \rangle$$
$$- a \sum g_m \langle 2a, 4 \rangle,$$

couples to the spontaneous emission $(2a, 2)$, to the stimulated emission $(2a+2, 2)$, to the spontaneous emission modified by additional electrons present in semiconductor systems $(2a, 4)$ and to possible two-photon processes generated by transitions in other shells $(2a, 4)$ (compare Eq. (2.34) and Eq. (2.35)). The desired EVs couple to EVs with a growing number of bose and fermi operators. To close this hierarchy it has to be truncated by a combination of $\Delta^{\mathcal{B}}$ and $\Delta^{\mathcal{F}}$ as depicted in Fig. 2.5.

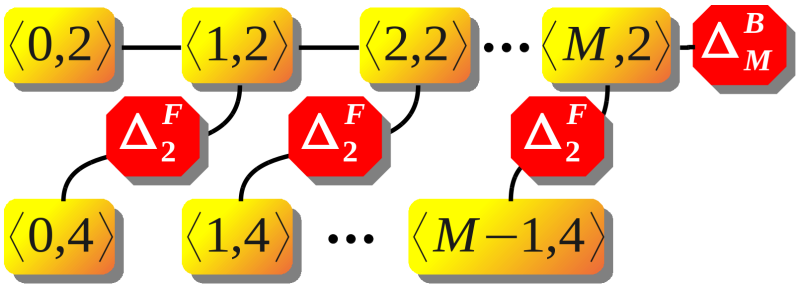

Figure 2.5: Illustration of the system of EoM (2.32-2.35) induced by the dipole Hamiltonian H_D. The hierarchy unfolds in two directions and therefore has to be truncated by a combination of $\Delta^{\mathcal{B}}$ and $\Delta^{\mathcal{F}}$. The sketch shows how the hierarchy is truncated in our framework in the fermionic direction at single-particle level by $\Delta_2^{\mathcal{F}}$ standing for $\Delta_{\langle 2 \rangle}^{\mathcal{F}}$ applicable to one-electron systems or for $\Delta_{\delta(2)}^{\mathcal{F}}$ applicable to semiconductor systems with more than one electron. The photonic direction of the hierarchy is truncated by $\Delta_M^{\mathcal{B}}$ standing for $\Delta_{\langle M \rangle}^{\mathcal{B}}$ with applications in cavity-quantum-electrodynamic systems or for $\Delta_{\delta(M)}^{\mathcal{B}}$ applicable, for example, in laser systems.

To illustrate the application of the combined truncation scheme, we will give examples that result in known models. To obtain these models, we show in the following how Eqs. (2.32,2.34) must be modified and truncated and in some cases augmented with additional EoM. Note that all systems in the following examples are considered to be in the incoherent regime where EVs like $\langle b^\dagger \rangle$, $\langle f_e^\dagger f_g \rangle$ vanish[Mølmer, 1997]. So far, we have only defined the interaction part of the Hamiltonian in an

abstract manner. To describe a real model, the free part of the Hamiltonian, the number of particles and the level structure of the particles must be declared and according to this the sum and indices in the dipole Hamiltonian. Furthermore, several external processes must be included into the equations, either by Lindblad terms or directly by adding phenomenological terms to the equations. However, the processes induced by an external bath do not change the necessity to truncate the hierarchy created by H_D. For the sake of simplicity, we will not consider the external processes explicitly.

Jaynes-Cummings model

A very basic example is the Jaynes-Cummings model (JCM) with N photons inside the cavity and one carrier that can occupy the ground or exited state ($a = 0 \dots N$ and $i = 1$ in Eqs. (2.32,2.34)). The application of $\Delta^{\mathcal{B}}_{\langle N\rangle}\Delta^{\mathcal{F}}_{\langle 2\rangle}$ is sufficient to describe this system. Since the JCM is a one-electron model all EV addressing two electrons are zero:

$$\Delta^{\mathcal{F}}_{\langle 2\rangle}\left\langle b^I f^\dagger f^\dagger f f\right\rangle = 0,$$

and because the number of photons is limited to N, the probability to find $N+1$ photons is zero, i.e.

$$\Delta^{\mathcal{B}}_{\langle N\rangle}\left\langle b^{\dagger N+1} b^{N+1} f^\dagger f\right\rangle = 0.$$

In Fig. 2.6 this EoM approach is compared to the cluster expansion, which is totally inappropriate for this finite system (see end of Sec. 2.2.2). Figure 2.6 shows the time evolution of the second-order photon-autocorrelation function Eq.(1.42) at zero delay time for the JCM with the electron initially in the exited state and the cavity prepared in a Fock state with 1 photon ($|\psi_0\rangle = |e\rangle^{\mathcal{F}}|1\rangle^{\mathcal{B}}$). The system oscillates between the initial state and a two-photon state with the electron in the ground state ($|\psi_1\rangle = |g\rangle^{\mathcal{F}}|2\rangle^{\mathcal{B}}$) consequently the photon-autocorrelation function oscillates between $g^{(2)}(0) = 0$ and $g^{(2)}(0) = 0.5$ with the Rabi-frequency ω_R. The result of the EoM truncated with $\Delta^{\mathcal{B}}_{\langle 4\rangle}$ is in perfect agreement with the exact analytical result. The results obtained with the cluster expansion (i. e. by applying $\Delta^{\mathcal{B}}_{\delta(N)}$) diverge dramatically from the exact solution and exhibit even unphysical behavior ($g^{(2)}(0) < 0$). Going to higher orders enlarges the time interval in which the cluster expansion matches the exact results. However, the algebraic effort is tremendous and still the cluster expansion of order twelve is not able to monitor a half Rabi circle for this system. Only the inclusion of an infinite number of CFs would be able to compensate the vanishing EV, which is facilitated by $\Delta^{\mathcal{B}}_{\langle 4\rangle}$ in a very natural fashion. Further details on this approach to the JCM and on the convergence properties of the cluster expansion can be found in Leymann et al. [2013b].

Four-level laser rate equations

Allowing the index i to be $\{1, 2\}$ and limiting the number of carriers per atom to one gives the basis of a four-level laser model ($a = 0, 1$ and $i = 1, 2$ in Eqs. (2.32,2.34)). The application of $\Delta^{\mathcal{B}+\mathcal{F}/2}_{\delta(2)}$ gives the basis for the laser rate equations with

$$\mathbf{F}^{-1}\Delta^{\mathcal{B}+\mathcal{F}/2}_{\delta(2)}\,\mathbf{F}\left\langle b^\dagger b f^\dagger f\right\rangle \approx \left\langle b^\dagger b\right\rangle\left\langle f^\dagger f\right\rangle,$$

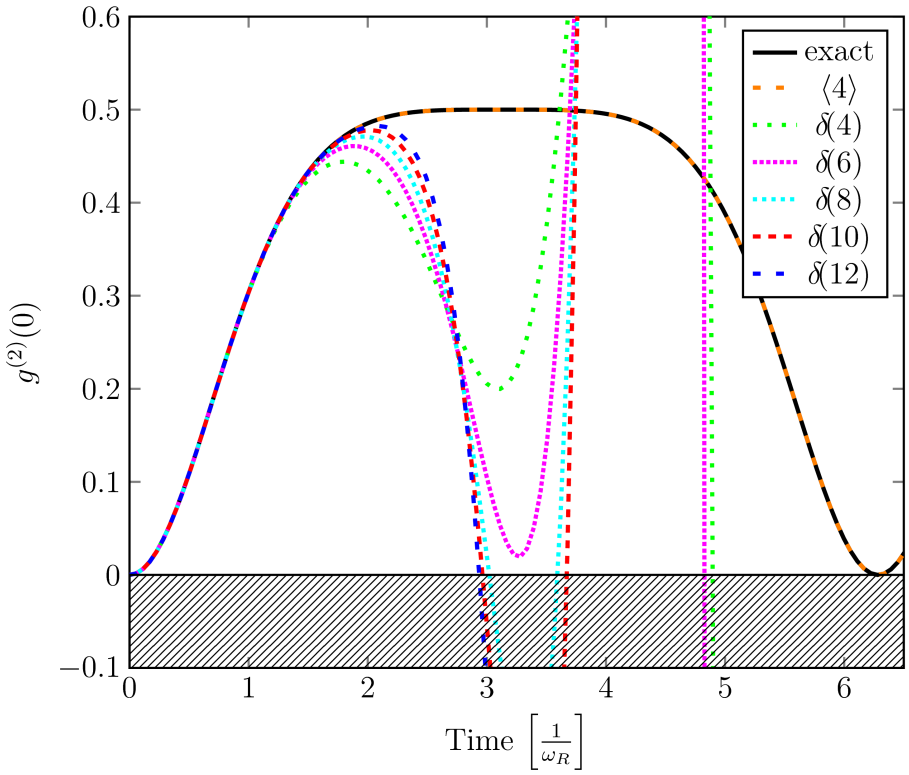

Figure 2.6: Dynamics of the photon-autocorrelation function $g^{(2)}(0)$ of the JCM for an initially exited electron and the cavity field prepared in a Fock state with $\langle b^\dagger b\rangle = 1$ and $\langle b^{\dagger n} b^n\rangle = 0$ for $n > 1$. The time is measured in units of the Rabi frequency ω_R. Depicted is the analytical exact solution compared to various numerical solutions of the EoM from Eqs. (2.32,2.34). The fermionic part is truncated by $\Delta^{\mathcal{F}}_{\langle 2\rangle}$ since the JCM is a one electron model, the photonic part is truncated by $\Delta^{\mathcal{B}}_{\langle 4\rangle}$ or $\Delta^{\mathcal{B}}_{\delta(N)}$with $N = \{4, 6, 8, 10, 12\}$. Note that the analytical exact solution and the numerical exact solution ($\Delta^{\mathcal{B}}_{\langle 4\rangle}$) lie on top of each other. The results obtained by the cluster expansion fail to describe the dynamics of this system and the orders eight to twelve even reach unphysical values below zero marked by the gray hatched area. The curves shown here were all obtained by the expectation value based cluster expansion. The corresponding curves obtained by the traditional cluster expansion would lie on top of them since both approaches differ only in the formulation but not in the results.

as the main approximation [Rice and Carmichael, 1994]. Since the gain medium is considered to consist of one-electron systems the two-electron quantities vanish $\Delta^{\mathcal{F}}_{\langle 2\rangle} \left\langle f^\dagger f^\dagger f f\right\rangle = 0$. This model provides no statistical information about the photons other than the mean photon number $\left\langle b^\dagger b\right\rangle$, but can easily be extended within our framework by including higher-order correlations.

Semiconductor model for a single quantum dot

Characteristic for a semiconductor QD is the presence of more than one carrier confined in the QD shell structure. Pauli blocking of recombination channels, Coulomb interaction and scattering with wetting layer carriers and phonons influence the dy-

namics of carriers in a semiconductor QD. We consider QDs with two shells ($i = s, p$ in Eqs. (2.32,2.34)) in the valence and the conduction band. Expectation values addressing two carriers are different from zero in this system and thus have to be considered. However, the Hilbert space corresponding to a single QD inside a cavity with only one resonant photonic mode is still small enough to allow for a numerically exact description ($a = 1 \dots N$). Single semiconductor QD systems have been studied for example by Ritter et al. [2010] by the direct solution of the vNL Eq. (1.8). The application of the truncation operators $\Delta^{\mathcal{F}}_{\langle 4\rangle}\Delta^{\mathcal{B}}_{\langle N\rangle}$ on the Eqs. (2.32, 2.34) gives a numerically exact semiconductor QD model in our formulation, when N is chosen sufficiently large. To obtain a complete model the EoM for the two-electron quantities $\left\langle b^I f^\dagger f^\dagger f f \right\rangle$ has to be derived using Eq. (1.9) and the corresponding Lindblad terms have to be included. The hierarchy is truncated at two-electron level, meaning that EV addressing three electrons vanish,

$$\Delta^{\mathcal{F}}_{\langle 4\rangle} \left\langle b^I f^\dagger f^\dagger f^\dagger f f f \right\rangle = 0.$$

This truncation is justified by the assumption that the QD initial state is uncharged and electrons and holes are pumped symmetrically; a discussion of the effects of a unsymmetrical pump can be found in Florian et al. [2013b]. Every photonic state that is produced by a single QD, be it a thermal or coherent state, can be approximated by a finite number of Fock states N so that EVs addressing $(N + 1)$ photons vanish,

$$\Delta^{\mathcal{B}}_{\langle N\rangle} \left\langle b^{\dagger N+1} b^{N+1} f^K \right\rangle = 0.$$

Semiconductor laser model for multiple quantum dots

In semiconductor QD microcavity lasers, typically, several QDs take part in the laser dynamics. To obtain a microscopic semiconductor laser model, all the processes mentioned in the single semiconductor QD model must be taken into account as well. For three or four QDs the size of the Hilbert space is still small enough so that the system can still be described by the vNL equation as in Florian et al. [2013a]. However, in the case of five or more QDs the fermionic part of the Hilbert space is too large for an exact treatment. When the laser operates above threshold the photon number grows too fast with the pump to set up a hierarchy that goes up to vanishing EVs. To truncate the EoM hierarchy for such a large system, CFs have to be neglected.

A model that is sufficient to describe an ensemble of semiconductor QDs coupled to a single cavity mode and to provide statistical information about the photons beyond the intensity is given when Eqs. (2.32,2.34) are carried up to order ($a = 0, 1, 2$) and the truncation operators $\Delta^{\mathcal{F}}_{\delta(2)}$ and $\Delta^{\mathcal{B}}_{\delta(4)}$ are applied. The hierarchy is closed in the fermionic subspace by factorizing all two-electron quantities:

$$\begin{aligned}&\mathbf{F}^{-1}\Delta^{\mathcal{F}}_{\delta(2)}\mathbf{F} \left\langle b^I f^\dagger f^\dagger f f \right\rangle \approx \\ &\sum c_{\{J,L,M\}} \left\langle b^J f^\dagger f \right\rangle \left\langle b^L f^\dagger f \right\rangle \left\langle b^M \right\rangle,\end{aligned}$$

where $I = J \cup L \cup M$ is the index set addressing the bose operators. In contrast to the single QD model, a large number (> 10) of QDs takes part in the laser dynamics.

Therefore, an exact treatment of the carriers is impossible and carrier-carrier correlations are not in focus of this model. The carriers can be treated on Hartree-Fock level since the Coulomb interaction is screened by the high carrier densities in the lasing regime [Schneider et al., 2001a] and correlations are strongly diminished by dephasing. In the bosonic subspace, the hierarchy is closed by factorizing all EVs containing more than four photon operators

$$\begin{aligned}
&\mathbf{F}^{-1}\Delta^{\mathcal{B}}_{\delta(4)}\mathbf{F}\left\langle b^\dagger b^\dagger b^\dagger b b f^K\right\rangle \approx \\
&+\sum c_{\{Q,R,S,T\}}\left\langle b^\dagger b f^Q\right\rangle\left\langle b^\dagger b f^R\right\rangle\left\langle b^\dagger f^S\right\rangle\left\langle f^T\right\rangle \\
&+\sum c_{\{Q',R',T'\}}\left\langle b^\dagger b^\dagger b b f^{Q'}\right\rangle\left\langle b^\dagger f^{R'}\right\rangle\left\langle f^{T'}\right\rangle \\
&+\sum c_{\{Q'',R'',T''\}}\left\langle b^\dagger b^\dagger b f^{Q''}\right\rangle\left\langle b^\dagger b f^{R''}\right\rangle\left\langle f^{T''}\right\rangle,
\end{aligned}$$

where $K = Q \cup R \cup S \cup T$ is the index set addressing the fermi operators. There are more possible factorizations, but these terms are zero in the incoherent regime or not driven by the Hamiltonian. Expectation values with up to four photon operators are considered in this model. Thereby we have access to the photon-autocorrelation function of the cavity photons at zero delay time $g^{(2)}(0)$. An equivalent model formulated in terms of CFs has been introduced by Gies et al. [2007].

We conclude this section with a comparison between the presented examples. Note the similarities between our first and third example, in both examples, a limited number of carriers interact with limited number of photons. The single semiconductor QD can be regarded as the extension of the JCM to the case of a many electron system. And finally, our fourth example can be considered as the extension of the four-level system laser to a semiconductor laser model that provides additional to the intensities, information about the photon statistics as well. All these models originate from the same hierarchy of EVs and differ, with respect to the truncation of the hierarchy, only in the order and combination of the truncation operators $\Delta^{\mathcal{F}}$ and $\Delta^{\mathcal{B}}$.

2.4.2 Laser transition in higher-order photon-autocorrelation functions

The presented approach to the microscopic semiconductor QD laser is extended further into the bosonic subspace. We take a closer look on the carrier-photon and photon-photon correlations driven by the laser cavity feedback. The carriers can still be treated on Hartree-Fock level due to the strong dephasing in this system. A systematic study of the influence of carrier correlations in a single QD can be found in Florian et al. [2013b] and will be subject to further investigations. Formally, the truncation operator $\Delta^{\mathcal{B}}_{\delta(4)}$ is changed in our example to $\Delta^{\mathcal{B}}_{\delta(N)}$with $N = \{6, 8, 10\}$. With this approach, we obtain converged values for lower-order quantities and information about higher-order photon-autocorrelation functions $g^{(n)}(0)$ Eq. (1.43) up to $n = N/2$. To demonstrate the capability of our theoretical framework, we show numerical results for a semiconductor QD microcavity laser with 20 identical QDs, a β-factor of 0.01 and all additional material parameters chosen as in Gies

et al. [2007]. We concentrate on the photon-autocorrelation functions $g^{(n)}(0)$. Experimentally, higher-order photon correlations of coupled quantum systems were investigated by several groups [Aßmann et al., 2009; Avenhaus et al., 2010; Stevens et al., 2010; Rundquist et al., 2014]. The behavior of $g^{(2)}(0)$ at the lasing threshold for a QD-based-microcavity laser is experimentally well studied and has been investigated with the cluster expansion [Gies et al., 2007; Wiersig et al., 2009; Leymann et al., 2013c]. The transition from non-lasing to lasing can be characterized by a change in the photon statistics from a thermal- to a Poisson-distribution. Therefore, the photon-autocorrelation functions $g^{(n)}(0)$ drops from $n!$ to one at the lasing threshold [Loudon, 2000; Garrison and Chiao, 2014].

Figure 2.7 shows the behavior of $g^{(2)}(0)$ over the pump rate. For the chosen β factor, the photon-autocorrelation function drops steeply from two to one at lasing threshold. Note that the deviations of the different orders are small and are becoming smaller with increasing order. The strongest deviations appear directly at the threshold because of the rapid change of photon correlations in this parameter region. Below threshold, photon correlations are small due to the thermal state of the photons and far above the threshold the dephasing induced by the pumping has strong influence on the system and damps out all higher-order carrier correlations.

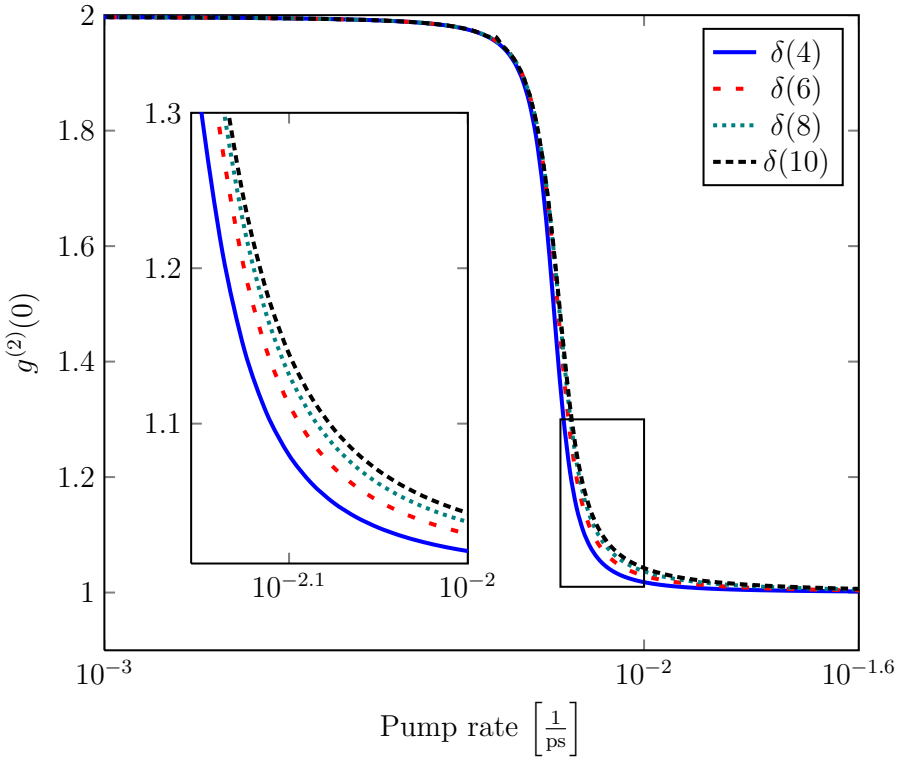

Figure 2.7: Numerical solution of the semiconductor laser model for $\beta = 0.01$ and 20 QDs. The convergence of the photon-autocorrelation function $g^{(2)}(0)$ for different truncation operators $\Delta^{\mathcal{B}}_{\delta(N)}$with $N = \{4, 6, 8, 10\}$ is shown. Further information about the model can be found in [Gies et al., 2007].

Laser light is coherent in all orders n, so the photon-autocorrelation functions of all orders is one [Glauber, 1963]. Therefore observing the mean photon number

and the two photon-autocorrelation function is not enough to monitor the laser transition. The state $|\psi_{\mathrm{nl}}\rangle = \frac{1}{\sqrt{2}}(|0\rangle + |2\rangle)$ for example, is not a lasing state at all, however, if one only looks at the photon number and the two-photon-autocorrelation function one could think $|\psi_{\mathrm{nl}}\rangle$ might be a laser state ($\langle b^\dagger b\rangle|_{\mathrm{nl}} = 1$, $g^{(2)}(0)|_{\mathrm{nl}} = 1$). With our approach, higher-order CFs are accessible so we can monitor the transition to laser light in higher orders of the photon-autocorrelation function. In Fig. 2.8(a) one can see how the autocorrelation functions $g^{(2\cdots5)}(0)$ drop from thermal values $n!$ to one. Note the logarithmic scale and that the deviation of $g^{(5)}(0)$ from one in relation to its thermal value $5! = 120$ is as large as the deviation for the lower-order photon-autocorrelations. To be able to better monitor the transition in the photon statistics we also depict scaled photon-CFs:

$$C^{(n)}(0) = \frac{\delta(b^{\dagger n}b^n)}{\langle b^\dagger b\rangle^n}\left(\frac{\delta(b^{\dagger n}b^n)|_{\mathrm{coh}}}{\langle b^\dagger b\rangle^n}\right)^{-1}, \tag{2.36}$$

were $\delta(b^{\dagger n}b^n)|_{\mathrm{coh}}$ is the value of the CF for a coherent field, which can be obtained by successively solving

$$g^{(n)}(0)|_{\mathrm{coh}} = 1 = \frac{\mathbf{F}\langle b^{\dagger n}b^n\rangle|_{\mathrm{coh}}}{\langle b^\dagger b\rangle^n}. \tag{2.37}$$

For $n = \{2, 3\}$ Eq. (2.37) reads:

$$\begin{aligned} g^{(2)}(0)|_{\mathrm{coh}} &= 1 = 2 + \frac{\delta(b^{\dagger 2}b^2)|_{\mathrm{coh}}}{\langle b^\dagger b\rangle^2} \\ g^{(3)}(0)|_{\mathrm{coh}} &= 1 = 6 + 9\frac{\delta(b^{\dagger 2}b^2)|_{\mathrm{coh}}}{\langle b^\dagger b\rangle^2} + \frac{\delta(b^{\dagger 3}b^3)|_{\mathrm{coh}}}{\langle b^\dagger b\rangle^3}. \end{aligned}$$

In Fig. 2.8(b) the $C^{(n)}(0)$ are depicted and one can see that all photon-CF are zero for low pump rates, which is consistent with Wick's theorem. For pump rates above threshold, all $C^{(n)}(0)$ approach one as assumed for a system emitting laser light. However, the four depicted $C^{(n)}(0)$ have not a common threshold pump rate. They all exhibit their maximum slope at different pump rates. So the term "threshold" becomes questionable not only because of the missing threshold in systems with a β-factor close to one in the input-output curve [Rice and Carmichael, 1994], but also for intermediate systems like ours with $\beta = 0.01$ where one can still see a threshold in the second-order photon-autocorrelation function. Taking a closer look at the photon-autocorrelation functions reveals that the threshold is different for the different CFs. In this context, it is more precise to speak of a threshold parameter region than of one threshold value. Comparing Fig. 2.8(a) and (b) one sees that both quantities $g^{(n)}(0)$ and $C^{(n)}(0)$ can be used to monitor the transition from thermal to laser light. For a comparison of the different orders of coherence, the scaled CFs $C^{(n)}(0)$ are more appropriate since all $C^{(n)}(0)$ have values between zero and one. To conclude this section, we recapitulate that we have formulated the EoM in terms of EVs to facilitate the computations. For the analysis, however, the formulation in terms of CFs is very helpful.

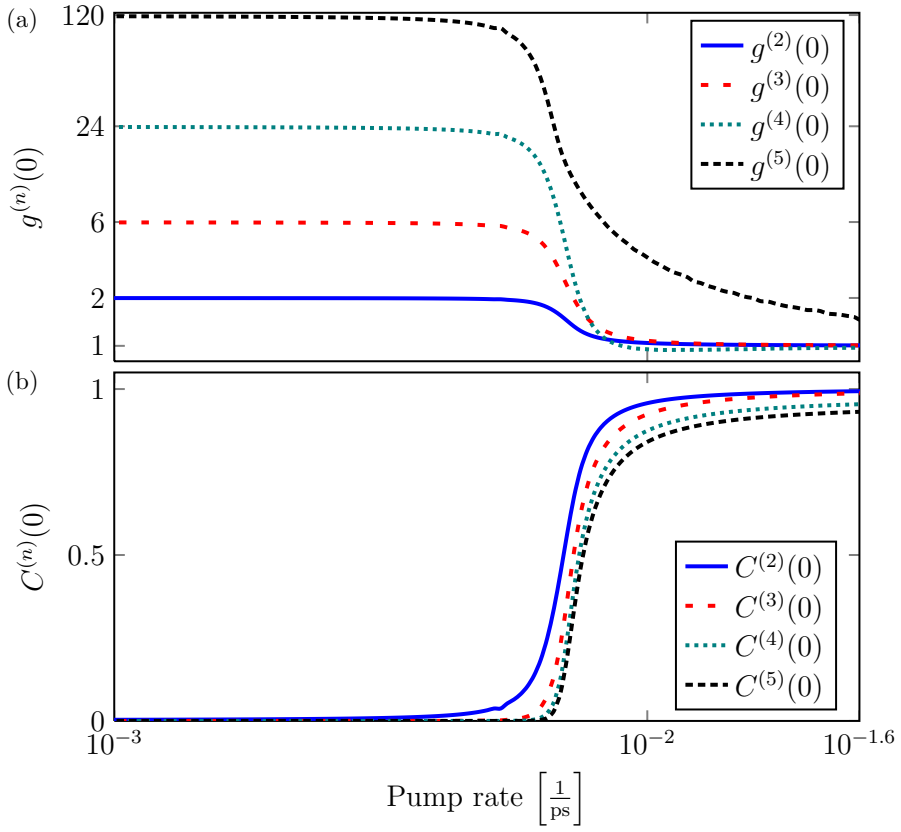

Figure 2.8: Numerical solution of the semiconductor laser model for $\beta = 0.01$ and 20 QDs for order $N = 10$. The higher-order photon-autocorrelation functions $g^{(n)}(0)$ in dependence of the pump rate are depicted in (a). The theoretical expected transition from thermal to coherent light could be approved up to $g^{(5)}(0)$ (note the logarithmic scale). In (b) the scaled photon-CFs $C^{(n)}(0)$ are depicted. For the thermal field at low pump rates, all CFs are zero. An ideal Poissonian distributed light field would produce $C^{(n)}(0) = 1$ for all n. The various $C^{(n)}(0)$ begin to approach one at different pump rates and not at one threshold pump rate.

2.5 Classification of former approaches by the proposed truncation scheme

At the end of this chapter, we will briefly touch on former approaches to truncate hierarchies of EoM. The formulation in the literature may differ from ours but the truncation techniques can all be regarded as an application of one or more truncation operators as defined in Eqs.(2.6,2.7). Our formulation offers a new perspective to the various approaches listed in Table 2.1.

Example (i) and (ii) in the table are concerned with relatively small systems that can still be treated numerical exact. In the first example (i), the vNL. Eq. (1.8) for the density operator ρ for a single QD laser is solved in the basis of the finite configuration states $|\phi_i\rangle$ numerically [Ritter et al., 2010], which could also be mapped onto an EV hierarchy truncated at the order corresponding to the size of the matrix $\rho_{ij} = \langle\phi_i|\rho|\phi_j\rangle$. The second example (ii) is formulated in EV and describes a

QD cavity system coupled to phonons, and the hierarchy is set up by the induction method [Carmele et al., 2010] referred to in Sec. 2.3. The single QD described by a finite Hilbert space investigated in the third example (iii) is coupled to a continuum of modes and has therefore be treated approximately by neglecting photon correlations. The EoM in this example are formulated in CF but the finite fermionic part of the system is treated exactly by factorizing CFs that address three or more carriers according to Eq. (2.12). Since this method is designed to set up a hierarchy of EoM for a finite fermionic system, it is called finite-size hierarchy (FSH) [Florian et al., 2013b]. Example (iv) treats its bosonic part exactly by using the photon probability up to N photons, which could be mapped on EVs $\left\langle b^{\dagger a} b^a \right\rangle$ with a up to N. The correlations between the two carriers are neglected and EVs with more than two fermi operators are factorized. This method combines the photon probability with the factorization of the carrier EVs according to the cluster expansion and is therefore called the photon probability cluster expansion (PPCE) [Richter et al., 2009]. The FSH and the PPCE can be regarded as opposite approaches as the FSH treats the fermi part exactly and factorizes bose EVs whereas the PPCE factorizes the fermi part and treats the bose part exactly. Example (v) is exactly the model described in Sec. 2.4.1 formulated in CFs [Gies et al., 2007]. Quantum wells are described by a continuous Hilbert space and are predesignated for the cluster expansion, i.e. the neglection of CFs as in example (vi), studying the effects of Coulomb and phonon interaction on exciton formation in semiconductor quantum wells [Hoyer et al., 2003]. Example (vii) is part of this thesis and is described in detail in Ch. 5. The configuration cluster expansion (CCE) describes the carriers confined in a single QD exactly with the configuration operators Q and allows to evaluate different approximation depths of inter-emitter correlations. This scheme allows for the systematical study of superradiance in QD lasers. Example (viii) is also part of this thesis in Ch. 4 and is concerned with the first order coherence properties of a bimodal microcavity laser. Technically example (viii) is like example (v) with the extension of a second mode and the calculation of coherence properties (see Sec. 2.3.4). The last example (xi) investigates the dynamics of Bose-Einstein condensates (BECs) in optical lattices and has therefore a purely bosonic Hilbert space. The hierarchy of EoM in this example is formulated in EVs. The influence of two-particle correlations is investigated and the hierarchy is truncated by the factorization of three-particle EV according to Eq. (2.11) and is called Bogoliubov backreaction approximation [Witthaut et al., 2011].

	Physical System	Dim $H^{\mathcal{B}}$	Dim $H^{\mathcal{F}}$	truncation	Formulation	Ref.
(i)	Single semiconductor QD laser	~ 40	6	$\Delta^{\mathcal{B}}_{\langle 80\rangle}$ $\Delta^{\mathcal{F}}_{\langle 4\rangle}$	vNL	[Ritter et al., 2010]
(ii)	2-level-cavity system coupled to phonons	$\sim 20, \sim 20$	2	$\Delta^{\mathcal{B}_c}_{\langle 40\rangle}$ $\Delta^{\mathcal{B}_{ph}}_{\langle 40\rangle}$ $\Delta^{\mathcal{F}}_{\langle 2\rangle}$	EV	[Carmele et al., 2010]
(iii)	Semiconductor QD PL into free space	$\sim \infty$	6	$\Delta^{\mathcal{B}_i}_{\delta(1)}$ $\Delta^{\mathcal{F}}_{\langle 4\rangle}$	FSH (CF)	[Florian et al., 2013b]
(iv)	Rabi oscillations in a QD-cavity system	$2 \sim 20$	4	$\Delta^{\mathcal{B}}_{\langle 30\rangle}$ $\Delta^{\mathcal{F}}_{\delta(2)}$	PPCE (EV)	[Richter et al., 2009]
(v)	Microcavity laser with semiconductor QDs	~ 1000	$\sim 6^{50}$	$\Delta^{\mathcal{B}}_{\delta(4)}$ $\Delta^{\mathcal{F}}_{\delta(2)}$	CF	[Gies et al., 2007]
(vi)	Quantum wells	$\sim \infty$	$\sim \infty$	$\Delta^{\mathcal{B}+\mathcal{F}/2}_{\delta(2)}$	CF	[Hoyer et al., 2003]
(vii)	Superradiance in a QD nanolaser	~ 1000	$\sim 6^{50}$	$\Delta^{\mathcal{B}+\mathcal{Q}}_{\delta(4)}$ $\Delta^{\mathcal{Q}}_{\delta(1/2)}$	CCE	[Leymann et al., 2015]
(viii)	Normal-Mode Coupling of semiconductor QDs	$\sim 100\,000$	$\sim 6^{50}$	$\Delta^{\mathcal{B}}_{\delta(2)}$ $\Delta^{\mathcal{F}}_{\delta(2)}$	EV	[Khanbekyan et al., 2015]
(ix)	BEC in an optical lattice	$> 10\,000$	0	$\Delta^{\mathcal{B}}_{\delta(4)}$	EV	[Witthaut et al., 2011]

Table 2.1: Overview of recent publications (which is by no means complete) applying methods that can be interpreted within our framework. Dim $H^{\mathcal{B}/\mathcal{F}}$ estimates the number of configurations the bosonic/fermionic part of the system can have. Dim $H^{\mathcal{B}/\mathcal{F}}$ is determined by the number of particles in the system and the number of states the single particles can occupy. The table illustrates that for coupled systems (in most examples here light-matter-coupling) the hierarchy must be truncated in various directions, and the choice of the truncation order and principle depends strongly on the investigated system.

2.6 Chapter conclusion

We have shown how the description of many-particle quantum systems can be facilitated by making use of the connection between EVs and CFs. We have observed that the formulation of the EoM in EVs or CFs is independent from the approximations that are made to truncate the infinite hierarchy. This independence allows for a description entirely formulated in terms of EVs. The use of EVs has several advantages: simple algebra can be used to derive the EoM for all orders, constraints like a limited particle number can be incorporated directly, and the effect of approximations typical for the cluster expansion is directly marked by the nonlinear terms in the otherwise linear equations. Additionally, we find it remarkable that our formulation of the cluster expansion shows that it is possible to approximate an infinite linear system of EoM by a finite, almost linear system of EoM. It is also worth mentioning that the traditional cluster expansion formulated in CFs is equivalent to this almost linear hierarchy of EVs. The linearity of the equations up to the order where actual approximations result in factorizations may be interesting for numerical implementation of the EoM as well as the possibility to give an inductive scheme to set up the EoM. Another aspect we have concentrated on is the truncation of hierarchies of EoM for systems containing different interacting particles and the implementation of constraints like a limited particle number. The flexibility that our approach offers, concerning the approximation principles, is expressed in the various combinations of the truncation operators $\Delta^{\mathcal{B}/\mathcal{F}}_{\delta\langle N\rangle/\langle M\rangle}$. Our formulation emphasizes the connections, similarities and differences between various techniques found in the literature. The capability of our approach is demonstrated in a specific example where we have extended the semiconductor laser model used by Gies et al. [2007] to higher orders and validated the convergence of the cluster expansion approach for this model. In microcavity systems, the common definition of the laser threshold is not questionable only due to smooth transition in the input output characteristic. Our results show different 'threshold' pump rates for increasing orders of photon-autocorrelation functions, thus speak of a threshold interval is more appropriate.

The introduced formulation can be useful in all situations where a systematic inclusion of higher-order correlations is desirable. Essentially, our method is applicable to all systems where the traditional cluster expansion is used, and with the algebraic simplifications higher-order correlations are accessible with our formulation as demonstrated for the semiconductor QD laser in Sec. 2.4.

Chapter 3

Computer-aided cluster expansion: An efficient algebraic approach for open quantum many-particle systems

Parts of this chapter are published in [Foerster et al., 2017]. The computer-aided cluster expansion and the code were developed from A. Foerster in collaboration with H.A.M. Leymann. The computational derivation of EoM and the numerical integration of the EoM was done by A. Foerster, all authors of [Foerster et al., 2017] discussed the results and implications of the results.

We introduce an equation of motion approach that allows for an approximate evaluation of the time evolution of a quantum system, where the algebraic work to derive the equations of motion is done by the computer. The introduced procedures offer a variety of different types of approximations applicable for finite systems with strong coupling as well as for arbitrary large systems where augmented mean-field theories like the cluster expansion can be applied.

3.1 Introduction

Driven open quantum systems represent a broad class of physical systems where an exact solution is not always feasible. However, in many cases numerically exact solutions for the time evolution of the density matrix are not required, and alternative approximation methods can be applied. The focus of this work is on driven open quantum systems, where we are interested in either the dynamics of the system, or in its non-equilibrium steady state. Such systems usually are hard to solve numerically exact (solution of the full von-Neumann–Lindblad equation) due to the large number of interacting particles and the size of the corresponding Hilbert space. The cluster expansion (CE) and related theories are approximation methods that have proven to be useful in various applications in many-body quantum mechanics, e.g. to describe quantum wells [Hoyer et al., 2003], BEC in an optical lattice [Witthaut et al., 2011], Rabi oscillations in a quantum dot (QD)-cavity system [Richter et al., 2009], and sub- and superradiance in semiconductor QD-lasers [Leymann et al., 2015; Jahnke et al., 2016]. The specification of the method is its comparatively small numerical effort, while the derivation of the equations of motion (EoM) is a tedious algebraic

task, especially when higher orders of approximations are required. To overcome this obstacle we introduce a symbolic manipulation program that carries out the algebra, so that the user can focus on the physical modeling and conceptual questions. The aim of this chapter is to share our experience in deriving EoM using the presented program and to allow the reader to apply the program to related problems. The program is written in `FORM` [Vermaseren, 2000] and we recommend the extensive and profound introduction [Heck, 2000].

The chapter is structured as follows: In Section 3.2 we recapitulate the basic mathematical operations and ideas behind the CE. To this end we define the operators that are generic to the CE: time derivative of an expectation values (EV) with enforced standard order of the quantum mechanical operators, factorization of EVs into correlation functions (CF), re-factorization of CF back to EV, and the actual approximation that neglects certain CFs or EVs. In Section 3.3 we outline the structure of our program. In Section 3.4 the generic CE operators that are introduced in Section 3.2 are implemented into `FORM` modules. Together with the general procedures to derive EoM, we present an example program that is used to study the threshold behavior of a high $\beta-$factor QD microcavity laser. To demonstrate the ability of our approach we present in Section 3.5 calculations up to the 10th order of the CE (EoM that if derived using pen and paper are usually truncated at the 4th order, for this kind of system [Gies et al., 2007]). A complete working program that contains all procedures and the QD laser-model is available for download[Foerster et al., 2016].

3.2 Deriving equation of motion

In this section we recapitulate the basic ideas of the CE and introduce operators that represent the different calculation steps to derive the equation of motion. The computer procedures that we present in the following sections are exact implementations of these CE operators. For a more detailed introduction to this operator based formulation of the CE we refer to Ch. 2 and [Leymann et al., 2014, 2013b].

In most cases, when encountering many-particle systems, one is interested only in specific physical observables (EV/ CF) and not in the complete density matrix. The first step of the CE is to calculate the time derivative using the generalized Ehrenfest equation (1.9) for the EV of operator A with the system Hamiltonian H which is summarized by the superoperator $\mathcal{L}$. The collapse operators representing the influence of the external bath in Lindblad form (cavity losses, spontaneous emission into non-lasing modes, scattering, and dephasing) are introduced in Ch. 1.6. For further calculations it is advisable to establish normal order of the operators, after the application of the generalized Ehrenfest equation, which is symbolized by $:A:$. As a combination of both operations we introduce the operator $:\frac{d}{dt}:$ that derives the EoM in normal order:

$$\left\langle :\frac{d}{dt}A: \right\rangle = \langle :\mathcal{L}(A):\rangle \,. \tag{3.1}$$

To obtain the dynamics of a many-particle problem one encounters a hierarchy of EoM that couples equations of $\mathcal{O}(N)$ to equations of $\mathcal{O}(N+1)$. By order $\mathcal{O}(N)$ we

mean the number of particles that are addressed by an EV or CF. In all practical cases the hierarchy has to be truncated, which can be accomplished in two ways by the truncation operator $\Delta_{\delta/\langle\rangle}$, either by neglecting CFs of order larger than N

$$\Delta_{\delta(N)}\delta(N+1) = \delta(N), \tag{3.2}$$

or by neglecting EVs of an order larger than N

$$\Delta_{\langle N\rangle}\langle N+1\rangle = \langle N\rangle . \tag{3.3}$$

Which one of these two truncation schemes is more appropriate depends on the physical system. We introduce two particular examples where the truncation leads to the exact solutions: For the ideal gas consisting of non-interacting particles one can set all N-particle CFs larger than $N = 1$ to zero, i.e. apply $\Delta_{\delta(1)}$. Whereas an interacting two-particle-system is highly correlated, but $\Delta_{\langle 2\rangle}$ truncates the hierarchy of EoM since all three particle EVs vanish exactly in this system.

To neglect CFs one needs to factorize EVs into CFs, i.e. one needs to express an EV by CFs and vice versa. In the following we recapitulate the factorization according to [Leymann et al., 2013b] which is strongly orientated on [Fricke, 1996b]. We define a set of indices $I = \{1, 2, \cdots, k\}$ and a product of Bosonic operators $b^I = b_1 b_2 \cdots b_k$. P is a partition of the set I meaning a set family of disjoint nonempty subsets J of I with $\cup_{J\in P} J = I$, and P_I is defined as the set of all partitions of I. The EV $\langle b^I\rangle$ is factorized into CFs $\delta(b^J)$ by applying the operator $\mathbf{F}$

$$\mathbf{F}\langle b^I\rangle = \sum_{P\in P_I}\prod_{J\in P}\delta(b^J). \tag{3.4}$$

One can define the inverse operation to re-factorize CFs into EVs as well by

$$\mathbf{F}^{-1}\delta(b^I) = \sum_{P\in P_I} c_P \prod_{J\in P}\langle b^J\rangle , \tag{3.5}$$

with $c_P = (-1)^{\#(P)-1}(\#(P)-1)!$. To close the infinite hierarchy of EoM of EVs induced by Eq. (1.9) for a system with a very large number of photons (type I) interacting with a small finite number of atoms (type II) we would have to apply $\mathbf{F}^{-1}\Delta^{I+II}_{\delta(N)}\mathbf{F}\Delta^{II}_{\langle M\rangle}$. Where M is chosen according to the number of atoms and N according to the interaction strengths. The algebraically most costly part is the factorization $\mathbf{F}$ and the inverse operation $\mathbf{F}^{-1}$. These operations are the reason why higher orders in general cannot be derived using pen and paper. To give an impression of the complexity of the factorization problem we display the factorization of the non-normalized photon-autocorrelation function $\langle b^\dagger b^\dagger bb\rangle$ with the bosonic creation and annihilation operator $b^\dagger$ and b

$$\begin{aligned}\mathbf{F}\langle b^\dagger b^\dagger bb\rangle =& \delta(b^\dagger b^\dagger bb) + 2\delta(b^\dagger b^\dagger b)\delta(b) + 2\delta(b^\dagger bb)\delta(b^\dagger) + \delta(b^\dagger b^\dagger)\delta(bb) \\ &+\delta(b^\dagger b^\dagger)\delta(b)^2 + 2\delta(b^\dagger b)^2 + \delta(b^\dagger)^2\delta(bb) + 4\delta(b^\dagger)\delta(b^\dagger b)\delta(b) + \delta(b^\dagger)^2\delta(b)^2.\end{aligned} \tag{3.6}$$

This example elucidates the high combinatorial complexity originating from the fact that every partition of the operators has to be regarded. Additional work steps are required for the factorization of EV of fermionic operators, when the shift in sign must be taken into count for every commutation of the fermionic operators.

3.3 FORM and general concepts

We use the symbolic manipulation system FORM version 4.1 (Jan 13 2014 64-bits) [Vermaseren, 2000]. We assume that the reader is familiar with the basic syntax and concepts of FORM. An introduction to FORM can be found at https://www.nikhef.nl/%7eform/. The advantage of FORM is that the user has full control over the working procedures, in contrast to commonly used computer algebra systems. The calculations performed in our program can actually be regarded as a combination of search and replace commands. Our implementation of the CE consists of procedures that are the implementation the CE operators introduced in the previous section, i.e. the Ehrenfest EoM of EVs with established standard order of the operators ($\langle : \frac{d}{dt} A : \rangle$), and the application of the factorization and truncation operators ($\mathbf{F}$, $\mathbf{F}^{-1}$, $\Delta_{\langle N \rangle, \delta(N)}$), see Eqs. (3.1)-(3.5). The basic working principle of the program is illustrated in the flowchart depicted in Fig. 3.1. At first we have to set up the problem by defining a Hamilton operator H and the collapse operators L_i in the dissipator in Lindblad form. The set of EoM is than derived by using the generalized Ehrenfest equation (1.9) and establishing standard order of the operators. In the next step the factorization and truncation operators are applied. Physical constraints can be added optionally in an additional step. In this way one obtains a closed set of EoM that can be integrated numerically.

To keep the discussion close to applications, the procedures in the next sections are explained along a semiconductor QD laser-model. Here we use a formulation based on EVs of operators in second quantization with the annihilation and creation operators $b/b^\dagger$ for the photons in the laser mode and configuration operators $Q_{ij}^M = |i\rangle^M \langle j|^M$ mapping the many-particle configuration state $|j\rangle$ of QD M to the state $|i\rangle$ with the commutation relation

$$[Q_{ij}^M, Q_{kl}^P] = (Q_{il}^M \delta_{j,k} - Q_{kj}^M \delta_{l,i}) \delta_{M,P}, \tag{3.7}$$

according to the model introduced in [Leymann et al., 2015]. Our program is not restricted to this formulation and alternative formulations can be used with small modifications, while leaving the core modules untouched.

3.4 The implementation of the CE operators in FORM procedures

In this section we describe the implementation of the CE operators. The main executable program is called EoM_main.frm and all definitions are made there. The following function-types and sets will be used in the program:

```
1 function [Q],[N],[b+],[v],[v+],[b],[L+],[L],D,EV,DD,L,R;
2 Cfunction ev,first,eps,hq,om,kappa,g,gst,gammam,gammarc,gammarv,
    gammasps,gammaspp,gammad,pcv,evv,dd,dummy,d(symmetric),conj;
3 symbol N,M,u,a,number;
4 index i,j,k,l,m,n,o,p,q,r,s,t;
5 set bose: [b+],[N],[b];
6 set operator:[b+],[N],[b],[Q],L,R;
7 set prefactor:g,gst,eps,pcv,kappa,gammam,gammarc,gammarv,gammasps,
    gammaspp,gammad;
```

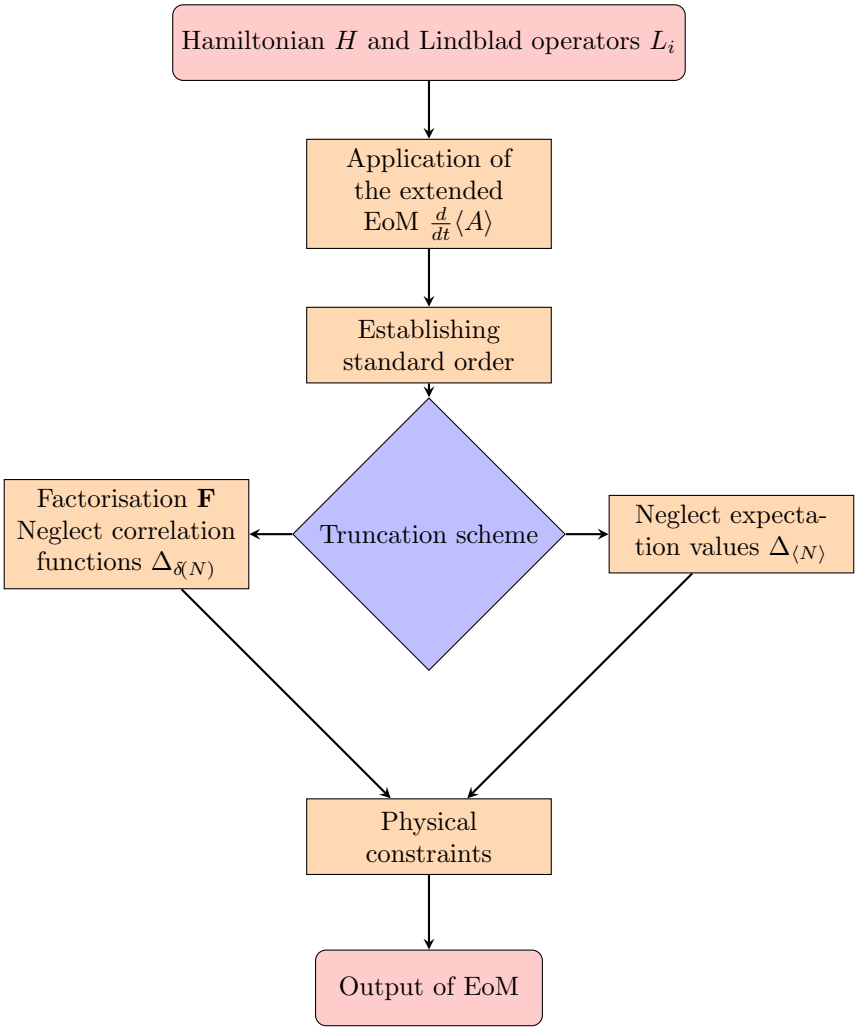

Figure 3.1: Schematic flowchart of the computer-aided derivation of EoM. At first we have to set up the problem by defining a Hamilton operator H and the collapse operators L_i in the dissipator in Lindblad form. The set of EoM is then derived by using the generalized Ehrenfest equation (1.9) and establishing standard order of the operators. In the next step the factorization and truncation operators are applied. Physical constraints can be added optionally in an additional step. In this way one obtains a closed set of EoM that can be integrated numerically.

`FORM` distinguishes between commutative(`Cfunction`) and non-commutative functions(`function`). In our notation, quantum mechanical operators are non-commutative functions that are always written in [..] brackets where [..+] symbolizes the adjoined operator. Further non-commutative auxiliary functions are written in capital letters. Commutative functions are the EV (`ev`) and the parameters like coupling strengths and decay rates. The type `symbol` is used as a generalized variable like the number of QDs `number` . For indices the letters $i, ..., t$ are used. `FORM` allows to define sets that facilitates access to certain functions, details will be given later.

The desired EVs are defined as `local` in the main file, i.e. the EV of the configuration operator $\langle Q_{ij}^M \rangle$:

```
local [dev([Q](i,l,M))]=ev([Q](i,l,M));
```

All operations in the following will be applied on these `local` expressions. We explain in Sec. 3.4.7 how one can define a closed set of EoM.

3.4.1 Defining the system

In the von-Neumann–Lindblad formalism the system is determined by its Hamiltonian and its coupling to the reservoir by the collapse operators. The declarations of the Hamiltonian is in the main file `EoM_main.frm`, the collapse operators are defined in `QDlindbladterms.prc`. First we define the Hamiltonian

$$H = H_0 + H_{ph} + H_D, \tag{3.8}$$

for the physical system which, in our case, consists of 3 parts. The electronic many-particle configuration that are used to model the QDs are illustrated in Fig. 3.2. In the diagonal part of the Hamiltonian the energy ε_N^M can be defined for every

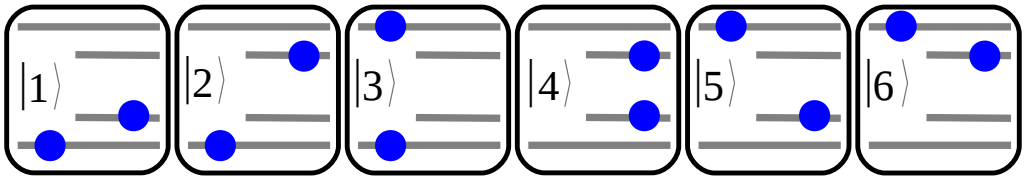

Figure 3.2: Illustration of the electronic configuration that are used in the 4-level QD model. The configurations are numbered as in the Hamiltonian (3.9),(3.11). Configuration $|1\rangle$ is the ground state, configuration $|2\rangle$ is the s-exciton, configuration $|3\rangle$ is the dark state in the p-shell, configuration $|4\rangle$ is the dark state in the s-shell, configuration $|5\rangle$ is the p-exciton and configuration $|6\rangle$ is the biexciton.

configuration N in every QD M separately

$$H_0 = \sum_M^{NQD} \sum_N^{CoN} \varepsilon_N^M Q_{N,N}^M, \tag{3.9}$$

```
[H0]=sum_(M,1,'NQD',sum_(N,1,'CoN',eps(M,N)*[Q](M,N,N)));
```

where the number of configurations (here 6) is called `CoN` and the number of QDs is called `NQD`. The variables `CoN` and `NQD` are defined as preprocessor variables in the main file `EoM_main.frm` to define the size of the system. The photonic part of the Hamiltonian is

$$H_{ph} = \hbar\omega b^\dagger b, \tag{3.10}$$

```
[Hph]=hq*om*[b+]*[b];
```

with the mode frequency ω and the reduced Planck constant $\hbar$. The light-matter interaction takes place in QD M between configuration $|2\rangle$ and $\langle 1|$ $(= Q_{1,2}^M)$ and between $|6\rangle$ and $\langle 5|$ $(= Q_{5,6}^M)$ (see Fig. 3.2) with the QD specific light-matter-coupling

constant $g(g^*)$ which describes the transition of s-shell electron between the conduction and the valence band under the emission/absorption of a cavity-photon

$$H_D = i \sum_{M}^{NQD} g_M b^\dagger (Q^M_{1,2} + Q^M_{5,6}) + \text{h.c.}, \tag{3.11}$$

```
1 [HD]=sum_(M,1,'NQD',i_*(-gst(M,1)*[b]*[Q](M,2,1)+g(M,1)*[b+]*[Q](M
    ,1,2)))+sum_(M,1,'NQD',i_*(-gst(M,1)*[b]*[Q](M,6,5)+g(M,1)*[b+]*[Q
    ](M,5,6)));
```

The whole Hamiltonian is then declared as the sum of the three different parts

```
1 local [H]=[H0]+[Hph]+[HD];
```

The collapse operators for this model are diagonal and have to be defined for each QD `'I'` individually. Note that we define the rate only in the $L_I^\dagger$ part instead of defining the square root in both parts L_I and $L_I^\dagger$. As an example

$$\begin{aligned} L_I^\dagger &= P^I Q^I_{1,5}, \\ L_I &= Q^I_{5,1}, \end{aligned} \tag{3.12}$$

```
1 #do I=1,('NQD')
2 local [L+'I']=pcv('I')*[Q]('I',1,5);
3 local [L'I']=[Q]('I',5,1);
4 #enddo
```

describes the pumping of an electron from the QD ground state $|1\rangle$ to the p-exciton $|5\rangle$ (see Fig. 3.2) with the pump rate `pcv`. The other collapse operators for the QDs can be implemented in an analogous fashion: carrier relaxation from the p-shell to the s-shell in the conduction band $(Q^I_{2,3}, Q^I_{4,5})$, carrier relaxation from the s-shell to the p-shell in the valence band $(Q^I_{2,4}, Q^I_{3,5})$ with the rates $\gamma^I_{\text{r},\{c,v\}}$ respectively, spontaneous losses of electron hole pairs in the p-shell $(Q^I_{1,5}, Q^I_{2,6})$ and the s-shell $(Q^I_{1,2}, Q^I_{5,6})$ with the rates $\gamma^{I,\{s,p\}}_{\text{sp}}$, direct dephasing in the s-shell $(Q^I_{2,2}, Q^I_{4,4}, Q^I_{6,6})$ and in the p-shell $(Q^I_{3,3}, Q^I_{5,5}, Q^I_{6,6})$ with the rates $\gamma^{I,\{s,p\}}_d$ and the cavity photon losses b with the loss rate κ, see [Leymann et al., 2015] for details.

3.4.2 Time derivative

This procedure applies the generalized Ehrenfest equation (1.9) to the previously defined EVs to derive their time derivatives. The corresponding `FORM` procedure is called `derivative.prc`.

After the Hamiltonian and the collapse operators are defined, the Ehrenfest equations can be applied to the operator EV $\langle A \rangle$:

```
1 id ev(?a)=L*D*EV(?a)*R;
2
3 id D*EV(?a)=i_*([H]*EV(?a)-EV(?a)*[H])+sum_(u,1,'NLT'*'NQD'+'NPM',2*[L
    +](u)*EV(?a)*[L](u)-[L+](u)*[L](u)*EV(?a)-EV(?a)*[L+](u)*[L](u));
4
5 #do v=1,'NLT'*'NQD'+'NPM'
```

```
6         id [L+]('v')=[L+{'v'}];
7         id [L]('v')=[L{'v'}];
8 #enddo
9 #call outfunction(EV,EV)
```

The `id` command is the central search and replace command in FORM. Its structure is `id search=replace`, where `search` stands for a mathematical expression that is to be replaced by the expression `replace`. To define a mathematical expression that is to be replaced FORM uses different types of wild-cards. The first type of wild-cards is encountered in the term `ev(?a)` where `?a` is the argument-field wild-card for any argument (of arbitrary number and complexity) entering the function `ev`. The `D` symbolizes the derivative operator $\frac{d}{dt}$ that is going to be applied. The auxiliary variables `L/R` mimic the brackets $\langle$ and $\rangle$ in the EVs and are an efficient way to implement a linear map in FORM. The function `EV` is used to conserve the non commutative property of the operators. The `do` loop identifies all collapse operators (`'NLT'*'NQD'+'NPM'` =(Number of Lindblad Terms * Number of QD) + Number of Photon Modes) declared in `QDlindbladt.prc` with the abstract collapse operators applied in line 3 in procedure `derivative.prc`. The last line `outfunction(EV,EV)` ensures that the auxiliary functions are removed and leaves the time derivative of $\langle A \rangle$ enclosed in the `L/R` brackets that stand for the linear map $\langle \cdot \rangle$, which is necessary for further processing.

Simplifications for subsystems with the same properties

If we are going to derive the EoM for a specific number of QDs `NQD` we can define this number at the beginning of the program and end this section here. However, for a physical system consisting of subsystems with the same properties (in this case QDs) vast simplifications can be made in the EoM. In this case only one representative of each quantity (EV of configurations) has to be calculated. One can use the number of QDs (NQD) in FORM as a new variable and derive the more general EoM in dependence of this variable. In this case the application of the Kronecker delta (from the commutation relations of the operators) proves to be problematic and vulnerable to errors. As a workaround we define a specific `NQD` and adapt the EoM in the main file `EoM_main.frm` subsequently to the more general case.

The many-particle nature of the system is considered account by replacing a summation over subsystems with the same properties by the factor `number` in the equations. This consideration is carried out analytically by checking whenever the sum over all QDs in the Hamiltonian appears in the equations. Because this step is different for every Hamiltonian and approximation scheme, we do not show the specific calculations for our model here and just give an example how it is implemented in our program.

We choose the number of QDs to be $NQD = 2$, so that all two-QD-configuration quantities are included in the EoM, which is sufficient for the desired approximation order ($\Delta^{Q}_{\delta(1)}$). At the end of the procedure the factor `number` is added to the EoM using the fact that we can predict the terms that have to be summed over all QDs. This is the case whenever the light-matter-coupling produces a product of two-QD-configurations [Leymann et al., 2015]. As one can see in the definition of the Hamiltonian Eqs. (3.8)-(3.11) we must sum over all QDs. Consequently, these

quantities appear `number-1` times, because the indices over the same QD contracts, e.g. $Q^M_{i,j}Q^M_{l,m} = Q^M_{i,m}\delta_{j,l}$. The second modification appears in the EoM of the generalized photon correlation [N](A) = $\langle (b^\dagger)^{\mathrm{A}} b^{\mathrm{A}} \rangle$. These EoM describe the common light-field interacting with all QDs and therefore must be summed over all QDs. According to the choice $NQD = 2$ we have to multiply the whole equation by `number/2` and since this affects also the damping we have to restore the original damping $-2\kappa \mathrm{A}\langle (b^\dagger)^{\mathrm{A}} b^{\mathrm{A}} \rangle$ by adding `+2*'A'*ev([N]('A'))*kappa*(number/2-1)` . The following lines of code are at the end of the main file `EoM_main.frm` :

```
id ev(?a,[Q](?b),[Q](?c))=(number-1)*ev(?a,[Q](?b),[Q](?c));
#do A=0,('PhC')/2
    local [d[N]('A')]=[d[N]('A')]*number/2+2*'A'*ev([N]('A'))*kappa*(
       number/2-1);
#enddo
```

The variable `PhC` here denotes the number of photon correlations that are taken into account by the truncation operator $\Delta^{\mathcal{B}/2+\mathcal{Q}}_{\delta(PhC)}$.

3.4.3 Establishing standard order

In the Ehrenfest EoM, the commutator with the Hamiltonian and sum of the collapse operators, produces 'strings of operators'[1] deviating from a yet to define standard order. To obtain a simple form of the EoM we need to establish a predefined standard order of the operators. The most convenient order for our purposes is the one that is closest to the normal order for operators in second quantization. We define the standard order of operators in three steps: (i) separate bose- and fermi-operators (bose left, fermi right), and within each group (ii) separate creation and annihilation operators (creation operators left, annihilation operators right), and within these groups (iii) alphanumeric order according to the letters of the operators and their indices. This standard order ensures that we have a unique representation of every EoM and that the set of EoM needs to be defined only for EVs of operators in standard order. The normal ordering of creation and annihilation operators also facilitates the implementation of the truncation operator $\Delta_{\langle N \rangle}$, that is applied to systems with a limited number of particles. The corresponding `FORM` procedure is called `standardorder.prc` .

(i) Separate bose and fermi operators To establish the standard order `FORM` searches for products of two operators that deviate from this order and replaces them according to their commutation relation. The code within the `repeat` / `endrepeat` -loop are executed until the expressions do not change further. The following lines of code separate the fermi or configuration operators that describe the state of the QDs from the bose operators that describe the cavity photons

```
repeat;
        id  [Q](?j)*[b+]?bose(?i)=[b+](?i)*[Q](?j);
endrepeat;
```

[1] This description has proven to be beneficial since for some operations in `FORM` the separations of operators by commas instead of a product is more useful.

To address specific (C)functions FORM has also the function wild-card ...? (instead of the field wild-card ?a). This wild-card is used in the following manner: type_of_function?set , where type_of_function specifies the type of the function for which FORM has to search for. The supplement set can be used to further specify the function that are to be replaced by previously defined sets. In this particular case FORM searches for all operators from the set bose=[b],[b+] . Altogether the code above means: replace all products of functions [Q] times functions [b+] from the set bose , regardless of their argument, by the very same bose function [b+] times the [Q] function with their arguments respectively. In other words, the commutation relation $[Q, b^{(\dagger)}] = 0$, between photon and configuration operators is applied until (i) is reached.

(ii) Normal order In the configuration operator formulation [Leymann et al., 2015] there are no carrier (i.e. fermionic) creation and annihilation operators used, therefore we only have to do this step for the bose operators. The following lines of code will establish normal order of the bose operators:

```
1 repeat;
2         id  [b]*[b+]=[b+]*[b]+1;
3         id  [b]*[N](a?)=a*[N](a-1)*[b]+[N](a)*[b];
4         id  [N](a?)*[b+]=a*[b+]*[N](a-1)+[b+]*[N](a);
5         id  [b+]*[N](a?)*[b]=[N](a+1);
6 endrepeat;
```

In the above we have used the generalized photon correlation [N](a) $=b^{\dagger a}b^{a}$, and the substitutions are performed according to the standard bosonic commutation relations.

(iii) Alphanumeric order To obtain alphanumeric order between the configuration operators we use a combination of id commands:

```
1 repeat;
2         id [Q](k?,i?,j?)*[Q](k?,l?,m?)=[Q](k,i,m)*d(j,l);
3         id disorder [Q](k?,i?,j?)*[Q](t?,l?,m?)=([Q](k,i,m)*d(j,l)-[Q
             ](k,l,j)*d(i,m))*d(k,t)+[Q](t,l,m)*[Q](k,i,j);
4 endrepeat;
5 id d(i?,i?)=1;
6 id d(i?,j?)=0;
```

In line 2 the contracting property of the configuration operator is reflected ($|i\rangle\langle j|^k \cdot |l\rangle\langle m|^k = |i\rangle\langle m|^k \delta_{jl}$). This line ensures that no products of configuration operators addressing the same QD are present in the EoM [Leymann et al., 2015]. Line 3 in the code above is the implementation of the commutation relation between the configuration operators Eq. (3.7) with the aim to establish numerical order with respect to the indices. The disorder option of the id command tells FORM to substitute a matching expression only when this results in an increased numerical order of an otherwise equivalent expressions. For example, id would replace $Q_{21} * Q_{12}$ by $Q_{12} * Q_{21}$ and then by $Q_{21} * Q_{12}$ and so on, while id disorder would replace $Q_{21} * Q_{12}$ by $Q_{12} * Q_{21}$ and then stop. The d(i,j) function is the Kronecker delta, which is implemented by the two lines id d(i?,i?)=1; and id d(i?,j?)=0; that can be placed at the end of every procedure using the Kronecker delta.

3.4.4 Factorization

In this section the implementation of the factorization operator $\mathbf{F}$ (Eq. (3.4)) and its inverse operation $\mathbf{F}^{-1}$ (Eq. (3.5)) are described. For details on the mathematical structure we refer to [Fricke, 1996b; Leymann et al., 2014]. The corresponding `FORM` procedure is in `createclustertable.frm` which is not part of the main program (see Sec. 3.4.8). The procedure described in this section is a direct implementation of

$$\left\langle b^I \right\rangle = \delta(b^I) + \sum_{I' \subsetneq I} \langle b^{I/I'} \rangle \delta(b^{I'}). \tag{3.13}$$

Equation (3.13) distributes operators in an EV into CFs multiplied by EVs, and when applied successively all EVs are substituted by CFs. This procedure uses the build-in combinatorial function `distrib_(type,n,f1,f2,x1,...,xm)` , which divides products of operators `[b+]?(?b)` into arguments of functions `EV,CF` [Vermaseren et al., 2000]. Our program contains no anticommutating operators and therefore these procedure is in general valid only for this kind of operators. However, with the modifications suggested in Appendix C the anticommutation relations of fermi operators can be taken into account. The following lines of code constitute the implementation of the factorization operator $\mathbf{F}$:

```
1  id ev(?a)=L*EV(?a)*R;
2
3 #do i=1,42
4         id EV([b+]?(?b),?a)=EV(first*[b+](?b),?a);
5         id EV(first*[b+]?(?b),?a)=distrib_(0,2,EV,CF,first*[b+](?b),?a
              );
6         id EV=1;
7         id CF=1;
8         id EV(?a,first*[b+]?(?c),?b)=0;
9         argument;
10                id first=1;
11        endargument;
12        .sort
13 #enddo
14
15 id L=1;
16 id R=1;
17 id CF(?a)=cf(?a);
```

The lines in the `#do` -loop above are repeated until complete factorization is reached. To prevent `FORM` from crashing the maximum number iterations is limited to an arbitrary but large enough number (here 42). The `argument` / `endargument` -loop is equivalent to the `repeat` -loop, only for this loop all commands are only applied to expressions that are arguments of functions. Note that the variable `first` is a dummy that marks the position of the summation in Eq. (3.13) where the EVs and CFs are distributed. Using Eq. (3.13) the 'refactorization', i.e. the application of $\mathbf{F}^{-1}$, can be implemented analogue to the one of $\mathbf{F}$:

```
1 id cf(?a)=L*CF(?a)*R;
2
3  #do i=1,42
4         id CF([b+]?(?b),?a)=CF(first*[b+](?b),?a);
```

```
5         id CF(first*[b+]?(?b),?a)=-distrib_(0,2,EV,CF,first*[b+](?b),?
              a)+EV([b+](?b),?a)+CF([b+](?b),?a);
6         id EV=1;
7         id CF=1;
8         id EV(?a,first*[b+]?(?c),?b)=0;
9         argument;
10                id first=1;
11        endargument;
12        .sort
13  #enddo
14
15 id L=1;
16 id R=1;
17 id EV(?a)=ev(?a);.
```

3.4.5 The truncation operator

In this section we describe how the application of the truncation operator $\Delta_{\langle N \rangle}$ is implemented. The corresponding FORM procedure for EVs is called `countandneglect.prc` . To determine the order of a CF or EV the `count` command is used, which counts the number of specified operators in a product and returns the number that corresponds to the order of the CF `count(typeofoperator_1,value_1,typeofoperator_2,value_2,...)` $= \sum_i \#(\texttt{typeofoperator\_i})*\texttt{value\_i}$. For this operation it is necessary to rewrite the `[N](a)` operator in terms of `[b+]` and `[b]` with `#call Natobkb` and to rewrite the operators in the EV that are separated by commas into one product of operators using `#call commatoproduct(ev,EV)` . The following lines of code are the implementation of a product of the truncation operators $\Delta^{\mathcal{B}}_{\langle \texttt{'N'} \rangle}$ (line 4) and $\Delta^{\mathcal{Q}}_{\langle \texttt{'M'} \rangle}$ (line 5):

```
1 #call Natobkb
2 #call commatoproduct(ev,EV)
3 argument ev;
4   if (count([b+],1,[b],1)>'N') discard;
5   if (count([Q],1)>'M') discard;
6 endargument;
7 id ev(0)=0;
8 #call producttocomma(ev,EV)
9 #call bkbtoNa
```

When the logical expression behind the `if` command is true the operators in the expectation value `ev` are discarded, i.e. replaced by zero. Expectation values with the argument zero are then replaced by the number zero. Finally the commands `#call Natobkb` and `#call commatoproduct(ev,EV)` are reversed with `#call bkbtoNa` and `#call producttocomma (ev,EV)` .

The application of an operator that truncates CFs ($\Delta^{\mathcal{B}}_{\delta(\texttt{'N'})}$) is implemented in the same way. In our formulation this operator can be applied on EVs with the aid of the factorization $\mathbf{F}^{-1}\Delta^{\mathcal{B}}_{\delta(\texttt{'N'})}\mathbf{F}$. This procedure is in `createclustertable.frm` which is further described in Sec. 3.4.8.

3.4.6 Physical constraints

This section shows how model-dependent physical constraints can be implemented in the FORM program. The factorization of a higher-order EV can produce new EVs that vanish exactly since they are not driven in the exact EoM. This could be, e.g. the conservation of energy or angular momentum or the vanishing of coherent terms like $\langle b \rangle$ in a system with incoherent excitation [Mølmer, 1997; Gies et al., 2007]. The corresponding FORM procedure can be found in `constraints.prc`. In the remainder of this sections we describe the implementation of physical constraints that are relevant to our model.

Balanced amount of creation and annihilation operators

Due to the initial conditions and the excitation method of our model, all EVs $\langle b^{\dagger m} b^n \rangle$ with $m \neq n$, which correspond to the coherent regime are zero

```
argument ev;
        if ((count([b+],1,[b],-1)!=0)&&(count([Q],1)==0)) discard;
endargument;
id ev(0)=0;
```

This procedure discards all EVs that contain an imbalanced amount of photon creation and annihilation operators `(count([b+],1,[b],-1)` and does not include a configuration operator `count([Q],1)==0)`.

Conservation laws

The formulation of the excitation conservation constraint depends on the definition of the configuration operators. For this reason we show one example, which is required in our QD model. The photon assisted s-exciton ground state polarization $\langle b^{\dagger m} b^n Q^M_{1,2} \rangle$ vanishes if no new photon is created, i.e. if $m + 1 \neq n$ holds.

```
argument ev;
                id [Q](i?,j?,2)= [Q](i,j,2)*[v+];
                id [Q](i?,2,j?)= [Q](i,2,j)*[v];
endargument;

argument ev;
        if (count([b+],1,[b],-1)!=count([v+],1,[v],-1)) discard;
endargument;

argument ev;
id [v]=1;
id [v+]=1;
endargument;

id ev(0)=0;
```

The first loop states that the configuration operator $|j\rangle\langle 2|$ annihilates one excitation `id [Q](i?,j?,2)= [Q](i,j,2)*[v+];` (note that the `[v]` operators are auxiliary operators to count the excitations) and the conjugate operator $|2\rangle\langle j|$ creates one excitation. In the second loop the procedure checks whether the number of exci-

tations is balanced with the number of photon creation and annihilation operators `if (count([b+],1,[b],-1)!=count([v+],1,[v],-1)) discard; .`

Selection rules

Selection rules constrain the possible transition in the QDs [Baer et al., 2007; Schulz et al., 2006]. To check the conservation of angular momentum we have to determine if all occurring EVs fulfill this condition. In our model the states $|3\rangle$ and $|4\rangle$ have different angular momenta since in $|3\rangle$ both electrons occupy the p-shell state and in $|4\rangle$ electrons occupy the s-shell state. The procedure therefore has to make sure that an EV consists of a balanced transition between these states.

```
1  argument ev;
2
3          id [Q](i?,j?,3)= [Q](i,j,3)*[v]*[v];
4          id [Q](i?,j?,4)= [Q](i,j,4)*[v+]*[v+];
5
6          id [Q](i?,3,j?)= [Q](i,3,j)*[v+]*[v+];
7          id [Q](i?,4,j?)= [Q](i,4,j)*[v]*[v];
8
9  endargument;
10
11
12 argument ev;
13         if (count([v+],1,[v],-1)!=0) discard;
14 endargument;
```

In the first step each configuration is multiplied with `[v]*[v]` and `[v+]*[v+]` (note that the `[v]*[v]` operators are auxiliary operators to count the angular momentum) depending whether it describes a transition from $|3\rangle$ to $|4\rangle$ or $|4\rangle$ to $|3\rangle$ respectively. Then `if (count([v+],1,[v],-1)!=0) discard;` checks whether the expression is balanced, otherwise it is discarded.

3.4.7 Definition of a closed set of equations of motion

With the previous described procedures, we are able to apply the Ehrenfest equations, and the computational application of the factorization and truncation operators ($\mathbf{F}$, $\mathbf{F}^{-1}$, $\Delta_{\langle N\rangle,\delta\langle N\rangle}$) is settled. In this section, we explain how one can derive a closed set of EoM. This step is not performed automatically in the current version of our program since it is not very time consuming to determine for which EVs EoM need to be derived. The set of EoM strongly depends on the chosen approximation scheme. Although all these considerations can be done completely analytically [Leymann et al., 2014], it is also instructive to use the program on a trial and error basis to obtain a closed set of equations. This works in the following steps: i) implement the desired boundary conditions and approximation ii) start to define the physical quantities you are interested in, e.g. $\langle b^\dagger b\rangle$ iii) derive the EoM for these quantities iv) search for unknown quantities in the EoM and go back to step ii) with the definition of the 'new' quantities until no more new quantities can be found in iv). This method is a good way to compare between analytic considerations and the actual outcome of the program. We strongly recommend this opportunity as a double check of your program that easily can consist of thousands of bulky differential equations.

3.4.8 Building cluster tables

The following section is not mandatory to obtain a closed set of EoM but we recommend to build a cluster table in advance independently from the main program, which can save a lot of computation time. As illustrated in Eq. (3.6) the factorization and the refactorization of an EV is the costliest part of the computer-aided cluster expansion. Typically, one has to derive several different sets of EoM, in some circumstances using different approximation schemes, until one obtains a set of EoM that delivers satisfying results. Therefore, it is advisable to outsource the factorization and instead of applying it to every EV separately, use the wild cards to declare general factorizations that apply for all EVs containing negligible CFs. We call this kind of procedures cluster tables and we use them also in the example program. The lowest order approximation in our program is `#procedure expectationvaluetableQDC1PhC2` which is the application of $\mathbf{F}^{-1}\Delta_{\delta(2)}^{\mathcal{B}/2+\mathcal{Q}}\Delta_{\delta(1)}^{\mathcal{Q}}\mathbf{F}$. For example we factorize

$$\begin{aligned}\langle b^\dagger b Q_{jk}^i\rangle &= \langle b^\dagger b\rangle\langle Q_{jk}^i\rangle \\ \langle Q_{jk}^i Q_{mn}^l\rangle &= \langle Q_{jk}^i\rangle\langle Q_{mn}^l\rangle,\end{aligned} \tag{3.14}$$

which reads in the cluster table as:

```
1 id ev([b+],[b],[Q](i?,j?,k?))=+ev([b+],[b])*ev([Q](i,j,k));
2 id ev([Q](i?,j?,k?),[Q](l?,m?,n?))=+ev([Q](i,j,k))
3                                     *ev([Q](l,m,n));
```

The cluster tables are generated with the `FORM` program `createclustertable.frm`. The output of this program is directly converted into a `FORM` procedure with the Perl script `createclustertable.pl`.

3.5 Application to a semiconductor quantum-dot laser model

In this section, we show results that have been produced using the previously described program. The system we are describing is based on the laser model presented in [Leymann et al., 2015]. These calculations illustrate the capability of our approach by providing photon correlations up to 10th-order ($\Delta_{\delta(10)}^{\mathcal{B}}$), so that results for the photon autocorrelation function of 5th-order ($g^{(5)}(0)$) are provided. For this model the number of equations increases by 14 with every second photon correlation included. Starting with 13 equations in second-order we end up with 69 equations in 10th-order. While the number of equations grows with a constant summand, the size of the equations (measured in kilobyte) more than doubles with every second photon correlations order. Starting with 2kB in second-order the size grows up to 94kB in the 10th-order. The execution of the main program `EoM_main.frm` takes only a few seconds on a regular desktop PC. The limiting factor to progress to further orders is given by the factorization scheme and the generation of the cluster tables `createclustertable.frm`. The cluster table for the second-order was generated in less than one second, whereas the 10th-order took several days.

We use the access to higher order photon autocorrelations to study the laser transition in high-β especially $\beta = 1$ lasers. Higher-order photon correlations of coupled

quantum systems have been investigated by several groups [Aßmann et al., 2009; Avenhaus et al., 2010; Stevens et al., 2010] experimentally. The threshold behavior of $g^{(2)}(0)$ for a QD-based-microcavity laser is experimentally and theoretically well studied [Gies et al., 2007; Wiersig et al., 2009; Leymann et al., 2013c]. The transition from non-lasing to lasing can be characterized by a change in the photon statistics from a thermal- to a Poisson-distribution [Rice and Carmichael, 1994]. The photon-autocorrelation functions Eq. (1.43) drops from $n!$ to one during the laser transition [Loudon, 2000; Garrison and Chiao, 2014; Leymann et al., 2014]. It is instructive to analyze the stimulated emission rate Γ_{stim} as well [Leymann et al., 2015], which provides a deeper insight into the lasing properties

$$\Gamma_{\text{stim}} = \frac{\langle b^\dagger b \text{Inv} \rangle}{\tau_{\text{Deph}}}, \tag{3.15}$$

with the inversion operator defined as

$$\text{Inv} = Q_{6,6} - Q_{5,5} + Q_{2,2} - Q_{1,1}, \tag{3.16}$$

and the total dephasing rate τ_{Deph}, which is the sum of the exciton dephasing

$$\tau^X_{\text{Deph}} = \frac{1}{\kappa + \gamma^s_{\text{sp}} + 2P}, \tag{3.17}$$

that consists of the cavity loss rate κ, the spontaneous loss rate in the s-shell γ^s_{sp} and the pump rate P. And the biexciton dephasing

$$\tau^{XX}_{\text{Deph}} = \frac{1}{\kappa + 2\gamma_{\text{r,c}} + 3\gamma^s_{\text{sp}}}, \tag{3.18}$$

with the carrier relaxation rate of the conduction band $\gamma_{\text{r,c}}$. Equation (3.15) indicates absorption of cavity photons when $\Gamma_{\text{stim}} < 0$ and an enhancement of the light emission for $\Gamma_{\text{stim}} > 0$ and is therefore a good indicator for lasing. Finally, we consider the scaled photon correlation functions Eq. (2.36) introduced in Ch. 2, which show the 'pure' many-particle correlations separated from their lower-order factorization. Using $C^{(n)}(0)$ we monitor the onset of lasing in each photon correlation and reveal a more complex behavior for the transition, since $C^{(n)}(0)$ behaves differently for every order n.

To compare the laser characteristics for different β-factors we identify the β-factor directly from its definition via the spontaneous emission rates into the lasing (τ_l) and non-lasing (τ_{nl}) modes [Musiał et al., 2015]

$$\beta = \frac{1}{\tau_l} \Big/ \left(\frac{1}{\tau_l} + \frac{1}{\tau_{nl}} \right) = \frac{2|g|^2}{\kappa + \gamma^s_{sp}} \Big/ \left(\frac{2|g|^2}{\kappa + \gamma^s_{sp}} + \gamma^s_{sp} + \gamma^p_{sp} \right). \tag{3.19}$$

In a first step, we examine a microlaser for varying β-factors close to 1 by changing the spontaneous losses into the non-lasing modes γ_{sp}. Figure 3.3 shows the corresponding input-output characteristics. With increasing β-factors more photons are directly emitted into the lasing mode. Therefore, we observe a transition into lasing at lower pump powers and a higher intensity. The saturation typical for a semiconductor QD laser is caused by Pauli blocking. In this model the spontaneous emission

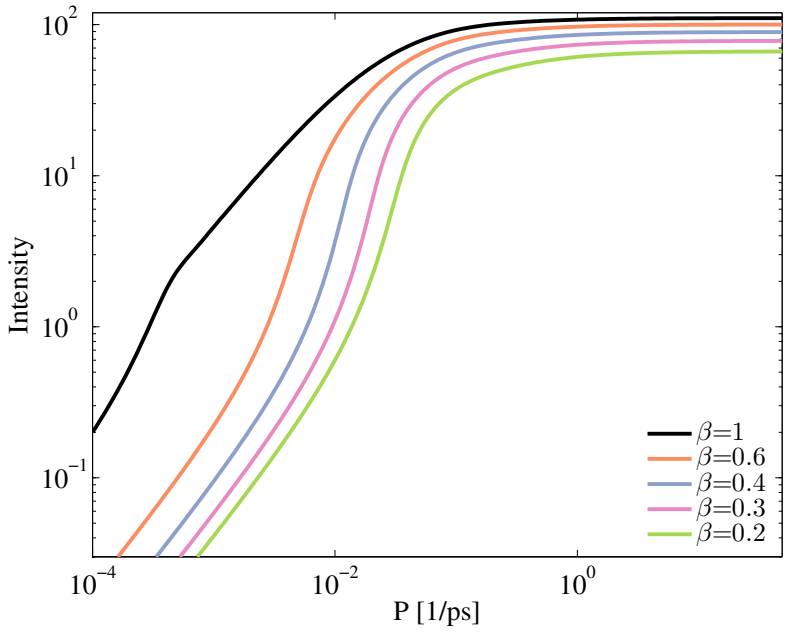

Figure 3.3: Input-output characteristics for different β-factors vs. pump power P. The following parameters were used: number of quantum dots $number = 100$, cavity losses $\kappa = 0.02 \left[\frac{1}{ps}\right]$, spontaneous losses in non-lasing modes $\beta = 1, 0.6, 0.4, 0.3, 0.2$, carrier relaxation rate $\gamma_{r,\{c,v\}} = 0.04 \left[\frac{1}{ps}\right]$, and light-matter-coupling strength $g = 0.015 \left[\frac{1}{ps}\right]$.

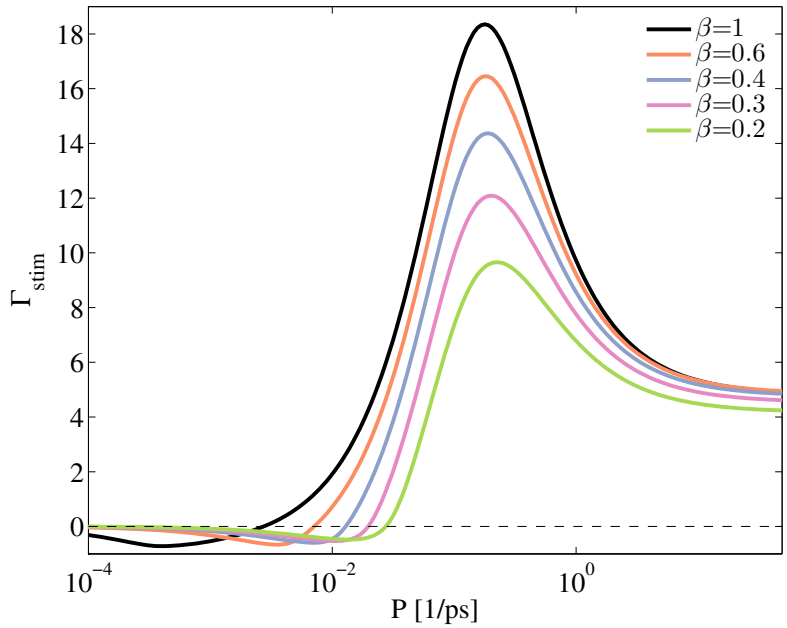

Figure 3.4: Stimulated emission for different β-factors in dependence on the pump power.

into non-lasing-modes (different β-factors) is altered by different cavities, but this does not affect the inversion saturation caused by the Pauli-blocking. The intensity differences are significantly larger in the low pump (non-lasing) regime, since here the different spontaneous emission rates have the strongest effect.

To further analyze the onset of lasing we study the stimulated emission rates Γ_{stim}. Once Γ_{stim} crosses the zero line the QDs begin to emit light due to stimulated emission. The numerical results in Fig. 3.4 reveal that the stimulated emission for higher β-factors is stronger suppressed in the non-lasing regime. The stimulated emission reaches its maximum when the combined rate $\tau_{\text{Deph}} = \tau^{X}_{\text{Deph}} + \tau^{XX}_{\text{Deph}}$ of exciton and biexciton is maximal. If the pump power is increased further the dephasing due to the pump damps out the excitonic contribution (3.17) and the stimulated emission saturates at the value of the biexciton contribution.

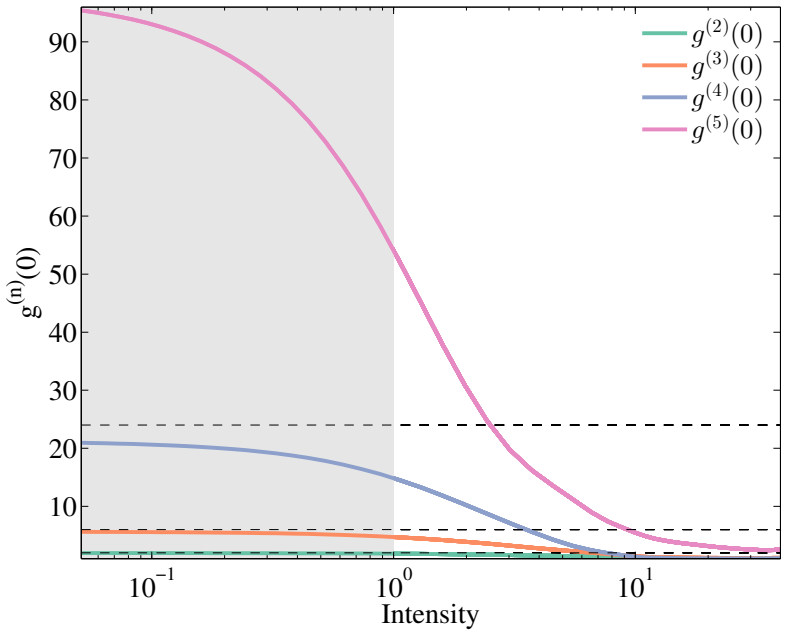

Figure 3.5: Autocorrelation functions $g^{(2)}(0)$ to $g^{(5)}(0)$ in dependence from the light intensity for a $\beta = 1$ laser. The gray shaded area marks the non-lasing sector with an average of less than 1 photon in the cavity mode. The dashed lines indicate the value for thermal light. For such a high β-value the laser is never really thermal, even if there is less than 1 photon in the cavity. The following parameters were used: number of quantum dots $number = 40$, cavity losses $\kappa = 0.0125 \left[\frac{1}{ps}\right]$, spontaneous losses into non-lasing modes $\gamma_{sp}^{\{s,p\}} = 0 \left[\frac{1}{ps}\right]$, carrier relaxation rate $\gamma_{r,\{c,v\}} = 0.05 \left[\frac{1}{ps}\right]$, light-matter-coupling strength $g = 0.02 \left[\frac{1}{ps}\right]$, and direct dephasing $\gamma_d = 0.5 \left[\frac{1}{ps}\right]$.

To gain a deeper insight how the photon correlations are affected by the laser transition we consider a $\beta = 1$ laser with only 40 QD emitter and a high quality mode, which leads to a very smooth laser-transition. Note that we depict the next figures in dependence on the light intensity [Chow et al., 2014]. The area with less than a single cavity photon on average, which would be the traditional laser

threshold, is shaded gray. Figure 3.5 reveals that the threshold softens considerably and that the lower-order autocorrelation function changes for lower pump rates to the coherent value $g^{(n)}(0) = 1$. This transition takes place at much higher intensity than one would suspect by applying the one-photon criterion for lasing. Figure 3.5 shows the known feature that the autocorrelation function for a $\beta = 1$ laser starts even for arbitrary small pump power with an autocorrelation value smaller than its thermal value [Gies et al., 2007; Rice and Carmichael, 1994]. This indicates that the built up of correlations between the photons is much stronger in systems without spontaneous emission losses. This behavior is studied further in Fig. 3.6, where we exhibit the scaled photon correlation function $C^{(n)}$ in Eq. (2.36), which visualizes the nth degree of coherence of the 'pure' photon correlations. In this figure it is revealed that photon pairs are partially correlated already for low pump powers, whereas the higher-order correlation built up gradually. This effect can only be observed for $\beta \approx 1$ lasers.

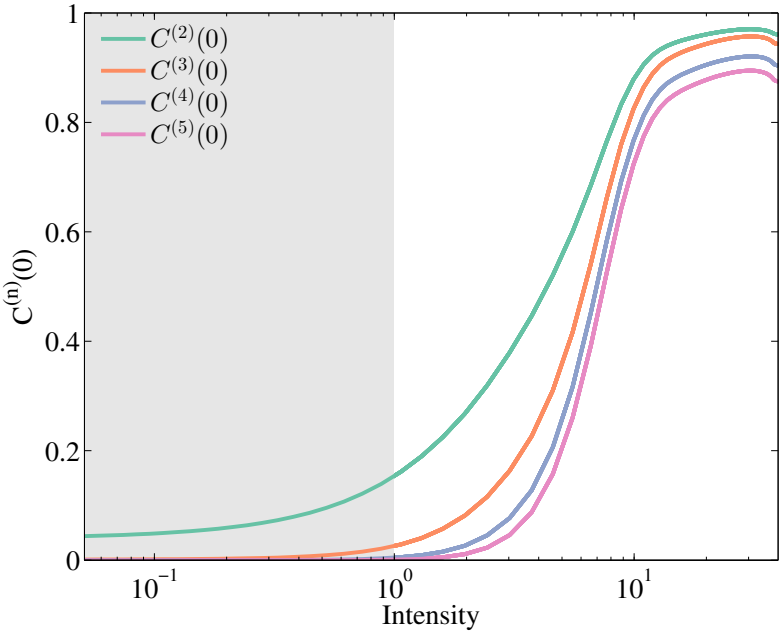

Figure 3.6: Scaled photon CFs in dependence on the light intensity for a $\beta = 1$ laser. The gray shaded area marks the non-lasing sector with an average of less than 1 photon in the cavity. The analysis of this function reveals that the two-photon correlation have a remarkable magnitude also for small excitations. We also observe that higher-order CFs built up at higher pump rates than low-order CFs.

Although we used a strongly improved QD laser-model in this chapter the results here may remind the reader on the results of the laser transition in higher-order photon-autocorrelation functions (Ch. 2.4.2). To clarify the improvements we like to point out the main differences. Beside the different choice of the β-factor, in this chapter we use a QD description that is based on configuration operators instead of the fermionic annihilation and creation operators which allows us to describe a single QD without the approximation in Ch. 2.4.2. The external bath here is described with the Lindblad processes introduced in Ch. 1.6 while the description in

the last chapter also uses some heuristic scattering/damping terms. Not only that this description makes the model more consistent it also allows for the definition of a pump dependent stimulated emission rate Γ_{stim} Eq. (3.15), which is an essential innovation.

3.6 Chapter conclusion

We introduced an implementation of the computer-aided CE for the calculation of the time evolution of quantum many-particle systems. We provided the reader with the theoretical concepts and detailed description of a basic example program that can be used as a starting point for further modifications. The implementation of the factorization of EVs and the inverse procedure is the most important and most versatile aspect of this program. All procedures and the complete program is available for download[Foerster et al., 2016]. We kindly ask the reader to use this program more as a development tool than as a black box. The application to a semiconductor QD laser model illustrated the efficiency of our approach that led to new physical insights. However, the field of application of the computer-aided CE is much bigger than our investigations on QD lasers. We also recommend the usage of regular expression, e.g. [Watt, 2005] so that the EoM created by `FORM` can easily be rewritten in any other format like LaTeX or ready to use code for the numerical calculations.

Chapter 4

Bimodal microcavity laser

In this chapter, we investigate the characteristics of quantum dot (QD) based bimodal microcavity lasers. Starting from an experimental study of a micropillar laser with two orthogonally polarized cavity modes it has been observed that one emission mode of this microlaser demonstrates a characteristic $\mathcal{S}$-shaped input-output curve while the output intensity of the second mode saturates and even decreases with increasing injection current above threshold. Further analyzing the photon autocorrelation function $g^{(2)}(\tau)$ of the light emission confirms the onset of lasing in the first mode with $g^{(2)}(0)$ approaching unity above threshold. In contrast, strong photon bunching associated with superthermal values of $g^{(2)}(0)$ is detected for the other mode for injection currents above threshold. We attribute this behavior to the gain competition of the two modes induced by the common gain material, which is confirmed by photon crosscorrelation measurements revealing a clear anti-correlation between emission events of the two modes

We develop a microscopic semiconductor theory for bimodal micropillar laser that is based on [Gies et al., 2007] and derive equation of motion(EoM) that can reproduce experimental results qualitatively. In a second step, we expand the theoretical model to calculate multi-time correlation functions (for the general theory see Ch. 2.3.4). We analyze the occurrence of normal-mode coupling (NMC) in bimodal lasers attributed to the collective interaction of the cavity field with a mesoscopic number of QDs. In contrast to the conventional NMC we observe locking of the frequencies and splitting of the linewidths of the eigenmodes of the system in the coherent coupling regime. The theoretical analysis of the incoherent regime is supported by an additional experimental observation where the emission spectrum of one of the orthogonally polarized modes of a bimodal QD micropillar laser that demonstrates a two-peak structure.

Parts of the study of gain competition in this chapter are published in [Leymann et al., 2013c,a]. The microscopic EoM where mainly derived by A. Foerster and H.A.M. Leymann, and the numerical integration of the EoM was mainly done by A. Foerster. M. Khanbekyan set the theory into context and provided physical insight to the results. The experiments where mainly performed by C. Hopfmann and F. Albert in the group of S. Reitzenstein, while the samples where produced by C. Schneider in the group of A. Forchel.

Parts of the investigation of NMC in this chapter are published in [Khanbekyan

et al., 2015]. M. Khanbekyan worked out the details of the connection between the conventional NMC and the unconventional NMC of the two laser modes. H.A.M. Leymann extended the theory for the first order coherence function to the two-mode case. A. Foerster and H.A.M. Leymann implemented the theory in FORM and derived the EoM. A. Foerster performed the numerical integration of the EoM. The experiments where mainly performed by C. Hopfmann from the group of S. Reitzenstein, while the samples where produced by C. Schneider in the group of S. Höfling. All authors of [Leymann et al., 2013c,a; Khanbekyan et al., 2015] discussed the results and their physical implications.

4.1 Microcavity lasers

The research on microcavity lasers so far has been focused mostly on emission features based on the interaction between a single laser mode and the QD gain medium. Going beyond this investigations, micropillar lasers with a bimodal emission spectrum allow one to address the coupling of two orthogonally polarized optical modes via the common gain medium which can lead to characteristic oscillations in the coherence properties [Ates et al., 2007], an enhanced sensitivity on external perturbations in the presence of optical self-feedback [Albert et al., 2011] and deterministic polarization chaos in the absence of optical feedback [Virte et al., 2013].

We present a detailed experimental and theoretical analysis of the mode coupling and gain competition of bimodal, electrically pumped micropillar lasers. A appropriate measure for the study of the statistical properties of the electromagnetic field emission is the intensity correlation function Eq. (1.41) which can be generalized to the case of two modes:

$$g^{(2)}_{\xi\zeta}(\tau) = \frac{\langle b^\dagger_\xi(t) b^\dagger_\zeta(t+\tau) b_\zeta(t+\tau) b_\xi(t)\rangle}{\langle b^\dagger_\xi(t) b_\xi(t)\rangle \langle b^\dagger_\zeta(t) b_\zeta(t)\rangle}, \tag{4.1}$$

where $\xi, \zeta = 1, 2$, with delay time τ and photon annihilation (creation) operators $b_1^{(\dagger)}$ and $b_2^{(\dagger)}$ of the mode 1 and the mode 2, respectively.

For the case of more than one mode the intensity correlation functions $g^{(2)}_{\xi\zeta}$ can be studied for all possible index combination $\{\xi, \zeta\}$. The gain competition is reflected in distinct differences in the input-output characteristic and the autocorrelation function $g^{(2)}_{\xi\xi}(\tau)$ of the two optical modes. Moreover, the crosscorrelation function $g^{(2)}_{\xi\zeta}(\tau)$ with $\xi \neq \zeta$ can reveal correlations between emission events from the two modes.

To describe and analyze these specific features of bimodal microlasers we extend the microscopic semiconductor model [Gies et al., 2007] accordingly by taking two modes into account. The microscopic semiconductor theory is applied to model the input-output characteristics, the intensity correlation functions of the laser and the gain competition between the two emission modes within the framework of the cluster expansion.

The chapter is organized as follows. In section 4.2 the experimental results obtained from an electrically pumped, bimodal micropillar laser are presented. Section 4.3 is concerned with the theoretical description of the experimental data. In

section 4.4 a conclusive analysis of the experimental and the theoretical results is presented. In section 4.5 NMC is introduced and the occurrence of NMC in the literature is discussed. In section 4.6 the theory of section 4.3 is expanded to the case of multi-time EoM. In section 4.7 the theory of two bimodal lasers is connected to NMC and its impact is discussed. In section 4.8 the theory of section 4.6 is used to calculate spectra for a bimodal laser and compares the results to the experiments.

4.2 Experiment

The electrically pumped micropillar lasers are based on a planar AlAs/GaAs microcavity structure which includes an active layer consisting of a single layer of $In_{0.3}Ga_{0.3}As$ QDs. High resolution electron-beam lithography, plasma enhanced etching and metal deposition have been applied to fabricate high quality electrically pumped microlasers. For more details on the sample processing we refer to [Reitzenstein et al., 2011]. The microlasers have been investigated at low temperature (20 K) using a high resolution micro-electroluminescence (μEL) setup. A linear polarizer in combination with a $\lambda/4$-wave-plate is installed in front of the entrance slit of the monochromator to perform polarization resolved measurements of the laser signal. The photon statistics of the emitted light has been studied by means of the measurement of the photon autocorrelation function $g^{(2)}_{\xi\xi}(\tau)$, that has been carried out using a fiber coupled Hanbury-Brown and Twiss (HBT) configuration with a temporal resolution $\tau_{\text{irf}} = 40$ ps. The HBT configuration is coupled to the output slit of the monochromator which has a focal length of $f = 0.75$ m. The interaction of the orthogonally polarized modes of the microlaser has been investigated by means of photon crosscorrelation $g^{(2)}_{12}(\tau)$ measurements. For this purpose, the light emitted by the microlaser is split by a polarization-maintaining 50/50 beamsplitter and coupled into two monochromators, each of which is equipped with a linear polarizer at the input slit and a fiber coupled single photon counting module at the output slit. This configuration allows to perform polarization resolved crosscorrelation measurements with a spectral resolution of 25 μeV. Within the present setup, it is not possible to perform photon number distribution measurements due to low ($\ll 1\mu W$) power of the microlaser, in contrast to the measurements presented recently for a standard laser diode with the output power of order of milliwatts [Roumpos and Cundiff, 2013]. First, let us focus on the input-output characteristics of the microlaser. Due to slight asymmetry of the cross-section(see Fig. 4.1) of the pillar and the ring-shaped contact the degeneracy of the fundamental mode in the pillar microcavity is lifted and two distinct linearly polarized modes are supported [Reitzenstein et al., 2007]. In this context, the spectral splitting Δ_{12} and accordingly the overlap between the two modes plays an important role for the studies of emission of bimodal cavities. Figure 4.2 shows representative polarization resolved spectra of an electrically pumped bimodal microlaser at threshold (injection current, $I_{inj} = 5.1$ μA). The two linearly polarized modes are split in energy by 103 μeV and have absorption limited Q-factors of $Q = 13900$ (mode 1) and $Q = 13100$ (mode 2) that are extracted from the linewidth at the threshold. The input-output characteristic of the bimodal microlaser is presented in Fig. 4.3(a). We observe pronounced differences between the two modes: while mode 1 shows a standard $\mathcal{S}$-shaped input-output characteristic

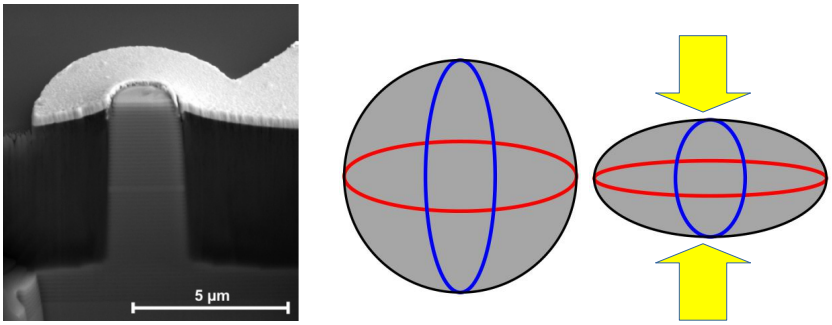

Figure 4.1: Illustration of the emergence of two linearly polarized modes in a micropillar (picture on the left taken from [Reitzenstein and Forchel, 2010b]). Due to slight asymmetry of the cross-section of the pillar and the ring-shaped contact(sketched on the right side) the degeneracy of the fundamental mode in the pillar microcavity is lifted and two distinct linearly polarized modes are supported [Sebald et al., 2009].

with a threshold current of about $I_{th} = 5.1$ μA, the intensity of mode 2 saturates at $I_{inj}/I_{th} = 2$ and even drops down for injection currents exceeding $I_{inj}/I_{th} = 2.5$. This behavior indicates a pronounced competition between the modes 1 and 2 which is mediated by the common QD gain material.

To study the lasing features, we extract the emission linewidths of the two modes and plot them as a function of the injection current in Fig. 4.3(b). Interestingly the linewidths of both modes have similar magnitude and decrease strongly at threshold which reflects enhanced temporal coherence in the lasing regime. While the linewidth of mode 1 stays at a resolution limited value of 25 μeV, a slight increase of the linewidth can be observed for mode 2 above $I_{inj}/I_{th} = 3$. This behavior is surprising because also mode 2 that loses the gain competition has a laser typical small linewidth which can only be explained due to NMC in Sec. 4.5.

To verify the interpretation of mode coupling, crosscorrelation measurements between the modes 1 and 2 at different injection currents have been performed. A representative example of such a measurement is presented in Fig. 4.3(e) for $I_{inj}/I_{th} = 3$. The cross-correlation function $g^{(2)}_{12}(\tau)$ demonstrates a pronounced dip $g^{(2)}_{12,min} = 0.62$ at $\tau = 0$ which indicates an anti-correlation between emission events from the two laser modes. The anti-correlated emission occurs at a characteristic timescale of $\tau_{12} = 3.8$ ns. Figure 4.3(d) reveals that the crosscorrelation function $g^{(2)}_{12}(0)$ strongly depends on the injection current. In the regime of certain injection currents above the threshold ($2.7 < I_{inj}/I_{th} < 3.3$), the anti-correlation between the modes is the strongest.

As it can be seen from Fig. 4.3(a), at these values of the injection currents above the threshold the intensity of mode 2 decreases. The interplay between the two emission modes is also accompanied by strong intensity fluctuations which are identified by measuring the photon autocorrelation function of the two competing modes for different injection currents. The respective dependencies, i.e. $g^{(2)}_{11}(0)$ and $g^{(2)}_{22}(0)$ versus injection current, are plotted in Fig. 4.3(c), while Fig. 4.3(f) shows the autocorrelation function $g^{(2)}_{22}(\tau)$ for $I_{inj}/I_{th} = 3$. The mode 1 shows the typical maximum

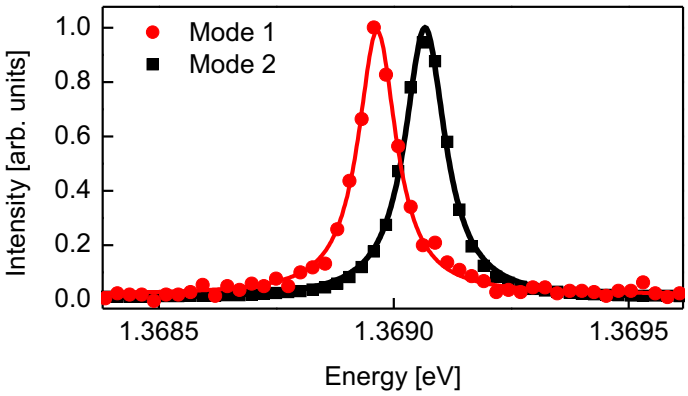

Figure 4.2: Polarization resolved μEL emission spectra of a microlaser with a diameter of 3 μm. The electromagnetic field emission features two orthogonally polarized cavity modes, the mode 1 ($Q = 13900$) and the mode 2 ($Q = 13100$) with a spectral separation of 103 μeV (Injection current: $I_{inj} = 5.1$ μA).

of $g_{11}^{(2)}(0)$ around threshold, which indicates the transition from spontaneous emission to stimulated emission, where $g_{11}^{(2)}(0)$ is lower than expected from theory due to the limited temporal resolution of the HBT configuration [Ulrich et al., 2007]. In contrast, as can be concluded from Fig. 4.3(c), the statistics of the mode 2 at certain injection currents demonstrates strongly super-Poissonian behavior, since the autocorrelation function $g_{22}^{(2)}(0)$ increases strongly at the pump rates well above threshold and reaches its maximum value of 3.08 at $I_{inj}/I_{th} = 3$. This value is significantly higher than $g_{22}^{(2)}(0) = 2$, expected for thermal light and indicates a different photon statistic that allows for superthermal bunching.

Similar statistical properties of the emission, i.e. strong super-Poissonian behavior for the weak mode, have also been observed for microlasers in the presence of an external mirror, where a delayed feedback of the emitted signal disturbs laser operation and leads to strong bunching for the weak mode [Albert et al., 2011; Schulze et al., 2014]. Optical feedback in the single photon limit has also been used to stabilize intrinsic quantum cavity electrodynamics [Carmele et al., 2013]. Despite the major similarities of the experimental results there has not been found a common theoretical basis of these effects.

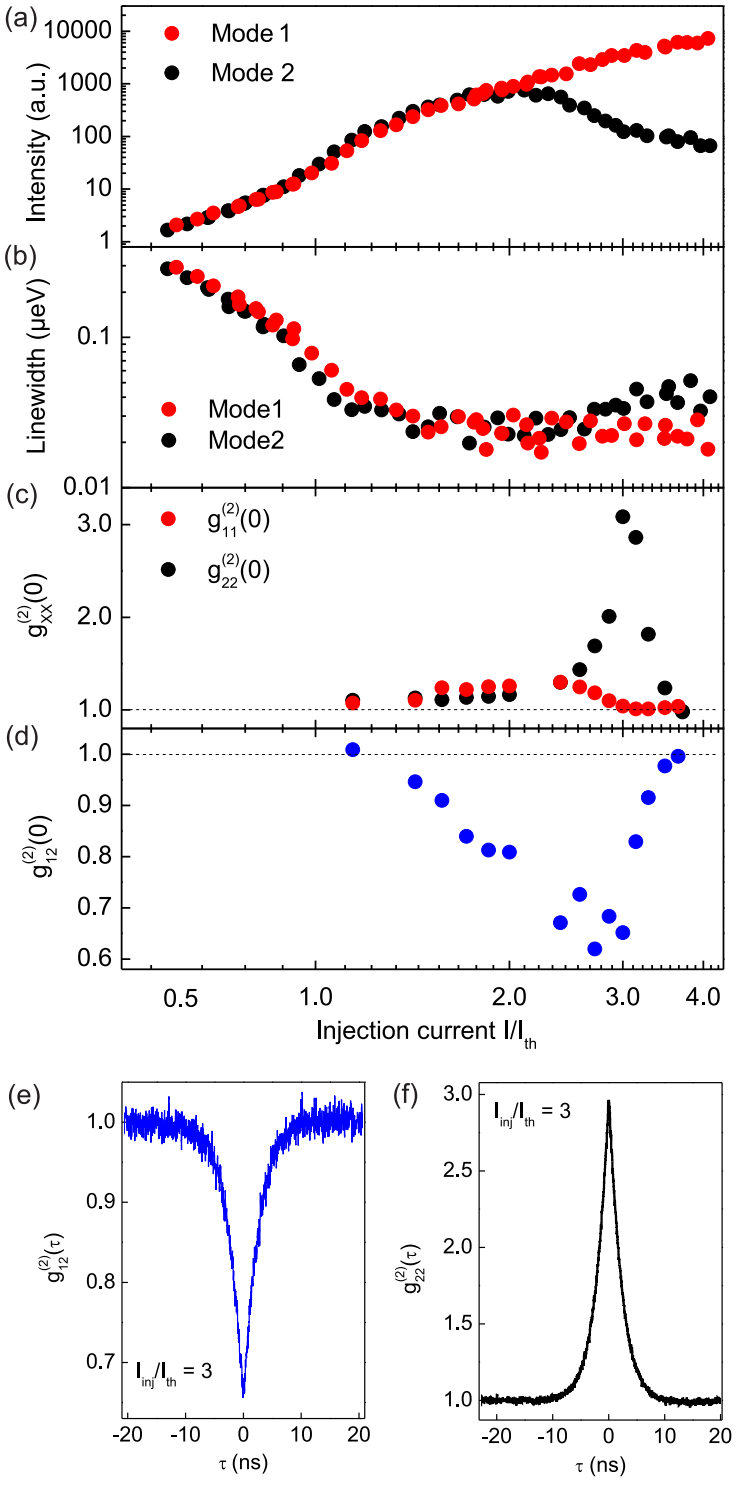

Figure 4.3: Experimental characteristics of a bimodal micropillar laser with a diameter of 3 μm. (a) Input-output characteristic, (b) emission mode linewidth and the photon (c) auto- and (d) crosscorrelation functions $g^{(2)}_{11}(0)$, $g^{(2)}_{12}(0)$ and $g^{(2)}_{22}(0)$ of emission from modes 1 and 2, respectively. Panels (e) and (f) show exemplary cross-correlation $g^{(2)}_{12}(\tau)$ and autocorrelation $g^{(2)}_{22}(\tau)$ measurements at an injection current of $I_{inj}/I_{th} = 3$.

4.3 Microscopic semiconductor theory

To study the interaction of QDs with the electromagnetic field inside an optical bimodal microcavity we have extended the microscopic semiconductor theory [Gies et al., 2007] to the case of two modes and photon crosscorrelation functions [Foerster, 2012]. The microscopic semiconductor theory allows for inclusion of many-body effects of the carriers and can be used to calculate correlations required to determine the statistics of the emission of microcavities with active QDs (for a review see, e. g., Ref. [Michler, 2009]). The calculations are based on the cluster expansion approach introduced in Ch. 2. In contrast to Ch. 2 the EoM are formulated here in terms of correlation functions. The calculations described in Sec. 2.4.1 are governed by the operator $\mathbf{F}^{-1}\Delta_{\delta(4)}^{\mathcal{B}+\mathcal{F}/2}\mathbf{F}\langle A\rangle$ basically stay the same for the two-mode case. In order to use the Ehrenfest EoM Eq.(1.9) the operator $\mathbf{F}^{-1}\delta(A)$ has to be applied. Then the operator $\Delta_{\delta(4)}^{\mathcal{B}+\mathcal{F}/2}\mathbf{F}\langle A\rangle$ can be applied to close the hierarchy. This approach has the advantage that we can directly compare the EoM to the single-mode case in [Gies et al., 2007].

In what follows we assume that only two confined QD shells (see Fig. 4) for both electrons and holes are relevant: whereas one of the modes interacts resonantly with the electromagnetic field of the bimodal cavity due to the coupling with the s-shell transition, the second mode is detuned. The carrier generation due to electrical pumping takes place in the p-shell. The assumption suits well also for an experimental situation, where the electrical pumping is to take place via injection of electrons and holes into the wetting layer and subsequent fast relaxation to the discrete electronic states of the QDs. Further, carrier-carrier and carrier-phonon scattering contributions to the dynamics are evaluated using a relaxation time approximation, where the relaxation towards quasi-equilibrium is given in terms of a relaxation rate [Nielsen et al., 2004]. Although the Lindblad formulation in Ch. 1 provides a more general approach the relaxation rates are used for a better comparison to the single-mode case in [Gies et al., 2007].

The Hamiltonian given by Eq. (1.1) together with Eqs. (1.18,1.31,1.32,1.33) determines the dynamical evolution of the carrier and field operators and, in particular, the time evolution for operator expectation values. The effect of the many-body Coulomb Hamiltonian can be discussed in two different regimes: (i) the regime of high-temperature and high-carrier density, (ii) the regime of low-temperature and low-carrier density. In (i) the interaction between the QDs and the wetting layer carriers leads to self-energy shifts for the QD transitions, while the Coulomb interaction between the QDs is screened by the high-carrier density [Schneider et al., 2001b,a]. In (ii) the interaction with the wetting layer carriers is neglectable due to the low-carrier density in the wetting layer [Schwab et al., 2006] and the interaction between the QDs creates intra- and interband effects. Here we are mainly interested in (ii) and similar to [Gies et al., 2007] the Coulomb interaction in the following is reflected by an effective transition energy and the oscillator strength for the coupling to the laser mode instead of taking the full Coulomb Hamiltonian into account. The equations of motion for quantities of interest, as for example the average photon number $\langle b_\xi^\dagger b_\xi\rangle$ in the cavity modes and the average electron population in the conduction $\langle c^\dagger c\rangle$ and valence $\langle v^\dagger v\rangle$ bands, have source terms that contain

operator expectation values of higher order. In this way, the approach bears an infinite hierarchy of equations of motion for various expectation values for photon and carrier operators. To perform a consistent truncation of the equations the cluster expansion scheme $\Delta_{\delta(4)}^{\mathcal{B}+\mathcal{F}/2}$ is applied (for details, see Ch. 2). Namely, starting from the expectation values of the first order of photon operators, the equations of motion for operator expectation values are replaced by equations of motion for correlation functions. For example, instead of the EoM for expectation values of amplitudes of the cavity mode operators $\langle b_\xi^\dagger b_\zeta\rangle$, the equations of motion for corresponding amplitude correlation functions $\delta(b_\xi^\dagger b_\zeta) = \langle b_\xi^\dagger b_\zeta\rangle - \langle b_\xi^\dagger\rangle\langle b_\zeta\rangle$ are used. Then, to achieve a consistent classification and inclusion of correlations up to a certain order the truncation of the equations for correlation functions rather than for expectation values is performed.

In particular, in the case of a system without coherent external excitation $\langle b_\xi^{(\dagger)}\rangle = 0$ and $\langle c_j^\dagger v_{j'}\rangle = 0$ hold. The amplitude correlation functions of the mode operators can be given by

$$\frac{d}{dt}\delta(b_\xi^\dagger b_\zeta) = -(\kappa_\xi + \kappa_\zeta)\delta(b_\xi^\dagger b_\zeta) + \sum_{j,p}\left(g_{\xi j}\delta(c_j^\dagger v_j b_\xi) + g_{\xi j}\delta(v_j^\dagger c_j b_\zeta^\dagger)\right), \tag{4.2}$$

where κ_ξ is the loss rate of the ξth cavity mode and $p = 1\ldots N$, with N being the total number of QDs. Note, that both cavity-mode amplitude correlation functions $\delta(b_\xi^\dagger b_\zeta)$ and the coupled photon-assisted polarization amplitude correlations $\delta(v_j^\dagger c_j b_\xi^\dagger)$ and $\delta(c_j^\dagger v_j b_\zeta)$ are classified as doublet terms $\mathcal{B} + \mathcal{F}/2 = 2$ in the cluster expansion scheme, i.e., they correspond to an excitation of two electrons (four carrier operators). The equation of motion for the photon-assisted polarization amplitude correlation read [see also Eq. (A.1) in Appendix A]:

$$\begin{aligned}\frac{d}{dt}\delta(v_j^\dagger c_j b_\xi^\dagger) = &-i(\Delta_{\xi j} - i\kappa_\xi - i\Gamma)\delta(v_j^\dagger c_j b_\xi^\dagger) + g_{\xi j}\delta(c_j^\dagger c_j)(1 - \delta(v_j^\dagger v_j)) \\ &+ \sum_{\xi'}\Big[g_{\xi' j}\delta(b_{\xi'}^\dagger b_\xi)(\delta(c_j^\dagger c_j) - \delta(v_j^\dagger v_j)) + g_{\xi' j}\delta(c_j^\dagger c_j b_{\xi'}^\dagger b_\xi) - g_{\xi' j}\delta(v_j^\dagger v_j b_{\xi'}^\dagger b_\xi)\Big],\end{aligned} \tag{4.3}$$

where $\Delta_{\xi j} = \varepsilon_j^c - \varepsilon_j^v - \hbar\omega_\xi$ is the detuning of the ξth cavity-mode from the QD transition and Γ is a phenomenological dephasing parameter describing spectral line broadening. In the case of a bimodal cavity only the cavity modes with indices $\xi = 1, 2$ are nearly resonantly coupled to the QDs. Whereas the modes with $\xi \neq 1, 2$ are not within the gain spectrum of the QD ensemble or have low Q-value. Since the population of the non-lasing modes $\langle b_\xi^\dagger b_\xi\rangle$ and the cross-correlation functions $\langle b_\xi^\dagger b_1\rangle$ and $\langle b_\xi^\dagger b_2\rangle$ with $\xi \neq 1, 2$ remain negligibly small, the third terms on the right-hand side of Eq. (4.3) for $\xi \neq 1, 2$ can be effectively set equal to zero. Thus, Eq. (4.3) for $\xi \neq 1, 2$ can be solved in the adiabatic limit yielding a time constant τ_{nl} that describes the spontaneous emission into non-lasing modes according to the Weisskopf-Wigner theory. The spontaneous emission of QDs into non-lasing modes leading to a loss of excitation is described by a β-factor defined as the ratio of the spontaneous emission rate into the lasing modes $1/\tau_l$ and the total spontaneous

emission rate enhanced by the Purcell effect $1/\tau_{sp}$:

$$\beta = \frac{\tau_l^{-1}}{\tau_{sp}^{-1}} = \frac{\tau_l^{-1}}{\tau_l^{-1} + \tau_{nl}^{-1}}. \tag{4.4}$$

The dynamics of carrier population of the electrons in the s-shell is given by

$$\frac{d}{dt}\delta(c_s^\dagger c_s) = -\sum_\xi \mathrm{Re}(g_{\xi q}\delta(c_s^\dagger v_s b_\xi)) + \delta(c_p^\dagger c_p)(1-\delta(c_s^\dagger c_s))\tau_c^{-1} - \delta(c_s^\dagger c_s)(1-\delta(v_s^\dagger v_s))\tau_{nl}^{-1}. \tag{4.5}$$

Here, the first term on the right-hand side originates from the interaction with the cavity-modes, the second term describes the relaxation of carriers from the p- to the s-shell with a relaxation timescale τ_c and the term represents the loss of excitation into the non-lasing modes.

Further, we assume, that the p-shell carriers are generated at a constant pump rate p. Then, like Eq. (4.5), the EoM for the carrier population of the electrons in the p-shell reads:

$$\frac{d}{dt}\delta(c_p^\dagger c_p) = p(\delta(v_p^\dagger v_p) - \delta(c_p^\dagger c_p)) - \delta(c_p^\dagger c_p)(1-\delta(c_s^\dagger c_s))\tau_c^{-1} - \delta(c_p^\dagger c_p)(1-\delta(v_p^\dagger v_p))\tau_{sp}^{-1}, \tag{4.6}$$

where the last term on the right-hand side describes spontaneous recombination of p-shell carriers. The corresponding equations for valence band carriers are relegated into Appendix A.

The form of the expression for the intensity correlation functions suggests (see Eq. (4.1)) that to exploit the statistical properties of the light emission using intensity correlations, a consistent treatment within the cluster expansion up to the quadruplet order is required. The equations of motion for cavity-mode intensity correlations read:

$$\begin{aligned}\frac{d}{dt}\delta(b_\xi^\dagger b_{\xi'}^\dagger b_\zeta b_{\zeta'}) &= -(\kappa_\xi + \kappa_{\xi'} + \kappa_\zeta + \kappa_{\zeta'})\delta(b_\xi^\dagger b_{\xi'}^\dagger b_\zeta b_{\zeta'}) \\ &+ \sum_j \Big(g_{\xi j}\delta(c_j^\dagger v_j b_{\xi'}^\dagger b_\zeta b_{\zeta'}) + g_{\xi' j}\delta(c_j^\dagger v_j b_\xi^\dagger b_\zeta b_{\zeta'}) + g_{\zeta j}\delta(v_j^\dagger c_j b_\xi^\dagger b_{\xi'}^\dagger b_{\zeta'}) + g_{\zeta' j}\delta(v_j^\dagger c_j b_\xi^\dagger b_{\xi'}^\dagger b_\zeta) \Big).\end{aligned} \tag{4.7}$$

The equations of motion for further correlation functions of the quadruplet order, which include correlation between the photon-assisted polarization and the photon number, can be found in Appendix A (see Eqs. (A.4)–(A.7)).

4.4 Analysis of intensity fluctuations

As described above, the quadruplet order of the cluster expansion leads to a system of coupled equations (see Eqs. (4.2)–(4.3), (4.5)–(4.6), (4.7) together with Eqs. (A.1)–(A.7)). The system of differential equations describes the dynamics of various correlations between carriers and cavity modes.The method makes it possible to obtain

both amplitude and intensity correlation functions of the cavity emission modes including the effects of the carrier-photon correlations and the many-body interaction. In the ensuing section the numerical analysis of the time evolution of the emission

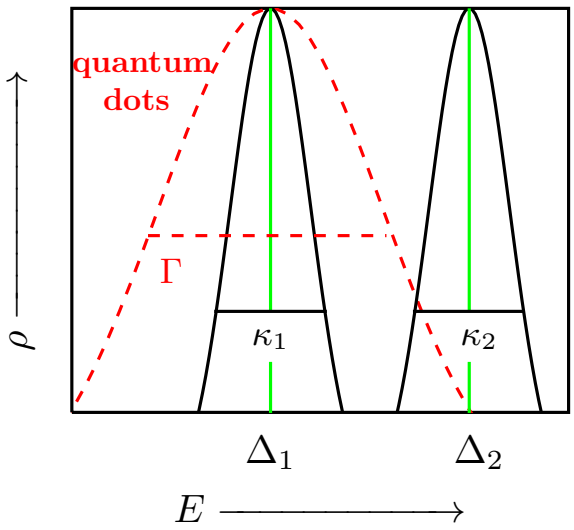

Figure 4.4: Sketch of the single-particle density of states in the theoretical description. The QDs have the inhomogeneous line broadening Γ that has an overlap with the linewidth κ_1 and κ_2 of the modes. The detuning of the modes to the QDs is measured with Δ_1 or respectively Δ_2.

correlation functions are presented. To relate our theory to the experimental results we estimate the number of QDs with effective gain contribution by starting with the initial density of present QDs and excluding the ones with negligible spectral and spatial overlap. Thus, we assume N identical QDs with an effective inhomogeneous line broadening Γ that has an overlap with the linewidth κ_1 and κ_2 of the modes (see Fig. 4.4). Further, we consider continuous carrier generation in the p-shell at a constant pump rate p as an excitation process.

To obtain a valid comparison with the experimental results we simulate the coupled system using numerical integration routines with a realistic set of parameters $\beta = 0.2$, $\kappa_1 = 0.03\,[1/\text{ps}]$, $\kappa_2 = 0.0318\,[1/\text{ps}]$, $\Gamma = 2.06\,[1/\text{ps}]$, $\tau_{sp} = 50\,[\text{ps}]$, $\tau_c = 1\,[\text{ps}]$ and $\tau_v = 0.5\,[\text{ps}]$. The number of carriers within the frequency region of interest is estimated from the total density of QDs to be $N = 40$. For the assumed $\beta = 0.2$ the carrier recombination is determined by the stimulated emission into the lasing modes 1 and 2 with a characteristic time scale $\tau_l = \tau_{sp}/\beta$ and into the non-lasing modes with a characteristic time scale that can be found from Eq. (4.4) for the given set of parameters. Further, we assume that the cavity mode 1 is in exact resonance with the QD transition ($\Delta_{11} = \Delta_{12} = \Delta_1 = 0$) and the mode 2 is detuned with $\Delta_{21} = \Delta_{22} = \Delta_2 = 0.2\,[1/\text{ps}]$. In Fig. 4.5 we present the simulation results for intensity functions for the modes $n_\xi = \langle b_\xi^\dagger b_\xi \rangle$, $\xi = 1, 2$, autocorrelation functions and crosscorrelation as a function of the pump power. Figure 4.5(a) reveals, that whereas the mode 1 shows a drastic increase of emission intensity, the intensity of the emission mode 2 reaches a maximum and then slowly decreases with increasing pump power in good agreement with the experimental data depicted in Fig. 4.3(a).

The calculations further show, that, again in agreement with the experimental data in Fig. 4.3(c), the dependencies of the autocorrelation functions for the cavity modes 1 and 2 on the pump power exhibit dramatically different behavior. As shown in Fig. 4.5(b) for low values of pump power, the autocorrelation function is equal to 2 which is characteristic for the statistics of thermal light. For higher rates of the pump power, the autocorrelation function of the mode 1 drops close to the value 1 indicating the emission of coherent laser light. In contrast, the autocorrelation function of mode 2 slightly decreases at first with increasing pump powers, but for larger values of the pump power, it increases and reaches values well above 2, which agrees with the behavior of the autocorrelation function detected in the experiment (see Fig. 4.3(c). The autocorrelation function below the threshold could not be measured because of the limited temporal resolution of the HBT configuration [Ulrich et al., 2007]). The gain competition behavior between the modes can be approved by plotting the crosscorrelation function (see Fig. 4.5(c)), that decreases to the values smaller than unity at the power pump values for which the lasing behavior of the mode 1 is observed (also, compare to Fig. 4.3(d)). Further, numerical calculations demonstrate that the observed effect is independent of the modification of the spontaneous emission rate due to the many-body interaction [Foerster, 2012]. One important parameter proves to be the detuning between the two modes as shown in Fig. 4.6. With zero detuning, there is no difference between the two modes and the system behaves as a single-mode laser. Increasing the detuning shows measurable effects if the detuning is bigger than the linewidth of the modes $\Delta_2 > \kappa$. This leads to higher and finally superthermal values of the autocorrelation function. If however, the detuning is increased much further the role of the detuned mode becomes negligible (not shown).

Note that the discrepancy of the experimental and theoretical results, i.e. the kink above the threshold for the autocorrelation function of mode 2 (Figs. 4.3(c) and 4.5(b), correspondingly) and the crosscorrelation function (Figs. 4.3(d) and 4.5(c), correspondingly) at the higher pump powers appears to be crosstalk between the modes, but can later be explained due to NMC (see Sec. 4.8).

The numerical simulation of the cluster expansion truncation scheme of the quadruplet order($\Delta^{\mathcal{B}+\mathcal{F}/2}_{\delta(4)}$) can be approved by plotting the emission mode autocorrelation functions for higher order of truncation $\Delta^{\mathcal{B}+\mathcal{F}/2}_{\delta(6\ldots10)}$ (not shown), which demonstrates qualitatively the same behavior of the functions independent of the order of truncation. It is important to note that since the framework of the microscopic semiconductor theory presented in this section is based on the truncation of the hierarchy of equations for correlation functions, the numerical results are valid in the regime when higher order correlations remain small. As it can be seen from the numerical evaluation of the truncated equations, this is not the case for pump power rates exceeding $2 \times 10^{-1}\,[1/\mathrm{ps}]$, where the correlation functions strongly increase. Furthermore in [Leymann et al., 2013c] we show that the photon statistics becomes a composition of a thermal and a coherent photon statistic and therefore the cluster expansion is not the ideal approximation method.

In conclusion, the system consisting of a single low-density layer of QDs and two spectrally split but overlapping modes with nearly equal Q-factors, induced from the double degenerate fundamental mode by slight cross-section asymmetry of the pillar,

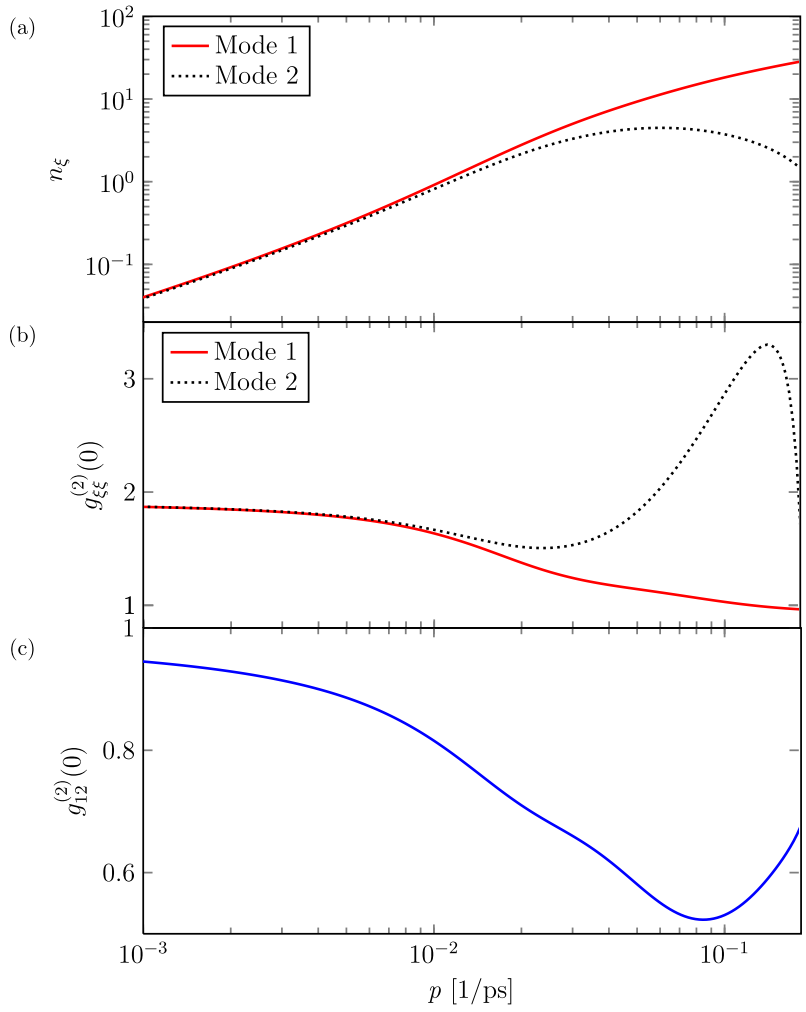

Figure 4.5: Laser characteristics calculated with the semiconductor model. (a) Intensity for the modes 1 and 2 as a function of the pump power in a log-log plot. (b) Autocorrelation functions of the two modes. (c) Crosscorrelation between the modes 1 and 2.

represents a viable platform for the study of the coupling of two cavity modes in the presence of a common gain medium. The polarization resolved measurements of the statistical properties of the emitted light reveal that the two competing modes display completely different features. One of the modes (mode 1) demonstrates typical statistical behavior of a laser mode, namely the mode intensity displays the usual $\mathcal{S}$-shaped input-output characteristic, and the autocorrelation function at zero-time delay indicates the transition from spontaneous to stimulated emission for increasing pump rates. The measurements of the input-output characteristic of mode 2 indicate the threshold behavior, but for further increasing pump rates the intensity saturates and even decreases, as the result of the competition of the two modes induced by the common gain material. Moreover, the autocorrelation function at zero-time delay of mode 2 at certain pump rates higher than the threshold values exhibits superthermal intensity fluctuation.

The theory allows to obtain the emission statistics of the carrier-photon system

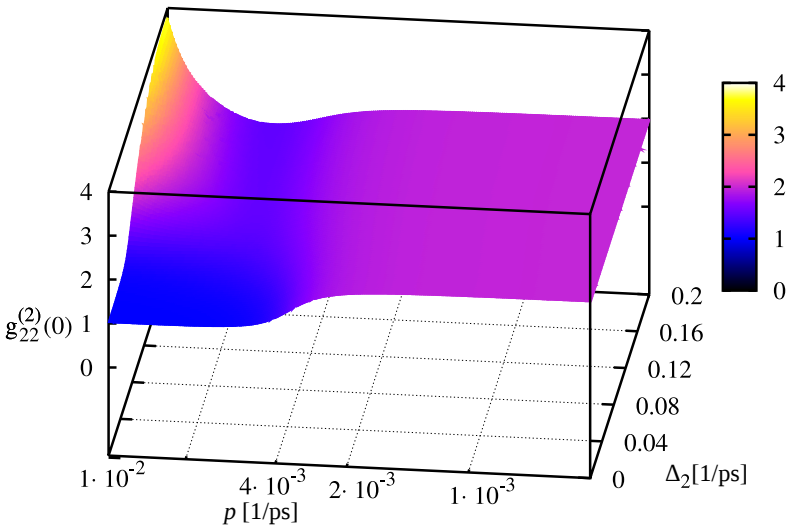

Figure 4.6: Calculations of the autocorrelation function $g_{22}^{(2)}(0)$ versus pumping power and detuning Δ_2 of the second mode (first mode is in resonance with the QDs). With zero detuning there, is no difference between the two modes and the system behaves as a single-mode laser. Increasing the detuning leads to higher and finally superthermal values of $g_{22}^{(2)}(0)$.

in the bimodal cavity considering the many-body effects. Importantly, within our approach the effects related to the coupling of the two modes of the bimodal cavity, induced by the interaction with the common QD carriers are consistently included on the microscopic level. The solution of the equations of motion for correlation functions using the cluster expansion scheme reveals, that indeed the autocorrelation function of the mode 2 for the pump rates larger than the threshold rate reaches values well above $g^{(2)}(0) = 2$, that would correspond to the thermal state of light. The decrease of the crosscorrelation function of the two modes below unity indicates anti-correlated behavior of the mode coupling at these pump rates. In fact, this effect can be explained by random intensity switching between the two modes, which has negligible influence on the photon statistics of the lasing mode, but strongly affects the mode 2 for which the relative strength of fluctuations is larger [Redlich et al., 2016; Lett, 1986]. It is worth to mention, that in the case of macroscopic two-mode ring lasers [Singh and Mandel, 1979] large intensity fluctuations have been also found in the statistics of the more lossy mode, as the result of the mode competition with the favored mode and emission switching of the common atomic ensemble.

4.5 Occurrence of normal-mode coupling

The last section has shown that the experimental results, e.g. the intensities, the autocorrelation and crosscorrelation functions can be reproduced and explained with the single-time semiconductor theory. In Sec. 4.2 the question was raised why both modes show laser typical small linewidths, which is not intuitively clear since the second mode is highly fluctuating ($g_{22}^{(2)}(0) > 2$). Therefore, we extend the single-time theory to multi-time correlation functions, which creates a connection to NMC. In

this section, we report the current status of research on strong coupling and NMC. We set this subject into context with bimodal microcavities before we explain the details of the multi-time semiconductor theory in the following section.

The study of cavity quantum electrodynamics (cQED) in the strong coupling regime between atom-like emitters and the confined light field of microcavities has been a subject of considerable attention. In the traditional cQED, low-mode volume resonators are used to enhance the coupling rate g between a single emitter and the field in comparison to the system damping rates. Prominent realizations of the strong coupling include experimental demonstrations of reversible exchange of excitation between a single emitter with the field from both atomic [Brune et al., 1996; McKeever et al., 2003; Nußmann et al., 2005] and solid-state [Reithmaier et al., 2004; Yoshie et al., 2004] systems. A typical evidence of the strong coupling regime represents splitting of the two degenerate modes, i.e. normal-mode splitting, that is a consequence of NMC e.g. between emitter polarization mode and field mode leading to a doublet cavity transmission spectrum [Shore and Knight, 1993]. In addition, NMC occurs i.a. in exciton-photon and phonon-photon interactions [Weisbuch et al., 1992] and optomechanical phenomena [Kippenberg and Vahala, 2008], where the cavity field couples to a mechanical mode [Dobrindt et al., 2008].

In view of the variety of implications of the regime of coherent coupling (see, e. g., [Monroe, 2002]), a different approach to achieve strong coupling has also attracted much attention. Instead of reducing the cavity mode-volume to achieve large g, the number of emitters N interacting with the field can be increased leading to the collective strong coupling regime, where the coupling rate scales as $\sqrt{N}g$ [Tavis and Cummings, 1968; Andreani et al., 1999]. Various experimental observations of the cavity mode spectra proportional to $\sqrt{N}g$ due to the collective coherent coupling with two [Reitzenstein et al., 2006; Albert et al., 2013] or multiple [Reitzenstein et al., 2006; Albert et al., 2013] emitters have been experimentally observed, including the case of multimode cavity [Wickenbrock et al., 2013]. In solid-state systems, the coherent coupling between a cavity mode and an ensemble of emitters has been achieved in the classical regime with semiconductor quantum wells [Weisbuch et al., 1992; Khitrova, 1999]. However, in the quantum regime the significant inhomogeneous broadening of emission from self-assembled QDs has so far hindered the observation of collective coherent coupling for semiconductor based quantum emitters.

In many different situations, (see e.g. Refs. [Brune et al., 1996; McKeever et al., 2003; Nußmann et al., 2005; Reithmaier et al., 2004; Yoshie et al., 2004; Shore and Knight, 1993; Kippenberg and Vahala, 2008; Dobrindt et al., 2008; Monroe, 2002; Tavis and Cummings, 1968; Andreani et al., 1999; Reitzenstein et al., 2006; Albert et al., 2013; Raizen et al., 1989; Tuchman et al., 2006; Wickenbrock et al., 2013; Weisbuch et al., 1992; Khitrova, 1999]), per convention coherent coupling of two (nearly degenerate) modes is commonly explained by studying the eigenvalues of the system,

$$\Lambda_{\pm} = \frac{\omega_1 + \omega_2}{2} - i\frac{\gamma_1 + \gamma_2}{4} \pm \{[(\omega_1 - \omega_2)/2 - i(\gamma_1 - \gamma_2)/4]^2 + Ng^2\}^{1/2}, \qquad (4.8)$$

where $\omega_{1,2}$ and $\gamma_{1,2}$ are the frequencies and decay rates of the modes, correspondingly. Analysis of this expression reveals that in the resonant case ($\omega_1 = \omega_2$) for

$\sqrt{N}g < |\gamma_1 - \gamma_2|/4$ the square root term is fully imaginary and modifies the decay rates of the modes. Further, for $\sqrt{N}g > |\gamma_1 - \gamma_2|/4$ it becomes real and the frequencies exhibit splitting attributed to NMC. Coherent coupling is also relevant to laser physics for achieving the regime of bistable lasing of the two-mode lasers [Meystre and Murray, 1999; Siegman, 1986]. In particular, in the case of large pump rates when strong coupling regime of emitter-field interaction is achieved and the Rabi frequency is larger than mode separation mode locking has been observed [Hillman et al., 1984; Wang et al., 2007]. Otherwise, bimodal cavities are investigated in the context of single-photon generation with whispering-gallery mode resonators [Dayan et al., 2008; Majumdar et al., 2012], where an atom strongly interacts with two cavity modes, or in QDs to control the properties of the photon on-the-fly and all-optically with a classical laser field [Heinze et al., 2015].

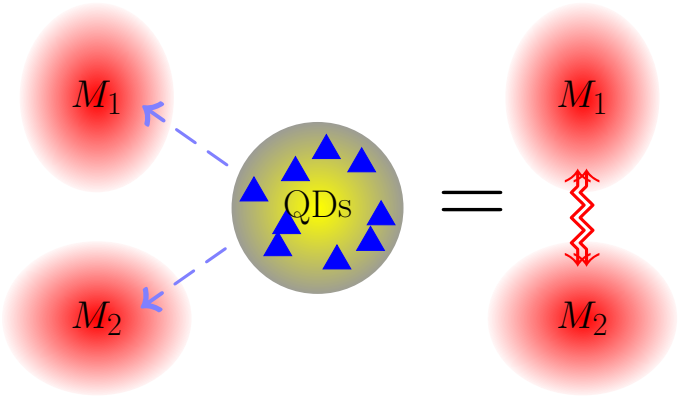

Figure 4.7: Illustration of the interaction of the modes M_1 and M_2 (cavity modes) of a passive microcavity with a mesoscopic number of QDs induces unconventional coherent coupling between these modes.

Here, we show that interaction (see Fig. 4.7) of the modes of a passive bimodal microcavity (cavity modes) with a mesoscopic number of quantum emitters induces unconventional coupling between these modes in the lasing regime. In contrast to the conventional NMC described above, here, in the case of the near-resonant cavity modes the eigenmodes of the total active system (eigenmodes) exhibit frequency locking, and the effective coupling rate with the emitters $\sqrt{N}g$ induces splitting of the linewidths of the eigenmodes. Further, for sufficiently large spectral splitting between the cavity modes, the incoherent coupling between the modes leads to a mixing of the "bare" cavity mode frequencies in the emission spectrum. We report below experimental observation of this mode mixing for bimodal micropillar lasers. Moreover, the theoretical study shows, that in the case of incoherent coupling and approximately equal mode-QD coupling rates the eigenmode linewidths demonstrate locking, leading to almost equal values of the coherence times of the cavity mode emission. This intriguing and unexpected scenario has been observed for bimodal microlasers in Sec. 4.4, where the inferior mode which exhibits large superthermal intensity fluctuations, indeed has a coherence time of the same order of magnitude as the dominant lasing mode.

4.6 Theory of multi-time correlation functions

The microscopic semiconductor model and the derivation of single time EoM has already been discussed in Sec. 4.3. The general approach to derive multi-time EoM in terms of the expectation value based cluster expansion can be found in Ch. 2.3.4. For the purposes of this section the lowest order approximation $\Delta_{\delta(2)}^{\mathcal{B}+\mathcal{F}/2}$ is best suited, since it allows us to trace the problem back on an eigenvalue equation that can be compared to Eq. (4.8).

The coherent features of the output radiation are described by the (normalized) first-order correlation function Eq. 1.40. This function is generalized to the case of two modes by

$$g_{\xi}^{(1)}(t,\tau) = \frac{G_{\xi\xi}^{(1)}(t,\tau)}{\langle b_{\xi}^{\dagger}(t) b_{\xi}(t)\rangle},\ \xi = 1,2, \tag{4.9}$$

with $G_{\xi\xi'}^{(1)}(t,\tau) = \langle b_{\xi}^{\dagger}(t+\tau) b_{\xi'}(t)\rangle$. The coherence times and the frequency spectra are given, respectively, by

$$\tau_{\xi}^{c} = 2\int_{0}^{\infty} \mathrm{d}\tau |g_{\xi}^{(1)}(\tau)|^2, \tag{4.10}$$

$$S_{\xi}(\omega) = 2\mathrm{Re}\int_{0}^{\infty} \mathrm{d}\tau g_{\xi}^{(1)}(\tau) e^{-2\pi i \tau \omega}. \tag{4.11}$$

We assume continuous wave excitation and that two-time quantities as the correlation function $g_{\xi}^{(1)}(t,\tau)$ are t-time independent in the steady-state regime for large enough t-times. According to Ch. 2.3.4 the two-time evolution problem can be separated into two single-time problems. Then, the equations of motion with respect to the delay time τ can be solved with initial values given by the stationary steady-state result of the t-time problem [Wiersig, 2010]. The Heisenberg equations of motion for expectation values of the quantities of interest lead to a hierarchy problem which can be treated by the cluster expansion (see Ch. 2 for details).

Further, assuming carrier generation in the p-shell at a fixed rate we derive a system of Heisenberg equations of motion and introduce phenomenological dissipative terms, where both pump and dissipative processes are of Lindblad form [Gardiner and Zoller, 2001]. To obtain the dynamical equations of the first-order coherence the cluster expansion up to doublet level $\Delta_{\delta(2)}^{\mathcal{B}+\mathcal{F}/2}$ is required, which implies the semi-classical factorization (in the following we omit the dependence on the time t, as $b_{\xi}(\tau) \equiv b_{\xi}(t,\tau)$, $b_{\xi} \equiv b_{\xi}(t,0)$ etc.)

$$\langle c_{j}^{\dagger}(\tau) c_{j}(\tau) b_{\xi}^{\dagger} b_{\xi}(\tau)\rangle \approx \langle c_{j}^{\dagger}(\tau) c_{j}(\tau)\rangle \langle b_{\xi}^{\dagger} b_{\xi}(\tau)\rangle, \tag{4.12}$$

where $\langle c_{j}^{\dagger}(\tau) c_{j}(\tau)\rangle$ in the stationary regime is τ-time-independent. Thus, assuming identical QDs with equal transition energies and coupling rates $g_{\xi} \equiv g_{\xi j}$, we obtain the closed system of linear differential equations for the correlation functions $G_{\xi\zeta} \equiv G_{\xi\zeta}^{(1)}(\tau)$ and $P_{\xi}(\tau) \equiv P_{\xi j}(\tau) = \langle c_{j}^{\dagger}(\tau) v_{j}(\tau) b_{\xi}\rangle$ in the rotating-wave approxima-

tion and in the frame rotating at $\varepsilon_j^c - \varepsilon_j^v$

$$\frac{\mathrm{d}}{\mathrm{d}\tau}P_\xi(\tau) = -\Gamma P_\xi(\tau) + Ig_1 G_{1\xi}(\tau) + Ig_2 G_{2\xi}(\tau), \tag{4.13}$$

$$\frac{\mathrm{d}}{\mathrm{d}\tau}G_{1\xi}(\tau) = (i\Delta_1 - \tfrac{1}{2}\kappa_1)G_{1\xi}(\tau) + Ng_1 P_\xi(\tau), \tag{4.14}$$

$$\frac{\mathrm{d}}{\mathrm{d}\tau}G_{2\xi}(\tau) = (i\Delta_2 - \tfrac{1}{2}\kappa_2)G_{2\xi}(\tau) + Ng_2 P_\xi(\tau), \tag{4.15}$$

where $\Delta_\xi \equiv \Delta_{\xi j} = \varepsilon_j^c - \varepsilon_j^v - \hbar\omega_\xi$ is the detuning of the cavity modes from the QD transition, and κ_1, κ_2 describe cavity mode losses. The inhomogeneous broadening is approximated by the spectral line broadening rate Γ in Eq. (4.13). The excitation of emitters with given pump rate is encoded into the steady-state inversion per QD, $I \equiv I_j(t) = \langle c_j^\dagger c_j\rangle - \langle v_j^\dagger v_j\rangle$, that represents an important pump rate-dependent parameter for the τ-dynamics.

4.7 Normal-mode coupling in bimodal lasers

The system of six equations above consists of two independent subsystems with $\xi = 1, 2$. Autocorrelation functions of two cavity modes $G^{(1)}_{\xi\xi}(\tau)$ are coupled to each other indirectly, namely, through $P_\xi(\tau)$ representing the common gain medium. To provide a simple understanding of the coupling of the two cavity modes, we use an approximation of fast relaxation of $P_\xi(\tau)$ compared to the time-scale of the dynamics of $G_{\xi\zeta}(\tau)$, typically valid for semiconductor systems [Alferov, 2001]. Then, we formally insert $(\mathrm{d}/\mathrm{d}\tau)P_\xi(\tau) = 0$ into Eq. (4.13) and reduce Eqs. (4.13)–(4.15) to

$$\frac{\mathrm{d}}{\mathrm{d}\tau}\begin{pmatrix} G_{1\xi} \\ G_{2\xi}\end{pmatrix} = i\begin{pmatrix} \Delta_1 + i\tilde{\kappa}_1/2 & -iNIg_1g_2/\Gamma \\ -iNIg_1g_2/\Gamma & \Delta_2 + i\tilde{\kappa}_2/2\end{pmatrix}\begin{pmatrix} G_{1\xi} \\ G_{2\xi}\end{pmatrix}, \tag{4.16}$$

which represents two 2×2 identical matrices and characterize the coupling of the two cavity modes. The eigenvalues of the matrix above read

$$\lambda_\pm = \frac{\Delta_1 + \Delta_2}{2} + i\frac{\tilde{\kappa}_1 + \tilde{\kappa}_2}{4} \pm \{[(\Delta_1 - \Delta_2)/2 + i(\tilde{\kappa}_1 - \tilde{\kappa}_2)/4]^2 - (NIg_1g_2/\Gamma)^2\}^{1/2}, \tag{4.17}$$

where from the notation $\tilde{\kappa}_\xi = \kappa_\xi - 2NIg_\xi^2/\Gamma$ follows, that increasing NIg_ξ^2/Γ effectively reduces the linewidths. The inspection of Eq. (4.17) reveals that the dependence of the eigenvalues on the involved parameters behave quite differently from the case of conventional NMC, Eq. (4.8). For $\Delta_1 = \Delta_2$ and $g_1 = g_2$, the square root term of $\lambda_\pm$ remains imaginary and modifies the peak widths independent on how large the effective coupling $|NIg_1g_2/\Gamma|$ is chosen in comparison with $|\kappa_1 - \kappa_2|$. In the case, when $\kappa_1 = \kappa_2$ and $g_1 = g_2$, the square root term leads to two regimes. For $|NIg_1g_2/\Gamma| < |\Delta_1 - \Delta_2|/2$, the regime of incoherent coupling, the term is real and modifies the peak positions of the modes. In the regime of coherent coupling, i.e. for $|NIg_1g_2/\Gamma| > |\Delta_1 - \Delta_2|/2$, it becomes imaginary and modifies the peak widths of the modes. Note, this striking behavior is qualitatively opposite from that of conventional NMC. Furthermore, since the effective coupling $|NIg_1g_2/\Gamma|$ is proportional

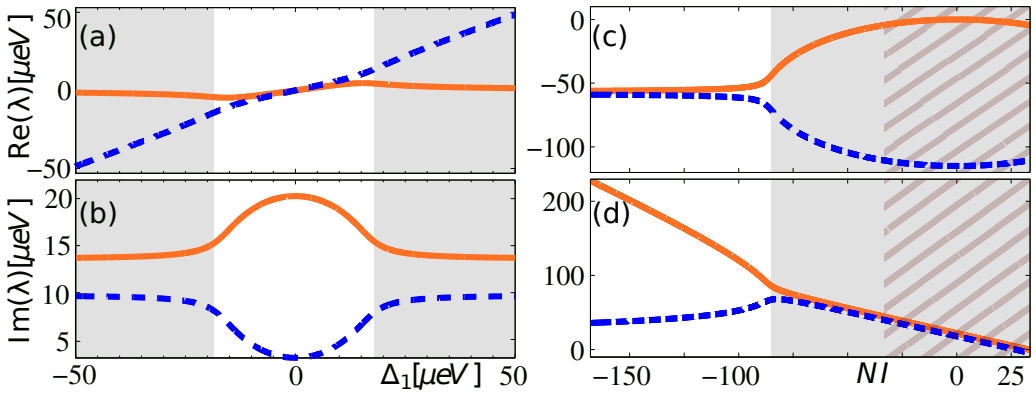

Figure 4.8: Real part of the eigenvalues corresponding to the peak positions (a), (c) and imaginary parts of the eigenvalues corresponding to the peak widths (b), (d) [cf. Eq. (4.17)] vs. Δ_1 for fixed pump strength [(a), (b), $I = 0.3$] and vs. NI [(c), (d), $\Delta_1 = 115$ μeV], $N = 42$, $\kappa_1 = 36$ μeV, $\kappa_2 = 44$ μeV, $\Delta_2 = 0$, $\Gamma = 1.38$ meV, $g_1 = 30.4$ μeV, and $g_2 = 30.3$ μeV. The shaded regions indicate incoherent coupling. The hatched area indicates experimentally accessible NI-range (see Fig. 4.10). The values of κ_ξ and Δ_ξ are measured in the experiment, and the values of N, Γ and g_ξ are estimated in correspondence to the experiment.

to $|I|$, the experimental observation of the coherent regime of collective coupling requires $|I|$ to be close to unity.

To demonstrate the unconventional NMC we plot the real and imaginary parts of the eigenvalues for a coupled bimodal cavity system in Fig. 4.8. The dependence on the detuning Δ_1 ($\Delta_2 = 0$) [Figs. 4.8(a) and (b)] reveals that in the near-resonant region where the coherent coupling regime is maintained, the splitting of the imaginary parts of the eigenvalues (peak widths) is observed. For increasing detuning between the cavity modes, in the incoherent coupling regime, the eigenvalues demonstrate splitting in the real parts (peak positions) and locking of the peaks widths. To illustrate the dependence on the effective coupling rate the eigenvalues are presented as functions of NI in Figs. 4.8(c,d). In the regime of incoherent coupling, for small effective coupling rate (small $N|I|$), the splitting of the peak positions is observed. In the regime of coherent coupling the splitting of the peak widths increases for increasing effective coupling rate. Whereas in the case of the conventional coherent NMC, Eq. (4.8), the splitting of the mode resonances increases for increasing N [Thompson et al., 1992].

4.8 Cavity Mode Spectra

Importantly, above discussed effects can be deduced starting with the more general Eqs. (4.13)–(4.15). In the following we use Eqs. (4.13)–(4.15) to obtain τ-dependent expressions for the auto-correlation functions. The initial values of quantities $P_\xi(\tau)$, $G_{\zeta\xi}(\tau)$ are taken as the stationary solutions of t-time-dependent problem. Figure 4.9 reveals that in the regime of incoherent coupling the coherence times of the dominant and inferior modes, which correspond to the decay rates of $|g_1^{(1)}(\tau)|$ and $|g_2^{(1)}(\tau)|$,

respectively, are of the same order of magnitude. This counter-intuitive behavior, which has been earlier experimentally observed (see Fig. 4.3(b)), is particularly interesting considering that the inferior mode features large superthermal intensity fluctuations with $g^{(2)}(0) \approx 3$ (Fig. 4.3(f)). The spectra of both modes (Fig. 4.9, inset) exhibit a two-peak structure according to the eigenvalues in Eq. (4.17). Indeed, for the chosen parameters $NI = 27.3$, which corresponds to the incoherent coupling, Figs. 4.8(c, d) reveal splitting of peak positions and locking of the widths. Obviously, emission in the basis of the two cavity modes carries both "bare" frequencies of the passive cavity modes due to NMC via the common gain medium. The emission peak positions and widths are established by the real and imaginary parts of the eigenvalues $\lambda_{\pm}$, since every mode carries both basis eigenvalue vectors. The mode coupling is also associated with the oscillations of $|g_{\xi}^{(1)}(\tau)|$ (easy to see in Fig. 4.9 for $|g_2^{(1)}(\tau)|$ but holds true for $|g_1^{(1)}(\tau)|$). The oscillation amplitudes are attributed to the corresponding frequency spectra peak heights, whereas the oscillation frequency is defined by the peak position difference, which in turn is related to the relative detuning of the cavity modes. Importantly, the oscillations of $|g_{\xi}^{(1)}(\tau)|$ originate from a double-peak feature of two cavity modes and need to be distinguished from those reported by Ates et al. [2007], which arise from the interference of emission in two different polarization directions.

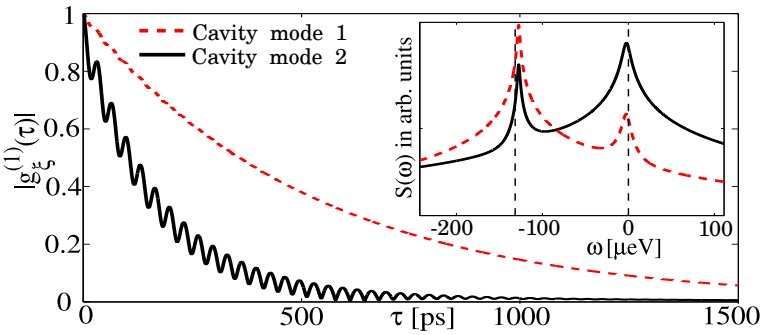

Figure 4.9: Absolute values of the autocorrelation functions and the frequency spectra (inset, semi-log scale) for the emission of the cavity modes for $I = 0.65$, $\Delta_1 = 115$ μeV and estimated cavity-enhanced QD spontaneous emission rate of 20 ns^{-1}. Other parameter values are from Figs. 4.8(c, d). The vertical lines mark the cavity mode frequencies.

For the comparison to the experiment we use a similar setup to the one presented in Sec. 4.2. The micropillar laser has a diameter of 3.6 μm, and the two modes of 0° and 90° polarizations and Q-factors of 10000 and 10800 are split by 115 μeV. The emission has been investigated at low temperature (10-20 K) by a micro-electroluminescence (μEL) setup (spectral resolution, 20 μeV). A linear polarizer in combination with a $\lambda/4$-wave plate is installed to perform polarization-resolved measurements.

The input-output dependence of the emission in 0° and 90° detection angle is depicted in Fig. 4.10(c). The emission mode in 0° polarization shows a threshold current of about $I_{th} = 4\mu$A. The smooth transition at threshold and the $\mathcal{S}$-shaped input-output characteristics indicates the high-β lasing with $\beta \approx 0.2$(see also

Sec. 4.4). A similar behavior is observed for emission in 90° polarization up to $I_{inj} \cong 1.5 I_{th}$. At higher injection currents saturation and even a decrease of the output intensity is observed. This anticorrelation between emission of the dominant mode in 0° and the inferior mode in 90° polarization is explained by means of the microscopic semiconductor model in terms of gain competition (see Sec. 4.4). Moreover, the model allows us to determine the inversion per pump rate which changes from -0.8 to 0.8 for the used parameter values (see Fig. 4.10(c)). The corresponding NI range is indicated in Fig. 4.8(c,d) as hatched area.

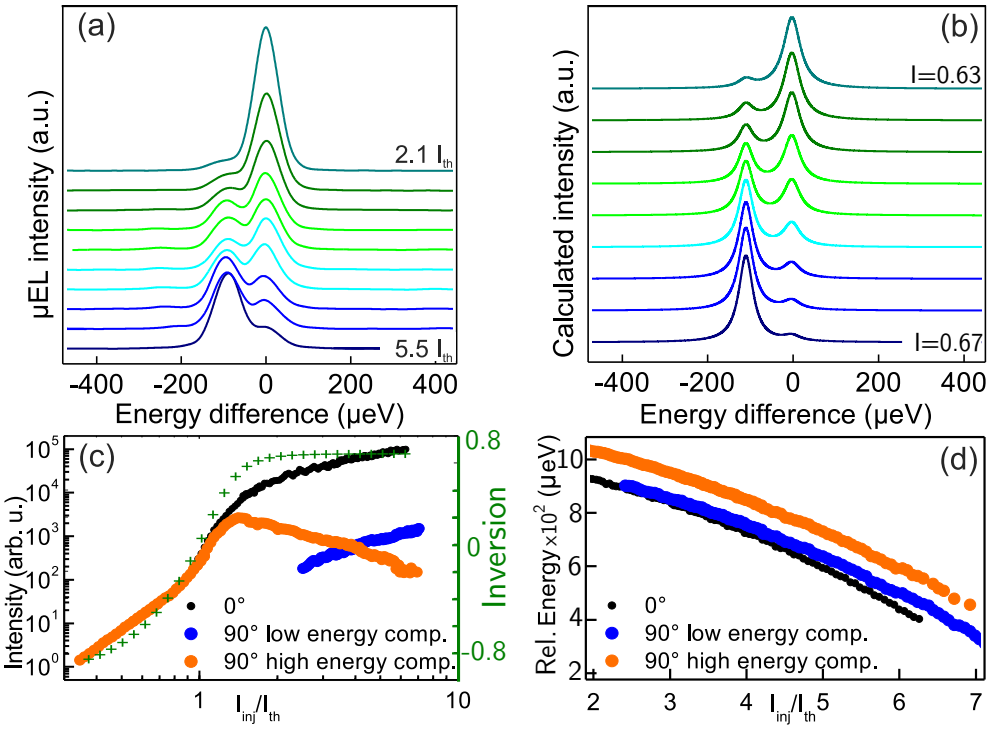

Figure 4.10: (a) Injection current-dependent μEL emission spectra in 90° polarization for $2.1 \leq I_{inj}/I_{th} \leq 5.5$, plotted relative to the high energy peak values to compensate for an injection current-dependent shift of the emission energy [cf. (d)]. (b) Calculated frequency spectrum in 90° polarization for inversion values $0.63 \leq I \leq 0.67$. Parameter values are the same as in Fig. 4.9. (c) Calculated inversion (green, crosses) vs. injection current and integrated μEL intensity for 0° and 90° polarizations. (d) Emission energy (relative to the reference point 1.366 eV) of the 0°-component and the two-mode features in 90° detection vs. injection current.

Interestingly, the intensity of emission in 90° polarization increases again for $I_{inj} \gtrsim 4 I_{th}$. To analyze this feature we study emission spectra for different injection currents. While in 0° orientation emission a single peak is observed (not shown), for the 90° component at injection currents exceeding about $1.5 I_{th}$ a transition of a single emission peak into a doublet occurs (see Fig. 4.10(a)), where the intensity of the low-energy component rises with increasing current and dominates for $I_{inj} > 5 I_{th}$. This double-peak feature of the 90° orientation emission and its peculiar current dependence is in very good agreement with the calculated emission spectra presented

in Fig. 4.10(b) for incoherent collective coupling [1]. Indeed, for the range of the chosen parameters $NI \approx 26 \ldots 28$ according to Figs. 4.8(c, d) corresponds to the region of incoherent coupling.

In Fig. 4.10(d) mode energies of 0° and 90° polarizations vs. injection current are plotted. At low injection currents the single-peak emission in both polarization directions correspond to the "bare" frequencies of the cavity modes. Moreover, the low-energy component of the 90° emission for low injection currents coincides spectrally with emission from the 0° emission, but at high excitation currents it approaches the energy of the high-energy peak in 90° orientation. This clearly shows that this emission does not originate from possible cross-talk between 0° and 90° components, but is in accordance with the theoretical prediction in Fig. 4.8(c), namely that the peak positions approach each other with increasing NI.

4.9 Chapter conclusion

We have investigated laser emission of electrically pumped QDs in a bimodal micropillar cavity with special emphasis to the effects induced by gain competition of the two orthogonally polarized modes.

Starting with the microscopic semiconductor model [Gies et al., 2007] we have developed a framework for the description of the interaction of two cavity modes with the QD gain medium.

Within this theory, we can reproduce and explain the mode competition of bimodal microcavity lasers. The decisive parameters, e.g. detuning and loss rates that enables mode competition and the high autocorrelation function of the losing mode have been analyzed. The theory also provides a good understanding of the experimental results and confirms the possibility of having light sources with high intensities and superthermal values of $g^{(2)}(0)$ at the same time. This kind of light sources could be used efficiently in the multi-photon spectroscopy, where more than one photon at a time is needed and samples can easily be damaged by radiation [Denk et al., 1990]. Light sources that have a high probability of emitting multiple photons at the same time could increase the performance enormously as shown in [Jechow et al., 2013].

In a second step, we have demonstrated the existence of collective NMC in bimodal microlasers. In contrast to the conventional case, here, in the coherent coupling regime, the increase of the effective coupling strength produces a splitting of the linewidths instead of the frequencies. In the incoherent coupling regime, increasing effective coupling induces splitting of frequencies and locking of linewidths. The consequence is the double-peak structure of the output spectra of the modes and the large coherence times for both dominant lasing and inferior modes, which has been confirmed experimentally in QD-based bimodal micropillar lasers. The latter offers unique possibilities to study collective coupling, since the stimulated emission of the dominant mode leads to clamping of the carrier density with large inversion ($I \approx 0.8$), while the inferior mode experiences collective coupling mediated

[1] These spectra were convoluted with a Lorentzian to consider the spectral resolution of 20 μeV of the experimental setup.

by multiple inverted emitters. Further interesting effects related to NMC in bimodal lasers in the coherent coupling regime which could be accessed by using micropillar cavities with small mode splitting and larger inversion.

The developed microscopic semiconductor theory of bimodal cavities is well-suited for further investigation of the emission properties for various interaction regimes depending on the cavity mode detuning and decay rates or effects related to the many-body interaction [Fanaei et al., 2016]. Thus, the theory lays the groundwork for investigations of the coupling of the modes in the bimodal cavity by means of interaction with the common gain media.

Chapter 5

Sub- and Superradiance in quantum-dot nanolasers

In this chapter, we present the most advanced laser theory of this thesis. We combine ideas of the expectation value based cluster expansion Ch. (2) with a configuration description of the quantum dots(QDs) [Florian et al., 2013b]. We use this theory to investigate the radiative coupling between emitters in QD nanolasers. For typical systems with tens to hundreds of active emitters, a strong impact of sub- and superradiance on steady-state properties is demonstrated. In a device-relevant parameter regime, it is shown that radiative coupling enhances spontaneous emission such that significantly fewer emitters are required to reach the lasing threshold. The formation of QD-QD correlations can seemingly change the β-factor by an order of magnitude. The results provide insight into a new kind of lasing in a highly efficient regime dominated by cavity quantum electrodynamics (cQED) effects.

Parts of this chapter are published in [Leymann et al., 2015]. The basic theory was developed in discussions between C. Gies, A. Foerster, and H.A.M. Leymann. The details of the theory were mainly worked out by H.A.M. Leymann while the equations of motion were mainly derived and integrated by A. Foerster. All authors of [Leymann et al., 2015] discussed the results.

5.1 Introduction

When the active material compensates photon losses from the cavity, a conventional laser crosses the threshold into coherent emission. In nanolasers, spontaneous emission is strongly enhanced, and the previous criterion must be augmented such that stimulated and spontaneous emission must compensate the cavity losses. The enhancement originates from the Purcell effect and the high β-factor that quantifies the coupling efficiency of spontaneous emission into the laser mode. The threshold condition is again modified when emitters of the gain material act no longer independently, but radiative coupling triggers a collective spontaneous emission. The radiative coupling originates from the exchange of photons via the high-Q cavity mode that establishes Dicke states [Garraway, 2011]. Super- and subradiance,

which is the enhancement or inhibition of emission due to radiative coupling, was first discussed as a collective effect in a gas of atoms coupled to a common radiation field [Dicke, 1954]. The work of Dicke has been the foundation for a vast number of studies on superradiance (SR), reaching from single-photon emission enhancement [Scully and Svidzinsky, 2009; Chen et al., 2012] over photosynthetic bio-complexes [Ferrari et al., 2014] to Dicke phase transitions [Liu et al., 2014; Baumann et al., 2010] and directional SR emission from statistically independent incoherent sources [Oppel et al., 2014]. Regarding semiconductor systems, radiative lifetime changes have been observed in a QD ensemble due to emitter-coupling effects [Scheibner et al., 2007]. Superfluorescent spontaneous-emission enhancement has been demonstrated in quantum well systems [Timothy Noe Ii et al., 2012]. Recent investigations have also addressed dynamical and statistical properties of SR coupling effects in cavities where QD emitters couple to a single mode [Temnov and Woggon, 2005, 2009; Auffèves et al., 2011].

This chapter is concerned with the impact of radiative coupling in continuously driven (cw) state-of-the-art nanolasers. Strong cavity enhancement and a limitation of the achievable gain due to the smallness of the resonator enhances many-particle correlations in these systems. As an example, non-classical antibunching has been observed within the broad threshold region to lasing in QD microcavity lasers [Wiersig et al., 2009]. While in conventional lasers stimulated emission completely dominates above threshold, this is not necessarily so in nanolasers, where spontaneously emitted photons can constitute a significant part of the laser emission. It is not farfetched to assume that inter-emitter coupling effects play a role in the emission properties, even though they are typically assumed to be weak in semiconductor systems due to strong dephasing. These collective effects are typically not contained in most applications of laser theories, which are derived and used under the assumption of individual uncoupled emitters. To this date, radiative coupling is seldom associated with steady-state properties. The possible coexistence of lasing and superradiance in systems with few (2–5) two-level systems was discussed in Ref. [Mascarenhas et al., 2013]. The prediction of emerging superradiance in a continuously driven gas of atoms [Meiser and Holland, 2010] has led to the recent demonstration of a new kind of "nearly photon-less" SR laser [Bohnet et al., 2012]. Collective effects are also expected to play an important role in random lasers, where the role of the cavity is replaced by multiple scattering events within the gain material [Wiersma, 2008; Baudouin et al., 2013].

We develop and apply a laser model for QD nanolasers that explicitly takes inter-emitter correlations and photon correlations into account. For a many-emitter gain medium, density-matrix approaches can account for inter-emitter coupling, but are limited to a small number of emitters ($\sim$ 10 two-level systems, $<$ 5 multi-level QDs on present-day computer systems) due to the rapidly increasing size of the Hilbert space [Auffèves et al., 2011; Florian et al., 2013a; Sitek and Manolescu, 2013; Lax and Louisell, 1969; Scully and Lamb, 1967]. Established quantum-optical master equations for the diagonal elements of the density matrix do not account for inter-emitter coupling [Rice and Carmichael, 1994], and rate equations are obtained under the assumption of individual emitters and prohibit access to the statistical emission properties [Moelbjerg et al., 2013; Rice and Carmichael, 1994; Yokoyama

and Brorson, 1989; Chow and Koch, 1999]. Monte-Carlo approaches have also been used to study SR [Meiser and Holland, 2010]. Here, we use a method that is based on the systematic inclusion of expectation values of QD-configuration and cavity-photon operators that allows to keep correlations up to a desired order and truncate higher clusters of operators. Photon-photon and inter-emitter correlations provide access to the photon autocorrelation function $g^{(2)}(0)$ and radiative emitter coupling. Related cluster-expansion or cumulant-expansion approaches have been used both in the atom [Meiser et al., 2009; Witthaut et al., 2011] and semiconductor fields [Chow et al., 2014; Gies et al., 2007; Kira and Koch, 2008; Carmele et al., 2009] to describe either extended systems, or systems with many emitters, as the numerical problem typically scales only linearly with particle number.

The laser model in configuration description is presented the Sec. 5.2. In Sec. 5.3, the impact of radiative coupling on the input/output curve is analyzed to reveal that correlations introduced by the radiative coupling drastically change the height of the jump in the input/output curve, as well as its slope in the spontaneous emission regime. In Sec. 5.4, the impact of radiative coupling is quantified by means of suitable pair-correlation functions for electronic and photonic degrees of freedom. These are used to introduce an effective rate of spontaneous emission and to explain the superthermal photon bunching that appears at low excitation powers. In Sec. 5.5, radiative coupling effects are quantified in terms of cavity-Q factor and emitter number and it is demonstrated that superradiance enhances the "coherence per photon", so that significantly fewer emitters suffice to reach lasing in comparison to the case of individual emitters. In Sec. 5.6 we study the influence of inhomogeneous broadening on the sub/superradiant features. In Sec. 5.7 we provide an illustrative explanation of the observed features in terms of Dicke states between pairs of emitters in the ensemble. The appendix B provides technical details about the underlying laser theory.

5.2 Laser theory in configuration description

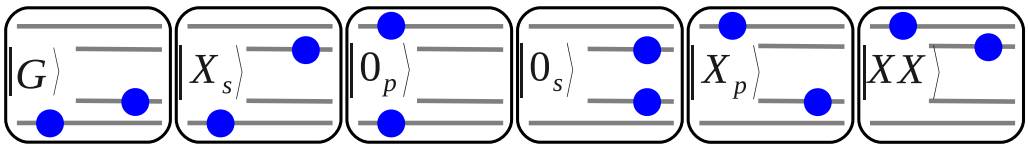

Figure 5.1: Illustration of the electronic configuration states $|i\rangle$ of a QD with two confined states for electrons and holes that accommodates two electrons ($i = \{G, X_s, 0_p, 0_s, X_p, XX\}$). The different configurations are the ground state $|G\rangle$, the s-exciton $|X_s\rangle$, the dark states with the electrons in the p-shell $|0_p\rangle$ and in the s-shell $|0_s\rangle$ respectively, the p-exciton $|X_p\rangle$ and the bi-exciton $|XX\rangle$.

We consider an ensemble of self-assembled QDs coupled to a single high-quality mode of an optical microcavity. Three-dimensional carrier confinement of the QDs leads to a discrete density of states below a quasi-continuum of states from the surrounding semiconductor material. Interaction with carriers in these states is source of capture, scattering and dephasing processes. For the laser model, we consider

generic QDs each having two localized states for electrons and holes. Assuming excitation by simultaneous capture of electron-hole pairs from the continuum states, six configurations are possible that represent bright and dark (multi-) exciton configurations $|i\rangle^{\alpha} = \{G, X_s, 0_p, 0_s, X_p, XX\}$ of QD α, as shown in Fig. 5.1. Both the X_s and XX configurations allow for an optical recombination of an s-shell electron-hole pair into the laser mode. This model captures the essential properties of a multi-level emitter that can accommodate bright and dark multi-exciton configurations [Gies et al., 2011]. We introduce the projection operator

$$Q_{ij}^{\alpha} = |i\rangle^{\alpha} \langle j|^{\alpha} \ . \tag{5.1}$$

For $i \neq j$, it describes the transition from configuration j to configuration i in QD α, whereas for $i = j$, its expectation value refers to the probability to find QD α in configuration i. In the picture of many-particle configurations, we define the excitation operator for the s-shell of QD α as

$$E_s^{\alpha\dagger} = Q_{X_s G}^{\alpha} + Q_{XX,X_p}^{\alpha} \ . \tag{5.2}$$

The product states $|i_1 \dots i_N, n\rangle$ span the Hilbert space of N QDs and photons of the cavity mode. The dimension $6^N \times n_{\max}$ of the Hilbert space grows quickly with emitter number, which is why a solution of the von Neumann equation for the full system density operator, popular for single-emitter systems, becomes costly already for a handful of emitters.

The dynamics of the microcavity-QD system is governed by the Hamiltonian $H = H_0 + H_D + H_C$ [1], with the free Hamiltonian $H_0 = \sum_{\alpha,i} \varepsilon_i^{\alpha} Q_{ii}^{\alpha} + \hbar\omega b^{\dagger} b$ that contains the configuration energies ε_i^{α} and the mode frequency ω, the light-matter interaction Hamiltonian H_D, and the Coulomb interaction Hamiltonian H_C. We have introduced the photon creation and annihilation operators $b^{\dagger}, b$ for photons in the laser mode. In terms of the configuration operators, in dipole- and rotating-wave approximation the dipole Hamiltonian is given by

$$H_D = -i \sum_{\alpha} g_{\alpha} [b^{\dagger} E_s^{\alpha} + \text{h.c.}] \tag{5.3}$$

and couples the s-shell recombination to the creation of a cavity photon, and vice versa. g_{α} is the light-matter coupling strength of the s-transition of QD α to the laser mode. In the scope of the present work, we take the Coulomb interaction into account by renormalized configuration energies and an effective light-matter coupling strength.

We obtain the system dynamics by deriving equations of motion for observable quantities with the generalized Ehrenfest EoM, in the formalism of the Expectation Value Based Cluster Expansion which is explained in Ch. 2. The two-particle nature of the dipole Hamiltonian creates two different hierarchies: 1) EVs with M photon operators are coupled to EVs with $M + 1$ photon operators. 2) EVs acting on transitions or occupations in one QD are coupled to EVs that couple transitions or occupations in different QDs. Both hierarchies do not end at low orders: 1)

[1] This is the same Hamiltonian that we described in Ch.1 but here reformulated in terms of configuration operators

is only limited if the cavity field is represented by a finite linear combination of number states, and 2) is limited by the finite, but possibly large number of emitters in the gain material. In the spirit of the cluster-expansion method (see Ch. 2.3.3), both hierarchies are truncated consistently at a desired level to close the set of coupled equations. Cluster-expansion methods have been used with great success to model quantum-well [Kira and Koch, 2008; Kira et al., 1999; Kira and Koch, 2011] and QD [Feldtmann et al., 2006; Gies et al., 2007; Richter et al., 2009; Leymann et al., 2014] systems. Our approach here differs in two ways from the conventional method: Rather than using single-particle operators, we work in the many-particle configuration picture using the operators Q^{α}_{ij} defined in Eq. (5.1), and we expand the hierarchy in terms of EVs rather than correlation functions. For details, we refer to Appendix B.2.

We start from the mean photon number $\langle b^{\dagger}b\rangle$ and the configuration probabilities $\langle Q^{\alpha}_{ii}\rangle$ in each QD and derive their equations of motion. Photon correlations are included up to $\langle b^{\dagger}b^{\dagger}bb\rangle$, because they are needed to access the second-order autocorrelation function Eq. (1.42). EVs containing more than 4 photon operators are factorized. Radiative emitter coupling is related to expectation values of the type $\langle (b^{\dagger})^{n}b^{m}Q^{\alpha}_{ij}Q^{\beta}_{i'j'}\rangle$, which contain operators Q acting on different emitters α, β. Higher order correlations of the kind $\langle (b^{\dagger})^{n}b^{m}Q^{\alpha}_{ij}Q^{\beta}_{i'j'}Q^{\gamma}_{i''j''}\rangle$ are factorized. In our results, we compare to the case of "individual emitters", which is obtained by performing a separate calculation, in which the hierarchy is truncated at the lowest level with respect to the Q operators, i.e. only EV of the type $\langle (b^{\dagger})^{n}b^{m}Q^{\alpha}_{ij}\rangle$ are explicitly considered.

Self-organized QDs are embedded systems, and their localized states are coupled to continuum states of wetting layer and barrier material. This enables efficient above-band-gap pumping. A simplified treatment consists of modeling incoherent carrier-capture into higher confined QD states and successive relaxation via a Lindblad term (see Ch. 1.6). This is a commonly used method with the twist that here, configurations are used, and the formalism needs to be spelled out in terms of the operators Q^{α}_{ij}. We use the following rates: P^{α} capture of e-h pairs into the QD p-shell (pump rate), $\gamma^{\alpha}_{\mathrm{r}}$ carrier relaxation, $\gamma^{\alpha,\{s,p\}}_{\mathrm{spont}}$ spontaneous losses of s and p-shell electron-hole pairs, and κ the loss rate of photons from the cavity. The Lindblad contributions are added to the EV-equations of motion by evaluating $\langle \dot{A}\rangle|_{\mathrm{Lindblad}} = \gamma_{\eta}\sum_{\{i,j\}}\langle([Q^{\alpha}_{ij},A]Q^{\alpha}_{ji} + Q^{\alpha}_{ij}[A,Q^{\alpha}_{ji}])\rangle$ for each pair $\{i,j\}$ of configurations connected by the underlying microscopic process η [Florian et al., 2013b]. A similar term using photon operators arises for cavity losses. Details are found in Appendix B.3. The large number of coupled equations of motion are generated by means of the computer-aided cluster expansion in Ch. 3. Inhomogeneous broadening is an inherent property of QD-emitter ensembles obtained from self-assembled growth techniques [Bimberg et al., 1999]. The number of QDs considered in our calculations corresponds to the number of QDs in the ensemble found in spectral vicinity to the cavity mode. For these emitters, we assume that radiative coupling effects are fully present. The effect of detuning is investigated separately with 3 three case studies in Sec. 5.6.

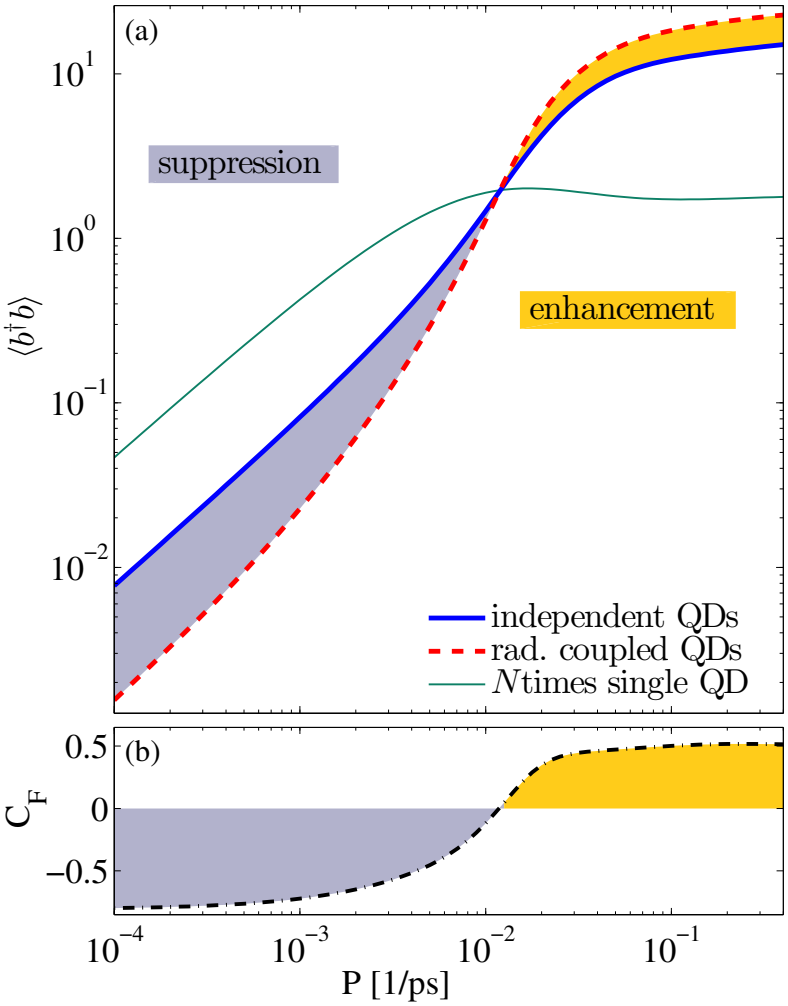

Figure 5.2: (a) Input/output curve for a typical nanolaser device [Lermer et al., 2013; Aßmann et al., 2010]. $N = 100$ QD emitters are used with a light-matter coupling of $g = 0.015/\text{ps}$, cavity loss rate $\kappa = 0.05/\text{ps}$ (corresponding to $Q = 20,000$), carrier relaxation rate $\gamma_\text{r} = 0.05/\text{ps}$, and spontaneous losses into leaky modes $\gamma_\text{spont} = 0.01/\text{ps}$. The solid blue curve results from a calculation without radiative coupling effects, the dashed red curve includes sub- and superradiant coupling between pairs of emitters. The thin solid green line shows the intensity produced by a single QD multiplied by the emitter number. (b) The cooperativity factor C_F (dash-dotted black curve) gives a measure of the change in photon output caused by the radiative coupling.

5.3 Signatures of radiative coupling in the input and output characteristics of nanolasers

In a conventional laser, a sudden intensity jump in the input/output curve over several orders of magnitude serves as an indicator for the onset of coherent emission. The height of the jump may be used to estimate the spontaneous-emission coupling factor β [Yokoyama and Brorson, 1989; Chow and Koch, 1999]. In microcavity

systems that approach the thresholdless $\beta \approx 1$ regime, a more gradual transition to coherent emission can be revealed by studying statistical properties of the emitted light [Jin et al., 1994; Khurgin and Sun, 2012; Rice and Carmichael, 1994; Strauf et al., 2006].

In Fig. 5.2(a), the input/output characteristics with (dashed line) and without (solid line) inter-emitter coupling are compared for a nanolaser with 100 emitters that are resonant with a high-quality ($Q = 20,000$) mode of the cavity. The system shows a transition into lasing at a pump rate of about 0.01 electron-hole pairs per ps and QD. It is striking that suppression of photon production below and enhancement above threshold increases the height of the gradual intensity jump. If rate- or master-equation approaches that neglect inter-emitter coupling were used to describe an experiment, in which strong inter-emitter coupling is present, one would erroneously conclude a β-factor that is smaller by about one order of magnitude. Furthermore, the radiative coupling visibly increases the slope of the input/output curve in the spontaneous emission regime.

To quantify the impact of the inter-emitter coupling, we define the cooperativity factor

$$C_F = \frac{I_{\text{rad. coupled QDs}}}{I_{\text{independent QDs}}} - 1, \tag{5.4}$$

which is shown in Fig. 5.2(b). It gives a direct measure whether radiative coupling enhances or inhibits photon production. In addition to the laser transition from thermal to coherent light emission, it reveals a second transition from the subradiant ($C_F < 0$) to the superradiant ($C_F > 0$) regime. C_F is obtained from two separate calculations in- and excluding the QD-QD coupling terms while keeping everything else unchanged. The possibility to do so is an advantage of our method over multi-emitter density-matrix approaches that compare the full system to N times a single-emitter system [Mascarenhas et al., 2013]. The latter method amplifies the effects of saturation and reduced absorption of the single emitter by a factor N, causing significant deviations from the N-emitter input/output curve especially for larger emitter numbers. This is demonstrated by the thin green line in Fig. 5.2(a) showing the input/output characteristics of a single QD-system multiplied with the number of QDs N. Comparing this result to the dashed red curve (calculated for N emitters including inter-emitter coupling) would result in an overestimation of the radiative coupling effects.

5.4 Statistical properties of the emission and effective spontaneous emission rate

In the following we demonstrate that superradiance enhances spontaneous emission in a way that fewer emitters are required to overcome the cavity losses of a nanolaser and to reach coherent emission. To this end, we chose slightly different parameters than in the previous section that are given in the caption of Fig. 5.3. Panels (a) and (b) depict input/output curve and the photon autocorrelation function $g^{(2)}(0)$ with and without radiative coupling effects. In the gray area with $C_F < 0$ ($P \lesssim 10^{-2}\,\text{ps}^{-1}$), the inter-emitter coupling reduces the photon output. Microcavity lasers

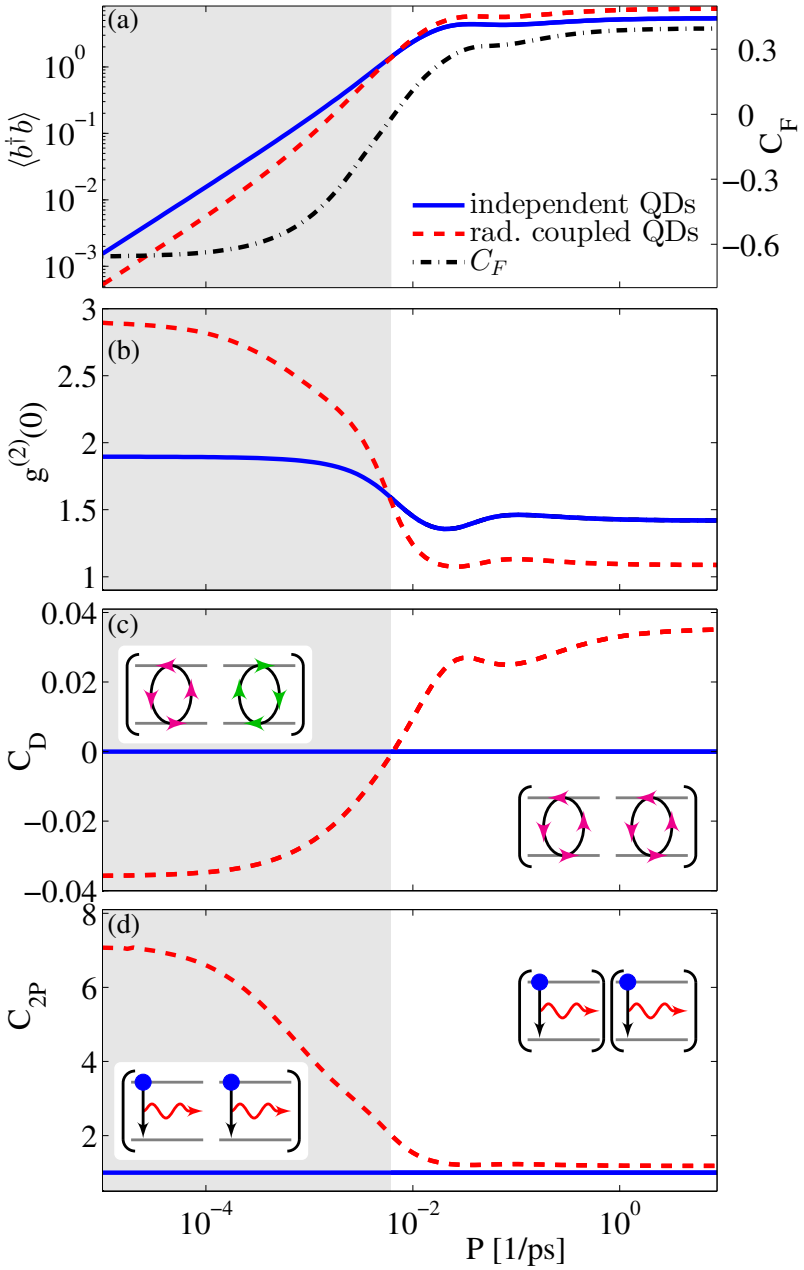

Figure 5.3: Stationary states for increasing pump rates into the QDs p-shell for the case with (dashed red curve) and without radiative coupling effects (solid blue curve). (a) The intensity is measured on the left y-axis in logarithmic scale and the cooperativity factor C_F is measured on the right y-axis, (b) photon autocorrelation function (c) dipole correlation function C_D (d) two-photon emission function C_{2P}. The gray area marks the subradiant regime where the cooperativity factor C_F is below zero. A schematic representation of both correlation functions in the sub- and superradiant regime is shown as insets. The calculations are performed for 20 QDs in resonance with the cavity mode. The photons have a loss rate of $\kappa = 0.0125/\text{ps}$, the other parameters are $g = 0.01/\text{ps}$, $\gamma_\text{r} = 0.05/\text{ps}$, $\gamma^p_\text{spont} = \gamma^s_\text{spont} = 0.005/\text{ps}$ (see Appendix B.3).

are well known to exhibit saturation effects at high excitation. This is owed to the limited amount of gain that can be obtained from the active medium [Strauf et al., 2006]. If saturation sets in before or during the threshold, it can prohibit lasing or suppress the development of the full intensity jump [Gies et al., 2008]. Here, coherent emission with $g^{(2)}(0) = 1$ is only reached when collective effects enhance the emission (red curves). Without SR coupling (blue curves), the system saturates before coherent emission is reached. The important finding that radiative emission enhancement reduces the number of emitters required to reach lasing is further analyzed in Sec. 5.5.

Enhancement of photon-intensity fluctuations with superthermal bunching values $g^{(2)}(0) > 2$ are observed at low pump rates and reflect the increased probability that two photons are emitted at the same time. Its microscopic origin is given by synchronous dipole transitions in separate QDs α and β as described by the expectation value $\langle b^\dagger b^\dagger E_s^\alpha E_s^\beta \rangle$, where E_s^α is defined in Eq. (5.2). To quantify the two-photon (2P) emission probability from pairs of radiatively coupled emitters, we use the normalized correlation function

$$C_{2P} = \sum_{\alpha \neq \beta} \frac{\langle b^\dagger b^\dagger E_s^\alpha E_s^\beta \rangle}{\langle b^\dagger E_s^\alpha \rangle \langle b^\dagger E_s^\beta \rangle}, \tag{5.5}$$

shown in Fig. 5.3(d).

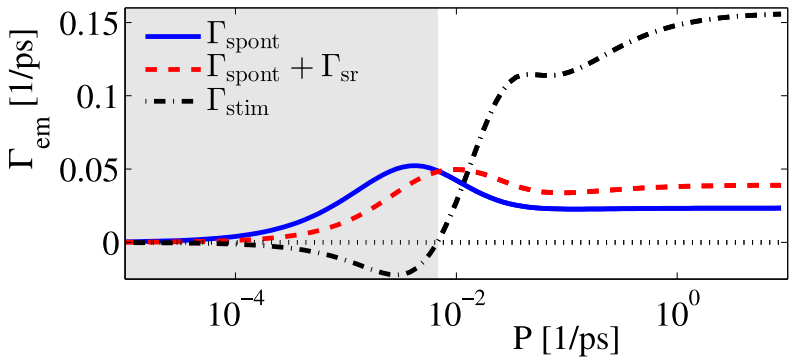

Figure 5.4: Contributions to the total emission rate Γ_{em} for the parameters used in Fig. 5.3 plotted versus pump rate P. The solid (dashed) curve represent the effective spontaneous emission rate excluding (including) radiative coupling effects. The end of the shaded area indicates the onset of lasing, where the stimulated contribution (dot-dashed line) changes from absorption to amplification.

More insight can be obtained by looking at the modification of spontaneous emission caused by the radiative coupling. In the commonly used rate-equation approach, independent emitters are considered, and spontaneous emission into the laser mode enters the dynamics via $\beta \times n_{ex}/\tau_{spont}$, with n_{ex} and τ_{spont} being the number of excitations in the gain medium and the total rate of spontaneous emission, respectively. In a semiconductor system, optical recombination is driven by electrons and holes, and the assumption of independent electron- and hole populations $f^{e,h}$ leads to the spontaneous recombination rate $\beta \times f^e f^h/\tau_{spont}$ [Chow and Koch, 1999; Gies et al., 2007]. We explicitly calculate the degree of correlations between electrons and

holes and the resulting spontaneous-emission contribution. With the dipole operator $D^\alpha = E_s^{\dagger\alpha} + E_s^\alpha$, we define the dipole correlation function [Meyer and Yeoman, 1997]

$$C_D^{\alpha\beta} = \frac{\langle D^\alpha D^\beta \rangle}{\langle E_s^{\dagger\alpha} E_s^\alpha + E_s^{\dagger\beta} E_s^\beta \rangle} \ , \tag{5.6}$$

where the diagonal EV $\langle D^\alpha D^\alpha \rangle$ is the spontaneous-emission contribution from QD α. Of interest is the off-diagonal EV $\langle D^\alpha D^\beta \rangle$, which is the spontaneous-emission contribution due to radiative inter-emitter coupling. In the following we use C_D, which is defined as the arithmetic mean of $C_D^{\alpha\beta}$ over all QD pairs $\alpha \neq \beta$. The sign of C_D indicates whether the dipoles of QD pairs are in phase ($C_D > 0$) or out of phase ($C_D < 0$). The results in Fig. 5.3(c) show a clear transition from out-of-phase to in-phase in the threshold region when the pumping is increased. Comparing Fig. 5.3(a,c) we see that dipoles that are in phase (out of phase) lead to an enhancement (suppression) of the emission into the cavity mode. An intuitive explanation of this effect is provided in Sec. 5.7. The impact of the SR emitter coupling can be cast into the form of an effective emission rate into the laser mode, as it is familiar from laser theories. It consists of three contributions

$$\Gamma_{\rm em} = \Gamma_{\rm spont} + \Gamma_{\rm sr} + \Gamma_{\rm stim} \ , \tag{5.7}$$

where $\Gamma_{\rm spont} = \sum_\alpha \langle D^\alpha D^\alpha \rangle / \tau_{\rm deph}$, and $\Gamma_{\rm sr} = \sum_{\beta\neq\alpha} \langle D^\alpha D^\beta \rangle / \tau_{\rm deph}$, see Appendix B.4. The first two terms constitute the total rate of spontaneous emission into the laser mode: The diagonal one is the usual contribution from independent emitters to the spontaneous emission, and the non-diagonal sum reflects the enhancement or suppression of spontaneous emission due to QD-QD correlations. For identical emitters, $\sum_{\beta\neq\alpha}$ leads to the well-known factor $N(N-1)$ in the spontaneous photon production rate [Mandel and Wolf, 1995]. The third term represents the contribution due to stimulated emission or absorption. For the situation discussed in Fig. 5.3, the three contributions as functions of pump rate are shown in Fig. 5.4. Sub-radiant coupling is seen to reduce the effective spontaneous emission rate until the onset of stimulated emission. Stimulated emission is reached when its contribution (dot-dashed curve) becomes positive. Then, lasing rapidly decreases the population of excitonic states, while excitation-induced dephasing increases with pump, thereby reducing the spontaneous emission (see Appendix B.4). We emphasize that the sub/superradiant suppression/enhancement of the spontaneous emission rate is not caused by a de/increase of exciton population, but solely by the build-up of correlations between QDs. Equation (5.7) also allows for an interpretation of the photon-less laser in Ref. [Bohnet et al., 2012]: There, by the absence of photons, coherence is only obtained from dipole correlations stored in the atoms. These are represented by $\Gamma_{\rm sr}$, which completely takes over the role of the stimulated contribution in conventional lasers.

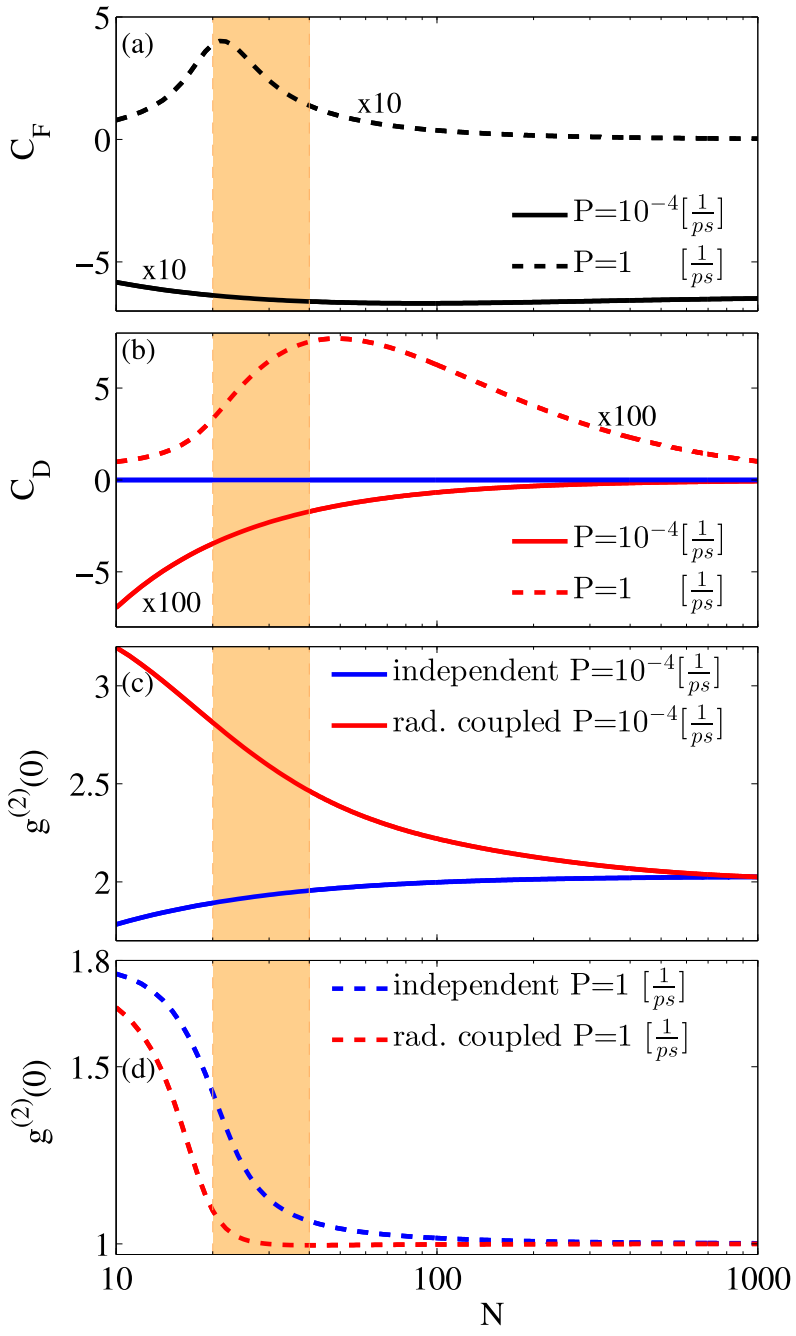

Figure 5.5: Stationary states for increasing number of QDs N at a low ($P = 10^{-4}$/ps solid lines), and a high pump rate ($P = 1$/ps dashed lines), all other parameters are the same as in Fig. 5.3. (a) Cooperativity factor C_F, (b) dipole correlation function C_D, (c) photon autocorrelation function $g^{(2)}(0)$ for low pump rates ((d): high pump rates). Compared are results for independent (blue) and radiatively coupled QDs (red). The shaded region marks the QD numbers where lasing is only possible due to radiative coupling effects.

5.5 Influence of the emitter number and coherence per photon

In Fig. 5.5 we study how the influence of the coupling changes with the number of emitters N. Values in the stationary regime of the discussed quantities are shown for two selected pump rates. At low excitation (solid lines), out-of-phase QD-QD-dipole alignment ($C_D < 0$) and superthermal bunching ($g^{(2)}(0) > 2$) are observed. They are strongest for few emitters and reach the values of independent-emitter theories in the limit of large N (c.f. panels (b) and (c)). At high excitation (dashed lines), the impact of radiative coupling also decreases for large QD numbers, as the system is then entirely dominated by stimulated emission.

Inter-emitter coupling effects have the most striking impact at low and intermediate QD numbers: In this regime, the presence or absence of SR coupling decides whether the system can reach coherent emission or not. This important finding is reflected in the autocorrelation function $g^{(2)}(0)$ at high excitation rates (panel (d)). Without radiative coupling (blue curves), lasing is reached with $N \gtrsim 40$ emitters in the cavity, indicated by a mean photon number above one and $g^{(2)}(0) \approx 1$. In the presence of radiative coupling (red curves), lasing by the same criteria is possible with only half the emitter number $N \gtrsim 20$. The regime, where lasing is possible only in the presence of the collective coupling effects is shaded in orange. In fact, many current realizations of microcavity laser systems operate in the regime of 20–100 emitters effectively coupling to the laser mode [Strauf and Jahnke, 2011].

Interestingly, in the presence of radiative coupling, the same level of coherence expressed in $g^{(2)}(0)$ is achieved at a much lower mean photon number ($\langle b^\dagger b \rangle \approx 8$ with and $\langle b^\dagger b \rangle \approx 35$ without radiative coupling). Thus, the creation of dipole-phase-correlations between the emitters, associated with a positive value for C_D, leads to an increase of the "coherence per photon", so that a lower mean photon number suffices to reach the same level of coherence in the emission.

The influence of the cavity-mode Q factor is studied in Fig. 5.6 for a range of values from 80,000 to 5,000. Shown are results for the high-excitation regime ($P = 1/\text{ps}$), in which lasing occurs when the emitter gain can compensate the photon losses. With increasing photon losses (decreasing Q), this requires emission from more emitters N in the gain material and effectively shifts the lower-Q curves to higher emitter numbers. Of particular interest is the region, in which lasing is only reached if radiative coupling is present. For each value of Q, this is indicated by the solid-colored bars. The width of these regions increases at higher N, as the emission enhancement seen in the cooperativity factor C_F scales with emitter number (top panel). While at Q=80,000, about half the number of emitters suffices to reach stimulated emission in the presence of the discussed enhancement, at Q=10,000 it is less than a fourth. At the same time, it is interesting to note that the strength of the dipole correlations between pairs of emitters (C_D, shown in lower panel) is largely independent of the cavity-Q factor and is solely determined by the light-matter coupling strength. We point out that the size of the resonator and the line width of the cavity provides a physical limit for the number of emitters that can effectively couple to a single mode. Nevertheless, the implications of the insensitivity of radiative coupling effects to the Q-factor may be of interest in devices that naturally offer lower quality factors, such

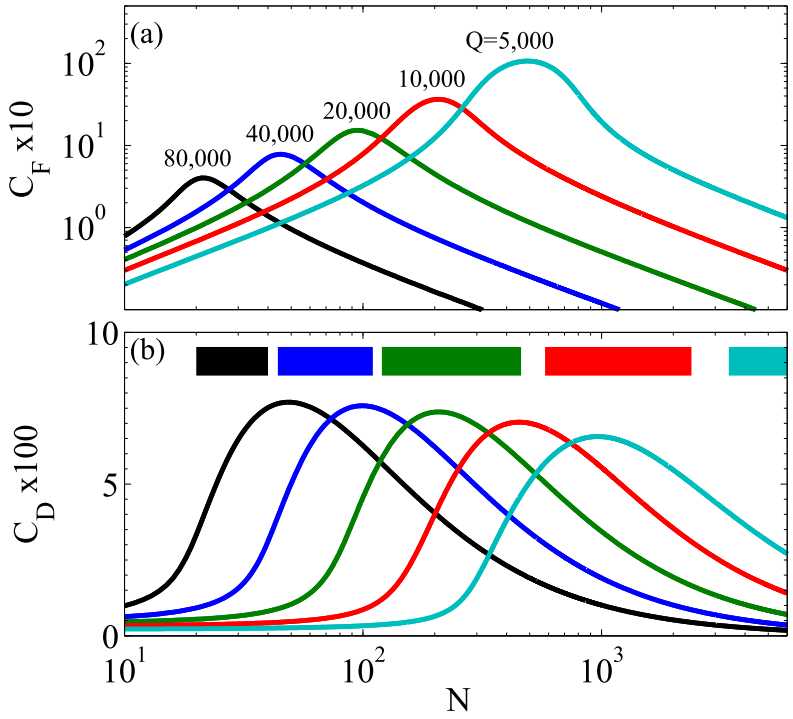

Figure 5.6: Stationary states of the cooperativity factor C_F (top) and dipole correlation function C_D as function of emitter number. Results are obtained for high pumping ($P = 1/\text{ps}$) and shown for cavities with Q-factors of 80,000, 40,000, 20,000, 10,000 and 5,000 from left to right. All other parameters are unchanged with respect to Fig. 5.5. The Q=80,000 results (black curves) are identical to the data in the top panels of Fig. 5.5. The solid bars indicate the interval of QD numbers N for which coherent emission is only reached when radiative coupling between the QDs is present (analogue to the shaded region in Fig. 5.5).

as surface plasmon lasers [Noginov et al., 2009].

5.6 Inhomogeneous broadened ensembles of quantum dots

In this section we investigate the influence of inhomogeneous broadening [Bimberg et al., 1999] on the sub/superradiant features discussed in the previous sections. Typically the inhomogeneous broadening of InGaAS QDs has values of a few ten electronvolts [Xie et al., 2000; Chow et al., 2015]. To get an idea of the general effect of detuning we introduce three distributions of QDs that are sketched in Fig. 5.7 as model examples. The laser theory described in Sec. 5.2 can still be applied with the difference that now all EVs must be calculated separately for each QD since they can have different values. For this reason we slightly change the parameters that are used in the last section to bound the computational effort that grows proportional to the number N of the QDs. We choose $Q = 100,000$ and $N = 15$ so that a significant difference between radiative coupled QDs and independent QDs is retained. The

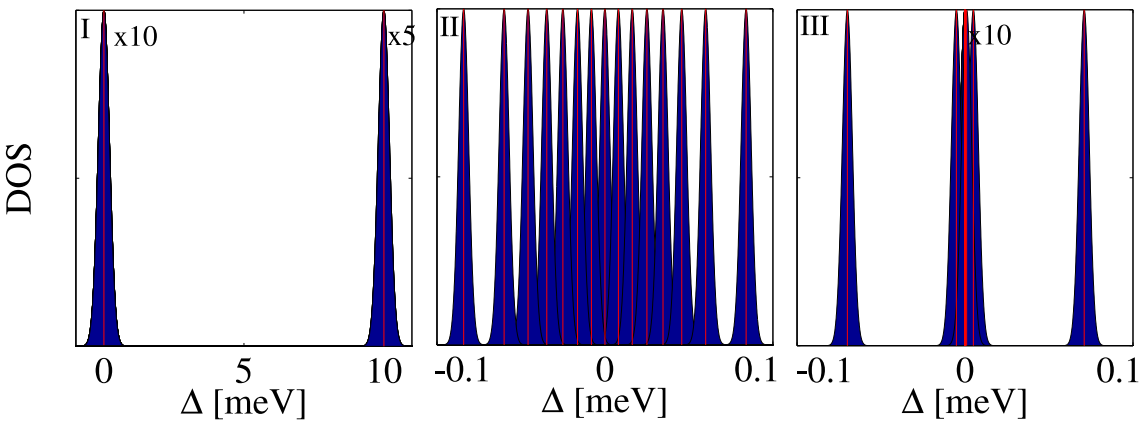

Figure 5.7: Sketch of the density of states(DOS) for the three distributions that are used to investigate the effect of inhomogeneous broadening. Δ is the detuning from the cavity mode in meV. Distribution I is an ensemble with 10 QDs that are exactly in resonance with the cavity mode and 5 QDs that have a detuning of 10 meV. Distribution II is an ensemble of 15 QDs that has a discretized shape of a Gaussian profile with a maximal detuning of $\pm$0.08meV. In distribution III 10 QDs are in resonance with the cavity mode and 5 additional QDs are detuned. One QD has a very small detuning of $\Delta = 0.001$meV and two other QDs have also a quite small detuning of $\Delta = 0.005$meV and $\Delta = -0.0051$meV. Two additional QDs are more off resonant with $\Delta \pm 0.07$meV.

three distributions that are sketched in Fig. 5.7 are chosen in the following way. Distribution I is an ensemble with 10 QDs that are exactly in resonance with the cavity mode and 5 QDs that have a detuning of 10meV. This ensemble is used to check weather QDs that have a big detuning can have an influence on the inter-emitter correlation of QDs with a small detuning. Distribution II is an ensemble of 15 QDs that have a discretized shape of a Gaussian profile with a maximal detuning of $\pm$0.08meV. With this ensemble, we try to find the limit of the detuning where QDs can built up inter-emitter correlation. In distribution III 10 QDs are in resonance with the cavity and 5 additional QDs are detuned. One QD has a very small detuning to the cavity mode with $\Delta = 0.001$meV and two other QDs have also a quite small detuning $\Delta = 0.005$meV and $\Delta = -0.0051$meV. Two additional QDs are more off resonant at $\Delta \pm 0.07$meV. With this ensemble we demonstrate a case where the features of the sub/superradiance are partly present.

The stationary states for the three distributions are shown in Fig. 5.8. The calculations show that the input/output curve and the photon autocorrelation of distribution I behave as if the 5 detuned QDs would not exist. Nevertheless, its dipole correlation is significant smaller since C_D is defined as arithmetic mean of $C_D^{\alpha\beta}$ (Eq. (5.6)) over all QD pairs. We can conclude from this case that far off-resonant QDs do not disturb the inter-emitter coupling of resonant QDs. For this reason we can neglect them in our calculations as done in the previous sections.

Distribution II has the highest output for very low pump rates while its output is between 10 and 15 resonantly coupled QDs for high pump rates. There are no

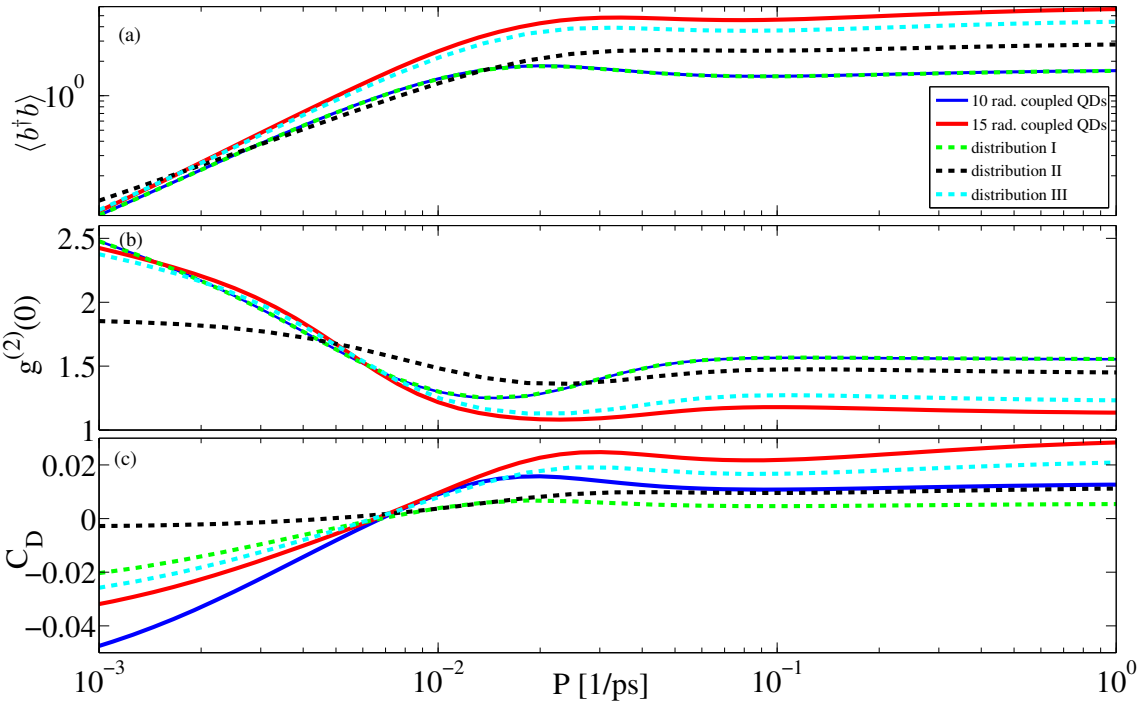

Figure 5.8: Stationary states for the three different distributions of QDs shown in Fig. 5.7 as function of the pump rate P. For a better comparison, we have added the characteristic curves of 10 and 15 radiative coupled QDs without detuning (solid lines). (a) Input/output curve, (b) photon autocorrelation function (c) dipole correlation function C_D of the 5 QD ensembles. The input/output curve and photon autocorrelation of distribution I behaves exactly like the 10 resonantly coupled QDs. The dipole correlation of distribution I is less pronounced since the 5 additionally QDs of this distribution do not contribute to the correlation. Distribution II has more output than the 10 resonantly coupled QDs and has a photon autocorrelation that shows no signatures of subradiance. Surprisingly the dipole correlation has only small values for low pump rates while at high pump rates it has a considerable magnitude. In consequence distribution II behave like 15 independent emitters in the subradiant regime and show some features of radiative coupling in the superradiant regime. Distribution III shows nearly the same behavior in the input/output curve and photon autocorrelation as the 15 radiative coupled QDs. In the subradiant regime the dipole correlation is less expressed than in the two reference cases (blue and red solid line) while it shows a higher correlation in the superradiant regime than the 10 radiative coupled QDs (blue solid line).

signatures of subradiance in the photon autocorrelation. Surprisingly, the dipole correlation has only small values for low pump rates while at high pump rates it has a considerable magnitude. In consequence distribution II behave like 15 independent emitters in the subradiant regime and show some features of inter-emitter coupling in the superradiant regime. In this case neglecting the detuning of the QDs would lead to significantly different results, in fact the independent description of resonant QDs is closer to the results than the radiative coupled description.

Distribution III shows nearly the same behavior in the input/output curve and photon autocorrelation as 15 resonantly radiative coupled QDs. A qualitative change in the dipole correlation becomes visible due to the change from the subradiant regime to the superradiant regime if one compares it to reference cases of 10 and 15 resonantly coupled QDs. While the dipole correlations are weak in the subradiant regime they become stronger than the dipole correlations of the 10 resonantly coupled QDs in the superradiant regime.

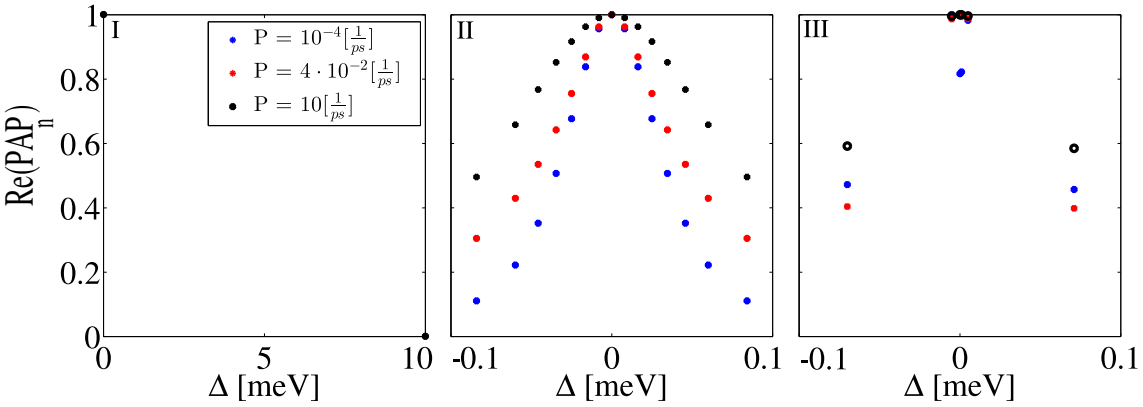

Figure 5.9: Normalized photon-assisted polarization ($\mathrm{PAP_n}$) in dependence of the detuning Δ for three different pump rates P. In distribution I, only the 10 resonant QDs contribute to the emission, while the other 5 QDs have negligible contributions. Distribution II reproduces the Gaussian shape also in its contribution to the photon-assisted polarization. It becomes visible that the relatively importance of the more detuned QDs increases with higher pump rates which is in accordance with their increasing dipole correlation in Fig. 5.8. Distribution III shows that for small pump rates the two detuned QDs with $\Delta = 0.005$meV and $\Delta = -0.0051$meV have the highest contribution to the photon-assisted polarization since they do not couple subradiantly to the 11 QD at $\Delta \approx 0$meV. With increasing pump rate these two QDs begin also to couple superradiantly so that now the 13 QDs ($\Delta < 0.051$meV) in the center contribute nearly in the same way to the photon-assisted polarization. The two further detuned QDs with $\Delta \pm 0.07$meV increase their relative contribution to the photon-assisted polarization also stronger with the pump rate compared the similar detuned QDs in distribution II.

To further analyze the contribution of each individual QD to the light field (see Appendix B.4) we show the real part of the normalized photon-assisted polarization $\mathrm{Re(PAP_n)}$ in Fig.5.9 where the maximum value of the photon-assisted polarization for each pump rate has been normalized to one. For distribution I, the impression of the stationary states is confirmed and we see that the detuned QDs are indeed negligible. In distribution II the shape of the photon-assisted polarization reflects it Gaussian profile. It becomes visible that with increasing pump rate the relative contribution of the further detuned QDs increase. This behavior can be used to understand the increasing dipole correlation since it shows that now also the weakly detuned QDs can built up a dipole correlation. Distribution III makes this even clearer. Here for low pump rates only the 11 QD with $\Delta \approx 0$meV couple subradiantly

while the two more detuned QDs with $\Delta = 0.005$meV and $\Delta = -0.0051$meV do not couple. Consequently, these two QDs have the strongest contribution to the photon-assisted polarization. With increasing pump, rate also these two QDs seem to build up a dipole correlation as they are now contributing equally to the light-field.

Although we have only shown three cases of inhomogeneous broadening we can deduce some general behavior of detuned QD ensembles. First, we can neglect far off-resonant emitters since they do not influence the inter-emitter correlations of resonant emitters. Second, the detuning is even more critical for the buildup of inter-emitter correlations than for their contribution to the light-field. Third, it is more likely to find superradiant effects at higher pump rate than to observe subradiant effects at low pump rates. Altogether a theory that includes radiative coupling should be favored also for detuned QDs if the parameters are in a sector where sub- and superradiance is important (see Fig. 5.5 and Fig. 5.6).

5.7 Dicke states of pairs of emitters

The origin of sub- and superradiance is often discussed in a simplified picture of two coupled two-level systems [Dicke, 1954; Meyer and Yeoman, 1997]. The eigenstates of the coupled system are the ground state $|\downarrow\downarrow\rangle$, the fully excited state $|\uparrow\uparrow\rangle$ and the two degenerate states $|\downarrow\uparrow \pm \uparrow\downarrow\rangle$. The antisymmetric state is, in general, dipole forbidden [Mandel and Wolf, 1995], on which basis one can explain the photon bunching in the subradiant regime [Auffèves et al., 2011]. By considering EVs of the type $\langle (b^\dagger)^n b^m Q_{ij}^\alpha Q_{i'j'}^\beta \rangle$ within our formalism, we have access to occupation probabilities of QD pairs, which corresponds to information contained in a reduced two-QD density matrix. In an ensemble of many emitters, the expectation value $\langle Q_{GG} Q_{GG} \rangle$ represents the averaged probability to find QD-pairs in the ground state $|\downarrow\downarrow\rangle$, and $\langle Q_{XX\,XX} Q_{XX\,XX} \rangle$ in the fully excited state $|\uparrow\uparrow\rangle$, respectively. When the $|\uparrow\uparrow\rangle$ state is likely to be occupied, not only single-photon emission is possible, but also correlated two-photon emission via the process $\langle b^\dagger b^\dagger E_\alpha E_\beta \rangle$, which leads to $C_{2P} > 1$. The dipole correlation function C_D contains information on whether pairs of QDs predominantly occupy the symmetric $|\downarrow\uparrow + \uparrow\downarrow\rangle$ ($C_D > 0$), or the antisymmetric $|\downarrow\uparrow - \uparrow\downarrow\rangle$ ($C_D < 0$) state. Analogous to the two-emitter case, in the antisymmetric configuration the excitation is trapped. This is reflected in the effective spontaneous emission rate (5.7), where negative values of C_D suppress the spontaneous emission into the laser mode. On the other hand, photon emission from the symmetric state is accelerated, as positive C_D enhances the emission rate into the laser mode. These two regimes are referred to in the literature as subradiance [Auffèves et al., 2011] or anti-superradiance [Mandel and Wolf, 1995] ($C_D < 0$), and superradiance ($C_D > 0$).

In contrast, on the level of independent emitters, EV between pairs of emitters are factorized: $\langle\downarrow\uparrow \pm \uparrow\downarrow\rangle \rightarrow \langle\downarrow\rangle\langle\uparrow\rangle$. This results in a much simpler structure of possible processes as illustrated in Fig. 5.10. In this case, a distinction between the discussed symmetric and antisymmetric states of QD pairs is not possible, and the corresponding emission inhibition or enhancement due to out-of-phase (in-phase) dipole moments is not accounted for. Neither is correlated two-photon emission ($C_{2P} > 1$) possible on the level of independent emitters, which results in the vanishing superthermal photon bunching with $g^{(2)}(0) > 2$.

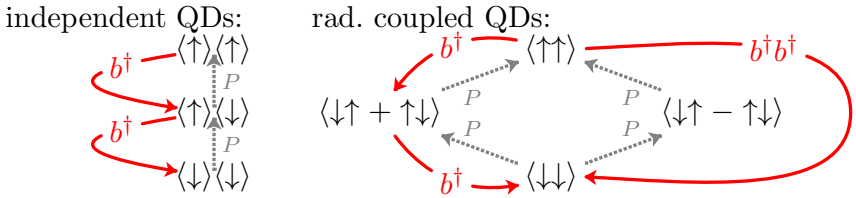

Figure 5.10: Illustration of the population and depopulation processes for the reduced two-QD density matrices. We compare the case of the product states of individual emitters, which is obtained when QD-QD correlations are factorized (left), to the case of radiatively coupled emitters (right). The solid red lines indicate the coherent photon emission into the cavity $b^\dagger$. Dotted gray lines indicate the effective incoherent pump P resulting from the electron-hole capture in the p-shell and the various relaxation and scattering processes.

Neumeier [2016] demonstrated in his master thesis that it is possible to transfer this illustrative explanation to rate equations. The obtained results show the basic features of sub- and superradiance and allow for a justification of our simplified picture.

5.8 Chapter conclusion

Current quantum-dot nanocavity devices challenge our understanding of lasers. The small mode volume sets a limit for the number of emitters that can effectively couple to a single cavity mode. Micropillar devices operate with about 20–200 emitters [Lermer et al., 2013], and even less in photonic-crystal resonators [Strauf and Jahnke, 2011]. In this extreme regime, cQED effects are known to enhance correlations and to alter the nature of the emitted light [Nomura et al., 2010; Wiersig et al., 2009]. In a range of Q values typical for current microcavity lasers, we predict correlations between the emitters to influence the output characteristics of cw-driven lasers significantly: In the presence of collective effects, coherent emission is reached with fewer emitters and at lower mean photon numbers. The increased "coherence per photon" reflects the presence of dipole correlations in the gain medium. At low excitation, sub-radiant suppression of emission increases the jump in the input/output curve that is typically associated with the β-factor. Theories that neglect radiative emitter coupling may underestimate the β-factor by an order of magnitude. These findings can explain the efficiency in photon production of current few-emitter nanolasers, which is often better than predicted from conventional laser models, and stimulate further experimental effort to identify the role of sub- and superradiance in these systems, e.g. by investigating the laser dynamics with respect to collective lifetime changes in the emission, or by high time-resolution measurements of the emission statistics to reveal superthermal photon bunching. Strong collective effects are also expected under pulsed excitation, which will be the topic of future work.

Our results are obtained from a laser theory that includes radiative inter-emitter coupling and photon correlations to obtain $g^{(2)}(0)$. The underlying configuration cluster-expansion is based on the factorization of higher-order expectation values

of electronic configuration and photon operators and allows for the description of systems with many of degrees of freedom. This is well suited to model the coupling of the multi-exciton states of several hundred solid-state emitters to a cavity mode in the present work. The method may also prove useful to describe collective effects in cold atomic gases, for which lifetime changes due to sub- and superradiant coupling have been reported [Bienaimé et al., 2013; Pellegrino et al., 2014], in the context of random lasers with many photonic modes [Wiersma, 2008], or in the description of collective effects in coupled microcavity arrays [Ruiz-Rivas et al., 2014].

Chapter 6

Final Conclusions

To conclude this thesis we split this chapter into three paragraphs: Advances in theory, Advances in physics, and Outlook and future prospects. The chapter structure in this thesis follows a logical order: at the beginning, we build up the theoretical foundations, and then we are investigate the properties of realistic quantum-dot microcavity lasers. The paragraph Advances in theory follows the chronological traces of the development so the reader can understand the motivations of the development process. Then the paragraph Advances in physics stresses the important physical results according to the chapter structure. In the last paragraph, we discuss interesting follow-up projects that can be investigated based on this work.

Advances in theory In this part of the conclusion we address the advances of the used theory and methods in the order of their chronological development so that the reader can understand in detail which improvements have been made.

The work on this thesis started with the project on bimodal lasers. From the beginning, we worked closely together with the experimental physics group of Prof. Reitzenstein at the TU Berlin where interesting features in experiments with bimodal quantum-dot microcavity lasers had been observed. To explain the experimental results we developed a bimodal laser theory (first part of chapter 4) that is an extension to the laser theory for a single-mode laser [Gies et al., 2007]. This theory could explain most features like mode competition and superthermal values of the autocorrelation function. Already at this level the theory contained 80 equations of motion, and it was helpful to use the computer in order to avoid mistakes. For this reason, we developed a previous version of the computer-aided cluster expansion (chapter 3). The work on this project made clear that formulating the equations in terms of correlation functions as Gies et al. [2007] was by no means simple and not well suited to be generalized. Additionally, to these problems, the usage of heuristic scattering/damping was problematic since they are known case false results when used inconsistently [Florian et al., 2013b].

The experience of this first project led to the development of the expectation value based cluster expansion in chapter 2. First, we proved that that the formulation of equations of motion in terms of expectation values is equivalent to the former formulation in terms of correlation functions. This is demonstratively shown in chapter 2 where we used the expectation value based cluster expansion to calculate

the autocorrelation function for a quantum-dot laser up to order 5 which is similar to the results with the correlation function [Foerster, 2012]. The advantage of this theory is a reduced algebraic effort and a much clearer presentation of the equations. Although all equations are nonlinear if we use the formulations in terms of correlation functions, the formulations in terms of expectation values are nonlinear for only the equations where we have applied an approximation. This advantage makes it easier to check the equations manually and more likely to be numerical stable. The study of various Hamiltonian systems also allowed us to understand the pitfalls of the cluster expansion approach. The truncation of finite systems as well as the treatment of mixed Hilbert spaces had been made possible within this formulation.

The next step was to implement the expectation value based cluster expansion in the computer program. With this theory it became easier to investigate the multi-time correlation functions which was used in the second part of chapter 4. As the main result, we could reproduce and explain the experimental spectra observed by the group of Prof. Reitzenstein. The mode coupling, which is mediated by the quantum dots is responsible for the occurrence of a second peak in the polarization resolved experiments. Without our theoretical background this was first suspected to be crosstalk between the two polarization directions, which we could disprove with our theory. By using the lowest order of approximation of our theory, we could show a formal equivalence to strong coupling and introduce unconventional normal-mode coupling. This 2x2 matrix formulation opened a new perspective on bimodal lasers and the connection between linewidth and mode splitting.

Still, this theory was using the heuristic damping terms that were introduced by Gies et al. [2007]. We resolved this problem in chapter 5 where we started to completely redesign the theoretical description of the quantum-dot model. Considering a single quantum dot as a closed entity described by a finite set of configurations we could built the configuration based cluster expansion, as extension of the expectation value based cluster expansion. Finally, using the Lindblad formulation to describe the scattering in a general valid form, this theory allowed us to switch the super-/ subradiantly coupling on and off. By taking the inter-emitter correlations into account or neglecting them, we were able to investigate the emergence of sub- and superradiance in nanolasers. We studied the effects of inter-emitter coupling on continuously driven lasers in chapter 5. In a separate project we also studied the effects of sub- and superradiance on quantum-dot nanolasers with pulsed excitation [Pistorius, 2015; Jahnke et al., 2016]. The advantage here was the direct access to experiments from the group of Prof. Bayer at the TU Dortmund that showed giant photon bunching and superradiant pulse emission. With our presented theory, we could reproduce and explain the experimental results which would have been impossible with the previous theory. This development led to the final stage of our program presented in chapter 3.

Advances in physics This part of the conclusion focuses on the physical results, while the underlying methodological advances of the theory were discussed in the previous paragraph.

As part of the investigation on high-β single-mode lasers we have extensively discussed the concept of the laser threshold in chapter 2 and in chapter 3. We can

conclude that neither having more than one photon in the cavity nor the inversion point nor a single value of the photon autocorrelation function $g^{(n)}(0)$ is adequate to define a strict lasing threshold. Instead our calculations on this subject suggest to treat the laser threshold as a parameter area rather than to define a single threshold value that is arbitrary.

Related to the laser threshold is the way to determine the β-factor from the intensity jump as suggested by the results of the laser rate equations [Rice and Carmichael, 1994]. This widely used method takes the jump height of the input-output curve as a direct measure of the β-factor. Our calculations, by contrast, have shown that a change in the theoretical model always leads to different intensity jumps. We have observed this for the direct dephasing (chapter 3), a second mode (chapter 4), or the inclusion of inter-emitter correlations (chapter 5). Consequently these jumps can only be regarded as a rough estimate for the β-factor in an experiment. Our calculations within the framework of the configuration based cluster expansion in chapter 5 revealed that a more detailed description proves the total emission rate into the laser mode to be pump dependent (Appendix B.4). All in all, one should not estimate a certain β-factor based on input-output characteristics only. Instead, a carefully adapted theory should be the basis of a realistic description of the laser threshold.

The most convenient way to represent the behavior of the modes in a bimodal laser is shown in Fig. 4.7. The interaction of the two cavity modes of a passive microcavity with a mesoscopic number of quantum emitters induces unconventional coupling between these modes in the lasing regime. If the difference between the modes is adequately high, features like mode competition in the input-output characteristics, enhanced autocorrelation functions of the competition losing mode, and a pronounced anti-correlation become visible. For sufficiently large spectral splitting between the cavity modes, the incoherent coupling between the modes leads to a mixing of the cavity mode frequencies in the emission spectrum. These results motivated the study of direct dissipative coupling between the laser modes [Fanaei et al., 2016] which found results similar to those in chapter 4. These results can be regarded as a justification of our much simpler master equation approach where we described the observed effects by an effective direct mode coupling [Leymann et al., 2013c] and were able calculate the full photon statistics of the bimodal laser.

The theory in chapter 5 made it possible to study the influence of sub- and superradiant coupling of the quantum dots for realistic devices. We were able to find situations where the inter-emitter coupling plays a critical role to reach the lasing regime. In these cases, macroscopic dipole-dipole correlations build up and modify the spontaneous emission rate significantly. We also investigated the limit when inter-emitter coupling becomes negligible. Namely the limit of many quantum dots and the case of large inhomogeneous broadening. Despite the discussed limitations our theory is supported by an experiment where we could show the super-/ subradiant features for a pulse-excited quantum-dot laser [Jahnke et al., 2016]. Additionally we introduced a simplified explanation based on Dicke states that could easily be transformed into a master equation approach [Neumeier, 2016].

Outlook and future prospects The directions of future research is hard to predict and is influenced by many factors. In this paragraph, we list the most obvious extensions of the presented work and some additional promising ideas.

The investigations on bimodal lasers have led to two new questions: (i) On the one hand the unconventional coherent coupling studies indicated a regime change in dependence from coupling strength and the detuning (Fig. 4.8). Currently there is no experimental evidence that shows these features and studies their impact on the laser properties. (ii) On the other hand, it has recently been found out that there is a close connection between multi-mode lasers and the physics of equilibrium Bose-Einstein condensation [Leymann et al., 2016]. This new insight allows for the question of whether these previously separated research topics can mutually benefit.

The study of super-/ subradiant coupling showed that already the lowest order of inter-emitter coupling can reproduce the experimentally observed features. Naturally an analysis of higher order coupling is necessary to gain a deeper understanding of those features. In addition a more detailed analysis of inhomogeneous broadening that is always present in quantum-dot lasers could provide a clear measure when super-/ subradiant coupling is important for a specific experiment. Moreover, the fluctuations in subradiant regime can be studied better with above mentioned master equation for superradiance that allows for the calculation of the full photon statistics.

Recently it has been shown that the complete photon statistics can be experimentally determined with a transition edge sensor [Schlottmann et al., 2016]. This technology now enables us to compare our calculations of the full photon statistics to experimental results without the direct measurement of $g^{(2)}(0)$. The specific shape of the two-photon statistics which have been predicted with our master equation approach [Leymann et al., 2013c] can be validated in the near future.

The general formalism of how to calculate the second order coherence function has been presented in chapter 2. This formalism can be used to easily calculate the autocorrelation function $g^{(2)}(\tau)$ within our theory. It can be anticipated that this theory can be generalized for calculating higher-order coherence functions which have not been examined for this system till the present day.

We also suggest to extend the usage of the master equation approach, as discussed for bimodal lasers and super-/ subradiant lasers. This approach could be used to verify explanation attempts or even hand weaving explanations of physical circumstances that could be comprehended in a simple picture like Fig. 5.10.

Finally, we would like to highlight the computer-aided cluster expansion. The field of application is certainly much wider than our investigations on quantum-dot lasers have demonstrated and modifications to our open source software [Foerster et al., 2016] can easily be made.

Appendix A

Equations of motion for the microscopic bimodal laser model

In this appendix, we provide supplementary material to the second section of chapter 4. We present the equations of motion that together with Eqs. (4.2), (4.3), (4.5), (4.6) and (4.7) complete the full set of equations of motion for one-time correlation functions on the quadruplet level of the cluster expansion:

$$\frac{d}{dt}\delta(c_j^\dagger v_j b_\xi) = i(\Delta_{\xi j} + i\kappa_\xi + i\Gamma)\delta(c_j^\dagger v_j b_\xi) + g_{\xi j}\delta(c_j^\dagger c_j)(1-\delta(v_j^\dagger v_j)) + \sum_\zeta \Big[g_{\zeta j}\delta(b_\zeta^\dagger b_\xi)(\delta(c_j^\dagger c_j) - \delta(v_j^\dagger v_j)) + g_{\zeta j}\delta(c_j^\dagger c_j b_\zeta^\dagger b_\xi) - g_{\zeta j}\delta(v_j^\dagger v_j b_\zeta^\dagger b_\xi)\Big] \tag{A.1}$$

$$\frac{d}{dt}\delta(v_s^\dagger v_s) = \left(\sum_\xi g_{\xi j}\delta(c_s^\dagger v_s b_\xi) + \text{H.c.}\right) - \delta(v_p^\dagger, v_p)(1-\delta(v_s^\dagger, v_s))\tau_v^{-1} + \delta(c_s^\dagger c_s)(1-\delta(v_s^\dagger v_s))\tau_{nl}^{-1} \tag{A.2}$$

$$\frac{d}{dt}\delta(v_p^\dagger v_p) = -P(\delta(v_p^\dagger v_p) - \delta(c_p^\dagger c_p)) + \delta(v_p^\dagger, v_p)(1-\delta(v_s^\dagger, v_s))\tau_v^{-1} + \delta(c_p^\dagger c_p)(1-\delta(v_p^\dagger v_p))\tau_{sp}^{-1} \tag{A.3}$$

$$\frac{d}{dt}\delta(c_j^\dagger c_j b_\xi^\dagger b_\zeta) = -(\kappa_\xi + \kappa_\zeta)\delta(c_j^\dagger c_j b_\xi^\dagger b_\zeta) - g_{\xi j}\delta(c_j^\dagger c_j)\delta(c_j^\dagger v_j b_\zeta) - g_{\zeta j}\delta(c_j^\dagger c_j)\delta(v_j^\dagger c_j b_\xi^\dagger) - \sum_{\xi'} g_{\xi' j}\Big(\delta(c_j^\dagger v_j b_\xi^\dagger b_{\xi'} b_\zeta) - \delta(c_j^\dagger v_j b_\zeta)\delta(b_\xi^\dagger b_{\xi'}) - \delta(v_j^\dagger c_j b_{\xi'}^\dagger b_\xi^\dagger b_\zeta) - \delta(v_j^\dagger c_j b_\xi^\dagger)\delta(b_{\xi'}^\dagger b_\zeta)\Big) \tag{A.4}$$

$$\frac{d}{dt}\delta(v_j^\dagger v_j b_\xi^\dagger b_\zeta) = -(\kappa_\xi + \kappa_\zeta)\delta(v_j^\dagger v_j b_\xi^\dagger b_\zeta) + \sum_{\xi'}\Big[g_{\xi' j}\delta(c_j^\dagger v_j b_\xi^\dagger b_{\xi'} b_\zeta) + g_{\xi' j}\delta(c_j^\dagger v_j b_\zeta)(1-\delta(v_j^\dagger v_j) + \delta(b_\xi^\dagger b_{\xi'})) + g_{\xi' j}\delta(v_j^\dagger c_j b_{\xi'}^\dagger b_\xi^\dagger b_\zeta) + g_{\xi' j}\delta(v_j^\dagger c_j b_\xi^\dagger)(1-\delta(v_j^\dagger v_j) + \delta(b_{\xi'}^\dagger b_\zeta))\Big] \tag{A.5}$$

$$\frac{d}{dt}\delta(c_j^\dagger v_j b_\xi^\dagger b_\zeta b_{\xi'}) = i[\Delta_{\xi' j} + \Delta_{\zeta j} - \Delta_{\xi j} + i(\kappa_\xi + \kappa_\zeta + \kappa_{\xi'}) + i\Gamma]\delta(c_j^\dagger v_j b_\xi^\dagger b_\zeta b_{\xi'})$$
$$- g_{\xi' j}\delta(c_j^\dagger c_j)(\delta(v_j^\dagger v_j b_\xi^\dagger b_\zeta) - \delta(v_j^\dagger v_j b_\xi^\dagger b_{\xi'}) + \delta(b_{\zeta'}^\dagger, b_\xi^\dagger b_\zeta b_{\xi'}))$$
$$+ \sum_{\zeta'}\Big[g_{\zeta' j}\delta(c_j^\dagger c_j b_\xi^\dagger b_\zeta)(1 - \delta(v_j^\dagger v_j) + \delta(b_{\zeta'}^\dagger b_{\xi'})) + g_{\zeta' j}\delta(c_j^\dagger c_j b_\xi^\dagger b_{\xi'})(1 - \delta(v_j^\dagger v_j) - \delta(b_{\zeta'}^\dagger b_\zeta))$$
$$- 2g_{\zeta' j}\delta(c_j^\dagger v_j b_\zeta)\delta(c_j^\dagger v_j b_{\xi'}) - g_{\zeta' j}\delta(v_j^\dagger v_j)\delta(b_{\zeta' j}^\dagger b_\xi^\dagger b_\zeta b_{\xi'})$$
$$-g_{\zeta' j}\delta(v_j^\dagger v_j b_\xi^\dagger b_\zeta)\delta(b_{\zeta'}^\dagger b_{\xi'}) - g_{\zeta' j}\delta(v_j^\dagger v_j b_\xi^\dagger b_{\xi'})\delta(b_{\zeta'}^\dagger b_\zeta)\Big] \quad \text{(A.6)}$$

$$\frac{d}{dt}\delta(v_j^\dagger c_j b_\xi^\dagger b_\zeta^\dagger b_{\xi'}) = i[-\Delta_{\xi j} - \Delta_{\zeta j} + \Delta_{\xi' j} + i(\kappa_\xi + \kappa_\zeta + \kappa_{\xi'}) + i\Gamma]\delta(v_j^\dagger c_j b_\xi^\dagger b_\zeta^\dagger b_{\xi'})$$
$$- g_j\delta(c_j^\dagger c_j)(\delta(v_j^\dagger v_j b_\xi^\dagger b_{\xi'}) - \delta(v_j^\dagger v_j b_\zeta^\dagger b_{\xi'}) + \delta(b_\xi^\dagger b_\zeta^\dagger b_n b_{\xi'}))$$
$$+ \sum_{\zeta'}\Big[g_{\zeta' j}\delta(c_j^\dagger c_j b_\xi^\dagger b_{\xi'})(1 - \delta(v_j^\dagger v_j) + \delta(b_\zeta^\dagger b_{\zeta'})) + g_{\zeta' j}\delta(c_j^\dagger c_j b_\zeta^\dagger b_{\xi'})(1 - \delta(v_j^\dagger v_j) + \delta(b_\xi^\dagger b_{\zeta'}))$$
$$- 2g_{\zeta' j}\delta(v_j^\dagger c_j b_\xi^\dagger)\delta(v_j^\dagger c_j b_\zeta^\dagger) - g_{\zeta' j}\delta(v_j^\dagger v_j)\delta(b_\xi^\dagger b_\zeta^\dagger b_{\zeta'} b_{\xi'})$$
$$-g_{\zeta' j}\delta(v_j^\dagger v_j b_\xi^\dagger b_{\xi'})\delta(b_\zeta^\dagger b_{\zeta'}) - g_{\zeta' j}\delta(v_j^\dagger v_j b_\zeta^\dagger b_{\xi'})\delta(b_\xi^\dagger b_{\zeta'})\Big] \quad \text{(A.7)}$$

Appendix B

Details of the laser theory formulated in configuration operators

In this appendix, we provide supplementary material to chapter 5.

B.1 Configuration operators

The confinement of electrons and holes in a QD in all three spatial dimensions leads to states with discrete energies. Because of the finite height of the confinement potential, a QD can provide only a limited number of electronic single-particle states. Distributing carriers in these states results in electronic configurations as shown in Fig. 5.1. The corresponding many-particle Hilbert space vectors $|i\rangle$ define the basis states of our QD model. For simplicity, we restrict ourselves to charge neutral states within one spin system, which couples to one circular polarization of the light field. A generalization to charged multi-exciton states or to QDs with a different level structure is possible without changing the fundamental aspects of this formulation. The electronic state of all carriers confined in multiple QDs is described by the tensor product of all single QD states:

$$|\psi\rangle = |i\rangle^1 |j\rangle^2 \cdots |k\rangle^\alpha \cdots |l\rangle^N, \tag{B.1}$$

where $|k\rangle^\alpha$ denotes QD α to be in configuration k. We assume that the QDs are spatially well separated. Therefore, the carriers confined in different QDs can be treated as distinguishable particles and we do not have to antisymmetrize the vector $|\psi\rangle$. In fact, the position of the configuration state $|k\rangle^\alpha$ in the tensor product is irrelevant since the index α always denotes a specific QD

$$|i\rangle^1 \cdots |j\rangle^\alpha |k\rangle^\beta \cdots |l\rangle^N = |i\rangle^1 \cdots |k\rangle^\beta |j\rangle^\alpha \cdots |l\rangle^N. \tag{B.2}$$

We define the QD configuration operators

$$Q_{ij}^\alpha = |i\rangle^\alpha \langle j|^\alpha \tag{B.3}$$

mapping the configuration j of QD α to the configuration i of the same QD. The algebraic properties of the configuration operators follow from the fact that all configuration states of the same QD are orthonormal, $\langle i^\alpha | j^\alpha \rangle = \delta_{ij}$, and can be summarized

by the commutation relation

$$[Q^{\alpha}_{ij}, Q^{\beta}_{kl}] = (Q^{\alpha}_{il}\delta_{j,k} - Q^{\alpha}_{kj}\delta_{l,i})\delta_{\alpha,\beta}. \tag{B.4}$$

To illustrate our approach and to connect it to former theories we give a few examples on how one can construct single-particle operators in second quantization with the configuration operators Q^{α}_{ij} for the model QD illustrated in Fig. 5.1. In the following $c_s^{(\dagger)\alpha}$ annihilates (creates) a conduction-band carrier in the single-particle s-state of QD α and $v_p^{(\dagger)\beta}$ annihilates (creates) a valence-band carrier in the single-particle p-state of QD β. Contributions from all configurations containing an (un)occupied single-particle state must be summed up to represent the corresponding single-particle operator. For example, the number operator of p-shell conduction-band electrons in QD α is given by $c_p^{\dagger\alpha}c_p^{\alpha} = Q^{\alpha}_{0_p0_p} + Q^{\alpha}_{X_pX_p} + Q^{\alpha}_{XX,XX}$. The annihilation of an s-shell electron-hole pair in QD β can be constructed by $v_s^{\dagger\beta}c_s^{\beta} = E_s^{\beta} = Q^{\beta}_{GX_s} + Q^{\beta}_{X_pXX}$. The total number of electrons in the valence band in QD γ is given by $\sum_i v_i^{\dagger\gamma}v_i^{\gamma} = 2Q^{\gamma}_{GG} + Q^{\gamma}_{X_sX_s} + Q^{\gamma}_{0_p0_p} + Q^{\gamma}_{0_s0_s} + Q^{\gamma}_{X_pX_p}$.

B.2 Equation of motion hierarchy

In this section we illustrate how the dipole Hamiltonian creates two hierarchies in the equations of motion (EoM) $\langle \dot{A} \rangle = i\langle [H, A] \rangle/\hbar$ for the photon- and QD-operator EVs. In the second half of this section we explain the technique we use to truncate this hierarchy. In terms of the configuration operators, the dipole Hamiltonian has the form

$$H_D = -i\sum_{\gamma}^{N} \tilde{g}_{\gamma} b^{\dagger}(Q^{\gamma}_{G,X_s} + Q^{\gamma}_{X_p,XX}) + \text{H.c.}, \tag{B.5}$$

where $b^{(\dagger)}$ is the photon annihilation (creation) operator of the laser mode, N is the number of QDs, and $\tilde{g}_{\alpha} = \hbar g_{\alpha}$ is the scaled light-matter interaction strength. The dipole Hamiltonian couples the photon operators of a single mode to N different QD-operators. To illustrate the structure of the hierarchies created by the dipole Hamiltonian, we first consider the time derivative of the occupation probability of the s-exciton configuration in QD α

$$\left.\frac{d}{dt}\right|_{H_D} \langle Q^{\alpha}_{X_sX_s}\rangle = -2g_{\alpha}\text{Re}\langle b^{\dagger}Q^{\alpha}_{GX_s}\rangle, \tag{B.6}$$

that couples to the photon-assisted polarization of the ground-state- to s-exciton-transition. This polarization is an EV with one additional photon operator. The EoM for the photon-assisted polarization

$$\left.\frac{d}{dt}\right|_{H_D} \langle b^{\dagger}Q^{\alpha}_{GX_s}\rangle = g_{\alpha}\langle Q^{\alpha}_{X_sX_s}\rangle + \sum_{\gamma\neq\alpha} g_{\gamma}\langle Q^{\alpha}_{GX_s}(Q^{\gamma}_{X_sG} + Q^{\gamma}_{XX,X_p})\rangle + g_{\alpha}\langle b^{\dagger}b(Q^{\alpha}_{X_sX_s} - Q^{\alpha}_{GG})\rangle$$

couples to EVs describing correlations between different QDs (second term) and to EVs describing correlations between the electronic configurations of the given QD and the cavity photons (third term). The two higher-order terms that occur here have one additional QD operator and one additional photon operator, giving rise to the mentioned hierarchies.

For the rest of this section, to make the considerations more transparent, we omit all configuration indices and prefactors and the information whether the considered photon operators create or annihilate photons. The following equations should be seen as illustrations of the hierarchy structure, that can be explored best by considering the time derivative of a general EV $\langle b^{(\dagger)n} Q^\alpha \dots Q^\omega \rangle$ containing a product of n photon operators and m QD operators addressing the QDs α to ω:

$$\left.\frac{d}{dt}\right|_{H_D} \langle b^{(\dagger)n} Q^\alpha \dots Q^\omega \rangle = \langle [H_D, b^{(\dagger)n}] Q^\alpha \dots Q^\omega \rangle$$
$$+ \langle b^{(\dagger)n} [H_D, Q^\alpha] \dots Q^\omega \rangle + \dots + \langle b^{(\dagger)n} Q^\alpha \dots [H_D, Q^\omega] \rangle.$$

We can evaluate this expression with $[H_D, b^{(\dagger)n}] = b^{(\dagger)n-1} \sum_\gamma Q^\gamma$ and $[H_D, Q^\alpha] = b^{(\dagger)} Q^\alpha$. By omitting all details and possible lower-order terms we obtain

$$\left.\frac{d}{dt}\right|_{H_D} \langle b^{(\dagger)n} Q^\alpha \dots Q^\omega \rangle = \sum_{\gamma \neq \{\alpha \dots \omega\}} \langle b^{(\dagger)n-1} Q^\alpha \dots Q^\omega Q^\gamma \rangle$$
$$+ \langle b^{(\dagger)n+1} Q^\alpha \dots Q^\omega \rangle.$$

In the first term on the right-hand side we can clearly see the emergence of QD-QD correlations that are induced by the interaction of different QDs with a common radiation field. These terms are not included in laser theories that do not account for inter-emitter coupling effects. The second term describes the coupling to higher-order photon correlations. It provides access to the next rung in the Jaynes-Cummings ladder. We see that the dipole Hamiltonian creates two different hierarchies. An EV with n photon operators and m QDs operator couples to EVs with one additional QD operator and one additional photon operator:

$$\left.\frac{d}{dt}\right|_{H_D} \langle b^{(\dagger)n} \underbrace{Q \dots Q}_{m} \rangle = \langle b^{(\dagger)n-1} \underbrace{Q \dots Q}_{m+1} \rangle + \langle b^{(\dagger)n+1} \underbrace{Q \dots Q}_{m} \rangle.$$

The first hierarchy only terminates exactly *i)* at the order $m = N$, where N is the number of QDs. Including the EV $\langle b^n \underbrace{Q \dots Q}_{N} \rangle$ i.e. all QD N operators of the system ($\Delta^{\mathcal{Q}}_{\langle N \rangle}$ in terms of the truncation operator from chapter 2). The second hierarchy only terminates exactly if *ii)* the photonic state of the system can be represented by a finite linear combination of Fock states. We need approximations to truncate the hierarchies consistently and at a computable level. Being interested in systems where up to several hundred QDs take part in the dynamics, it is impossible to match condition *i)* numerically. Condition *ii)* cannot be fulfilled because we are studying laser systems, whose coherent states cannot be represented by a small number of Fock states.

We introduce a variant of the well-established cluster expansion (see chapter 2) which we refer to as the configuration cluster expansion (CCE). The main differences of our formulation to the traditional cluster expansion [Kira et al., 1998] are that *a*) we formulate our theory in EVs instead of correlation functions (see chapter 2) and, more importantly, *b*) the electronic state of the QDs is described by the configuration operators Q_{ij}^{α} instead of single-particle creation (annihilation) operators. The configuration operators are considered as the elementary constituents of our theory and therefore the factorization of EVs is done in terms of the configuration operators. This method reduces the algebraic effort to a minimum and ensures that all many-particle states of the confined QD carriers are treated without further approximation.

In our system the two-particle nature of the dipole Hamiltonian is the source of higher-order correlations and the hierarchies in the EoM must be truncated according to the structure of the dipole Hamiltonian (see chapter 2). As we have shown, the dipole Hamiltonian couples a single-mode photon operator to all QD operators and hereby creates two hierarchies, one in the photonic and one in the electronic part of the part of the Hilbert space. To truncate the hierarchies all EVs containing a total number of operators ($b^{(\dagger)}$ and Q) larger than the desired order are factorized ($\Delta_{\delta(4)}^{\mathcal{Q}+\mathcal{B}}$). The factorization of the EV is accomplished by neglecting the corresponding correlation function according to the cluster expansion (see chapter 2). The intensity $I = \langle b^{\dagger} b \rangle$ is of second order. The photon autocorrelation function at zero delay time $G^{(2)}(0) = \langle b^{\dagger} b^{\dagger} b b \rangle$ and the correlated two-photon emission function $\langle b^{\dagger} b^{\dagger} E^{\alpha} E^{\beta} \rangle$ are both of fourth order. The fourth order of the CCE used in this chapter provides information about the photon statistics $g^{(2)}(0)$ Eq. (1.42). Additionally we introduce a truncation that addresses the QD-QD correlations. We use two variants of the theory: one with and one without inter-emitter correlations. To systematically neglect QD-QD correlations we factorize all EVs addressing two different QDs according to

$$\langle Q_{ij}^{\alpha} Q_{kl}^{\beta} \rangle \approx \langle Q_{ij}^{\alpha} \rangle \langle Q_{kl}^{\beta} \rangle, \tag{B.7}$$

which corresponds to a mean-field approximation[1] and the assumption of individual emitters ($\Delta_{\delta(1)}^{\mathcal{Q}}$). To take radiation-induced QD-QD correlations into account we have to include EVs of the form $\langle Q_{ij}^{\alpha} Q_{kl}^{\beta} \rangle$. At this level, three-QD EVs are factorized according to

$$\begin{aligned} \langle Q_{ij}^{\alpha} Q_{kl}^{\beta} Q_{mn}^{\gamma} \rangle \approx{}& \langle Q_{ij}^{\alpha} Q_{kl}^{\beta} \rangle \langle Q_{mn}^{\gamma} \rangle + \langle Q_{ij}^{\alpha} \rangle \langle Q_{kl}^{\beta} Q_{mn}^{\gamma} \rangle \\ &+ \langle Q_{kl}^{\beta} \rangle \langle Q_{ij}^{\alpha} Q_{mn}^{\gamma} \rangle - 2 \langle Q_{ij}^{\alpha} \rangle \langle Q_{kl}^{\beta} \rangle \langle Q_{mn}^{\gamma} \rangle, \end{aligned} \tag{B.8}$$

which corresponds to the application of $\Delta_{\delta(2)}^{\mathcal{Q}}$ and is formally equivalent to the Bogoliubov back-reaction method mentioned in chapter 2. In this way, our theory enables us to directly switch the QD-QD correlation effects on and off and to compare our approach to laser theories, in which QD-QD correlations are not contained, e.g. Refs. [Gies et al., 2007; Wiersig et al., 2009; Rice and Carmichael, 1994].

[1] Since we are using configuration operators that automatically treat all carriers confined to a QD exactly this mean-field means that the confined carriers in a QD are in the mean-field of all other carriers in the other QDs

B.3 Coupling to the continuum states

In this section we discuss the influence of the continuum states that arise from the interaction of QD carriers with carriers in the wetting-layer and barrier states, as well as the out-coupling of photons from the cavity. These environment states are not represented by configuration and photon operators but by the Lindblad form

$$\left.\frac{d}{dt}\right|_{\text{Lindblad}} \langle A\rangle = \sum_i \gamma_{\eta_i} \langle [\eta_i^\dagger, A]\eta_i + \eta_i^\dagger [A, \eta_i]\rangle$$

in the general EoM. First, we enlist the various microscopic processes generated by the operators η_i that are triggered by the coupling of the confined-state carriers to the continuum states. Then we give explicit examples for the resulting terms in the EoM, showing that the process η_i transfers occupation probability from one configuration to another while dephasing the corresponding polarization.

The microscopic processes in QD α are the following: electron-hole capture in the QD p-shell with rate P^α (pump) generated by $\eta^\alpha_{P,1} = Q^\alpha_{X_pG}$ and $\eta^\alpha_{P,2} = Q^\alpha_{XX,X_s}$, carrier relaxation from the p-shell to the s-shell in the conduction band generated by $\eta^\alpha_{\text{r},c,1} = Q^\alpha_{X_s0_p}$ and $\eta^\alpha_{\text{r},c,2} = Q^\alpha_{0_sX_p}$, carrier relaxation from the s-shell to the p-shell in the valence band generated by $\eta^\alpha_{\text{r},v,1} = Q^\alpha_{X_s0_s}$ and $\eta^\alpha_{\text{r},v,2} = Q^\alpha_{0_pX_p}$ with the rates $\gamma^\alpha_{\text{r},\{c,v\}}$ respectively, spontaneous losses of electron hole pairs in the p-shell generated by $\eta^{\alpha,p}_{\text{spont},1} = Q^\alpha_{GX_p}$ and $\eta^{\alpha,p}_{\text{spont},2} = Q^\alpha_{X_sXX}$, and in the s-shell generated by $\eta^{\alpha,s}_{\text{spont},1} = Q^\alpha_{GX_s}$ and $\eta^{\alpha,s}_{\text{spont},2} = Q^\alpha_{X_pXX}$ with the rates $\gamma^{\alpha,\{s,p\}}_{\text{spont}}$ and the cavity-photon losses $\eta_{\text{ph}} = b$ with the loss rate κ.

As a first example we discuss the impact of spontaneous electron-hole recombination in the s-shell on the s-exciton configuration

$$\left.\frac{d}{dt}\right|_{\eta^\alpha_{\text{spont},s}} \langle Q^\alpha_{X_sX_s}\rangle = -2\gamma^{\alpha,s}_{\text{spont}} \langle Q^\alpha_{X_sX_s}\rangle, \tag{B.9}$$

the ground-state configuration

$$\left.\frac{d}{dt}\right|_{\eta^\alpha_{\text{spont},s}} \langle Q^\alpha_{GG}\rangle = +2\gamma^{\alpha,s}_{\text{spont}} \langle Q^\alpha_{X_sX_s}\rangle, \tag{B.10}$$

and the photon-assisted polarization between the ground- and s-exciton state

$$\left.\frac{d}{dt}\right|_{\eta^\alpha_{\text{spont},s}} \langle b^\dagger Q^\alpha_{GX_s}\rangle = -\gamma^{\alpha,s}_{\text{spont}} \langle b^\dagger Q^\alpha_{GX_s}\rangle. \tag{B.11}$$

The process generates a direct transfer of population from the s-exciton to the ground state and dephases the polarization between these states. Note that no additional terms are needed to take account for Pauli-blocking. As a second example, we discuss the impact of carrier relaxation in QD α from the s-shell to the p-shell in the valence band on the correlation between the p-exciton configuration of QD α and the ground-state configuration of QD β

$$\left.\frac{d}{dt}\right|_{\eta^\alpha_{\text{r},v}} \langle Q^\alpha_{X_pX_p} Q^\beta_{GG}\rangle = -2\gamma^\alpha_{\text{r},v} \langle Q^\alpha_{X_pX_p} Q^\beta_{GG}\rangle, \tag{B.12}$$

the correlation between the dark p-shell configuration of QD α and the ground-state configuration of QD β

$$\left.\frac{d}{dt}\right|_{\eta^{\alpha}_{\mathrm{r},v}} \langle Q^{\alpha}_{0_p0_p} Q^{\beta}_{GG}\rangle = +2\gamma^{\alpha}_{\mathrm{r},v}\langle Q^{\alpha}_{X_pX_p} Q^{\beta}_{GG}\rangle, \tag{B.13}$$

and on the correlation between the photon-assisted polarization of the p-exciton configuration and biexciton configuration in QD α and the ground-state configuration of QD β

$$\left.\frac{d}{dt}\right|_{\eta^{\alpha}_{\mathrm{r},v}} \langle b^{\dagger} Q^{\alpha}_{X_pXX} Q^{\beta}_{GG}\rangle = -\gamma^{\alpha}_{\mathrm{r},v}\langle b^{\dagger} Q^{\alpha}_{X_pXX} Q^{\beta}_{GG}\rangle. \tag{B.14}$$

As in the example before, the microscopic process generates a direct transfer of population from one configuration to the other and dephases a polarization connected to the initial state. In this example, all occupations and processes in QD α are correlated with an occupation in QD β. However, since the microscopic process $\eta^{\alpha}_{\mathrm{r},v}$ takes place in QD α it has no influence on a possible correlation with QD β.

B.4 Total emission rate into the laser mode

The total emission rate into the laser mode, Γ_{em}, can be obtained from the EoM for the mean photon number

$$\begin{aligned}\frac{d}{dt}\langle b^{\dagger}b\rangle =& -2\kappa\langle b^{\dagger}b\rangle + 2\sum_{\alpha} g_{\alpha}\mathrm{Re}(\langle b^{\dagger}Q^{\alpha}_{GX_s}\rangle + \langle b^{\dagger}Q^{\alpha}_{X_pXX}\rangle)\\ =& -2\kappa\langle b^{\dagger}b\rangle + \Gamma_{\mathrm{em}}\ .\end{aligned} \tag{B.15}$$

To simplify the discussion in the main text, an approximate expression of Γ_{em} has been used there. This facilitates a comparison to laser theories that consider only one bright configuration, i.e. [Rice and Carmichael, 1994]. In the following, we derive the exact expression that is used to compute the curves in Fig. 5.4. To this end we solve the EoM for the photon-assisted polarization adiabatically and insert the solution into Eq. (B.15). The adiabatic solution for the photon-assisted polarization of the s-exciton and biexciton can be written as

$$\begin{aligned}\langle b^{\dagger}Q^{\alpha}_{GX_s}\rangle =& g\tau^{X}_{\mathrm{Deph}}\sum_{\beta\neq\alpha}\langle Q^{\alpha}_{GX_s}(Q^{\beta}_{X_sG} + Q^{\beta}_{XX,X_p})\rangle\\ &+g\tau^{X}_{\mathrm{Deph}}\left(\langle b^{\dagger}b(Q^{\alpha}_{X_sX_s} - Q^{\alpha}_{GG})\rangle + \langle Q^{\alpha}_{X_sX_s}\rangle\right)\ ,\end{aligned} \tag{B.16}$$

$$\begin{aligned}\langle b^{\dagger}Q^{\alpha}_{X_p,XX}\rangle =& g\tau^{XX}_{Deph}\sum_{\beta\neq\alpha}\langle Q^{\alpha}_{X_p,XX}(Q^{\beta}_{X_sG} + Q^{\beta}_{XX,X_p})\rangle\\ &+g\tau^{XX}_{\mathrm{Deph}}\left(\langle b^{\dagger}b(Q^{\alpha}_{XX,XX} - Q^{\alpha}_{X_pX_p})\rangle + \langle Q^{\alpha}_{XX,XX}\rangle\right)\end{aligned} \tag{B.17}$$

respectively, with the exciton and biexciton dephasing times

$$\tau^{X}_{\mathrm{Deph}} = \frac{1}{\kappa + \gamma_{\mathrm{spont}} + 2P},$$

and

$$\tau_{\mathrm{Deph}}^{XX} = \frac{1}{\kappa + 2\gamma_{\mathrm{r}} + 3\gamma_{\mathrm{spont}}}.$$

For the sake of simplicity of our discussion, we choose the light-matter interaction $g_\alpha = g$, and relaxation and spontaneous loss rates $\gamma_{\mathrm{spont}}^{\alpha,\{s,p\}} = \gamma_{\mathrm{spont}}$, $\gamma_{\mathrm{r},\{s,p\}}^{\alpha} = \gamma_{\mathrm{r}}$ to be equal for all QDs. Comparison to Eq. (B.15) leads to an expression of the total emission rate in terms of the right-hand side of Eqs. (B.16) and (B.17)

$$\begin{aligned}
\Gamma_{\mathrm{em}} = {} & 2g^2\tau_{\mathrm{Deph}}^{X} \sum_{\beta\neq\alpha} \langle Q_{GX_s}^{\alpha}(Q_{X_sG}^{\beta} + Q_{XX,X_p}^{\beta})\rangle \\
& + 2g^2\tau_{\mathrm{Deph}}^{X} \sum_{\alpha} \langle b^\dagger b(Q_{X_sX_s}^{\alpha} - Q_{GG}^{\alpha})\rangle + 2g^2\tau_{\mathrm{Deph}}^{X} \sum_{\alpha} \langle Q_{X_sX_s}^{\alpha}\rangle \\
& + 2g^2\tau_{\mathrm{Deph}}^{XX} \sum_{\beta\neq\alpha} \langle Q_{X_p,XX}^{\alpha}(Q_{X_sG}^{\beta} + Q_{XX,X_p}^{\beta})\rangle \\
& + 2g^2\tau_{\mathrm{Deph}}^{XX} \sum_{\alpha} \langle b^\dagger b(Q_{XX,XX}^{\alpha} - Q_{X_pX_p}^{\alpha})\rangle + 2g^2\tau_{\mathrm{Deph}}^{XX} \sum_{\alpha} \langle Q_{XX,XX}^{\alpha}\rangle \ . \qquad \text{(B.18)}
\end{aligned}$$

To connect our results to theories that consider only one bright configuration, the assumption of equal dephasing of the bright configurations allows the definition of a common dephasing rate

$$\tau_{\mathrm{Deph}}^{-1} \approx 2g^2\tau_{\mathrm{Deph}}^{X} \approx 2g^2\tau_{\mathrm{Deph}}^{XX} \ .$$

Rewriting Eq. (B.18) in terms of the dipole operator $D^\alpha = E_s^{\dagger\alpha} + E_s^\alpha$ we obtain the simple form of Eq. (5.7) for the total emission rate used in the main text:

$$\begin{aligned}
\Gamma_{\mathrm{em}} &= \frac{\sum_\alpha \langle D^\alpha D^\alpha\rangle}{\tau_{\mathrm{Deph}}} + \frac{\sum_{\beta\neq\alpha}\langle D^\alpha D^\beta\rangle}{\tau_{\mathrm{Deph}}} + \frac{\langle b^\dagger b\mathrm{Inv}\rangle}{\tau_{\mathrm{Deph}}} \\
&= \Gamma_{\mathrm{spont}} + \Gamma_{\mathrm{sr}} + \Gamma_{\mathrm{stim}}
\end{aligned}$$

with the total inversion operator defined as

$$\mathrm{Inv} = \sum_\alpha (Q_{XX,XX}^{\alpha} - Q_{X_pX_p}^{\alpha} + Q_{X_sX_s}^{\alpha} - Q_{GG}^{\alpha}) \ .$$

Note that in all numerical calculations, the correct dephasing rates are used.

Appendix C

Factorization with fermion anticommutation relations

The following lines of code are an exemplary implementation of fermionic anticommutation relations in the CE [Fricke, 1996b]. The introduction of this additional procedure is necessary because `distrib_(type,n,f1,f2,x1,...,xm)` does not respect the sign change when two fermi operators are swapped. Therefore, our exemplary code should be added in line 14 in the factorization and refactorization in Sec. 3.4.4 when fermi creation and annihilation operators are used. The fermi operators `[c],[c+]` and the non commutative auxiliary function `SIG` have to be declared as new functions in the header of the main file `function [c],[c+],SIG;`. The sign of the factorized/refactorized EV or CF is determined inside the function `SIG` with the usage of anticommutation relations.

```
1  id L=L*SIG;
2
3  repeat;
4  id SIG(?a)*'ff'(?b)=SIG(?a,?b)*'f'(?b);
5  endrepeat;
6
7  #call commatoproduct(SIG,SIG)
8
9  argument SIG;
10
11         repeat;
12                 id  [c](?j)*[b+]?bose(?i)=[b+](?i)*[c](?j);
13                 id  [c+](?j)*[b+]?bose(?i)=[b+](?i)*[c+](?j);
14         endrepeat;
15
16         repeat;
17           id disorder [c+](?i)*[c+](?j)=-[c+](?j)*[c+](?i);
18           id disorder [c](?i)*[c](?j)=-[c](?j)*[c](?i);
19         endrepeat;
20
21 id [c]?(?a)=1;
22 endargument;
23
24 id SIG(1)=1;
25 id SIG(-1)=-1;
```

We introduce the sign keeping function and copy all the information of the function 'ff' (CF or EV) into the functions SIG and 'f' (cf or ev). The following operations are only executed in the function SIG . Basically we are establishing the standard order inside this function and replace afterwards all operators inside the function by 1. The lines 16 to 19 are the anticommutation relations of the fermi operators. The last lines of this code replace the argument of the auxiliary function SIG by 1 or -1.

Bibliography

Albert, F., Hopfmann, C., Reitzenstein, S., Schneider, C., Höfling, S., Worschech, L., Kamp, M., Kinzel, W., Forchel, A., and Kanter, I. (2011). Observing chaos for quantum-dot microlasers with external feedback. *Nat Commun*, 2:366.

Albert, F., Sivalertporn, K., Kasprzak, J., Strauß, M., Schneider, C., Höfling, S., Kamp, M., Forchel, A., Reitzenstein, S., Muljarov, E. A., and Langbein, W. (2013). Microcavity controlled coupling of excitonic qubits. *Nat Commun*, 4:1747.

Alferov, Z. (1970). Electroluminescence of heavily-doped heterojunctions palxga1-xas-ngaas. *JOL*, 1:869 – 884.

Alferov, Z. I. (2001). Nobel Lecture: The double heterostructure concept and its applications in physics, electronics, and technology. *Rev. Mod. Phys.*, 73(3):767–782.

Andreani, L. C., Panzarini, G., and Gérard, J.-M. (1999). Strong-coupling regime for quantum boxes in pillar microcavities: Theory. *Phys. Rev. B*, 60(19):13276–13279.

Arakawa, Y. and Sakaki, H. (1982). Multidimensional quantum well laser and temperature dependence of its threshold current. *Appl. Phys. Lett.*, 40(11):939–941.

Aßmann, M., Veit, F., Bayer, M., Gies, C., Jahnke, F., Reitzenstein, S., Höfling, S., Worschech, L., and Forchel, A. (2010). Ultrafast tracking of second-order photon correlations in the emission of quantum-dot microresonator lasers. *Phys. Rev. B*, 81(16):165314.

Aßmann, M., Veit, F., Bayer, M., Poel, M. v. d., and Hvam, J. M. (2009). Higher-Order Photon Bunching in a Semiconductor Microcavity. *Science*, 325(5938):297–300.

Ates, S., Gies, C., Ulrich, S. M., Wiersig, J., Reitzenstein, S., Löffler, A., Forchel, A., Jahnke, F., and Michler, P. (2008). Influence of the spontaneous optical emission factor β on the first-order coherence of a semiconductor microcavity laser. *Phys. Rev. B*, 78(15):155319.

Ates, S., Ulrich, S. M., Michler, P., Reitzenstein, S., Löffler, A., and Forchel, A. (2007). Coherence properties of high-β elliptical semiconductor micropillar lasers. *Appl. Phys. Lett.*, 90(16):161111.

Auffèves, A., Gerace, D., Portolan, S., Drezet, A., and Santos, M. F. (2011). Few emitters in a cavity: from cooperative emission to individualization. *New J. Phys.*, 13(9):093020.

Auffèves, A., Gérard, J.-M., and Poizat, J.-P. (2009). Pure emitter dephasing: A resource for advanced solid-state single-photon sources. *Phys. Rev. A*, 79:053838.

Avenhaus, M., Laiho, K., Chekhova, M. V., and Silberhorn, C. (2010). Accessing Higher Order Correlations in Quantum Optical States by Time Multiplexing. *Phys. Rev. Lett.*, 104(6):063602.

Baer, N., Gies, C., Wiersig, J., and Jahnke, F. (2006). Luminescence of a semiconductor quantum dot system. *Eur. Phys. J. B*, 50(3):411–418.

Baer, N., Schulz, S., Gartner, P., Schumacher, S., Czycholl, G., and Jahnke, F. (2007). Influence of symmetry and Coulomb correlation effects on the optical properties of nitride quantum dots. *Phys. Rev. B*, 76:075310.

Baer, N., Schulz, S., Schumacher, S., Gartner, P., Czycholl, G., and Jahnke, F. (2005). Optical properties of self-organized wurtzite innâgan quantum dots: A combined atomistic tight-binding and full configuration interaction calculation. *Appl. Phys. Lett.*, 87(23).

Baudouin, Q., Mercadier, N., Guarrera, V., Guerin, W., and Kaiser, R. (2013). A cold-atom random laser. *Nat Phys*, 9(6):357–360.

Baumann, K., Guerlin, C., Brennecke, F., and Esslinger, T. (2010). Dicke quantum phase transition with a superfluid gas in an optical cavity. *Nature*, 464(7293):1301–1306.

Bayer, M., Reinecke, T. L., Weidner, F., Larionov, A., McDonald, A., and Forchel, A. (2001). Inhibition and Enhancement of the Spontaneous Emission of Quantum Dots in Structured Microresonators. *Phys. Rev. Lett.*, 86(14):3168–3171.

Bienaimé, T., Bachelard, R., Piovella, N., and Kaiser, R. (2013). Cooperativity in light scattering by cold atoms. *Fortschr. Phys.*, 61(2-3):377–392.

Bimberg, D., Grundmann, M., and Ledentsov, N. N. (1999). *Quantum dot heterostructures*. John Wiley & Sons.

Björk, G., Karlsson, A., and Yamamoto, Y. (1994). Definition of a laser threshold. *Phys. Rev. A*, 50(2):1675–1680.

Bohnet, J. G., Chen, Z., Weiner, J. M., Meiser, D., Holland, M. J., and Thompson, J. K. (2012). A steady-state superradiant laser with less than one intracavity photon. *Nature*, 484(7392):78–81.

Breuer, H.-P. and Petruccione, F. (2002). *The Theory of Open Quantum Systems*. Oxford University Press.

Brune, M., Schmidt-Kaler, F., Maali, A., Dreyer, J., Hagley, E., Raimond, J. M., and Haroche, S. (1996). Quantum Rabi Oscillation: A Direct Test of Field Quantization in a Cavity. *Phys. Rev. Lett.*, 76(11):1800–1803.

Cao, H. and Wiersig, J. (2015). Dielectric microcavities: Model systems for wave chaos and non-Hermitian physics. *Rev. Mod. Phys.*, 87(1):61–111.

Carmele, A., Kabuss, J., Schulze, F., Reitzenstein, S., and Knorr, A. (2013). Single Photon Delayed Feedback: A Way to Stabilize Intrinsic Quantum Cavity Electrodynamics. *Phys. Rev. Lett.*, 110(1):013601.

Carmele, A., Knorr, A., and Richter, M. (2009). Photon statistics as a probe for exciton correlations in coupled nanostructures. *Phys. Rev. B*, 79(3):035316.

Carmele, A., Richter, M., Chow, W. W., and Knorr, A. (2010). Antibunching of Thermal Radiation by a Room-Temperature Phonon Bath: A Numerically Solvable Model for a Strongly Interacting Light-Matter-Reservoir System. *Phys. Rev. Lett.*, 104(15):156801.

Carmichael, P. H. J. (1999). Dissipation in Quantum Mechanics: The Master Equation Approach. In *Statistical Methods in Quantum Optics 1*, Texts and Monographs in Physics, pages 1–28. Springer Berlin Heidelberg.

Chen, G.-Y., Lambert, N., Li, C.-M., Chen, Y.-N., and Nori, F. (2012). Delocalized single-photon Dicke states and the Leggett-Garg inequality in solid state systems. *Sci. Rep.*, 2.

Chow, W. W., Jahnke, F., and Gies, C. (2014). Emission properties of nanolasers during the transition to lasing. *Light Sci Appl*, 3(8):e201.

Chow, W. W. and Koch, S. W. (1999). *Semiconductor-Laser Fundamentals: Physics of the Gain Materials*. Springer Science Business Media.

Chow, W. W., Liu, A. Y., Gossard, A. C., and Bowers, J. E. (2015). Extraction of inhomogeneous broadening and nonradiative losses in InAs quantum-dot lasers. *Appl. Phys. Lett.*, 107(17):171106.

Dähne, M., Eisele, H., and Jacobi, K. (2008). *The Atomic Structure of Quantum Dots*, pages 123–137. Springer Berlin Heidelberg, Berlin, Heidelberg.

Dayan, B., Parkins, A. S., Aoki, T., Ostby, E. P., Vahala, K. J., and Kimble, H. J. (2008). A Photon Turnstile Dynamically Regulated by One Atom. *Science*, 319(5866):1062–1065.

del Valle, E., Laussy, F. P., and Tejedor, C. (2009). Luminescence spectra of quantum dots in microcavities. II. Fermions. *Phys. Rev. B*, 79(23):235326.

Denk, W., Strickler, J., and Webb, W. (1990). Two-photon laser scanning fluorescence microscopy. *Science*, 248(4951):73–76.

Dicke, R. H. (1954). Coherence in Spontaneous Radiation Processes. *Phys. Rev.*, 93(1):99–110.

Dingle, R. and Henry, C. H. (1976). Quantum effects in heterostructure lasers. *Patent*, US 3982207.

Dingle, R., Wiegmann, W., and Henry, C. H. (1974). Quantum states of confined carriers in very thin $Al_xGa_{1-x}As$-GaAs-$Al_xGa_{1-x}As$ heterostructures. *Phys. Rev. Lett.*, 33:827–830.

Dobrindt, J. M., Wilson-Rae, I., and Kippenberg, T. J. (2008). Parametric Normal-Mode Splitting in Cavity Optomechanics. *Phys. Rev. Lett.*, 101(26):263602.

Einstein, A. (1917). Zur Quantentheorie der Strahlung. *Physik.Zeitschr.*, 18:121–128.

Fanaei, M., Foerster, A., Leymann, H. A. M., and Wiersig, J. (2016). Effect of direct dissipative coupling of two competing modes on intensity fluctuations in a quantum-dot-microcavity laser. *Phys. Rev. A*, 94:043814.

Feldtmann, T., Schneebeli, L., Kira, M., and Koch, S. W. (2006). Quantum theory of light emission from a semiconductor quantum dot. *Phys. Rev. B*, 73(15):155319.

Ferrari, D., Celardo, G., Berman, G., Sayre, R., and Borgonovi, F. (2014). Quantum Biological Switch Based on Superradiance Transitions. *J. Phys. Chem. C*, 118(1):20–26.

Florian, M., Gartner, P., Gies, C., and Jahnke, F. (2013a). Phonon-mediated off-resonant coupling effects in semiconductor quantum-dot lasers. *New J. Phys.*, 15(3):035019.

Florian, M., Gies, C., Jahnke, F., Leymann, H. A. M., and Wiersig, J. (2013b). Equation-of-motion technique for finite-size quantum-dot systems: Cluster expansion method. *Phys. Rev. B*, 87(16):165306.

Foerster, A. (2012). *Berechnung von Korrelationsfunktionen in Halbleiter Quantenpunktsystemen*. Diploma Thesis, Magdeburg.

Foerster, A., Leymann, H. A. M., and Wiersig, J. (2016). Computer-aided cluster expansion: An efficient algebraic approach for open quantum many-particle systems. `http://dx.doi.org/10.17632/fjwxr28j3d.1`. [Online;].

Foerster, A., Leymann, H. A. M., and Wiersig, J. (2017). Computer-aided cluster expansion: An efficient algebraic approach for open quantum many-particle systems. *Computer Physics Communications*, 212:210 – 219.

Fricke, J. (1996a). Transport Equations Including Many-Particle Correlations for an Arbitrary Quantum System: A General Formalism. *Annals of Physics*, 252(2):479–498.

Fricke, J. (1996b). *Transportgleichungen für quantenmechanische Vielteilchensysteme*. Cuvillier.

Gardiner, G. W. and Zoller, P. (2001). *Quantum Noise*. Springer Verlag.

Garraway, B. M. (2011). The Dicke model in quantum optics: Dicke model revisited. *Phil. Trans. R. Soc. A*, 369(1939):1137–1155.

Garrison, J. and Chiao, R. (2014). *Quantum Optics*. Oxford University Press.

Gartner, P. (2011). Two-level laser: Analytical results and the laser transition. *Phys. Rev. A*, 84(5):053804.

Gérard, J. M., Sermage, B., Gayral, B., Legrand, B., Costard, E., and Thierry-Mieg, V. (1998). Enhanced Spontaneous Emission by Quantum Boxes in a Monolithic Optical Microcavity. *Phys. Rev. Lett.*, 81(5):1110–1113.

Gies, C., Florian, M., Gartner, P., and Jahnke, F. (2011). The single quantum dot-laser: lasing and strong coupling in the high-excitation regime. *Opt. Express*, 19(15):14370–14388.

Gies, C., Florian, M., Jahnke, F., and Gartner, P. (2012). 3 - modeling single quantum dots in microcavities. In *Quantum Optics with Semiconductor Nanostructures*, Woodhead Publishing Series in Electronic and Optical Materials, pages 78 – 114.

Gies, C., Wiersig, J., and Jahnke, F. (2008). Output Characteristics of Pulsed and Continuous-Wave-Excited Quantum-Dot Microcavity Lasers. *Phys. Rev. Lett.*, 101(6):067401.

Gies, C., Wiersig, J., Lorke, M., and Jahnke, F. (2007). Semiconductor model for quantum-dot-based microcavity lasers. *Phys. Rev. A*, 75(1):013803.

Glauber, R. J. (1963). The Quantum Theory of Optical Coherence. *Phys. Rev.*, 130(6):2529–2539.

Hall, R. N., Fenner, G. E., Kingsley, J. D., Soltys, T. J., and Carlson, R. O. (1962). Coherent light emission from gaas junctions. *Phys. Rev. Lett.*, 9:366–368.

Haug, H. and Koch, S. (2004). *Quantum Theory of the Optical and Electronic Properties of Semiconductors*. World Scientific Publishing Company.

Heck, A. (2000). `FORM` for Pedestrians. `https://www.nikhef.nl/%7eform/maindir/documentation/tutorial/online/online.html`. [Online;].

Heinze, D., Breddermann, D., Zrenner, A., and Schumacher, S. (2015). A quantum dot single-photon source with on-the-fly all-optical polarization control and timed emission. *Nat. Commun.*, 6:8473.

Hillman, L. W., Krasiński, J., Boyd, R. W., and Stroud, C. R. (1984). Observation of Higher Order Dynamical States of a Homogeneously Broadened Laser. *Phys. Rev. Lett.*, 52(18):1605–1608.

Hohenester, U. and Pötz, W. (1997). Density-matrix approach to nonequilibrium free-carrier screening in semiconductors. *Phys. Rev. B*, 56(20):13177–13189.

Hoyer, W., Kira, M., and Koch, S. W. (2003). Influence of Coulomb and phonon interaction on the exciton formation dynamics in semiconductor heterostructures. *Phys. Rev. B*, 67(15):155113.

Hoyer, W., Kira, M., and Koch, S. W. (2004). Cluster Expansion in Semiconductor Quantum Optics. In Morawetz, D. K., editor, *Nonequilibrium Physics at Short Time Scales*, pages 309–335. Springer Berlin Heidelberg.

Jahnke, F., Gies, C., Aßmann, M., Bayer, M., Leymann, H. A. M., Foerster, A., Wiersig, J., Schneider, C., Kamp, M., and Höfling, S. (2016). Giant photon bunching, superradiant pulse emission and excitation trapping in quantum-dot nanolasers. *Nat. Comm.*, 7:11540.

Jaynes, E. and Cummings, F. W. (1963). Comparison of quantum and semiclassical radiation theories with application to the beam maser. *Proceedings of the IEEE*, 51(1):89–109.

Jechow, A., Seefeldt, M., Kurzke, H., Heuer, A., and Menzel, R. (2013). Enhanced two-photon excited fluorescence from imaging agents using true thermal light. *Nat Photon*, 7(12):973–976.

Jin, R., Boggavarapu, D., Sargent, M., Meystre, P., Gibbs, H. M., and Khitrova, G. (1994). Photon-number correlations near the threshold of microcavity lasers in the weak-coupling regime. *Phys. Rev. A*, 49(5):4038–4042.

Kabuss, J., Carmele, A., Brandes, T., and Knorr, A. (2012). Optically Driven Quantum Dots as Source of Coherent Cavity Phonons: A Proposal for a Phonon Laser Scheme. *Phys. Rev. Lett.*, 109(5):054301.

Kabuss, J., Carmele, A., Richter, M., Chow, W. W., and Knorr, A. (2011). Inductive equation of motion approach for a semiconductor QD-QED: Coherence induced control of photon statistics. *Phys. Status Solidi (b)*, 248(4):872–878.

Kapetanakis, M. D. and Perakis, I. E. (2008). Spin Dynamics in (III,Mn)V Ferromagnetic Semiconductors: The Role of Correlations. *Phys. Rev. Lett.*, 101(9):097201.

Khanbekyan, M., Leymann, H. A. M., Hopfmann, C., Foerster, A., Schneider, C., Höfling, S., Kamp, M., Wiersig, J., and Reitzenstein, S. (2015). Unconventional collective normal-mode coupling in quantum-dot-based bimodal microlasers. *Phys. Rev. A*, 91(4):043840.

Khitrova, G. (1999). Nonlinear optics of normal-mode-coupling semiconductor microcavities. *Rev. Mod. Phys.*, 71(5):1591–1639.

Khurgin, J. B. and Sun, G. (2012). How small can "Nano" be in a "Nanolaser"? *Nanophotonics*, 1(1):3–8.

Kim, J., Wang, L.-W., and Zunger, A. (1998). Comparison of the electronic structure of InAs/GaAs pyramidal quantum dots with different facet orientations. *Phys. Rev. B*, 57:R9408–R9411.

Kippenberg, T. J. and Vahala, K. J. (2008). Cavity Optomechanics: Back-Action at the Mesoscale. *Science*, 321(5893):1172–1176.

Kira, M., Jahnke, F., Hoyer, W., and Koch, S. (1999). Quantum theory of spontaneous emission and coherent effects in semiconductor microstructures. *Progress in Quantum Electronics*, 23(6):189–279.

Kira, M., Jahnke, F., and Koch, S. W. (1998). Microscopic Theory of Excitonic Signatures in Semiconductor Photoluminescence. *Phys. Rev. Lett.*, 81(15):3263–3266.

Kira, M. and Koch, S. W. (2008). Cluster-expansion representation in quantum optics. *Phys. Rev. A*, 78(2):022102.

Kira, M. and Koch, S. W. (2011). *Semiconductor Quantum Optics*. Cambridge University Press.

Kirstaedter, N., Ledentsov, N., Grundmann, M., Bimberg, D., Ustinov, V., Ruvimov, S., Maximov, M., KOP'EV, P. S., Alferov, Z. I., Richter, U., et al. (1994). Low threshold, large to injection laser emission from (InGa) as quantum dots. *Electron. Lett.*, 30(17):1416–1417.

Köhler, T. and Burnett, K. (2002). Microscopic quantum dynamics approach to the dilute condensed Bose gas. *Phys. Rev. A*, 65(3):033601.

Kroemer, H. (1963). A proposed class of hetero-junction injection lasers. *Proceedings of the IEEE*, 51(12):1782–1783.

Lax, M. (1967). Quantum Noise. X. Density-Matrix Treatment of Field and Population-Difference Fluctuations. *Phys. Rev.*, 157(2):213–231.

Lax, M. and Louisell, W. H. (1969). Quantum Noise. XII. Density-Operator Treatment of Field and Population Fluctuations. *Phys. Rev.*, 185(2):568–591.

Lee, S., Oyafuso, F., von Allmen, P., and Klimeck, G. (2004). Boundary conditions for the electronic structure of finite-extent embedded semiconductor nanostructures. *Phys. Rev. B*, 69:045316.

Lermer, M., Gregersen, N., Lorke, M., Schild, E., Gold, P., Mørk, J., Schneider, C., Forchel, A., Reitzenstein, S., Höfling, S., and Kamp, M. (2013). High beta lasing in micropillar cavities with adiabatic layer design. *Appl. Phys. Lett.*, 102(5):052114–052114–4.

Lett, P. (1986). Investigation of first-passage-time problems in the two-mode dye laser. *Phys. Rev. A*, 34(3):2044–2057.

Leymann, H. A. M., Foerster, A., Jahnke, F., Wiersig, J., and Gies, C. (2015). Sub- and Superradiance in Nanolasers. *Phys. Rev. Applied*, 4(4):044018.

Leymann, H. A. M., Foerster, A., Khanbekyan, M., and Wiersig, J. (2013a). Strong photon bunching in a quantum-dot-based two-mode microcavity laser. *Phys. Status Solidi B*, 250(9):1777–1780.

Leymann, H. A. M., Foerster, A., and Wiersig, J. (2013b). Expectation value based cluster expansion. *Phys. Status Solidi (c)*, 10(9):1242–1245.

Leymann, H. A. M., Foerster, A., and Wiersig, J. (2014). Expectation value based equation-of-motion approach for open quantum systems: A general formalism. *Phys. Rev. B*, 89(8):085308.

Leymann, H. A. M., Hopfmann, C., Albert, F., Foerster, A., Khanbekyan, M., Schneider, C., Höfling, S., Forchel, A., Kamp, M., Wiersig, J., and Reitzenstein, S. (2013c). Intensity fluctuations in bimodal micropillar lasers enhanced by quantum-dot gain competition. *Phys. Rev. A*, 87(5):053819.

Leymann, H. A. M., Vorberg, D., Lettau, T., Hopfmann, C., Schneider, C., Kamp, M., Höfling, S., Ketzmerick, R., Wiersig, J., Reitzenstein, S., and Eckardt, A. (2016). Pump-power-driven mode switching in a microcavity device and its relation to Bose-Einstein condensation. *arXiv:1612.04312*.

Liu, C., Di Falco, A., and Fratalocchi, A. (2014). Dicke Phase Transition with Multiple Superradiant States in Quantum Chaotic Resonators. *Phys. Rev. X*, 4(2):021048.

Lodahl, P., Floris van Driel, A., Nikolaev, I. S., Irman, A., Overgaag, K., Vanmaekelbergh, D., and Vos, W. L. (2004). Controlling the dynamics of spontaneous emission from quantum dots by photonic crystals. *Nature*, 430(7000):654–657.

Loudon, R. (2000). *The Quantum Theory of Light*. Oxford University Press.

Maiman, T. H. (1960). Stimulated optical radiation in ruby. *Nature*, 187(4736):493–494.

Majumdar, A., Bajcsy, M., Rundquist, A., and Vučković, J. (2012). Loss-Enabled Sub-Poissonian Light Generation in a Bimodal Nanocavity. *Phys. Rev. Lett.*, 108(18):183601.

Mandel, L. and Wolf, E. (1995). *Optical Coherence and Quantum Optics*. Cambridge University Press.

Mascarenhas, E., Gerace, D., Santos, M. F., and Auffèves, A. (2013). Cooperativity of a few quantum emitters in a single-mode cavity. *Phys. Rev. A*, 88(6):063825.

McKeever, J., Boca, A., Boozer, A. D., Buck, J. R., and Kimble, H. J. (2003). Experimental realization of a one-atom laser in the regime of strong coupling. *Nature*, 425(6955):268–271.

Meiser, D. and Holland, M. J. (2010). Steady-state superradiance with alkaline-earth-metal atoms. *Phys. Rev. A*, 81(3):033847.

Meiser, D., Ye, J., Carlson, D. R., and Holland, M. J. (2009). Prospects for a Millihertz-Linewidth Laser. *Phys. Rev. Lett.*, 102(16):163601.

Meyer, G. M. and Yeoman, G. (1997). Cavity-Induced Interference Pattern with Dark Center from Two Fluorescing Atoms. *Phys. Rev. Lett.*, 79(14):2650–2653.

Meystre, P. and Murray, S. (1999). Interaction Between Atoms and Quantized Fields. In *Elements of Quantum Optics*, pages 286–306. Springer Berlin Heidelberg.

Michler, P., editor (2009). *Single Semiconductor Quantum Dots*. NanoScience and Technology. Springer Berlin Heidelberg.

Michler, P., Kiraz, A., Becher, C., Schoenfeld, W. V., Petroff, P. M., Zhang, L., Hu, E., and Imamoglu, A. (2000). A Quantum Dot Single-Photon Turnstile Device. *Science*, 290(5500):2282–2285.

Moelbjerg, A., Kaer, P., Lorke, M., Tromborg, B., and Mork, J. (2013). Dynamical Properties of Nanolasers Based on Few Discrete Emitters. *IEEE Journal of Quantum Electronics*, 49(11):945–954.

Mølmer, K. (1997). Optical coherence: A convenient fiction. *Phys. Rev. A*, 55(4):3195–3203.

Monroe, C. (2002). Quantum information processing with atoms and photons. *Nature*, 416(6877):238–246.

Mu, Y. and Savage, C. M. (1992). One-atom lasers. *Phys. Rev. A*, 46(9):5944–5954.

Musiał, A., Hopfmann, C., Heindel, T., Gies, C., Florian, M., Leymann, H. A. M., Foerster, A., Schneider, C., Jahnke, F., Höfling, S., Kamp, M., and Reitzenstein, S. (2015). Correlations between axial and lateral emission of coupled quantum dot-micropillar cavities. *Phys. Rev. B*, 91(20):205310.

Nathan, M. I., Dumke, W. P., Burns, G., Dill, F. H., and Lasher, G. (1962). Stimulated emission of radiation from GaAs p-n junctions. *Appl. Phys. Lett.*, 1(3):62–64.

Neumeier, S. (2016). *Ratenmodell für gekoppelte 2-Niveau Quantenpunktpaare in Einmoden-Nanolasern*. Master Thesis, Magdeburg.

Nielsen, T. R., Gartner, P., and Jahnke, F. (2004). Many-body theory of carrier capture and relaxation in semiconductor quantum-dot lasers. *Phys. Rev. B*, 69(23):235314.

Nobelprize.org (2000). The 2000 nobel prize in physics - advanced information. `http://www.nobelprize.org/nobel_prizes/physics/laureates/2000/advanced.html`. [Online;].

Noda, S. (2006). Seeking the Ultimate Nanolaser. *Science*, 314(5797):260–261.

Noginov, M. A., Zhu, G., Belgrave, A. M., Bakker, R., Shalaev, V. M., Narimanov, E. E., Stout, S., Herz, E., Suteewong, T., and Wiesner, U. (2009). Demonstration of a spaser-based nanolaser. *Nature*, 460(7259):1110–1112.

Nomura, M., Kumagai, N., Iwamoto, S., Ota, Y., and Arakawa, Y. (2009). Photonic crystal nanocavity laser with a single quantum dot gain. *Opt. Express*, 17(18):15975–15982.

Nomura, M., Kumagai, N., Iwamoto, S., Ota, Y., and Arakawa, Y. (2010). Laser oscillation in a strongly coupled single-quantum-dot-nanocavity system. *Nat Phys*, 6(4):279–283.

Nußmann, S., Hijlkema, M., Weber, B., Rohde, F., Rempe, G., and Kuhn, A. (2005). Submicron Positioning of Single Atoms in a Microcavity. *Phys. Rev. Lett.*, 95(17):173602.

Oppel, S., Wiegner, R., Agarwal, G. S., and von Zanthier, J. (2014). Directional Superradiant Emission from Statistically Independent Incoherent Nonclassical and Classical Sources. *Phys. Rev. Lett.*, 113(26):263606.

Pellegrino, J., Bourgain, R., Jennewein, S., Sortais, Y., Browaeys, A., Jenkins, S., and Ruostekoski, J. (2014). Observation of Suppression of Light Scattering Induced by Dipole-Dipole Interactions in a Cold-Atom Ensemble. *Phys. Rev. Lett.*, 113(13):133602.

Pistorius, T. (2015). *Einfluss von Vielteilcheneffekten auf die Kohärenzeigenschaften von Halbleiter-Quantenpunkt-Laser*. Master Thesis, Magdeburg.

Raizen, M. G., Thompson, R. J., Brecha, R. J., Kimble, H. J., and Carmichael, H. J. (1989). Normal-mode splitting and linewidth averaging for two-state atoms in an optical cavity. *Phys. Rev. Lett.*, 63(3):240–243.

Redlich, C., Lingnau, B., Holzinger, S., Schlottmann, E., Kreinberg, S., Schneider, C., Kamp, M., Höfling, S., Wolters, J., Reitzenstein, S., and Lüdge, K. (2016). Mode-switching induced super-thermal bunching in quantum-dot microlasers. *New Journal of Physics*, 18(6):063011.

Reithmaier, J. P., Sęk, G., Löffler, A., Hofmann, C., Kuhn, S., Reitzenstein, S., Keldysh, L. V., Kulakovskii, V. D., Reinecke, T. L., and Forchel, A. (2004). Strong coupling in a single quantum dot-semiconductor microcavity system. *Nature*, 432(7014):197–200.

Reitzenstein, S. (2012). Semiconductor Quantum Dot Microcavities for Quantum Optics in Solid State. *IEEE Journal of Selected Topics in Quantum Electronics*, 18(6):1733–1746.

Reitzenstein, S. and Forchel, A. (2010a). Quantum dot micropillars. *J. Phys. D: Appl. Phys.*, 43(3):033001.

Reitzenstein, S. and Forchel, A. (2010b). Quantum dot micropillars. *J. Phys. D: Appl. Phys.*, 43(3):033001.

Reitzenstein, S., Heindel, T., Kistner, C., Albert, F., Braun, T., Hopfmann, C., Mrowinski, P., Lermer, M., Schneider, C., Höfling, S., Kamp, M., and Forchel, A. (2011). Electrically Driven Quantum Dot Micropillar Light Sources. *IEEE Journal of Selected Topics in Quantum Electronics*, 17(6):1670–1680.

Reitzenstein, S., Heindel, T., Kistner, C., Rahimi-Iman, A., Schneider, C., Höfling, S., and Forchel, A. (2008). Low threshold electrically pumped quantum dot-micropillar lasers. *Appl. Phys. Lett.*, 93(6):061104.

Reitzenstein, S., Hofmann, C., Gorbunov, A., Strauß, M., Kwon, S. H., Schneider, C., Löffler, A., Höfling, S., Kamp, M., and Forchel, A. (2007). AlAs GaAs micropillar cavities with quality factors exceeding 150.000. *Appl. Phys. Lett.*, 90(25):251109.

Reitzenstein, S., Löffler, A., Hofmann, C., Kubanek, A., Kamp, M., Reithmaier, J. P., Forchel, A., Kulakovskii, V. D., Keldysh, L. V., Ponomarev, I. V., and Reinecke, T. L. (2006). Coherent photonic coupling of semiconductor quantum dots. *Opt. Lett.*, 31(11):1738–1740.

Rice, P. R. and Carmichael, H. J. (1994). Photon statistics of a cavity-QED laser: A comment on the laser-phase-transition analogy. *Phys. Rev. A*, 50(5):4318–4329.

Richter, M., Carmele, A., Sitek, A., and Knorr, A. (2009). Few-Photon Model of the Optical Emission of Semiconductor Quantum Dots. *Phys. Rev. Lett.*, 103(8):087407.

Ritter, S., Gartner, P., Gies, C., and Jahnke, F. (2010). Emission properties and photon statisticsof a single quantum dot laser. *Opt. Express*, 18(10):9909–9921.

Roumpos, G. and Cundiff, S. T. (2013). Photon number distributions from a diode laser. *Opt. Lett.*, 38(2):139–141.

Ruiz-Rivas, J., del Valle, E., Gies, C., Gartner, P., and Hartmann, M. J. (2014). Spontaneous collective coherence in driven dissipative cavity arrays. *Phys. Rev. A*, 90(3):033808.

Rundquist, A., Bajcsy, M., Majumdar, A., Sarmiento, T., Fischer, K., Lagoudakis, K. G., Buckley, S., Piggott, A. Y., and Vučković, J. (2014). Nonclassical higher-order photon correlations with a quantum dot strongly coupled to a photonic-crystal nanocavity. *Phys. Rev. A*, 90(2):023846.

Santoprete, R., Koiller, B., Capaz, R. B., Kratzer, P., Liu, Q. K. K., and Scheffler, M. (2003). Tight-binding study of the influence of the strain on the electronic properties of inas/gaas quantum dots. *Phys. Rev. B*, 68:235311.

Schawlow, A. L. and Townes, C. H. (1958). Infrared and optical masers. *Phys. Rev.*, 112:1940–1949.

Scheibner, M., Schmidt, T., Worschech, L., Forchel, A., Bacher, G., Passow, T., and Hommel, D. (2007). Superradiance of quantum dots. *Nat Phys*, 3(2):106–110.

Schliwa, A. and Winkelnkemper, M. (2008). *Semiconductor Nanostructures*, chapter Theory of Excitons in InGaAs/GaAs Quantum Dots, pages 139–164. Springer Berlin Heidelberg.

Schlottmann, E., von Helversen, M., Krüger, F., Schmidt, M., Gericke, F., Kreinberg, S., Schneider, C., Kamp, M., Höfling, S., Beyer, J., and Reitzenstein, S. (2016). Determining the photon number distribution of a bimodal quantum dot microlaser via a transition edge sensor. NOEKS 13.

Schneider, H. C., Chow, W. W., and Koch, S. W. (2001a). Many-body effects in the gain spectra of highly excited quantum-dot lasers. *Phys. Rev. B*, 64:115315.

Schneider, H. C., Fischer, A. J., Chow, W. W., and Klem, J. F. (2001b). Temperature dependence of laser threshold in an ingaasn vertical-cavity surface-emitting laser. *Appl. Phys. Lett.*, 78(22):3391–3393.

Schulz, S., Schumacher, S., and Czycholl, G. (2006). Tight-binding model for semiconductor quantum dots with a wurtzite crystal structure: From one-particle properties to coulomb correlations and optical spectra. *Phys. Rev. B*, 73:245327.

Schulze, F., Lingnau, B., Hein, S. M., Carmele, A., Schöll, E., Lüdge, K., and Knorr, A. (2014). Feedback-induced steady-state light bunching above the lasing threshold. *Phys. Rev. A*, 89(4):041801.

Schwab, M., Kurtze, H., Auer, T., Berstermann, T., Bayer, M., Wiersig, J., Baer, N., Gies, C., Jahnke, F., Reithmaier, J. P., Forchel, A., Benyoucef, M., and Michler, P. (2006). Radiative emission dynamics of quantum dots in a single cavity micropillar. *Phys. Rev. B*, 74(4):045323.

Schwabl, F. (2008). *Quantenmechanik für Fortgeschrittene (QM II)*. Springer-Lehrbuch. Springer Berlin Heidelberg.

Scully, M. O. and Lamb, W. E. (1967). Quantum Theory of an Optical Maser. I. General Theory. *Phys. Rev.*, 159(2):208–226.

Scully, M. O. and Svidzinsky, A. A. (2009). The Super of Superradiance. *Science*, 325(5947):1510–1511.

Sebald, K., Kruse, C., and Wiersig, J. (2009). Properties and prospects of blueâgreen emitting iiâvi-based monolithic microcavities. *Phys. Status Solidi (b)*, 246(2):255–271.

Sheng, W., Cheng, S.-J., and Hawrylak, P. (2005). Multiband theory of multi-exciton complexes in self-assembled quantum dots. *Phys. Rev. B*, 71(3):035316.

Shore, B. W. and Knight, P. L. (1993). The Jaynes-Cummings Model. *Journal of Modern Optics*, 40(7):1195–1238.

Siegman, A. (1986). *Lasers*. University Science Books.

Singh, S. and Mandel, L. (1979). Mode competition in a homogeneously broadened ring laser. *Phys. Rev. A*, 20(6):2459–2463.

Singleton, J. (2001). *Band Theory and Electronic Properties of Solids*. Oxford Master Series in Physics 2.

Sitek, A. and Manolescu, A. (2013). Dicke states in multiple quantum dots. *Phys. Rev. A*, 88(4):043807.

Stevens, M. J., Baek, B., Dauler, E. A., Kerman, A. J., Molnar, R. J., Hamilton, S. A., Berggren, K. K., Mirin, R. P., and Nam, S. W. (2010). High-order temporal coherences of chaotic and laser light. *Opt. Express*, 18(2):1430–1437.

Stier, O., Grundmann, M., and Bimberg, D. (1999). Electronic and optical properties of strained quantum dots modeled by 8-band k·p theory. *Phys. Rev. B*, 59:5688–5701.

Strauf, S., Hennessy, K., Rakher, M. T., Choi, Y.-S., Badolato, A., Andreani, L. C., Hu, E. L., Petroff, P. M., and Bouwmeester, D. (2006). Self-Tuned Quantum Dot Gain in Photonic Crystal Lasers. *Phys. Rev. Lett.*, 96(12):127404.

Strauf, S. and Jahnke, F. (2011). Single quantum dot nanolaser. *Laser & Photonics Reviews*, 5(5):607–633.

Tavis, M. and Cummings, F. W. (1968). Exact Solution for an N-Molecule-Radiation—Field Hamiltonian. *Phys. Rev.*, 170(2):379–384.

Temnov, V. V. and Woggon, U. (2005). Superradiance and Subradiance in an Inhomogeneously Broadened Ensemble of Two-Level Systems Coupled to a Low-Q Cavity. *Phys. Rev. Lett.*, 95(24):243602.

Temnov, V. V. and Woggon, U. (2009). Photon statistics in the cooperative spontaneous emission. *Opt. Express*, 17(7):5774–5782.

Thompson, R. J., Rempe, G., and Kimble, H. J. (1992). Observation of normal-mode splitting for an atom in an optical cavity. *Phys. Rev. Lett.*, 68(8):1132–1135.

Timothy Noe Ii, G., Kim, J.-H., Lee, J., Wang, Y., Wójcik, A. K., McGill, S. A., Reitze, D. H., Belyanin, A. A., and Kono, J. (2012). Giant superfluorescent bursts from a semiconductor magneto-plasma. *Nat Phys*, 8(3):219–224.

Trimborn, F., Witthaut, D., Hennig, H., Kordas, G., Geisel, T., and Wimberger, S. (2011). Decay of a Bose-Einstein condensate in a dissipative lattice - the mean-field approximation and beyond. *Eur. Phys. J. D*, 63(1):63–71.

Tuchman, A. K., Long, R., Vrijsen, G., Boudet, J., Lee, J., and Kasevich, M. A. (2006). Normal-mode splitting with large collective cooperativity. *Phys. Rev. A*, 74(5):053821.

Ulrich, S. M., Gies, C., Ates, S., Wiersig, J., Reitzenstein, S., Hofmann, C., Löffler, A., Forchel, A., Jahnke, F., and Michler, P. (2007). Photon Statistics of Semiconductor Microcavity Lasers. *Phys. Rev. Lett.*, 98(4):043906.

Vahala, K. J. (2003). Optical microcavities. *Nature*, 424(6950):839–846.

Vermaseren, J., Kuipers, J., Tentyukov, M., Uedam, T., and Vollinga, J. (2000). `FORM` Reference manual. `https://www.nikhef.nl/%7eform/maindir/documentation/reference/online/online.html`. [Online;].

Vermaseren, J. A. M. (2000). New features of FORM. *arXiv:math-ph/0010025*.

Virte, M., Panajotov, K., Thienpont, H., and Sciamanna, M. (2013). Deterministic polarization chaos from a laser diode. *Nat Photon*, 7(1):60–65.

Wang, C. Y., Diehl, L., Gordon, A., Jirauschek, C., Kärtner, F. X., Belyanin, A., Bour, D., Corzine, S., Höfler, G., Troccoli, M., Faist, J., and Capasso, F. (2007). Coherent instabilities in a semiconductor laser with fast gain recovery. *Phys. Rev. A*, 75(3):031802.

Wang, W. H., Ghosh, S., Mendoza, F. M., Li, X., Awschalom, D. D., and Samarth, N. (2005). Static and dynamic spectroscopy of Al,Ga)AsGaAs microdisk lasers with interface fluctuation quantum dots. *Phys. Rev. B*, 71(15):155306.

Watt, A. (2005). *Beginning Regular Expressions*. Wiley India Pvt. Limited.

Weisbuch, C., Nishioka, M., Ishikawa, A., and Arakawa, Y. (1992). Observation of the coupled exciton-photon mode splitting in a semiconductor quantum microcavity. *Phys. Rev. Lett.*, 69(23):3314–3317.

Wickenbrock, A., Hemmerling, M., Robb, G. R. M., Emary, C., and Renzoni, F. (2013). Collective strong coupling in multimode cavity QED. *Phys. Rev. A*, 87(4):043817.

Wiersig, J. (2010). Microscopic theory of first-order coherence in microcavity lasers based on semiconductor quantum dots. *Phys. Rev. B*, 82(15):155320.

Wiersig, J., Gies, C., Jahnke, F., Aßmann, M., Berstermann, T., Bayer, M., Kistner, C., Reitzenstein, S., Schneider, C., Höfling, S., Forchel, A., Kruse, C., Kalden, J., and Hommel, D. (2009). Direct observation of correlations between individual photon emission events of a microcavity laser. *Nature*, 460(7252):245–249.

Wiersma, D. S. (2008). The physics and applications of random lasers. *Nat Phys*, 4(5):359–367.

Witthaut, D., Trimborn, F., Hennig, H., Kordas, G., Geisel, T., and Wimberger, S. (2011). Beyond mean-field dynamics in open Bose-Hubbard chains. *Phys. Rev. A*, 83(6):063608.

Wu, Y. and Yang, X. (2007). Strong-coupling theory of periodically driven two-level systems. *Phys. Rev. Lett.*, 98:013601.

Xie, Q., Brown, J. L., Jones, R. L., Nostrand, J. E. V., and Leedy, K. D. (2000). Growth of vertically self-organized ingaas quantum dots with narrow inhomogeneous broadening. *Appl. Phys. Lett.*, 76(21):3082–3084.

Xie, Z. G., Götzinger, S., Fang, W., Cao, H., and Solomon, G. S. (2007). Influence of a Single Quantum Dot State on the Characteristics of a Microdisk Laser. *Phys. Rev. Lett.*, 98(11):117401.

Yokoyama, H. and Brorson, S. D. (1989). Rate equation analysis of microcavity lasers. *J. Appl. Phys.*, 66(10):4801–4805.

Yoshie, T., Scherer, A., Hendrickson, J., Khitrova, G., Gibbs, H. M., Rupper, G., Ell, C., Shchekin, O. B., and Deppe, D. G. (2004). Vacuum Rabi splitting with a single quantum dot in a photonic crystal nanocavity. *Nature*, 432(7014):200–203.

Yu, P. Y. and Cardona, M. (2010). *Fundamentals of Semiconductors: Physics and Materials Properties*. Springer Berlin Heidelberg, Berlin, Heidelberg.

Acknowledgments

Der Mensch bringt sogar die Wüsten zum Blühen. Die einzige Wüste, die ihm noch Widerstand bereitet, befindet sich in seinem Kopf.

Ephraim Kishon

In this sense, I like to thank everybody who supported me during the work on this thesis. The greatest thanks, however, goes to my supervisor Prof. Dr. Jan Wiersig who took the patience and the time to help me with all my (scientific) problems. His way of thinking about science and research became my starting point that allowed me to finish this work.

At least as much as important as my own work is the work of my cooperation partners that put their own dedication on this subject and allowed me to embed my results in broader context. Therefore I like to thank my colleagues M. Khanbekyan and A. Leymann and my cooperation partners from other univerities M. Florian, C. Gies and F. Jahnke from the university of Bremen; C. Hopfmann, A. Musiał, T. Heindel, F. Albert, and S. Reitzenstein from the TU Berlin; C. Schneider, A. Forchel, M. Kamp, and S. Höfling from the TU Würzburg; M. Aßmann and M. Bayer from the TU Dortmund.

I also like to thank the group of Prof. Wiersig, that allowed for a great work atmosphere. Not only the amusing conversations during the coffee breaks but also the willingness to help me with problems will remain engraved in my memory. Therefore I like to thank G. Kasner, J.B. Shim, J. Unterhinninghofen, A. Eberspächer, J. Kullig and S. Simon.

It was a special pleasure for me to work so closely together with A. Leymann who became a real friend to me. Together we had the most interesting mail conversations one could imagine and had always fun working out new ideas.

Finally, I would like to thank my family for their love and support. Especially my parents who encouraged me to study such an incomprehensible subject as physics and of course my girlfriend Yuliya who helped me and motivated me to my best performance.

Thank you all!

List of Publications

- **Foerster, A.**, Leymann, H. A. M., and Wiersig, J., *Computer-aided cluster expansion: An efficient algebraic approach for open quantum many-particle systems.* Comput. Phys. Commun. **212**, 210 10 pages(2017).

- M. Fanaei, **Foerster, A.**, Leymann, H. A. M., and Wiersig, J., *The effect of direct dissipative coupling of two competing modes on intensity fluctuations in a quantum-dot-microcavity laser.* Phys. Rev. A. **98**, 043814 8 pages(2016).

- Jahnke F., Gies C., Aßmann M., Bayer M., Leymann, H. A. M., **Foerster A.**, Wiersig J., Schneider C., Kamp M., Höfling S., *Giant photon bunching, superradiant pulse emission and excitation trapping in quantum-dot nanolasers.* Nat. Comm. **7**, 11540 7 pages(2016).

- Leymann, H. A. M., **Foerster, A.**, Jahnke, F., Wiersig, J., and Gies, C., *Sub- and Superradiance in Nanolasers.* Phys. Rev. Applied, **4**, 044018 13 pages (2015).

- Musiał, A., Hopfmann, C., Heindel, T., Gies, C., Florian, M., Leymann, H. A. M., **Foerster, A.**, Schneider, C., Jahnke, F., Höfling, S., Kamp, M., and Reitzenstein, S., *Correlations between axial and lateral emission of coupled quantum dot-micropillar cavities.* Phys. Rev. B, **91** 205310 10 pages (2015).

- Khanbekyan, M., Leymann, H. A. M., Hopfmann, C., **Foerster, A.**, Schneider, C., Höfling, S., Kamp, M., Wiersig, J., and Reitzenstein, S., *Unconventional collective normal-mode coupling in quantum-dot-based bimodal microlasers.* Phys. Rev. A, **91** 043840 5 pages (2015).

- Leymann, H. A. M., **Foerster, A.**, and Wiersig, J., *Expectation value based equation-of-motion approach for open quantum systems: A general formalism.* Phys. Rev. B, **89** 085308 11 pages (2014).

- Leymann, H. A. M., Hopfmann, C., Albert, F., **Foerster, A.**, Khanbekyan, M., Schneider, C., Höfling, S., Forchel, A., Kamp, M., Wiersig, J., and Reitzenstein, S., *Intensity fluctuations in bimodal micropillar lasers enhanced by quantum-dot gain competition.* Phys. Rev. A, **87** 053819 10 pages (2013).

- Leymann, H. A. M., **Foerster**, A., and Wiersig, J., *Expectation value based cluster expansion.* physica status solidi C, **10** 1242 4 pages (2013).

- Leymann, H. A. M., **Foerster, A**., Khanbekyan, M., and Wiersig, J., *Strong photon bunching in a quantum-dot-based two-mode microcavity laser.* Phys. Status Solidi B, **250** 1777 4 pages (2013).

Erklärung

Hiermit erkläre ich, dass ich die von mir eingereichte Dissertation zu dem Thema

Theory of Semiconductor Quantum-Dot Microcavity Lasers
Computational modeling and significance for experimental realization

selbständig verfasst, nicht schon als Dissertation verwendet habe und die benutzten Hilfsmittel und Quellen vollständig angegeben wurden.

Weiterhin erkläre ich, dass ich weder diese noch eine andere Arbeit zur Erlangung des akademischen Grades doctor rerum naturalium (Dr. rer. nat.) an anderen Einrichtungen eingereicht habe.

Dipl.-Phys. Alexander Foerster
Magdeburg, den 15.03.2017